Diffusion Tensor Imaging at High Magnetic Field

by

Corey Allan Baron

A thesis submitted in partial fulfillment of the requirement for the degree of

Doctor of Philosophy

Department of Biomedical Engineering

University of Alberta

Abstract

Diffusion magnetic resonance imaging (dMRI) measures the diffusion (i.e. random molecular motion) of water. Since the motion of water is inhibited by cellular membranes, dMRI provides insight into the microstructural characteristics of the tissue. However, distinguishing between small anatomical subdivisions can be difficult due to dMRI methods having an inherently low resolution. Increasing the resolution necessarily reduces the signal-to-noise ratio, and to compensate for this a higher static magnetic field and larger diffusion gradients can be utilized. In addition, there are newly emerging dMRI techniques that have not been successfully implemented in the human brain due to insufficient signal and gradient strengths on clinical MRI systems. However, increasing these parameters introduces new challenges.

The goal of this thesis was to address the challenges of performing dMRI with a stronger magnetic field and gradients, and then to use the extra signal for higher resolution and to enable new techniques that require more signal. To do this, a 4.7 T human MRI system with 60 mT/m gradients was utilized, which is a three times stronger field and 50% larger gradients compared to typical clinical scanners. Approximately half of the thesis work involved solving challenges at high field or gradient strengths, while the remainder involved applications enabled by the high strength MRI system.

The first challenge investigated was a previously undocumented issue for dMRI introduced by strong gradients, concomitant gradient fields. Errors introduced by these concomitant fields was found to be considerable in certain cases, and techniques to mitigate them were explored. Another challenge involved developing robust methods to perform parallel imaging, which is a technique used to prevent distortions that worsen at higher field strengths. A

final challenge investigated was errors introduced by the unwanted signal that stems from cerebrospinal fluid. Traditional approaches to mitigate the error do not translate well to high field, and an alternative method was sought and characterized.

A potential application of the high strength MRI system involves the probing of different tissue microstructure length scales. Typical dMRI techniques are only sensitive to length scales longer than typical microstructural dimensions because of a long "diffusion time". However, the newly developed oscillating gradient spin-echo (OGSE) technique is more sensitive to smaller length scales because it can achieve much shorter diffusion times, which may give new insight into healthy development or disease. Accordingly, OGSE was used to investigate the microstructural length scale dependence of dMRI as a function of diffusion direction for the first time in healthy subjects and in patients with stroke. The former subject group was required to better understand the healthy brain and provide a reference point for comparison with disease. The latter cohort of subjects helps to elucidate the underpinnings of why standard dMRI is sensitive to stroke, which is still not well understood even though dMRI is routinely used in its diagnosis. In addition, dMRI of stroke is traditionally performed using thick slices to maintain low scan times. Accordingly, by utilizing a high resolution dMRI sequence in stroke patients, it was found in this thesis that thinner slices yield more precise measurements of lesion volume and diffusion parameters.

In summary, the thesis work shows that dMRI can be successfully translated to large magnetic field and gradient strengths. The advantages of doing so are the ability to perform novel dMRI techniques and improved performance of existing techniques. While this work was performed at a field strength not commonly utilized for human MRI (4.7 Tesla), all the work described in this

thesis could be translated to 7 Tesla or 3 Tesla with modern radiofrequency coil arrays.

Preface

This thesis is an original work by Corey Allan Baron. Chapter 2 of this thesis has been published as Baron CA, Lebel RM, Wilman AH, Beaulieu C. "The Effect of Concomitant Gradient Fields on Diffusion Tensor Imaging". Magn Reson Med. 68:1190-201 (2012) doi: 10.1002/mrm.24120. Concept formation was developed by me with the assistance of R. M. Lebel, Professor A. Wilman, and C. Beaulieu. I was responsible for all other aspects of the work, including pulse sequence development, data collection, analysis, and manuscript composition. C. Beaulieu was the supervisory author and was involved with manuscript composition. Chapter 4 of this thesis has been published as Baron CA, Beaulieu C. "Acquisition Strategy to Reduce Cerebrospinal Fluid Partial Volume Effects for Improved DTI Tractography". Magn Reson Med. Epub Early View DOI: 10.1002/mrm.25226. I was responsible for all aspects of the work, including pulse sequence development, data collection, analysis, and manuscript composition. C. Beaulieu was the supervisory author and was involved with concept formation and manuscript composition. Chapter 5 of this thesis has been published as Baron CA, Beaulieu C. "Oscillating Gradient Spin-Echo (OGSE) Diffusion Tensor Imaging of the Human Brain". Magn Reson Med. Epub Early View DOI: 10.1002/mrm.24987. I was responsible for all aspects of the work, including pulse sequence development, data collection, analysis, and manuscript composition. C. Beaulieu was the supervisory author and was involved with concept formation and manuscript composition.

Some of the research conducted for this thesis in Chapters 6 and 7 forms part of a research collaboration led by Professor C. Beaulieu (Biomedical Engineering; University of Alberta), with M. Kate (Neurology; University

of Alberta), L. Gioia (Neurology; University of Alberta), K. Butcher (Neurology; University of Alberta), D. Emery (Radiology; University of Alberta), and Professor M. Budde (Neurosurgery, Medical College of Wisconsin). Patient recruitment for Chapters 6 and 7 was aided by M. Kate (Neurology), L. Gioia (Neurology), K. Butcher (Neurology), and D. Emery (Radiology). The beading simulations referred to in Chapter 6 were carried out by M. Budde (Wisconsin). All other aspects of the research were my original work.

The research projects of which this thesis is a part received research ethics approval from the University of Alberta Research Ethics Board, Project Name "MRI of Cerebrovascular Disease" (Pro00000912) for the scanning of stroke in-patients, and Project Name "Development of Magnetic Resonance Imaging and Its Application to Human Disease" (Pro00002112) for the scanning of healthy volunteers.

Acknowledgments

I would like to acknowledge financial support generously provided by the Natural Sciences and Engineering Research Council of Canada and Alberta Innovates Health Solutions. Projects were funded by the Canadian Institutes of Health Research and the Heart and Stroke Foundation of Alberta, NWT, and Nunavut . MRI infrastructure was funded by the Canada Foundation for Innovation, Alberta Science and Research Authority, Alberta Heritage Foundation for Medical Research, and the University Hospital Foundation.

It has been great to work with all the students in Biomedical Engineering at the University of Alberta. The atmosphere in the department was truly refreshing and made for many great memories. I would especially like to thank Marc Lebel, who was always willing to lend an ear and help out a new student first learning about MRI, and Rob Stobbe for many interesting discussions. I would like to thank the collaborators I have had the pleasure of working with, with a special thanks to Mahesh Kate, Laura Gioia, and Kenneth Butcher, who enabled all the stroke patient scanning. Thank you to the helpful professors and staff within the department who are approachable and always friendly. Also thank you Karim Damji, for always keeping the MRI and RF coils in peak working condition.

I would like to thank my supervisor, Christian Beaulieu. You have given me the freedom to choose how to approach the research while always being available for help or advice. You have taught me a great deal and working with you has been a great experience.

Thank you to my friends and family, who have always been supportive and not been too hard on me for still not having a "real" job. Thank you for providing wonderful distractions that helped to rejuvenate me. Thank you to

my parents, for always being supportive and encouraging.

Finally, my most earnest thanks go to my family. Thank you June for supporting me every step of the way, patiently listening to me ramble about my research, listening to all my talks, volunteering in the scanner (many times!), and giving great advice (research or otherwise). Thank you for helping me through the tough spots and sharing in celebrating successes. Also, thank you to Rosie, for those big brown eyes that light up when I get home.

Table of Contents

1 Introduction **1**

1.1 Overview 1

1.2 Scope of Thesis 2

1.3 The Brain 4

1.3.1 Brain Tissue 4

1.3.2 Stroke 6

1.4 Magnetic Resonance Imaging Fundamentals 8

1.4.1 Nuclear Magnetic Resonance 8

1.4.2 Image Encoding 11

1.4.3 k-space 13

1.4.4 Echo Planar Imaging 16

1.5 Diffusion Tensor Imaging 23

1.5.1 Sensitizing the Signal to Diffusion 23

1.5.2 Diffusion Measurements in Tissue 27

1.5.3 Diffusion Tensor Imaging Metrics 29

1.5.4 Probing Diffusion Length Scales 30

1.5.5 High Field DTI 35

1.6 Summary 39

2 The Effect of Concomitant Gradient Fields on Diffusion Tensor Imaging **40**

2.1 Introduction 40

2.2 Theory 43

2.2.1 Concomitant Gradient Fields for Diffusion Imaging . . 43

2.2.2 In-Plane Dephasing 45

2.2.3 Intravoxel Dephasing 46
2.2.4 Corrections 49
2.3 Methods 50
2.4 Results 53
2.4.1 In-Plane Dephasing 53
2.4.2 Intravoxel Dephasing 57
2.4.3 Corrections and DTI Metrics 59
2.5 Discussion 63
2.6 Results Additional to the Published Paper 70
2.7 Collaborators 71

3 Motion Insensitive GRAPPA for Echo-Planar Imaging 72
3.1 Introduction 72
3.2 Theory 73
3.3 Methods 77
3.3.1 Simulation 77
3.3.2 Image Acquisition 80
3.3.3 Image Analysis 81
3.4 Results 82
3.4.1 Simulation 82
3.4.2 In vivo 82
3.5 Discussion 84

4 Acquisition Strategy to Reduce Cerebrospinal Fluid Partial Volume Effects for Improved DTI Tractography 89
4.1 Introduction 89
4.2 Methods 92
4.2.1 Optimization of Parameters 92

4.2.2 Image Acquisition 96
4.2.3 Fibre Tracking 100
4.3 Results 102
4.4 Discussion 108
4.5 Addition to the Published Paper 115

5 Oscillating Gradient Spin-Echo (OGSE) Diffusion Tensor Imaging of the Human Brain 118

5.1 Introduction 118
5.2 Theory 121
5.3 Methods 124
5.3.1 Image Acquisition 124
5.3.2 Fiber Tracking and Statistical Analysis 126
5.4 Results 131
5.5 Discussion 138
5.6 Additional Content to the Published Paper 143
5.6.1 Derivation of Diffusion Time for Trapezoidal Gradients 143
5.6.2 Comparing b300 to b1000 145
5.6.3 Potential Impact of Perfusion 145

6 Oscillating Gradient Spin-Echo (OGSE) Diffusion Tensor Imaging Yields Mechanistic Insights in Acute Human Stroke 147

6.1 Introduction 147
6.2 Methods 150
6.2.1 Subjects 150
6.2.2 MRI Acquisition 150
6.2.3 MRI Analysis 151
6.2.4 Monte Carlo Diffusion Simulations 152

6.3 Results . . . 153
6.4 Discussion . . . 157
6.5 Collaborators . . . 163

7 High Resolution Diffusion Weighted Imaging of Stroke 164
7.1 Introduction . . . 164
7.2 Methods . . . 167
7.2.1 Subjects . . . 167
7.2.2 MRI Acquisition . . . 167
7.2.3 MRI Analysis . . . 168
7.3 Results . . . 168
7.4 Discussion . . . 171
7.5 Collaborators . . . 174

8 Discussion and Conclusions 175
8.1 Limitations . . . 175
8.1.1 Partial Volume Effects . . . 175
8.1.2 Magnetic Field Inhomogeneity . . . 176
8.1.3 Receiver Array Sensitivity . . . 176
8.1.4 SAR Monitoring . . . 176
8.1.5 Data Bottlenecks . . . 178
8.1.6 Gradient Duty Cycle . . . 179
8.1.7 Contraindications . . . 179
8.1.8 Scanning Preparation . . . 179
8.1.9 Sample Size and Subjects . . . 180
8.1.10 Portability . . . 180
8.2 Conclusions and Future Directions . . . 180

Appendices 185

A Common Methods 185

A.1 The Diffusion Weighted Echo-planar Imaging Pulse Sequence 185

A.2 Echo-planar Imaging Reconstruction 188

A.3 Diffusion Imaging Calculations and Analysis 195

B Lesion Delineation Tool 197

References **198**

List of Tables

2.1 Main Effect of Concomitant Fields for Various Gradient Combinations and Cardinal Planes 48

4.1 DTI protocols for reducing CSF signal (TR+b, TR, b) versus standard (S) and high resolution (highres) scans without any CSF suppression 97

5.1 DTI Protocols 125

5.2 Mean percent change ($\pm$ standard deviation) of $\lambda_{||}$, $\lambda_{\perp}$, and FA for diffusion times of 4 ms (OGSE) relative to 40 ms (PGSE) in seven healthy subjects 137

List of Figures

1.1 The Neuron 5

1.2 Diffusion MRI of Stroke 7

1.3 Slice Selection 13

1.4 Aliasing 15

1.5 Linearity of the Fourier Transform 17

1.6 Echo-Planar Imaging Pulse Sequence 18

1.7 Echo-Planar Imaging k-space 18

1.8 Fat Saturation in EPI 21

1.9 T_2^* Blurring in Spin-Echo EPI 22

1.10 Stejskal-Tanner Diffusion Encoding 26

1.11 Diffusion Tensor Imaging in Tissue 28

1.12 DTI Metrics 31

1.13 Velocity Autocorrelation and the Diffusion Spectrum 33

1.14 OGSE Gradients and Spectra 34

1.15 B_1 Inhomogeneity 38

2.1 DTI Pulse Sequence Sensitivity to Concomitant Fields 44

2.2 k-space Shifting Simulations 54

2.3 k-space Shifting Results 56

2.4 Intravoxel Dephasing 58

2.5 Prospective Correction 60

2.6 *In vivo* Results 61

2.7 Example MD and FA 62

2.8 Simulations of Error Versus Field and Gradient Strengths . . . 65

2.9 Simulations of Correction Performance 69

2.10 Measurement of Phase from Concomitant Fields 71

3.1 Parallel Imaging Reference Scan Diagrams 74
3.2 Simulations 78
3.3 Simulation Algorithm 79
3.4 Results: Qualitative 83
3.5 Results: Quantitative 84
3.6 Results: Physiological Motion 85

4.1 Optimization of TR and b_{min} 95
4.2 Short TR Slice Re-ordering 98
4.3 Tractography of the Fornix and SLF 101
4.4 Raw Images 103
4.5 Tractography for the Five Methods in One Subject 104
4.6 Tractography in All Subjects 106
4.7 Quantitative Results 107
4.8 CSF Suppression with High Resolution 112
4.9 Non-Guassian Diffusion in the SLF 113

5.1 OGSE Gradients and Spectra 122
5.2 B_0 Eddy Current Correction 127
5.3 Tractography Examples 128
5.4 OGSE Images 132
5.5 Eigenvalue Difference for $\Delta_{eff} = 4.1$ ms versus 40 ms 133
5.6 Color-coded FA for $\Delta_{eff} = 4.1$ ms versus 40 ms 134
5.7 Results in Phantom 135
5.8 Results *in vivo* 136
5.9 Derivation of Δ_{eff} for Trapezoidal OGSE 143
5.10 Comparison of b = 300 s/mm^2 and 1000 s/mm^2 146

6.1 Beading Schematic 148
6.2 PGSE and OGSE Pulse Sequences 151
6.3 OGSE in Stroke Experimental Results 154
6.4 OGSE in Stroke Experimental Results 156
6.5 OGSE in Stroke Simulation Results 157
6.6 OGSE in Stroke Simulation Results - *in vivo* Comparison . . . 158
6.7 OGSE in Stroke Simulation Difference 159

7.1 Volume and MD Estimation of Stroke Lesions 166
7.2 High Resolution DWI of Stroke 169
7.3 Quantitative Measurements 170
7.4 Number of Averages 172
7.5 High Resolution at Typical Field Strength 173

8.1 Receiver Sensitivity and B_0 Distortions 177

A.1 Echo-Planar Imaging Pulse Sequence 185
A.2 Partial Fourier Undersampling 186
A.3 Nyquist Ghosting 190
A.4 Zero Filling 195
A.5 Quantitative Measurements 197

List of Abbreviations

ACS	autocalibration signal
ADC	apparent diffusion coefficient
b0	b = 0 s/mm^2 acquisition
b300	b = 300 s/mm^2 acquisition
CSF	cerebrospinal fluid
CT	x-ray computed tomography
dMRI	diffusion magnetic resonance imaging
DTI	diffusion tensor imaging
DWI	diffusion weighted imaging
ECF	extracellular fluid
EPI	echo-planar imaging
FA	fractional anisotropy
FE	frequency encode
FOV	field of view
GE	gradient-echo
GM	gray matter
GRAPPA	generalized autocalibrating partially parallel acquisitions
HR	high resolution
LR	low resolution
MD	mean diffusivity
MRI	magnetic resonance imaging
NIHSS	National Institute of Health Stroke Scale
NMR	nuclear magnetic resonance
OGSE	oscillating gradient spin-echo
PGSE	pulsed gradient spin-echo
PE	phase encode
PPM	parts per million
RF	radiofrequency
rMD	relative mean diffusivity
ROI	region of interest
RMS	root mean squared
SAR	specific absorption rate
SE	spin-echo
SGSSE	split-gradient single spin-echo
SNR	signal to noise ratio
TE	echo time
TR	repetition time
UD	undersampled data
WM	white matter

List of Symbols

b	diffusion MRI b-value
b_{min}	minimum b-value
b_{max}	maximum b-value
B	magnetic field
B_0	main static magnetic field
B_1	RF magnetic field
B_C	concomitant gradient field
D	diffusion coefficient
f	frequency (hertz)
k	spatial frequency
F	k-spectra from diffusion gradients
G	magnetic field gradient
I_G	net background ghost signal intensity
I_{STD}	signal intensity standard deviation
M	magnetization
M_z	longitudinal magnetization
M_{xy}	transverse magnetization
M_0	equilibrium magnetization
n, N	total number
p, P	p-value from a t-test
$R_{CSF/WM}$	signal ratio of CSF to white matter
S	signal intensity
sw	data sampling sweep width
t	time
T_1	spin-lattice relaxation time
T_2	spin-spin relaxation time
T_2'	relaxation time from B_0 inhomogeneity
T_2*	net relaxation from spin-spin interaction and B_0 inhomogeneity
v	velocity
w	slice width
W	GRAPPA weighting factors
x, y, z	space
δ	duration of diffusion gradient lobe
Δ	separation of diffusion gradient lobes
Δ_{eff}	effective diffusion time
$\lambda_{\|}$	parallel diffusion tensor eigenvalue
$\lambda_{\perp}$	perpendicular diffusion tensor eigenvalue
ϕ	phase
θ	rotation angle
ω	frequency (radians)
τ	duration of phase accumulation from concomitant gradients
γ	gyromagnetic ratio

Chapter 1

Introduction

1.1 Overview

Medical imaging has become essential in clinical practice and research given its ability to non-invasively investigate anatomy. A large number of imaging modalities exist, including x-ray computed tomography (CT), ultrasound, positron emission tomography, single-photon emission tomography, and magnetic resonance imaging (MRI). The advantages of MRI include excellent soft-tissue contrast with customizable contrast mechanisms and the use of non-ionizing radiofrequency (RF) radiation. However, the price paid for such beneficial traits is extremely low signal, which leads to long scan times, and contraindications for metallic foreign bodies and electronics, such as cardiac pacemakers.

As stated above, an advantage of MRI is the multitude of contrast mechanisms, and the ability to tailor an imaging protocol to target one specifically, such as magnetization relaxation rates, blood flow, magnetization transfer, or diffusion of water. Diffusion MRI (dMRI) has been utilized predominantly in the brain, where microstructural information is obtained because

the diffusion (i.e. random molecular motion) of water is inhibited by cellular membranes. This unique contrast mechanism has found extensive clinical use for stroke due to a high sensitivity to the brain tissue changes that occur immediately following ischemic attack. Another common clinical application is the visualization of tumors in oncology. In addition, by probing the directional dependence of brain diffusion using diffusion tensor imaging (DTI) the structure of axons can be inferred, granting unprecedented insight into fiber pathways of the brain. While clinical use of DTI has so far been limited to assessment of white matter tract locations for presurgical planning, its use in research of neurodevelopment and neurological conditions such as epilepsy and dementia has been substantial [1–3].

Diffusion MRI has numerous advantages, but it is not without limitation. While DTI can detect major fiber tracts or lesions in the brain, measuring small features can be difficult due to an inherently low resolution. Increasing the resolution necessarily reduces the signal strength, and to compensate for this a higher static magnetic field and larger gradients (for DTI) can be utilized. In addition, there are newly emerging dMRI techniques that have been utilized in animal MRI systems, such as oscillating gradient spin-echo (OGSE) dMRI [4–6], but have not been successfully implemented in the human brain due to insufficient signal and gradient strengths on clinical MRI systems. However, increasing the magnetic field and gradient strengths introduces new challenges.

1.2 Scope of Thesis

The goal of this thesis was to address the challenges of performing dMRI with a stronger magnetic field and gradients, and to apply it for high

resolution and advanced techniques. To do this, a 4.7 T human MRI system with 60 mT/m gradients was utilized, which is a three times stronger field and 50% stronger gradients compared to typical clinical scanners. Chapters 2 – 4 involve solving challenges at high field or gradient strengths, while Chapters 5 – 7 involve applications enabled by the high strength MRI system.

Chapter 2 characterizes and offers solutions for a previously unreported issue for dMRI introduced by strong gradients, concomitant gradient fields. The MRI signal is made sensitive to diffusion by applying large magnetic field gradients. While all the static magnetic fields in MRI are ideally collinear along a single direction, producing the gradients necessarily introduces small unwanted tangential components of magnetic field [7]. In this thesis, the erroneous effect of these concomitant fields on DTI was found to be considerable in certain cases, and techniques to mitigate them were introduced.

Parallel imaging is a multiple RF receiver technique that can be utilized to address the high-field challenge of B_0 inhomogeneity. Chapter 3 shows that typical methods for performing parallel imaging for dMRI are sensitive to subject motion. Therefore, a robust parallel imaging method for dMRI was developed in the thesis work and is shown to have better performance than the standard technique.

Measurements in the brain using dMRI can be severely corrupted by cerebrospinal fluid (CSF) in the brain that partially occupies voxels with tissue [8–11]. While RF-based methods have been developed to reduce these errors [12], they do not translate well to higher magnetic field strengths due to RF heating concerns. Therefore, Chapter 4 introduces high-field compatible methods to reduce cerebrospinal fluid partial volume effects.

Although dMRI indirectly probes cellular microstructure through measurement of water diffusion, typical dMRI techniques are only sensitive to

length scales longer than typical microstructural dimensions because of a long "diffusion time". However, the newly developed oscillating gradient spin-echo (OGSE) technique is more sensitive to smaller length scales because it can achieve much shorter diffusion times, which may give new insight into healthy development or disease. Chapter 5 takes the first step in utilizing OGSE by using it to investigate the microstructural length scale dependence of dMRI in healthy subjects. Chapter 6 moves beyond the healthy brain by exploring new insights into the microstructure changes that occur upon stroke via OGSE dMRI in stroke patients. This may help elucidate why standard dMRI is sensitive to stroke, which has eluded the scientific community since its discovery over 20 years ago [13].

Clinical dMRI of stroke has traditionally been performed using thick slices to maintain low scan times. However, it has been shown that using thinner slices causes more lesions to be visible [14–16]. Chapter 7 validates these findings, and additionally shows that thinner slices also yields more precise measurements of lesion volume and diffusion parameters.

Background regarding brain tissue, stroke, MRI acquisition, and dMRI are provided in the rest of this chapter.

1.3 The Brain

1.3.1 Brain Tissue

The primary functional cell of the brain is the neuron, which operates by transporting electrical signal to neighboring cells.[1] The neuron consists of a cell body, a large process called an axon, and many small processes called

[1]The basics of brain tissue discussed in this section can be found in almost any introductory textbook on neuroanatomy, such as *Clinical Neuroanatomy* by Waxman [17].

dendrites (Figure 1.1). The dendrites receive electrical signals from the axons

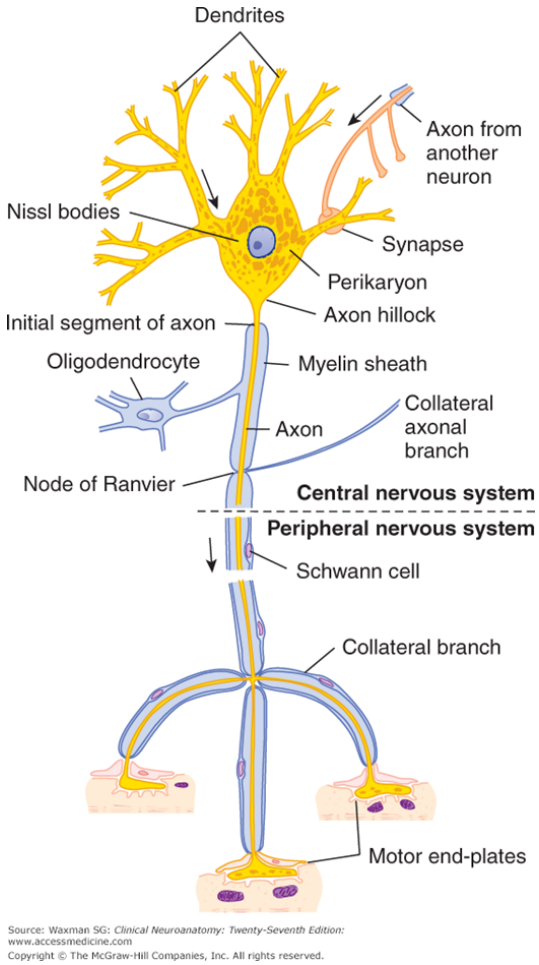

Figure 1.1: Diagram of a neuron. Figure from *Clinical Neuroanatomy* 27 Edition [17].

of other neurons, the body contains the components for basic cellular maintenance including the nucleus, and the axon is designed to transmit electrical signals over potentially long distances. Many neurons have axons that are covered by myelin (Figure 1.1), which provides electrical insulation and increases the travelling speed of electric signals. Approximately 50% of the volume of the brain is occupied by neurons, while the other half of the volume consists of glial cells [18]. Glial cells are a broad category of cells that regulate the contents of extracellular fluid (astrocytes), provide the myelin covering the axons (oligodendrocytes), and provide immune functions (microglia).

The major components of the brain are gray matter, white matter, and cerebrospinal fluid (CSF). Grey matter is the home of groups of neuronal cell bodies, while white matter primarily consists of long-range bundles of myelinated axons that allow communication between different gray matter regions. Grey matter can be further sub-divided into cortical gray matter, which lines the outer surface of the brain, and deep gray matter, which consists of specialized processing units deep in the brain. The CSF is a protective fluid that fills the subarachnoid space that surrounds the brain and ventricular spaces deep in the brain. In addition to providing a physical buffer for the brain, the CSF helps regulate the chemical environment of the central nervous system.

1.3.2 Stroke

Stroke is an acute medical event that is associated with suddenly impaired blood supply to the brain. The two major classes of stroke are hemorrhagic, which stems from a ruptured blood vessel, or ischemic, which stems from a blocked blood vessel. In hemorrhagic stroke, the brain tissue may be damaged from direct toxic effects from the blood and distortions and ischemia that results from increased pressure. In contrast, ischemic stroke is only associated with ischemia itself. Ischemia causes a deprivation of oxygen and glucose, which halts ATP production and causes ion ATPase pumps to cease functioning within minutes. The ion pumps normally keep the concentration of Na^+ low in the cell and high in the extracellular space, but with their failure, Na^+ builds up in the cell via diffusion. Thus, an osmotic gradient is formed and water is shifted into the cell from the extracellular space in a process known as cytotoxic edema. While cytotoxic edema may be reversible for partial ischemia if it is resolved quickly (30 – 60 min), for extended durations the disrupted

ionic balance results in the activation of enzymes that break the cells down, culminating in cell death (i.e. infarction) [19].

Stroke is clinically diagnosed through a combination of symptom assessment and diagnostic imaging. The severity of a stroke is quantified by a score generated from the symptoms, the National Institute of Health Stroke Scale Score (NIHSSS). Typically the first imaging test performed is CT due to its speed and its ability to easily identify hemorrhaging and rule out some disorders that can mimic stroke. However, the sensitivity of CT for detecting ischemic stroke is low. In contrast, with dMRI the infarct core is visible within minutes due to an acute decrease in the apparent diffusion coefficient of water [13] (Figure 1.2). The mechanisms responsible for the reduced apparent

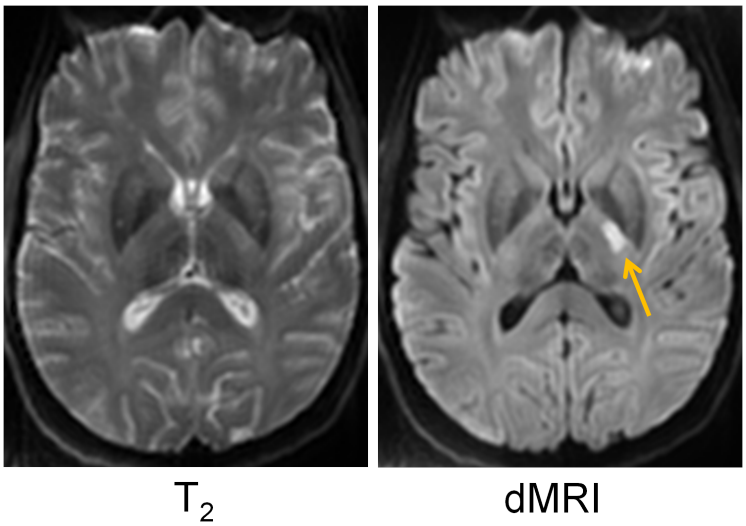

Figure 1.2: While the stroke lesion is not conspicuous on a standard T_2 weighted image, a diffusion MRI (dMRI) image clearly shows the infarct core (arrow).

diffusion coefficient are still not well understood, which is the motivation for Chapter 6. With a confirmed ischemic stroke with no hemorrhage, clot-busting medication (tissue plasminogen activator, tPA) can be administered to mitigate the extent of infarction if the stroke is within a 4.5 hr window. This is not done for hemorrhagic strokes because it would result in worsening of the

bleeding. For blockages in large vessels a mechanical thrombectomy may be performed to remove the clot.

1.4 Magnetic Resonance Imaging Fundamentals

1.4.1 Nuclear Magnetic Resonance

In atoms with an odd number of protons and/or neutrons, the nucleus will have a non-zero magnetic moment. The microscopic interaction of a nuclear magnetic moment with an external magnetic field is governed by the laws of quantum mechanics, which dictates that it will align obliquely to the field and precess in a process known as nuclear magnetic resonance (NMR)[2]. For macroscopic groups of atoms, the net magnetization will behave in a similar manner. To create an initial magnetization M_0 in an NMR or MRI experiment, the sample is immersed in a large background magnetic field $\mathbf{B_0} = B_0\hat{z}$. With smaller, time dependent fields applied so that the net magnetic field is $\mathbf{B}(t) = (B_x(t)\hat{x}, B_y(t)\hat{y}, (B_0 + B_z(t))\hat{z})$, the influence on the net magnetization $\mathbf{M}$ is given by the Bloch equations [20],

$$\frac{d\mathbf{M}}{dt} = \gamma\mathbf{M} \times \mathbf{B} + \frac{(M_0 - M_z)\hat{z}}{T_1} - \frac{M_x\hat{x} + M_y\hat{y}}{T_2} \tag{1.1}$$

where γ is the gyromagnetic ratio, which is a quantum mechanical property of atoms that relates the nuclear magnetic moment to the spin angular momentum. For the hydrogen atom, which is the species measured most often in MRI, $\gamma = 2\pi 42.576$ rad/T/s. T_1 is the spin-lattice relaxation constant,

[2] A comprehensive overview of MRI fundamentals can be found in *Magnetic Resonance Imaging* by Haacke [20].

which is the characteristic time it takes for nuclei to exchange energy with surrounding atoms or molecules (i.e. the lattice) and recover to a less energetic state. Accordingly, this causes the longitudinal magnetization, M_z, to return to equilibrium, M_0. T_2 is the spin-spin relaxation constant, which describes the desynchronization of the precession of individual magnetic moments (i.e. spins) due to the change of precessional frequencies that occur when the spins pass through the neighboring magnetic moments of other atoms. When neighboring magnetic moments are dephased relative to each other, the net magnetization in the transverse plane (i.e. perpendicular to $\mathbf{B_0}$) is reduced through destructive interference.

With only the background field present (i.e. $\mathbf{B} = B_0\hat{z}$), the solution to the Bloch equations is

$$\begin{aligned} M_{xy}(t) &= M_{xy}(0)e^{-i\gamma B_0 t}e^{-t/T_2} \\ M_z(t) &= M_0 + (M_z(0) - M_0)e^{-t/T_1} \end{aligned} \tag{1.2}$$

where $M_{xy}(t) \equiv M_x(t) + iM_y(t)$ is the transverse magnetization in the xy-plane in complex phasor notation and M_z is the longitudinal magnetization along $\hat{z}$. The complex exponential term $e^{-i\gamma B_0 t}$ in Equation 1.2 shows that the static B_0 field causes the transverse magnetization to precess at the so-called "Larmor frequency",

$$\omega_0 = \gamma B_0 \tag{1.3}$$

In addition, the magnitude of the transverse magnetization decays to zero over time due to T_2 relaxation, while the longitudinal magnetization recovers back to the equilibrium magnetization at a rate governed by T_1.

To generate transverse magnetization in the first place (i.e. $M_{xy}(0)$ in Equation 1.2), the equilibrium magnetization is tipped into the transverse

plane by applying a radiofrequency (RF) magnetic field. For a transverse RF field $B_1(t) = B_1 e^{-i\omega_0 t}$ (i.e. rotating at the Larmor frequency), the tip angle is given by

$$\theta = \gamma \int B_1 dt \tag{1.4}$$

Accordingly, a tip angle of 90° converts the entire equilibrium magnetization into transverse magnetization, while a tip angle of 180° results in a longitudinal magnetization with negative polarity.

Dephasing and the Spin-Echo

For a signal receiver tuned at the Larmor frequency, the net acquired signal, $S(t)$, is the integral of transverse magnetization throughout the sample,

$$\begin{aligned} S(t) &= \int\int\int M_{xy}(x,y,z,t) e^{-i\phi(x,y,z,t)} dx dy dz \\ \phi(x,y,z,t) &= \gamma \int_0^t \Delta B(t') dt' \end{aligned} \tag{1.5}$$

where non-zero phase, ϕ, is imparted by magnetic field offsets, ΔB, from the static B_0 field. A possible source of ΔB is magnetic susceptibility, which is a tissue property that causes the magnetic field to be offset from the external B_0 field. The presence of phase varying throughout the sample (or voxel) causes the net signal amplitude to decrease because of destructive interference between spins (Equation 1.5). This effectively decreases T_2 to become T_2^*,

$$\frac{1}{T_2^*} = \frac{1}{T_2} + \frac{1}{T_2'} \tag{1.6}$$

where T_2' is the contribution to dephasing from susceptibility. To reverse the signal loss from susceptibility, a 180° RF "refocusing" pulse can be applied at a time τ after the initial excitation to reverse the polarity of any accumulated

phase, which causes the phase to recover towards zero as time continues. This results in a re-phasing of all the spins, a "spin-echo", at a time τ after the refocusing pulse (i.e. 2τ after the initial excitation). Accordingly, at the spin-echo the net signal is only decreased via T_2 and not T_2^*. Notably, dephasing from magnetic susceptibility (i.e. T_2') is reversible because the associated magnetic field offsets are static and slowly varying with respect to the microscopic motion of the atoms (i.e. do not depend on time at the time scale of the MRI experiment). T_2 dephasing is not reversible because it stems from dephasing at a microscopic scale from the magnetic moments of neighboring atoms whose position is not static.

1.4.2 Image Encoding

The signal measured is simply the sum of all the transverse magnetization throughout the sample (Equation 1.5). To encode the spatial dependence of M_{xy} into the measured signal, combinations of magnetic field gradients along each orthogonal direction, (G_x, G_y, G_z), are typically applied such that the magnetic field offset is $\Delta B(x, y, z) = xG_x + yG_y + zG_z$. Ignoring other sources of phase-accumulation (e.g. chemical shift), this results in ϕ having the form

$$\phi(x, y, z, t) = \gamma \left(x \int_0^t G_x(\tau) d\tau + y \int_0^t G_y(\tau) d\tau + z \int_0^t G_z(\tau) d\tau \right) \tag{1.7}$$

The equations can be condensed by making the variable substitution

$$k_j(t) = \frac{\gamma}{2\pi} \int_0^t G_j(\tau) d\tau \tag{1.8}$$

where j can be x, y, or z. As such, Equation 1.5 can be re-written as

$$S(t) = \int \int \int M_{xy}(x, y, z, t) e^{-i2\pi(xk_x + yk_y + zk_z)} dx dy dz \tag{1.9}$$

Equation 1.9 serendipitously represents a 3D Fourier transform, which can be efficiently computed numerically and has well-known properties (see Section 1.4.3). Since k_j are known ahead of time, the spatial dependence of the transverse magnetization can be easily computed from $S(t)$ using an inverse Fourier transform

$$M_{xy}(x,y,z,t) = \int\int\int S(k_x,k_y,k_z,t)e^{i2\pi(xk_x+yk_y+zk_z)}dk_xdk_ydk_z \qquad (1.10)$$

thus providing a 3D image volume. Accordingly, a goal of any MRI acquisition is to play out gradients to measure the signal in a grid of (k_x, k_y, k_z) locations, or "k-space", which can be inverted with the inverse Fourier transform to create a 3D volume of images.

It is not always necessary or desirable to obtain images of the full 3D volume. Instead, only a single slice (or slab) can be acquired at a time by specifying a gradient during application of the excitation RF pulse. As described in Section 1.4.1, the magnetization is most efficiently tipped if the frequency of the excitation pulse matches the Larmor frequency. By applying a gradient, the Larmor frequency varies with position, and only positions with frequencies within the bandwidth of the excitation pulse will have their magnetization tipped (Figure 1.3). Typically a sinc shaped RF pulse is used because it has a rectangular bandwidth profile; accordingly, the slice ends up with a rectangular transverse magnetization as a function of position along the slice. Notably, the presence of the gradient during the excitation also results in dephasing across the slice by the time excitation is complete, which can be negated by the application of a rephasing gradient that is approximately half the area of the excitation gradient (Figure 1.3). For a thin slice at z_S and

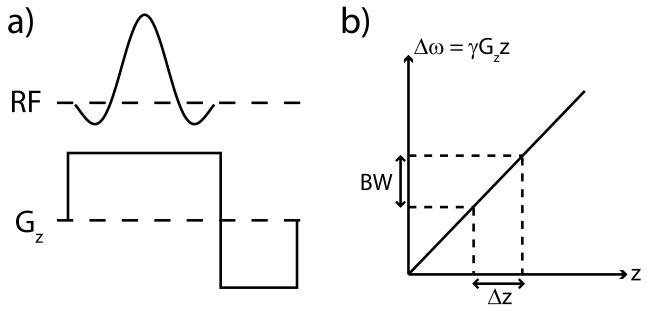

Figure 1.3: (a) A gradient is applied during the RF pulse to enable excitation of only a slice. The negative gradient lobe after the RF pulse is required to reverse dephasing that occurs across the slice during excitation. (b) The gradient, G_z, causes the resonant frequency of the spins to deviate from the Larmor frequency by $\Delta\omega$ as a function of position, z. The RF pulse only interacts with positions where the resonant frequency lies with the RF pulse bandwidth, BW, to create a slice with thickness $\Delta z = BW/(\gamma G_z)$.

$k_z = 0$, Equation 1.10 simplifies to

$$M_{xy}(x, y, z_S, t) = \int\int S(k_x, k_y, t) e^{i2\pi(xk_x + yk_y)} dk_x dk_y \tag{1.11}$$

1.4.3 k-space

Understanding k-space and the interplay between physical phenomena, k-space, and the final images is a critical foundation for advanced MRI topics. As described previously, MRI data is acquired in a grid in k-space. For simplicity, only 1D k-space will be considered; however, the concepts are easily generalized to 2 or 3 dimensions.

Nyquist Criterion

While Equation 1.11 would ideally be solved with k and x values having all possible values from $-\infty$ to ∞, in practice only a discrete subset can be acquired. As such, a grid of k-space is acquired with N points, where $k_x = n\Delta k_x$ and $x = m\Delta x$, and Δx is the grid spacing of the image to be reconstructed.

This converts Equation 1.11 to a summation (in only one dimension here for simplicity),

$$M_m = \sum_{n=0}^{N-1} S_n e^{-i2\pi mn\Delta k_x \Delta x} \tag{1.12}$$

The above Equation has the same form as the discrete Fourier Transform, $M_m = \sum_{n=0}^{N-1} S_n e^{-i2\pi mn/N}$, where $\Delta k_x \Delta x = 1/N$. It is important to cast the signal equation into a useful transform like the discrete Fourier Transform because it is reversible and efficiently computed numerically. Since the maximum k-space position sampled is $k_{max} = N\Delta k_x/2$, the definition $\Delta k_x \Delta x = 1/N$ can be rearranged to describe the resolution of the MRI acquisition,

$$\Delta x = \frac{1}{2k_{max}} \tag{1.13}$$

In addition, a critical property of Equation 1.12 is that the computed M_m will repeat every N points (i.e. $M_{m+N} = M$) because $e^{i\phi} = e^{i(\phi+n2\pi)}$. Accordingly, the effective field of view (FOV) of the imaging experiment is given by $N\Delta x$, which combined with $\Delta k_x \Delta x = 1/N$ yields

$$\Delta k = \frac{1}{FOV} \tag{1.14}$$

Equations 1.13 and 1.14 form an important duality that describes how the discretization of k-space is related to the images that are obtained.

If the FOV is smaller than the object, the repeated signals will overlap and cause aliasing (Figure 1.4). To avoid aliasing, one must ensure that the FOV is larger than the maximum extent of the object, FOV_{min}, which combined with Equation 1.14 reveals the so-called Nyquist criteria

$$\Delta k \leq \frac{1}{FOV_{min}} \tag{1.15}$$

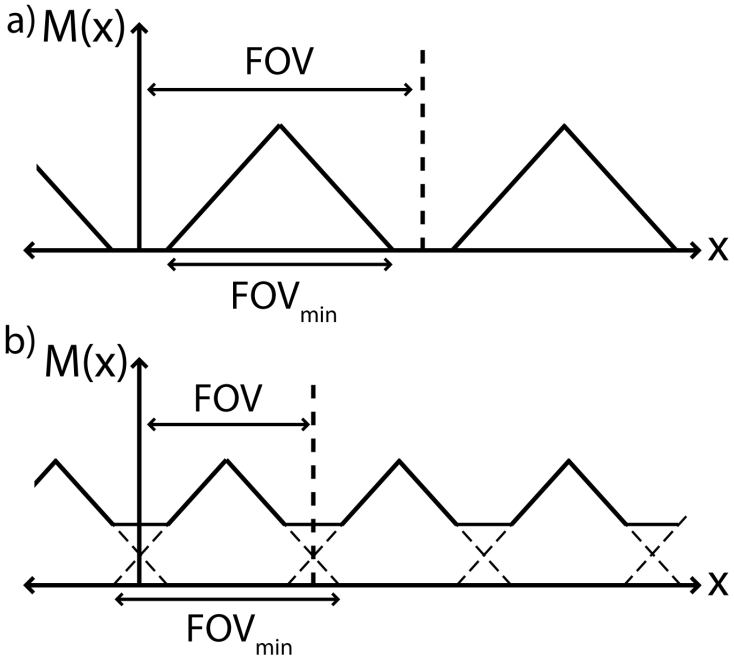

Figure 1.4: (a) The discrete Fourier transform of the acquired k-space implicitly assumes that the image space signal, $M(x)$, repeats over a distance given by the FOV (Equation 1.14). (b) When the FOV is smaller than the extent of the object, FOV_{min}, the repeated signals overlap in what is referred to as aliasing.

Important Properties of the Fourier Transform

The shift property of the Fourier transform is useful for understanding how phase accumulation for various sources (e.g. motion or B_0 inhomogeneity) affects images. The property states that shifting an image is equivalent to adding a linearly varying phase in k-space, or vice versa,

$$\begin{aligned} M(x - x') &= e^{-i2\pi x' k} S(k) \\ S(k - k') &= e^{i2\pi x k'} M(x) \end{aligned} \tag{1.16}$$

where S is the Fourier transform of the image domain signal M, and x' and k' are the shifts in image space and k-space, respectively. Equation 1.16 shows that the slope of the phase ramp is exactly equal to the shift multiplied by 2π.

As an example of how this can provide insight into k-space sampling and the resultant images, the effect of a global B_0 offset by ΔB can be considered. For a constant gradient G and sampling interval τ, additional phase of $\gamma \Delta B \tau$ will accumulate between each k-space sample. Accordingly, a phase ramp across k-space with slope $\Delta B/G$ will form, and the resultant image will be shifted along the gradient direction by $\Delta B/G$.

Another well known property of the Fourier transform is linearity, which states

$$M(x) = AM_1(x) + BM_2(x) \Leftrightarrow S(k) = AS_1(k) + BS_2(k) \tag{1.17}$$

While this property appears quite trivial, it aids in the interpretation of MRI phenomena. In particular, it dictates that the net k-space of an image is the sum of the k-spaces that correspond to each individual object space voxel or group of voxels, or vice versa (Figure 1.5). Therefore, the above example regarding image shift due to B_0 offsets can be generalized to B_0 offsets that vary with position (i.e. B_0 inhomogeneity), where the k-space corresponding to each region will have a phase ramp that causes a shift of signal in image space. Regions having different B_0 offsets will have different shifts of signal in image space, resulting in distortions.

1.4.4 Echo Planar Imaging

Diffusion MRI typically utilizes echo-planar imaging (EPI) [21], which acquires the entire extent of 2D k-space after a single excitation (Figure 1.6). This feature is important for dMRI since it reduces sensitivity to physiological and gross head motion, which is vital for a technique that attempts to measure microscopic motion of molecules from diffusion (see Section 1.5.1). The RF

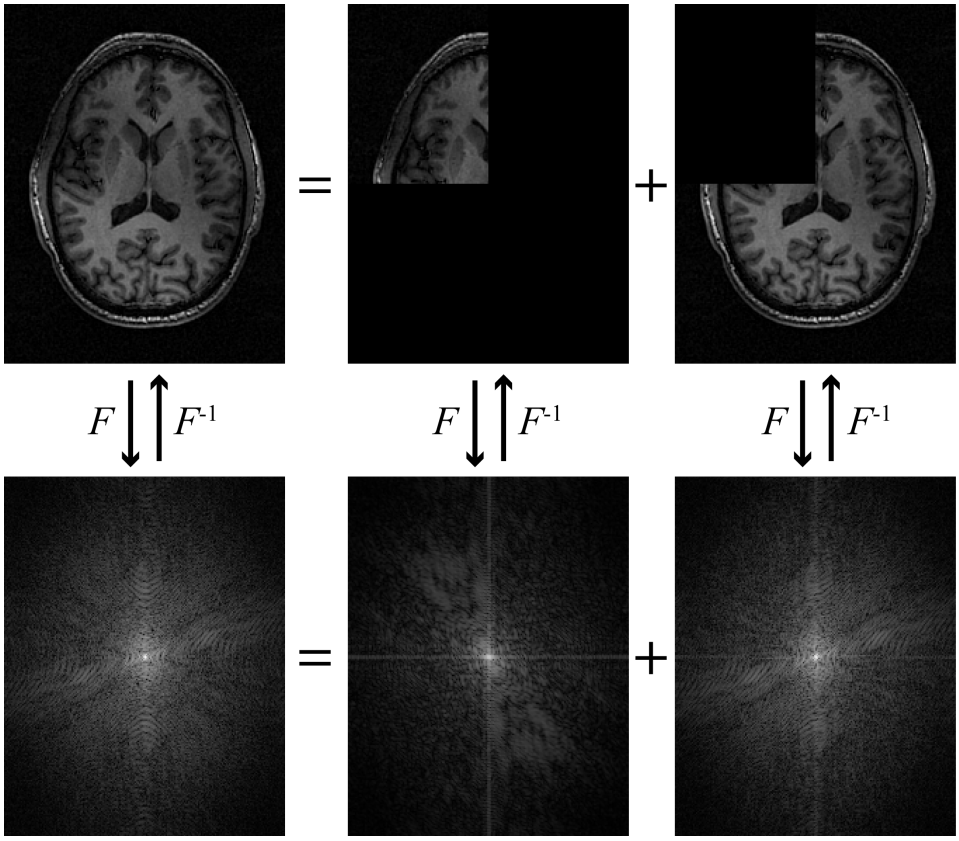

Figure 1.5: The linearity property of the Fourier transform allows the k-space that corresponds to different regions of the subject to be considered independently. The forward and inverse Fourier transforms are denoted by F and F^{-1}, respectively.

features are a 90° excitation pulse and associated slice-selection gradients (A) and a 180° refocusing pulse (B) to attain a spin-echo at the echo-time (TE). The large "crusher" gradients on either side of the 180° pulse (C) strongly dephase transverse magnetization excited by any deviations from a perfect 180° flip angle. Likewise, the large "spoiling" gradients at the end of the sequence (D) dephase any remaining transverse magnetization so that it does not interfere with neighboring slices or repeated acquisitions. The oscillating gradients on the frequency encode (FE) gradient channel combined with the phase-encode (PE) blips (E) results in a side-to-side motion through k-space (Figure 1.7), during which time the signal is sampled at a frequency called the

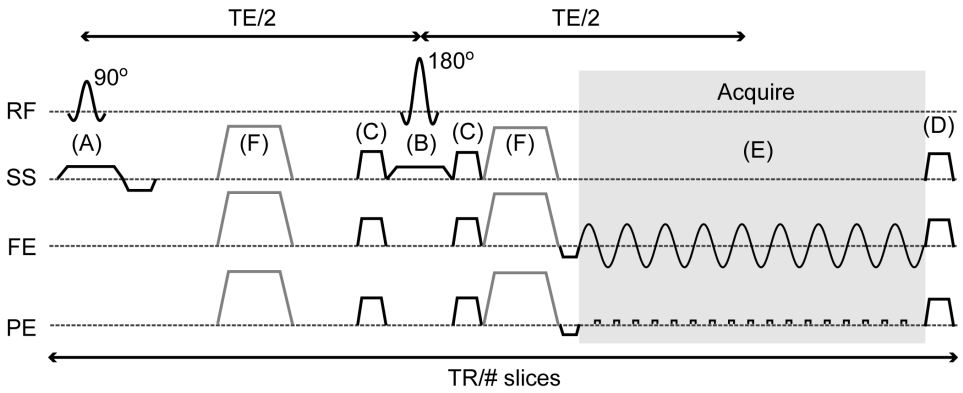

Figure 1.6: (a) The pulse sequence for diffusion MRI using echo-planar imaging (EPI), where the application of radiofrequency (RF) pulses, slice select (SS) gradients, frequency encode (FE) gradients, and phase encode (PE) gradients are shown as a function of time. The spin-echo at TE occurs at the center of k-space, and the TR is the total time to repeat the pulse sequence for all slices. The main features are (A) slice selective excitation, (B) refocusing, (C) crusher gradients, (D) spoiler gradients, (E) EPI readout, and (F) diffusion gradients.

sweep width (sw). The small negative polarity gradients immediately prior to

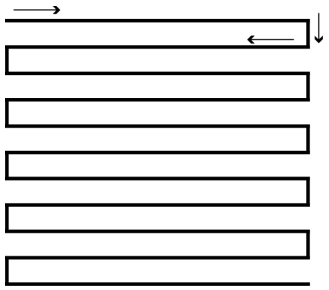

Figure 1.7: Because of the oscillating FE gradients and PE gradient blips in the EPI pulse sequence, alternating lines of k-space are sampled in reverse directions.

the oscillating gradients are required to get to the corner of k-space. While a trapezoidal FE gradient shape would result in uniform sampling of k-space, a sinusoidal shape was used in this work to mitigate the effects of eddy currents and vibrations [22]. The non-uniform sampling can be accounted for by re-sampling the k-space data onto a uniform grid [23, 24]. The gradients required for encoding the signal to diffusion (more details in Section 1.5.1) are placed on either side of the 180° pulse (F). The spin-echo at the TE is chosen to align

with the center of k-space since the signal-to-noise ratio is primarily dictated by the signal when $k = 0$. The repetition time (TR) is the time delay between re-excitations of the same slice. Typically, all of the slices are acquired before acquiring the same slice a second time (e.g. for another average). The TE is long compared to the T_2 of brain tissue, which causes tissues with differing T_2 to appear with different signal intensities in the final image (i.e. the signal from regions with different T_2 will decay to different values by the time the data is sampled). The TR is also long compared to the T_1 of brain tissue, which causes T_1 to have little influence on the image contrast because the longitudinal magnetization of all tissue almost fully recovers during the TR. Therefore, EPI acquisitions are generally T_2-weighted.

For sinusoidal frequency encoding gradients the k-space accumulated between samples varies and Nyquist criteria must be satisfied for the largest k-space step. Around the sinusoid maximum where the gradient is G_{max}, the k-space sample separation is given by $2\pi\Delta k = \gamma G_{max}/sw$, which dictates a sw minimum of $\gamma G_{max} FOV/(2\pi)$ via Equation 1.15.

Details of the EPI image reconstruction used in this work are in Appendix A.

Fat Suppression for Spin-Echo EPI

Protons in fat have a resonant frequency differing from water by approximately 3.5 parts per million (PPM). Accordingly, phase accumulates during the EPI readout and creates a phase ramp for the k-space corresponding to the fat and the fat signal is shifted relative to the water signal in object space (See Equation 1.16 and recall from Section 1.4.3 that the k-space from different regions can be considered independently), which causes an artifact where fat signal overlaps with the desired water signal in the fi-

nal image. Similarly, the fat is also excited in a slice location offset from the water by $\Delta z = (3.5 \times 10^{-6})B_0/G_{90}$, where G_{90} is the slice-select gradient height. Therefore, to suppress the fat signal and prevent this artifact a different gradient height can be used for the 180° RF pulse, making the fat slice affected by the 180° RF pulse offset from the fat excitation slice by $(3.5 \times 10^{-6})B_0(1/G_{90} - 1/G_{180})$ [25] (Figure 1.8a). With the fat refocusing slice offset from the excited slice, the excited fat slice transverse magnetization ends up getting spoiled by the gradients surrounding the 180° pulse and do not contribute to the measured signal (Figure 1.8b).

Other methods that are commonly used for the suppression of fat signal are: 1. fat saturation, where the fat magnetization is selectively saturated with a narrow band RF pulse and spoiled (leaving the water unaffected); 2. narrow-band RF pulses that only excite water. Both of these methods and the fat-water slice offset method described above are based on chemical shift and have similar performance; however, fat saturation and water only excitation methods increase RF power and scan time, whereas the slice offset method does not.

Limitations of EPI

One of the primary limitations of EPI is the resolution. The readout of the entire grid of k-space after one RF excitation requires a long duration relative to T_2 and T_2^*, which results in significant signal loss (long TE relative to T_2) and blurring (T_2^* signal decay during readout). The signal decay and blurring occurs primarily along the PE direction because of the long time it takes to traverse k-space in that direction. For spin-echo EPI, the signal

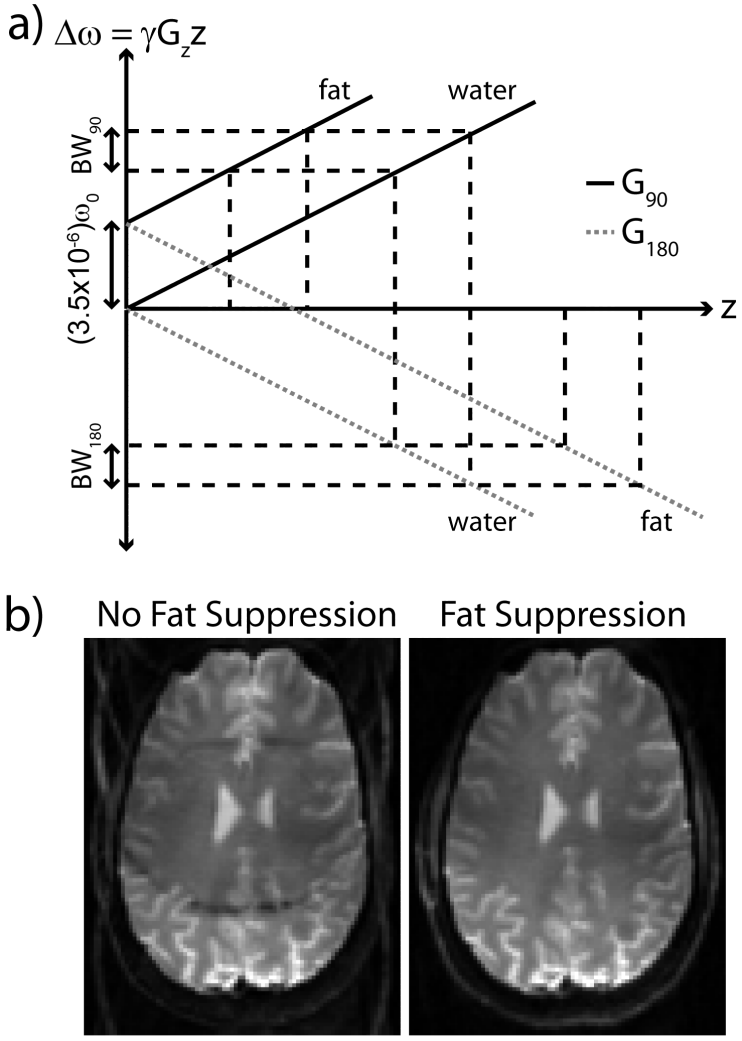

Figure 1.8: (a) The chemical shift in fat causes the resonance frequency to be shifted by 3.5 PPM relative to the Larmor frequency ω_0. If different gradient heights are used for the 90° (G_{90}) and 180° (G_{180}) RF pulses (in this example the gradients are negative of each other), the fat slices that get excited and refocused do not overlap. The different gradient heights also requires different bandwidths and frequency offsets for the RF pulses (BW_{90} and BW_{180}). This causes any fat signal in the transverse plane to get dephased by the crusher gradients (Figure 1.6) and thus total removal of the fat signal, as demonstrated by the EPI images in (b).

envelope along the PE direction in k-space (k_{PE}) is given by [20]

$$S_{envelope} = e^{-t/T_2} . * exp\left(-\left(|t| - TE\right)/T_2'\right) \tag{1.18}$$

where $1/T_2^* = 1/T_2 + 1/T_2'$, which translates to a similar envelope along k_{PE} (Figure 1.9). The blurring can be better understood by performing the Fourier

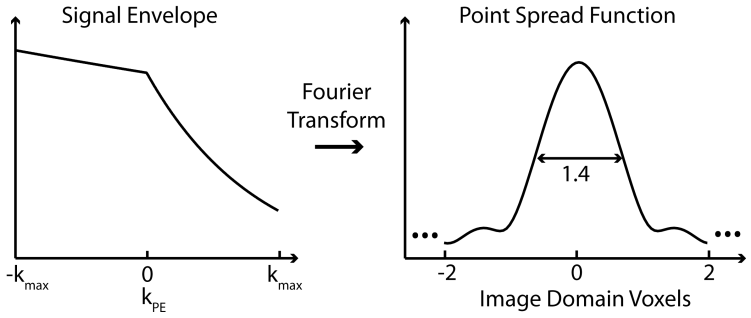

Figure 1.9: Signal decay from T_2^* results in a signal envelope along the PE direction in k-space (k_{PE}) given by Equation 1.18 for spin-echo EPI. The width of the point spread function (the Fourier transform of the signal envelope) shows that the effective resolution is larger than the prescribed voxel size. The signal envelope was estimated for typical EPI at 4.7T with 2 mm isotropic voxels, $T_2 = 55$ ms [26], and $T_2^* = 30$ ms [27].

transform of the signal decay envelope to obtain the point-spread function (PSF). The acquired image is equal to the true image without T_2 or T_2^* decay convolved with the PSF, and the width of the PSF gives the effective resolution. For typical EPI parameters, this can impair the resolution by 40% for a typical EPI readout (Figure 1.9).

Another significant limitation of EPI is its sensitivity to magnetic field inhomogeneities that stem from interfaces between tissue and air (e.g. near the sinuses). If the magnetic field in a particular region is offset by ΔB, a phase ramp with slope $a = \gamma \Delta B t_{PE}/\Delta k_{PE}$ is formed in k-space, where t_{PE} is the time it takes to acquire adjacent phase encode lines separated by Δk_{PE}. As shown in Equation (1.16), this results in the signal in the final image being shifted by $a/2\pi$. When the offset varies with position, different regions undergo

different shifts which results in distortions. EPI is sensitive to these distortions because the k-space traversal rate in the PE direction, $\Delta k_{PE}/t_{PE}$, is slow due to the time required to acquire each FE line.

1.5 Diffusion Tensor Imaging

1.5.1 Sensitizing the Signal to Diffusion

How the MRI signal depends on diffusion can be understood by first considering Fick's second law, which governs how particles are distributed over time under the influence of thermal random motion,

$$\frac{dn}{dt} = D\nabla^2 n \tag{1.19}$$

where D is the diffusion coefficient, and $n(\mathbf{r}, t)$ is the probability of finding the particle at a position $\mathbf{r}$ and time t. Torrey made the association that this equation could be adapted to the Bloch equations (Equation 1.1) to describe the self-diffusion of local magnetization when a gradient is present [28]

$$\frac{dM_{xy}}{dt} = -i\gamma \mathbf{G} \bullet \mathbf{r} - \frac{M_{xy}}{T_2} + D\nabla^2 M_{xy} \tag{1.20}$$

The solution to Equation 1.20 is [29]

$$M_{xy} = e^{-i\gamma \int_0^t \mathbf{r}\cdot\mathbf{g}(t')dt'} \cdot e^{t/T_2} \cdot e^{-D\gamma^2 \int_0^t \left(\int_0^{t'} \mathbf{G}(t'')dt''\right)^2 dt'} \tag{1.21}$$

The first and second terms are just the usual phase imparted by the gradient and the attenuation from T_2, respectively, while the last term represents the effect of diffusion, which turns out to be a signal attenuation. This is not unexpected, since the diffusing spins will experience different phase accumulation

depending on their motion through the gradient which results in net signal dephasing. The signal attenuation from diffusion is more simply depicted by making the substitution for k (Equation 1.8) and defining

$$b_{\mathbf{r}} = 4\pi^2 \int_0^t k_{\mathbf{r}}(t')^2 dt' \tag{1.22}$$

where $\mathbf{r}$ describes the direction of the gradient. At the gradient echo (i.e. TE, where $k = 0$) the magnetization is

$$M_{xy} = M_{xy}^{b0} e^{-b_{\mathbf{r}} D_{\mathbf{r}}} \tag{1.23}$$

where M_{xy}^{b0} is the magnetization at TE when $b = 0$ and $D_{\mathbf{r}}$ is the diffusion coefficient along the direction of $\mathbf{r}$. It is clear from Equation 1.23 that the sensitivity of an experiment to diffusion can be increased by increasing the b-value, which in turn can be increased by increasing the magnitude and duration of applied gradients. The diffusion coefficient can be experimentally estimated, then, by rearranging Equation 1.23:

$$D_{\mathbf{r}} = -\ln\left(\frac{M_{xy}}{M_{xy}^{b0}}\right) / b_{\mathbf{r}} \tag{1.24}$$

In tissue the diffusion coefficient is generally directionally dependent (see Section 1.5.2) and better described by a second order tensor, $\underline{\mathbf{D}}$, which necessitates replacement of the diffusion term in Equation 1.20 with $\nabla \underline{\mathbf{D}} \nabla M_{xy}$. This causes b to also be a tensor with elements l, m that correspond to pairings of three orthogonal directions (i.e. x, y, z) so that [30]

$$b_{l,m} = 4\pi^2 \int_0^t k_l(t') k_m(t') dt' \tag{1.25}$$

$$M_{xy} = M_{xy}^{b0} e^{-\mathbf{b}\cdot\underline{\mathbf{D}}} \tag{1.26}$$

The diffusion tensor describes the directional dependence of diffusion relative to the laboratory frame. To obtain the axes of principal diffusion, the eigenvalues and eigenvectors of $\underline{\mathbf{D}}$ are computed. At least 6 gradient directions are required to determine all 6 unique components of $\underline{\mathbf{D}}$ (instead of 9 because the 3×3 diffusion tensor is symmetric). With more than 6 directions, a least squares solution for $\mathbf{D}$ must be performed via the pseudo-inverse of $\mathbf{b}_{all}$ [31]:

$$\begin{aligned} \mathbf{D} &= \left(\mathbf{b}_{all}^T \mathbf{b}_{all}\right)^{-1} \mathbf{b}_{all}^T \mathbf{M}_{all} \\ \mathbf{M}_{all} &= \left[\begin{array}{cccc} -\ln\left(\frac{M_{xy}^1}{M_{xy}^{b0}}\right) & -\ln\left(\frac{M_{xy}^2}{M_{xy}^{b0}}\right) & \cdots & -\ln\left(\frac{M_{xy}^N}{M_{xy}^{b0}}\right) \end{array} \right]^T \end{aligned} \tag{1.27}$$

where N is the number of directions, $\mathbf{b}_{all}$ is an $N \times 6$ matrix of the b-tensor (a symmetric 3×3 matrix with 6 unique elements) for each direction, and $\mathbf{M}_{all}$ is an $N \times 1$ vector of the imaging data. Equation 1.27 is carried out separately for each voxel.

The first reliable method reported for obtaining a large enough b-value to measure diffusion coefficients in tissue was the Stejskal-Tanner method, where two large gradient lobes are placed on either side of the refocusing RF pulse in a spin-echo acquisition with no imaging gradients [32] (Figure 1.10). Stejskal and Tanner included the effect of a background gradient, $\mathbf{G}_0$, in their analysis, which leads to a b-value given by

$$\begin{aligned} b =& \gamma^2 \left[\delta^2 \left(\Delta - \frac{\delta}{3} \right) G^2 + \frac{2}{3}\tau^3 G_0^2 \right. \\ & \left. -\delta \left(t_1^2 + t_2^2 + \delta\left(t_1 + t_2\right) + \frac{2}{3}\delta^2 - 2\tau^2 \right) \mathbf{G}_0 \bullet \mathbf{G} \right] \end{aligned} \tag{1.28}$$

where G is the diffusion gradient amplitude, δ and Δ are the duration and

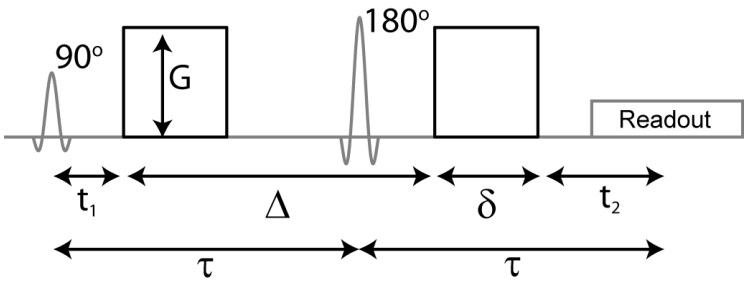

Figure 1.10: Diffusion encoding gradients relative to the RF pulses for the Stejskal-Tanner method, where G is the net gradient amplitude over all three gradient channels.

separation of the diffusion gradients, respectively, τ is the separation between the 90° and 180° pulses, t_1 is the time from the 90° pulse to the start of the first diffusion gradient, and t_2 is the time from the end of the second diffusion gradient to the spin-echo. A possible source of background gradients is magnetic susceptibility; however, it has been experimentally shown that they do not cause any measurable affect of DTI parameters (to be discussed in more detail in the next section). Therefore, the effect of background gradients is usually ignored to yield the b-value equation for Stejskal-Tanner diffusion preparation as

$$b = \gamma^2 G^2 \delta^2 \left(\Delta - \frac{\delta}{3} \right) \tag{1.29}$$

In 1990, Turner implemented a Stejskal-Tanner diffusion gradient preparation in combination with EPI, as depicted in Figure 1.6 [33]. Single-shot EPI is used for the signal readout because physiological or head motion during the diffusion gradients results in signal phase that varies from shot to shot. If the data was acquired in multiple shots, the phase inconsistencies from slight variations in motion from shot to shot would introduce artifacts. When single shot EPI is used, any coherent motion in a voxel results in non-zero phase in the voxel after the diffusion gradients, while intravoxel incoherent motion results in signal loss. Accordingly, only the magnitude of the images are used

in Equation 1.26 to remove the effects of bulk motion. Both diffusion and perfusion can result in intravoxel incoherent motion [34]; however, at the large b-values typically used (1000 s/mm^2) the signal is dominated by diffusion effects.

While the Stejskal-Tanner method is still often used, many scanners utilize more complex arrangements of gradients and refocusing RF pulses to mitigate eddy currents induced by the large gradients [35]. In the thesis work, gradient pre-compensation [36, 37] resulted in effective mitigation of eddy current effects, allowing use of the classic Stejskal-Tanner approach.

1.5.2 Diffusion Measurements in Tissue

In a medium with no boundaries, the probability distribution obtained from the solution to Fick's second law (Equation 1.19) has a Gaussian spatial profile, with a width determined by the time elapsed. In a medium with boundaries, the random motion of molecules will be hindered or restricted and the probability distribution will no longer be Gaussian. Therefore, the solution of Equation 1.23, which assumes Gaussian diffusion, provides an *apparent* diffusion coefficient (ADC) rather than a true self-diffusion coefficient. For more restriction of diffusion by boundaries, the shorter the distance molecules are permitted to diffuse and the smaller the ADC. If boundaries change with direction the ADC also varies with direction, which can be probed by the measurement of the eigenvalues of the diffusion tensor (Equation 1.26) (Figure 1.11). Another consequence of non-Gaussian restricted diffusion is that the ADC measurements generally depend on b-value [38]. It is observed that the ADC decreases as the b-value increases because the molecules are not allowed to move as far as self-diffusion would dictate (because of boundaries), and the disparity between the measured signal and what the signal should be

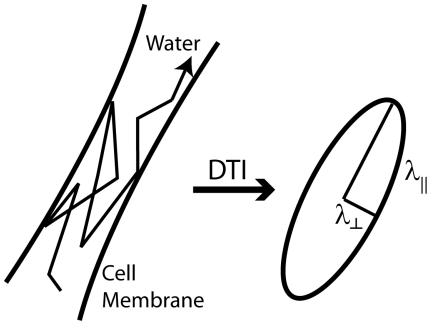

Figure 1.11: If the diffusion of water is impeded by cellular microstructure, the diffusion ellipsoid measured with DTI has its long axis, $\lambda_{||}$, aligned with the direction along which motion is least impeded. The size of the ellipsoid is given by the eigenvalues of the diffusion tensor (i.e. $\lambda_{||}$ and $\lambda_{\perp}$) and the orientation is given by the eigenvector.

with Gaussian diffusion is worsened as the b-value increases.

In gray matter, DTI measurements show relatively isotropic diffusion, while DTI measurements in white matter are highly anisotropic. The longitudinally oriented structural components of white matter that were originally postulated to contribute to anisotropic DTI measurements were myelin, the axonal membrane, and neurofibrils (microtubules and neurofilaments). In addition, potential non-structural sources that were considered were fast axonal transport and magnetic susceptibility. Various experiments in ex-vivo nerve samples in the 1990's provided evidence for or against the various postulated sources of diffusion anisotropy:

- *Susceptibility* A potential source of anisotropy that was proposed was susceptibility induced magnetic field gradients that would anisotropically modulate the local b-value. The effect of the background gradients can be eliminated with the application of bipolar gradient pulses. In both ex-vivo nerves [39] and in-vivo human brain [40] no difference in ADC was observed for the insensitive method compared to the normal Stejskal-Tanner method, suggesting little influence of magnetic susceptibility on diffusion anisotropy.

- *Fast Axonal Transport and Neurofibrils* In garfish nerves that were treated to break down microtubules and inhibit fast axonal transport, diffusion anisotropy was preserved [41], suggesting that neither fast axonal transport nor microtubules themselves strongly influence diffusion anisotropy. Also, ADC values measured in the axoplasmic space of the giant axon of a squid [42] and giant reticulospinal axons of the lamprey [43] (i.e. the measurements were in a region lacking membranes) were near the value in pure water and anisotropy was low, suggesting that neurofilaments overall have a low impact on ADC measurements.

- *Axonal Membranes and Myelin* Strongly anisotropic ADC was measured in non-myelinated garfish olfactory nerves [41] and the non-myelinated white matter of human neonates [44, 45]. In myelin deficient rats, anisotropy was decreased only a small amount compared to normal controls [46], suggesting that while not required for anisotropic ADC measurements, myelin may modulate the amount of anisotropy.

In summary, anisotropy in ADC measurements primarily stems from membranes. While evidence suggests that myelin likely modifies anisotropy, it is difficult to delineate its effect from the membranes because other properties may be different between myelinated and non-myelinated axons, such as axon density and diameters.

1.5.3 Diffusion Tensor Imaging Metrics

As described earlier, the diffusion tensor can be represented by its three eigenvalues (e.g. λ_1, λ_2, and λ_3) and three eigenvectors, where the eigenvalues describe the ADC along the principle axes defined by the eigenvectors. Typically the largest eigenvalue (λ_1) is assumed to have its eigenvector along

the direction of the underlying white matter tracts, and is thus referred to as the parallel or longitudinal diffusivity, $\lambda_{||}$. The two smaller eigenvalues are averaged to obtain the perpendicular diffusivity, $\lambda_{\perp} = (\lambda_2 + \lambda_3)/2$. The mean diffusivity, MD $= (\lambda_1 + \lambda_2 + \lambda_3)/3$ describes the mean ADC averaged over all directions. The anisotropy of the diffusion over different direction is characterized by the fractional anisotropy (FA), which is given by the variance of the eigenvalues normalized to be a value between 0 (perfectly isotropic; $\lambda_1 = \lambda_2 = \lambda_3$) and 1 (perfectly isotropic; $\lambda_{\perp} = 0$),

$$FA = \sqrt{\frac{3}{2}} \frac{\sqrt{(\lambda_1 - MD)^2 + (\lambda_2 - MD)^2 + (\lambda_3 - MD)^2}}{\sqrt{\lambda_1^2 + \lambda_2^2 + \lambda_3^2}} \tag{1.30}$$

Example brain maps of MD, FA, $\lambda_{||}$, and $\lambda_{\perp}$ are shown in Figure 1.12, where it is evident that MD has little contrast between white and grey matter, whereas FA clearly identifies the major white matter tracts. While it is not common to display $\lambda_{||}$ and $\lambda_{\perp}$ parameter maps, contrast between white and grey matter is nevertheless observed.

1.5.4 Probing Diffusion Length Scales

The mean squared displacement of a particle with a Gaussian probability distribution (i.e. intrinsic self-diffusion) in one dimension was shown by Einstein to be [47]

$$\left\langle x^2 \right\rangle = 2Dt \tag{1.31}$$

Here, it is observed that the expected squared distance away from the starting position that a molecule is found increases linearly with time. In a DTI experiment, the period of time over which the diffusion coefficient is probed is approximated as the diffusion time, Δ_{eff}. If Δ_{eff} is so short that most of the molecules do not have enough time to reach any boundaries in the tissue (i.e.

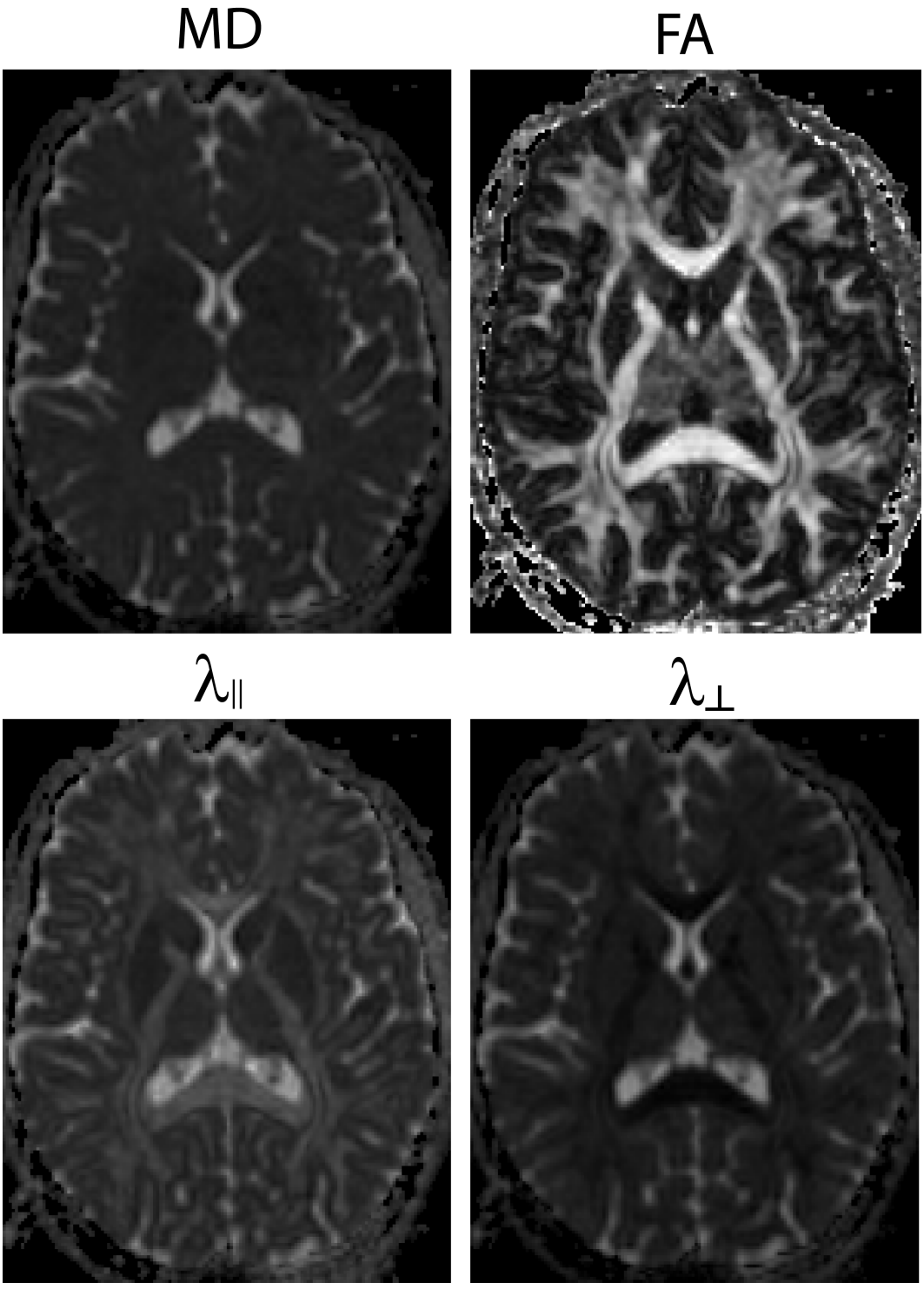

Figure 1.12: Examples of mean diffusivity (MD), fractional anisotropy (FA), and parallel ($\lambda_{||}$) and perpendicular ($\lambda_{\perp}$) eigenvalue maps for a healthy subject.

$\Delta_{eff} << \Delta x^2_{barriers}/2D_{intrinsic}$ via Equation 1.31), the ADC will be equivalent to the intrinsic diffusion coefficient of the water in the tissue [42, 43]. However, as the diffusion time increases and the molecules interact with more barriers, the ADC values decrease to an asymptotic value. In brain tissue, where length scales are ≈ 1 μm ($\Delta x^2_{barriers}/2D_{intrinsic} \approx 0.2$ ms), standard DTI experiments where $\Delta_{eff} > 20$ ms are in the asymptotic long time regime. While a long Δ_{eff} is not a limitation in itself, measuring how ADC values change at shorter diffusion times may permit additional insight into tissue microstructure.

In a Stejskal-Tanner experiment, if the gradients are assumed to be much narrower than their separation (i.e. $\delta << \Delta$ in Figure 1.10), the diffusion time Δ_{eff} is derived from the b-value equation by setting $b = \gamma^2 G^2 \delta^2 \Delta_{eff}$ [4, 48] to obtain

$$\Delta_{eff} = \Delta - \delta/3 \tag{1.32}$$

In practice, though, small Δ_{eff} (i.e. less than 20 ms) are difficult to attain with a Stejskal-Tanner implementation because of gradient hardware limitations. Early attempts to address these limitations and achieve short Δ_{eff} were to apply multiple, short Δ_{eff} pairs of bipolar gradients. While a single bipolar gradient pair has a small b-value, the b-value will scale up linearly with the number of bipolar pairs. However, for this case the approximation $\delta << \Delta$ is no longer true and the validity of the equation for diffusion time is not strictly valid; thus, a different interpretation is warranted. Additionally, estimation of tissue length scales by inserting the diffusion time and ADC into Equation 1.31 is not ideal, since Equation 1.31 is only valid for diffusion with no boundaries.

A more general definition of the diffusion coefficient that is more readily applied to diffusion with boundaries is given by the velocity autocorrelation

formalism [49],

$$D(t) = \frac{1}{2}\int_0^t \langle v(t')v(0)\rangle \, dt' \tag{1.33}$$

where v is the velocity of the particles and $\langle v(t')v(0)\rangle$ is the velocity autocorrelation. Using a Fourier transform, one can define the diffusion spectrum,

$$D(\omega) = \frac{1}{2}\int_0^\infty \langle v(t')v(0)\rangle \, e^{i\omega t'} dt' \tag{1.34}$$

In pure water at room temperature the velocities become decorrelated in less than a nanosecond [50], which effectively makes $\langle v(t')v(0)\rangle$ a delta function and the diffusion spectrum independent of frequency. With barriers present (permeable or impermeable), a long lasting negative correlation exists due to reflections from the boundaries [51], which results in a diffusion spectrum with a notch at $\omega = 0$ (Figure 1.13). The value of $D(\omega = 0)$ is equivalent to the diffusion coefficient measured with an infinite diffusion time (i.e. D_∞), and higher frequencies correspond to smaller length scales of diffusion. $D(\omega)$ is

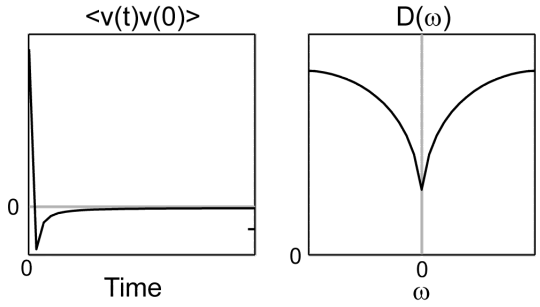

Figure 1.13: In a environment with barriers to diffusion, a long lasting negative velocity autocorrelation, $\langle v(t')v(0)\rangle$, exists due to reflections from the boundaries [51]. The initial delta-function of positive correlation results from velocity correlations at extremely short time scales before any boundaries are reached. The resultant diffusion spectrum, $D(\omega)$, has a notch at $\omega = 0$.

related to the measured signal in an analogous way to Equations 1.25 and 1.26 [49],

$$M_{xy} = M_{xy}^{b0} e^{-2\pi \int_{-\infty}^{\infty} \mathbf{k}(\omega)\mathbf{D}(\omega)\mathbf{k}(\omega)d\omega} \tag{1.35}$$

$$\mathbf{k}(\omega) = \frac{\gamma}{2\pi} \int_0^\infty \left(\int_0^{t'} \mathbf{G}(t'')dt'' \right) e^{i\omega t'} dt' \tag{1.36}$$

where $k(\omega)$ is the Fourier transform of k.

It is implicit from Equation 1.36 that the frequency components of the ADC that are measured in a DTI experiment are those where $k(\omega)$ is non-zero. Accordingly, this gives a basis for designing gradient waveforms that produce a narrow bandwidth of $k(\omega)$, where higher frequencies correspond to smaller scales of microstructure. For the standard Stejskal-Tanner diffusion preparation (i.e. pulsed gradient spin-echo, PGSE), $k(\omega)$ is centered at $\omega = 0$ (Figure 1.14). For decreasing diffusion time (i.e. decreased separation of

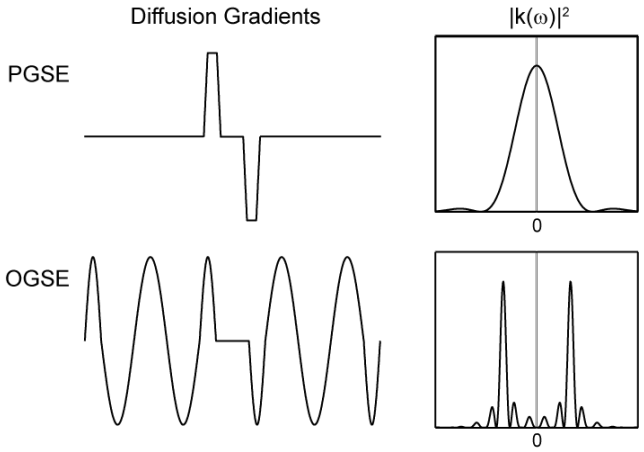

Figure 1.14: PGSE gradients produce a k-spectra that is centered at $\omega = 0$, while cosine-modulated gradients produce a narrow spectra at a non-zero frequency. A 180° RF pulse is assumed to occur between the gradient pairs, and it is accounted for in the diagram by reversing the polarity of the gradients after the RF pulse.

the gradient lobes) $k(\omega)$ becomes wider; thus, while decreasing the diffusion time grants access to higher frequencies, a large contribution from $D(0)$ (i.e. infinite diffusion time) persistently remains. In contrast, a cosine gradient waveform with the end lobes replaced with twice frequency sinusoidal lobes (i.e. oscillating gradient spin-echo, OGSE, diffusion MRI) produces a narrow

high-frequency spectrum with no zero-frequency component (Figure 1.14). By sweeping through several frequencies $D(\omega)$ can be estimated, which may lend insight into the microstructural characteristics of the medium.

1.5.5 High Field DTI

As was first introduced in the overview (Section 1.1), DTI is generally a low resolution technique. To better understand how the resolution might be improved, it is instructive to review the formula for signal to noise ratio (SNR) in an MRI acquisition (assuming that body resistance dominates the noise) [52],

$$SNR \propto M_0 V \sqrt{t_{aq}} C \tag{1.37}$$

where M_0 is the equilibrium magnetization $\propto B_0$, V is the volume of a voxel, t_{aq} is the total time spent acquiring signal, and C is signal changes from the contrast (e.g. e^{-TE/T_2} for T_2 weighted scans). Thus, the minimum achievable voxel volume is limited by the available SNR. DTI only has sufficient SNR for fairly low resolutions for two primary reasons: (1) the diffusion gradients require a long duration, which makes the TE long and the net signal low, and (2) signal loss introduced by the diffusion gradients further decreases the available signal ($\approx 50\%$ for the typical b = 1000 s/mm^2 in brain tissue). In addition, OGSE dMRI requires even longer TE than standard DTI because oscillating gradients are inefficient at creating large b-values and many oscillations must be used, which further lengthens the TE. Also, the lower b-value results in sub-optimal sensitivity of ADC calculations to noise. Both of these issues create extremely stringent SNR conditions for OGSE dMRI, making it difficult to perform in-vivo; only one in vivo human paper on OGSE dMRI exists in the current literature aside from the work presented in this thesis [53].

To increase the SNR without increasing scan time, the B_0 field can be increased to increase M_0 (Equation 1.37). However, there are several well known challenges to performing DTI at higher magnetic field strengths, which are increased distortions from B_0 inhomogeneity, increased specific absorption rate (SAR), and increased B_1 inhomogeneity. The work in this thesis was performed at the high field strength of 4.7T, approximately 3 times larger than typical. The techniques used to mitigate these challenges are described below.

- *Distortions* As discussed in Section 1.4.4, the distortions caused by B_0 inhomogeneity are dictated by the equation $\Delta x = \gamma \Delta B t_{PE}/\Delta k_{PE}$, where t_{PE} is the time it takes to acquire phase encode lines separated by Δk_{PE}. At high magnetic field strengths, ΔB is larger and the distortions are worsened. The above equation also reveals that distortions can be reduced by traversing through k-space at a faster rate (i.e. decrease $t_{PE}/\Delta k_{PE}$). In the thesis work, this was performed by using rate $R = 2$ generalized autocalibrating partially parallel acquisitions (GRAPPA) [54], which enables collection of only half the normally required number of k-space samples (via skipping of alternate phase encode lines). This causes Δk_{PE} to be twice as large for the same t_{PE}, thus reducing distortions by a factor of 2. The primary trade-off for using parallel imaging is a decrease in the SNR by a factor of $\sqrt{R}$ due to the reduced time spent acquiring signal; however, this limitation is offset by the reduced TE that parallel imaging enables for EPI. Spatially dependent noise increases may also occur from non-optimal receive coil sensitivity profiles, which is quantified by the geometry factor (g-factor). For the work in this thesis, g-factors were typically within the range 0.8 to 1.2 (note that g-factors less than 1 can occur for GRAPPA [55]).

GRAPPA for EPI may also introduce additional sensitivity to motion, which is described in Chapter 3.

- *Specific Absorption Rate* When the radiofrequency pulses are applied, transient electric fields are induced by Faraday induction of current from the changing B_1 field. Resistance in the body results in tissue heating, and the specific absorption rate (SAR) of RF power must be kept at safe levels to prevent injury. The energy deposited from RF pulses is proportional to $B_0^2 B_1^2$ [20], which causes SAR to become a limiting factor at high field strengths. In the spin-echo EPI sequence relevant to this thesis, the primary contribution to SAR stems from 180° RF pulses. The work in this thesis was primarily performed using only one 180° pulse, compared to multiple refocusing pulses that are often utilized [35], which resulted in manageable SAR for most cases. In rare cases where SAR was still too high the TR was slightly lengthened to reduce the average power deposited.

- B_1 *Inhomogeneity* For increasing B_0, the Larmor frequency also increases (Equation 1.3). Accordingly, the wavelength of the B_1 field in the medium, $\lambda = 2\pi c/(\omega_0 n)$ (where c is the speed of light and n is the index of refraction) decreases for increasing B_0. When the wavelength becomes comparable to the size of the sample, standing waves cause the B_1 field amplitude to be non-uniform. In a spin-echo acquisition with multiple refocusing 180° pulses, each 180° RF pulse will modulate the amplitude of the transverse magnetization by a factor $\sin^2(\theta/2)$ [20], where θ is the actual flip angle that results from B_1 inhomogeneity (Figure 1.15a). The effect of B_1 inhomogeneity is easily visible in a large water phantom because the RF wavelength is shorter compared to in brain tissue (Figure

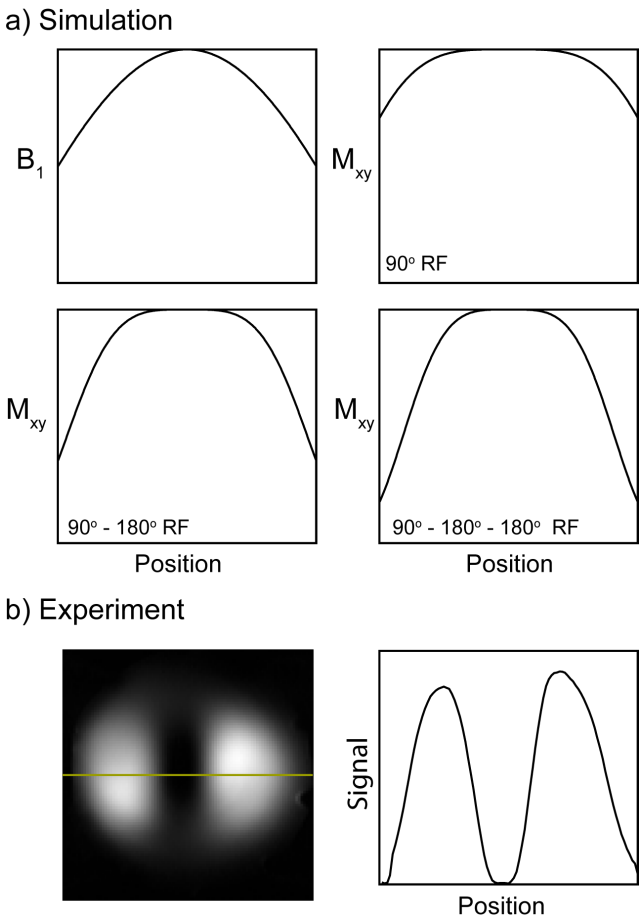

Figure 1.15: (a) For an inhomogeneous B_1 field, the transverse magnetization, M_{xy}, becomes more inhomogeneous as more 180° pulses are added after the initial 90° excitation pulse (stimulated echoes are ignored). (b) Extreme inhomogeneity can be experimentally observed in a large phantom of pure water using spin-echo EPI with one 180° pulse. The line in the image indicates the location of the signal profile shown on the right. Notably, B_1 inhomogeneity is not nearly as severe in the human brain.

1.15b). By using only one refocusing pulse in the spin-echo EPI sequence this effect was mitigated. Also, dMRI is a quantitative approach where the diffusion weighted signal is divided by the non-diffusion weighted signal (Equation 1.24). Because the B_1 inhomogeneity is equivalent for both images that are divided, it does not affect quantitative ADC values. However, it does reduce the SNR in some regions, which increases the uncertainty of the calculated ADC.

1.6 Summary

The background presented in this chapter represents the basic knowledge required for the research projects described in this thesis. Good resources for additional details are *Clinical Neuroanatomy* by Waxman [17] for brain physiology, *Magnetic Resonance Imaging* by Haacke [20] for MRI fundamentals, and *Diffusion MRI: Theory, Methods, and Applications* by Jones [31] for dMRI fundamentals.

Chapter 2

The Effect of Concomitant Gradient Fields on Diffusion Tensor Imaging[1]

2.1 Introduction

In MRI, magnetic field gradients are used for spatial encoding and to provide contrast for particular sequences. While the applied gradient fields are typically assumed to be linear and along the principle magnetic field direction, Maxwell's equations dictate that small non-linear components are also present in the transverse direction. The magnetic field amplitude offset caused by these concomitant gradient fields scales inversely with the static magnetic field strength and have historically been a concern in low-field applications [7, 56, 57]. While concomitant gradient fields can usually be ignored for common pulse sequences at most field strengths, there are some pulse sequences that are susceptible to their effects, such as echo-planar imaging (EPI) [58–60], fast spin-echo [61], spiral trajectories [62, 63], phase contrast MRI [64], balanced steady-state free precession [65], and combined gradient and spin-

[1]A version of this chapter has been published: Baron CA, Lebel RM, Wilman AH, Beaulieu C. The Effect of Concomitant Gradient Fields on Diffusion Tensor Imaging. Magn Reson Med. 68:1190-201 (2012) doi: 10.1002/mrm.24120

echo acquisition [66]. Generally, concomitant fields introduce additional phase variation. Depending on the k-space sampling scheme and slice orientation, this can cause mis-registration of k-space data, which may result in signal loss or image shifting, warping, and/or blurring. Depending on the pulse sequence, corrections can sometimes be performed using preparation gradients before a 180° refocusing radiofrequency (RF) pulse to pre-warp the image phase [59], or by taking the mis-registration into account during reconstruction [58, 63, 64, 67]. The amplitude of concomitant gradient fields scales with the square of gradient strength; therefore, with the advent of increasingly high amplitude gradient hardware, the effects of concomitant gradient fields will likely become increasingly relevant.

In diffusion weighted imaging (DWI) and diffusion tensor imaging (DTI), there is considerable motivation to utilize stronger gradients to achieve higher diffusion-sensitizing factors (i.e. b-value) and to reduce the echo time for a given b-value, thereby increasing the signal per shot and reducing scan time via a shorter TR (given the reduced TE for each slice). The effect of concomitant gradient fields on diffusion imaging has been partly discussed in the context of asymmetric gradient coils by Meier et al. [68], where concomitant gradient effects can be more severe than for symmetric gradient coils. It was shown that a diffusion preparation containing bipolar gradients can yield concomitant gradient fields that create a linear phase ramp along the phase-encode direction, which can potentially shift the center of k-space out of the acquisition window, particularly when using partial Fourier undersampling. Note that diffusion pulse sequences containing bipolar gradients, as opposed to the pair of monopolar gradients applied on either side of the 180° refocusing RF pulse as in the Stejskal-Tanner method [32], minimize eddy current effects [35, 69]. Meier et al. also introduced a prospective correction that

mitigates this specific source of error. They did not consider, however, errors in quantification of the apparent diffusion coefficient (ADC) that can arise from non-linear phase variations or through-plane phase variations imparted by concomitant gradient fields. The directionality and non-linearity of the phase accrual generated by concomitant gradient fields has a dependence on net gradient direction, which represents a considerable concern in DTI, where numerous gradient directions (6 or greater) are acquired with simultaneous gradients that are often at maximum strength. This directionally-dependent signal decay beyond diffusion will adversely impact the tensor and higher order models used for the determination of anisotropy and the orientation of white matter tracts.

In the current work, the potential errors of diffusion measurements associated with these unaddressed sources of concomitant gradient fields are investigated by performing simulations based on theoretical derivation and experimental validation using phantoms and healthy human subjects. Eddy-current minimizing diffusion preparation schemes that are sensitive to concomitant gradient fields, namely the usual Reese twice refocused [35] and the split-gradient single spin echo (SGSSE) (sometimes used in place of the twice-refocused preparation in favour of fewer 180° RF pulses) [69, 70] preparations, are compared to the Stejskal-Tanner preparation [32], which is immune to error from concomitant gradient fields. Examples are shown experimentally at 4.7 Tesla with a maximum gradient amplitude of 60 mT/m per axis. A prospective correction scheme that is a generalization of the specific scheme introduced in earlier work [68] is proposed and verified to reduce the diffusion measurement error. Error predictions from simulations are also presented for a range of common gradient and static field strengths.

2.2 Theory

2.2.1 Concomitant Gradient Fields for Diffusion Imaging

The net amplitude of the magnetic field is augmented by the presence of concomitant gradient fields, where the Taylor expansion to second order for symmetric gradient coils, with x- and y- gradient sets related by 90°, is repeated here (detailed derivations can be found elsewhere [64, 68]):

$$B_C = \frac{\left(G_x^2 + G_y^2\right) z^2}{2B_0} + \frac{G_z^2 \left(x^2 + y^2\right)}{8B_0} - \frac{G_x G_z xz}{2B_0} - \frac{G_y G_z yz}{2B_0} \tag{2.1}$$

A potential concern is the impact of B_C on b-value, which can be calculated via a spatial derivative of Equation 2.1. Within a 20 cm region surrounding isocenter, b-value variations are on the order of 10^{-4}% for a 4.7 T system with 60 mT/m gradients, which is completely negligible. While the impact on b-value is inconsequential, the concomitant fields from the large diffusion-sensitizing gradient lobes can cause spatially non-linear phase accrual. For gradients placed symmetrically about an RF refocusing pulse (shaded regions in Figure 2.1), phase accrual from B_C is refocused. As such, the net phase accrual occurs over the cumulative duration, τ, of gradients that are not symmetrically placed about the RF refocusing pulse (Figure 2.1), and is given by:

$$\phi(x, y, z, \tau) = \gamma \int_{\tau} B_C(x, y, z) dt \approx \gamma \tau B_c(x, y, z) \tag{2.2}$$

It is unknown to what extent that this phase accrual could impart error into quantitative diffusion measurements. In contrast to the SGSSE and twice-refocused preparations, all phase accrual from B_C is RF refocused in the

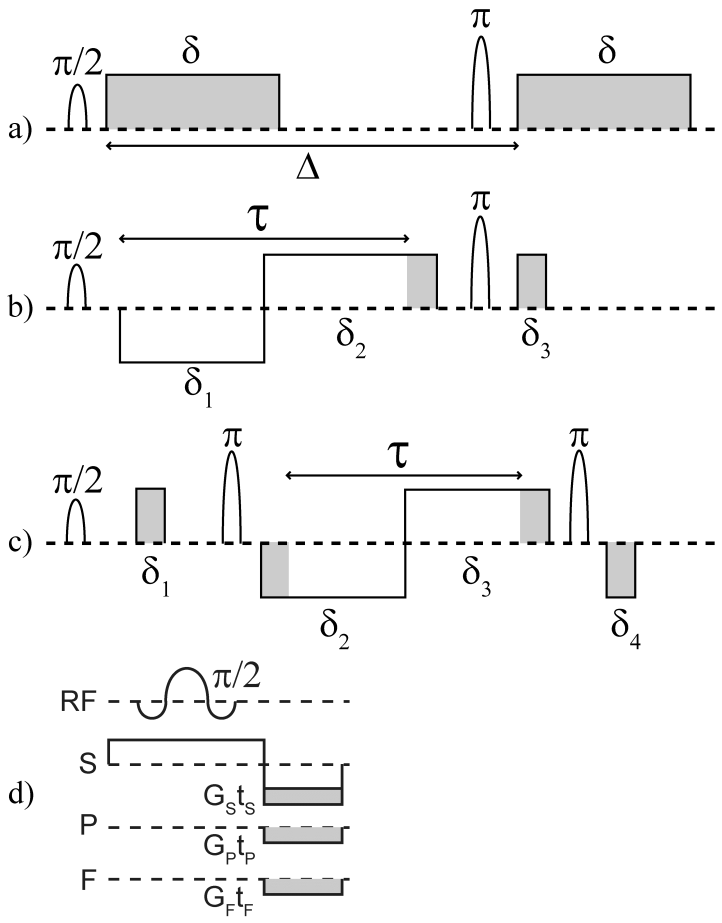

Figure 2.1: Basic timing of RF pulses and diffusion gradient lobes for (a) Stejskal-Tanner, (b) split-gradient single-spin-echo (SGSSE), and (c) Reese double-spin-echo preparations. The shaded regions indicate the portion of the gradient lobes where the phase accumulation from concomitant gradient fields are refocused by the 180° RF pulses. For (a)-(c), slice select, spatial encoding, and spoiler gradient waveforms are omitted for clarity. (d) Proposed correction gradient lobes with areas $G_S t_S$, $G_P t_P$, and $G_F t_F$ applied on the slice-select (S), phase-encode (P), and frequency-encode (F) gradient channels, respectively.

Stejskal-Tanner preparation. Phase variation along the slice plane (i.e. in-plane dephasing) can cause warping of k-space data that is incompatible with partial Fourier acquisition techniques. Intravoxel dephasing causes a decrease in image intensity which would corrupt measurements of the apparent diffusion coefficient (ADC).

2.2.2 In-Plane Dephasing

From Equation 2.1, concomitant gradient fields can introduce a parabolic phase variation within the imaging plane, which causes a blurring of k-space because the signal from voxels spatially distant from iso-center re-phase away from the center of k-space.[2] Additionally, the G_iG_j cross terms in Equation 2.1 can cause a linear phase ramp in image space, which corresponds to a bulk k-space translation. These two concepts will be referred to as k-space blurring and k-space shifting, respectively. Image artefacts can occur from these two sources if data is pushed near or outside the edge of the acquisition window; artefact severity is strongly enhanced with partial Fourier undersampling. When this occurs, low spatial-frequency components of the MR signal are artificially attenuated. While artefacts stemming from similar effects have been discussed in other contexts [58, 61, 63, 65], concomitant field induced k-space blurring has not been previously discussed in the context of DTI. Conversely, k-space shifting in DTI has been introduced elsewhere [68]. It is instructive to evaluate the expected fractional translation of k-space data along the undersampled direction (with respect to width of entire k-space), δk. For frequency-encode, phase-encode, and slice-select axes along the unit-vectors $\hat{r}_F$, $\hat{r}_P$, and $\hat{r}_S$, respectively, and undersampling along $\hat{r}_P$, the magnitude of

[2] i.e. the spatially distant voxels have phase ramps in image space that causes their respective contributions to k-space to be shifted - see Section 1.4.3

the maximum shift (positive or negative) of any frequency component is given by:

$$\delta k_P = \frac{FOV_P}{2\pi N_P}\gamma\tau\left(\max\left(|\hat{r}_P \bullet \nabla B_C(x,y,z)|\right)\right) \tag{2.3}$$

In the above equation, FOV_P and N_P are the field-of-view and number of image pixels, respectively, along the phase-encode direction. For undersampling in the frequency-encode direction, all parameters with P subscripts are replaced with their frequency-encode analogues. For axial slices and symmetric gradient coils, Equation 2.3 simplifies to:

$$\begin{aligned} \delta k_P &= \delta k_{P,Bl} + \delta k_{P,Sh} \\ \delta k_{P,Bl} &= \frac{FOV_P G_z^2 y_M \gamma\tau}{8\pi N_P B_0} \\ \delta k_{P,Sh} &= \frac{FOV_P G_y G_z z_S \gamma\tau}{4\pi N_P B_0} \end{aligned} \tag{2.4}$$

In Equation 2.4, the contributions to δk_P from k-space blurring and shifting are given by $\delta k_{P,Bl}$ and $\delta k_{P,Sh}$, respectively, z_S is the slice position, and y_M is the farthest position in the image from iso-center. For an object that fills the entire field-of-view, $y_M = FOV_P/2$. The signal loss associated with δk is in general dependent on the subject geometry because the amount of k-space data shifted out of the acquisition window is dependent on the width of the k-space spectrum. In addition, while $\delta k_{P,Sh}$ vanishes as the slice position approaches iso-center for axial slices, $\delta k_{P,Bl}$ is equally present for all slices.

2.2.3 Intravoxel Dephasing

Intravoxel dephasing from concomitant gradient fields results in a decrease of signal intensity and has not been previously considered in the context of DTI. The decrease in signal is given by the integral of the phase dispersion

across any given voxel. Assuming that the magnetization is uniform across the slice thickness, w, and that the dephasing is predominantly perpendicular to the slice[3], the signal is:

$$S(r_F, r_P, r_{S,0}) = S_0(r_F, r_P, r_{S,0}) \frac{1}{w} \int_{r_{S,0}-w/2}^{r_{S,0}+w/2} e^{-i\gamma\tau B_C(r_F, r_P, r_S)} dr_S \tag{2.5}$$

The distances along the frequency encode, phase encode, and slice select directions are given by r_F, r_P, and r_S, respectively, $r_{S,0}$ is the position of the center of the slice, and S_0 is the signal received if concomitant fields were not present. For a thin slice, the dephasing from concomitant gradient fields can be approximated as a linear phase ramp at any voxel within the slice. Considering only the signal magnitude and using a linear approximation, one obtains:

$$\begin{aligned} \left| \frac{S(r_F, r_P, r_{S,0})}{S_0(r_F, r_P, r_{S,0})} \right| &= \frac{1}{w} \left| \int_{r_{S,0}-w/2}^{r_{S,0}+w/2} e^{-i\gamma\tau r_S(\hat{r}_S \bullet \nabla B_C)} dr_S \right| \\ &= \left| \text{sinc} \left(\frac{1}{w} \gamma\tau (\hat{r}_S \bullet \nabla B_C) \right) \right| \end{aligned} \tag{2.6}$$

This signal attenuation propagates into the ADC computation by falsely attributing phase dispersion to diffusion attenuation. For a reference measurement where $b = 0$ s/mm^2 denoted as S_{REF}, $ADC = -\ln|S/S_{REF}|/b$. With the error-free value given by $ADC_0 = -\ln|S_0/S_{REF}|/b$, the error is:

$$\begin{aligned} \delta ADC_{Th} &\equiv ADC(r_F, r_P, r_{S,0}) - ADC_0 \\ &= -\ln \left(\text{sinc} \left(\frac{1}{w} \gamma\tau (\hat{r}_S \bullet \nabla B_C) \right) \right) / b \end{aligned} \tag{2.7}$$

[3]A triple integral over the entire voxel would ideally be taken; however, this would preclude an analytical representation of the signal loss. Further, for axial slices (most common for DTI) intravoxel dephasing from concomitant fields is predominantly across the slice direction (see Equation 2.1).

Interestingly, Equation 2.7 shows that δADC_{Th} is sample-independent. δADC_{Th} is generally dependent on position within the slice, with specific spatial dependencies dictated by the diffusion gradient direction and slice prescription. For an axial slice using symmetric gradient coils:

$$\delta ADC_{Th}(x,y) = -\ln\left(\operatorname{sinc}\left(\frac{\left(G_x^2+G_y^2\right) z_S w\gamma\tau}{2B_0} - \frac{\left(G_x G_z x + G_y F_z y\right) w\gamma\tau}{4B_0}\right)\right)/b \tag{2.8}$$

where z_S is the position of the slice, and x, y is the position of a voxel in the slice.

Since the artefacts encountered depend on both slice and diffusion gradient orientations, Table 2.1 summarizes the expected artefacts for several gradient combinations for the three standard views, where the slice-select directions are along the z-, x-, and y-directions for axial, sagittal, and coronal views, respectively.

Table 2.1: Main Effect of Concomitant Fields for Various Gradient Combinations and Cardinal Planes

Gradient Combination	Axial Slices	Sagittal Slices	Coronal Slices
G_x, G_y, or $G_x + G_y$	In	Bl	Bl
G_z	Bl	In,Bl	In,Bl
$G_x + G_z$	In,Bl,Sh	In,Bl,Sh	In,Bl
$G_y + G_z$	In,Bl,Sh	In,Bl	In,Bl,Sh
$Gx + G_y + G_z$	In,Bl,Sh	In,Bl,Sh	In,Bl,Sh

In = intravoxel dephasing, Bl = k-space blurring, Sh = k-space shifting

2.2.4 Corrections

The linear component of dephasing caused by concomitant gradient fields can be mitigated by applying an appropriate gradient lobe to refocus the spins. In Ref. [68], this is suggested for the correction of k-space shifting, and similar approaches have been used in the context of EPI [60, 66]. Here, we generalize this prospective correction to apply to both k-space shifting and intravoxel dephasing. In cases where the dephasing varies throughout the slice, some residual error will remain away from the reference point used for the linear approximation of the dephasing. By choosing a position at the center of the anatomy of interest in the slice, x_C, y_C, z_C, the average error will be reduced. Accordingly, the gradient area, $G_i t_i$, required for each gradient channel, $i = S, P, F$, is:

$$G_i t_i = -\tau \left(\hat{r}_i \bullet \nabla B_C\right)_{\{x_C, y_C, z_C\}} \tag{2.9}$$

A suitable implementation of the correction is to add $G_S t_S$ to the gradient area required for the rephasing gradient of the excitation pulse, and simultaneously apply $G_P t_P$ and $G_F t_F$, as shown in Figure 2.1d. For an axial slice of a subject centered on the z-axis, the corrective gradient areas for symmetric gradient coils reduce to:

$$\begin{aligned} G_S t_S &= -\frac{\left(G_x^2 + G_y^2\right) z_S \tau}{B_0} \\ G_P t_P &= -\frac{G_y G_z z_S \tau}{2B_0} \\ G_F t_F &= -\frac{G_x G_z z_S \tau}{2B_0} \end{aligned} \tag{2.10}$$

While the proposed measures can correct for much of the error introduced by the concomitant gradient fields, the application of gradient lobes

cannot correct for errors that result from non-linear dephasing, such as k-space blurring. To mitigate ADC errors from this, a retrospective phase correction using low-frequency phase information is implemented before partial Fourier reconstruction [71, 72]. While this approach can not correct for data shifted outside the acquisition window nor have any impact on intravoxel dephasing, it de-blurs and centers the acquired k-space data before partial Fourier reconstruction.

2.3 Methods

To examine the effect of concomitant gradient fields on DTI, simulations based on the above theoretical derivations were performed first, and then the theory was experimentally validated in a phantom and healthy human subjects. Experiments were performed using a Varian Unity Inova (Walnut Creek, CA) 4.7 T whole body imaging system utilizing a symmetric gradient coil with a maximum gradient amplitude of 60 mT/m per axis. RF transmission and reception were performed using a 27 cm diameter birdcage coil. Data was acquired using Stejskal-Tanner (δ = 9.1 ms, Δ = 28.1 ms), SGSSE (δ_1 = 12.6 ms, δ_2 = 14.9 ms, δ_3 = 2.3 ms), and Reese twice-refocused (δ_1 = 3.0 ms, δ_2 = 11.4 ms, δ_3 = 11.7 ms, δ_4 = 2.7 ms) preparations (Figure 2.1). All sequences utilized single shot echo planar imaging (EPI) readouts with FOV = 24 cm, matrix size 96 $\times$ 96, and slice thickness 3.0 mm. The τ-values were 25.2 ms and 17.8 ms for the SGSSE and twice-refocused preparations, respectively. All scans (and simulations) were performed with axial slices since DTI is predominantly performed parallel to the anterior-posterior commissure axis, which is typically less than 10° from pure axial. Note that the concomitant phase errors caused by EPI gradients may affect the concomitant phase errors from

the diffusion gradients. To mitigate this as a source of error when comparing the different diffusion preparations, the EPI readout used was identical for all scans.

Simulations of the error from concomitant gradient fields were performed using acquisition parameters consistent with the experimental values stated above. Two values were calculated as a function of slice position: δk_P (Equation 2.3) and the mean δADC_{Th} (Equation 2.8). In the calculation of δk_P, y_M was chosen as half the field of view. Both a 6 direction diffusion encoding scheme that applies gradients on two axes simultaneously for each direction and a 30 direction diffusion encoding scheme (results similar for any scheme with gradients distributed about a sphere) [73] were investigated.

To validate the theoretical predictions offered by Equations 2.3 and 2.8, images of a phantom containing ST0-50 silicone oil (Clearco Products Co. Inc., Bensalem, PA) were acquired with six diffusion-encoding directions. This phantom was chosen because the B_1 field is uniform within it, which mitigates the additional sensitivity of the twice-refocused preparation to B_1 inhomogeneity in comparison to the Stejskal-Tanner and SGSSE preparations. Moreover, the diffusion coefficient of the phantom is many orders of magnitude smaller than that of water, and the signal loss from diffusion weighting is primarily from concomitant gradient induced error. Thirty-four slices (3 mm thick) with an inter-slice gap of 3 mm (to avoid cross-talk) were obtained with a scan time of 2 minutes (TR = 6 s; TE = 92 ms). The single-axis diffusion gradient strength was 60 mT/m (b = 1000 s/mm^2), and partial Fourier undersampling was not implemented (i.e. partial Fourier fraction, pff = 1). A diffusion orientation of (0, -1, 1) was chosen to create in-plane dephasing for comparison with Equation 2.4. It is expected that signal intensity errors from in-plane dephasing are dependent on pff; therefore, pff values of 3/4 and 5/8 were sim-

ulated by using homodyne reconstruction [74] with only a portion of the fully acquired k-space data. The retrospective correction was not performed prior to homodyne reconstruction, and the nominal number of over-scans are used (i.e. k-space shifts are not taken into account in the homodyne reconstruction) to show the amount of error if k-space shifting is not considered. The diffusion orientation of (1, 1, 0) was chosen to study the error caused by intravoxel dephasing and to validate Equation 2.8 for slice positions ranging from -10 cm to 10 cm. To experimentally obtain δADC, the ADC's obtained using a Stejskal-Tanner diffusion preparation (insensitive to concomitant fields) were subtracted from those obtained using either SGSSE or twice-refocused diffusion preparations (sensitive to concomitant fields) to create a difference image; voxels containing signal within the image were averaged to obtain an experimental δADC. While these types of subtractions are not typically done in DTI, they serve to eliminate other sources of ADC error that are consistent for all of our acquisitions, such as concomitant field effects from the EPI readouts [58–60] or gradient non-linearity induced errors [75]. The diffusion gradient direction dependence was examined for the 6 direction DTI protocol.

To validate the corrections, δADC was calculated for two healthy human volunteers (with informed consent) using pff = 3/4 and diffusion gradient orientations of (0, -1, 1) (i.e. in-plane dephasing) and (1, 1, 0) (i.e. intravoxel dephasing) with and without the application of both the prospective and retrospective corrections. 20 slices (3 mm thick; 3 mm inter-slice gap) were obtained using 6 averages and a scan time of 3 min (TR = 4 sec; TE = 68 ms). The subject's brain was positioned such that slices near 0 cm and 10 cm correspond to the inferior and superior regions of the brain, respectively (i.e. subject centered 5 cm off iso-center). While the subject is normally centered at iso-center, this shifted positioning allows demonstration of the effectiveness of the correction

for the larger amount of error that occurs for slices farther from iso-center. To validate the theoretical predictions that δADC_{Th} depends on neither the ADC of the subject nor the pff (Equation 2.8), the (1,1,0) data was also compared to the analogous phantom data described in the above paragraph. To illustrate the impact of concomitant gradient fields on DTI, a 6-direction DTI scan was performed on five healthy subjects (with informed consent). First, a slice was acquired at iso-center (0 cm). The same anatomical slice at 5 cm was then acquired after positioning the subject 5 cm from iso-center. This experimental technique demonstrates how the slice position-dependent artefacts manifest using consistent anatomy between the slice positions. The impact of concomitant fields, and the influence of the corrections, on fractional anisotropy (FA) and mean diffusivity (MD) in white matter was investigated by manually specifying regions of interest within the corticospinal tract and splenium of the corpus callosum. To isolate grey matter, thresholds of $MD < 1 \times 10^{-3}$ mm^2/s and $FA < 0.2$ were used in the Stejskal-Tanner data sets (i.e. data not impacted by concomitant gradient fields) to create masks that were applied to both the SGSSE and twice-refocused data. Mis-registration was mitigated by hardware based eddy current compensation and retrospective correction of motion and any remaining eddy current induced distortions [76]. Note that differences of image distortions were not apparent between the three diffusion preparations.

2.4 Results

2.4.1 In-Plane Dephasing

Simulation results of in-plane dephasing for both SGSSE and twice-refocused preparations show a strong dependence of δk_P on diffusion gradient

direction (Figure 2.2). The error increases with distance from iso-center. The

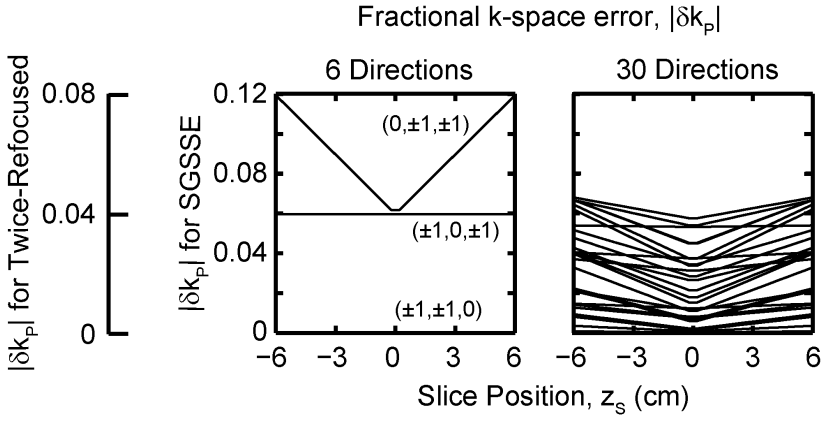

Figure 2.2: Simulation results (Equation 2.4) for the concomitant gradient field induced fractional k-space error, δk_P (unitless), from in-plane dephasing for axial slices. Simulations for both 6 direction and 30 direction standard DTI protocols have been performed for both SGSSE ($\tau = 25.2$ ms) and Reese twice-refocused ($\tau = 17.8$ ms) diffusion preparations. Since δk_P is linearly proportional to τ, the differing τ between SGSSE and twice-refocused preparations results in a simple scaling of δk_P relative to each other. Various diffusion directions have been plotted in each graph; note that the curves for some pairs of directions are identical in the 6-direction cases. In all cases, direction-dependent error that worsens with distance from iso-center is observed, with the 6 direction SGSSE preparation representing the most severe case. The 30 direction protocol is less sensitive to errors than the 6 direction protocol due to a smaller net gradient amplitude ($\sqrt{2} \times 60$ mT/m = 85 mT/m for 6 direction and 60 mT/m for 30 direction).

twice-refocused preparation exhibits a lower sensitivity to concomitant gradient fields than the SGGSE preparation due to a smaller τ (the cumulative duration of non-RF-refocused diffusion gradients). The 30 direction protocol is less sensitive to errors than the 6 direction protocol due to a smaller net gradient amplitude ($\sqrt{2} \times 60$ mT/m = 85 mT/m for 6 directions and 60 mT/m for 30 directions).

The k-space magnitudes (logarithmically scaled) for the silicone oil phantom with a diffusion gradient orientation of (0,-1,1) show no discernible error with a Stejskal-Tanner diffusion preparation, where the dephasing from

concomitant gradient fields is completely refocused (Figure 2.3a). In contrast, the SGSSE and twice-refocused cases show both k-space blurring and k-space shifting. The k-space blurring (i.e. a larger full-width-half-maximum, FWHM) is observed at both slice positions (9 mm and 51 mm), while shifting is only observed for $z_S = 51$ mm. For SGSSE, the FWHM is narrower at 51 mm compared to at 9 mm because k-space shifting causes the k-space peak to no longer be acquired at the spin-echo. Away from the spin-echo the signal varies due to T_2^* decay, artificially narrowing the FWHM. The amount of k-space shifting increases with distance from iso-center, which is observed in the experimentally measured δk_{Sh} (using centroid of k-space peak) for slices ranging from -10 cm to 10 cm for both SGSSE and twice-refocused, in agreement with that predicted from Equation 2.4 (Figure 2.3b). The signal intensity errors that result from in-plane dephasing, which is measured by the ratio of the diffusion weighted and non-diffusion weighted image intensities, I_b/I_0, strongly depends on the partial Fourier fraction, pff (Figure 2.3c). Since the diffusion coefficient of silicone oil is many orders of magnitude smaller than that of water, $I_b/I_0 \approx 1$ is expected. For the Stejskal-Tanner preparation a deviation from unity by less than 5% is observed for all pff's investigated; however, for pff < 1 the SGSSE and twice-refocused preparation have I_b/I_0 that are well below unity. For the slice at 9 mm, k-space shifting is negligible and the error (as high as 20% for SGSSE and pff = 5/8) is due to k-space blurring. For the slice at 51 mm, both k-space shifting and k-space blurring contribute to the error (as high as 45% for SGSSE and pff = 5/8). For the k-space shifted data, additional signal loss from T_2^* decay also contributes to the error in I_b/I_0. By applying the retrospective correction before homodyne reconstruction, the errors decrease to less than 10% for all cases shown in Figure 2.3c (data not shown). Note that since the (0,-1,1) diffusion direction creates relatively little

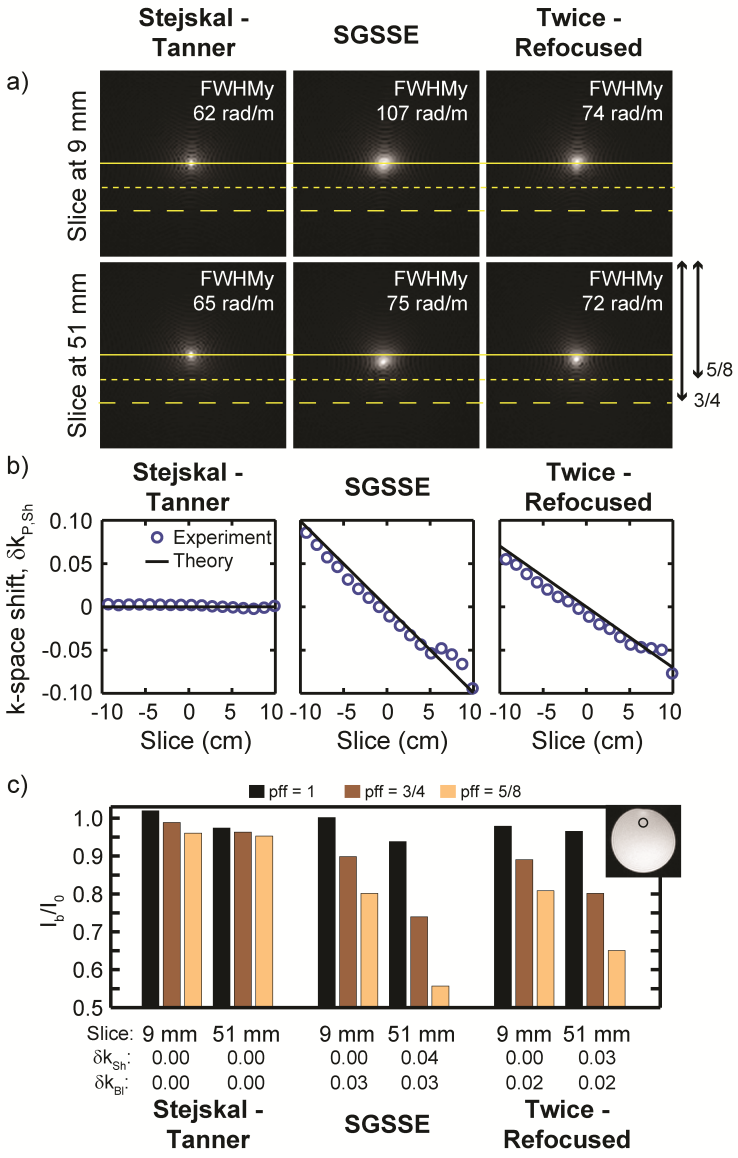

Figure 2.3: (a) k-space for axial DTI data acquired with a diffusion gradient orientation of (0,-1,1) (single axis gradient 60 mT/m; b = 1000 s/mm^2) for a silicone oil phantom for slice positions of 9 mm and 51 mm. In the SGSSE and twice-refocused cases, k-space blurring is observed for both slice positions (the full-width-half-max along the y-direction is identified in each panel) and shifting is observed for the slice at 51 mm. (b) Comparison of experimentally obtained k-space shifting fraction to theoretical prediction (Equation 2.3). The slight deviation for slices near 8 cm is due to B_0 inhomogeneity near the edge of the phantom. (c) Partial Fourier fractions (pff) of 3/4 and 5/8 are simulated from the fully acquired k-space data, and the signal ratio between diffusion-weighted and non-diffusion-weighted images (I_b/I_0) within the region specified in the inset is calculated.

intravoxel dephasing, the expected signal amplitude error from intravoxel dephasing (Equation 2.6) is less than 3% for all slice positions, pff, and diffusion preparation types shown in Figure 2.3c.

2.4.2 Intravoxel Dephasing

Analogously to in-plane dephasing, the simulation results of intravoxel dephasing for both a SGSSE and twice-refocused preparation show a strong dependence of δADC_{Th} on diffusion gradient direction, and the error increases with distance from iso-center (Figure 2.4a). The twice-refocused preparation exhibits a lower sensitivity to concomitant gradient fields than the SGGSE preparation due to a smaller τ, and the 30 direction protocol is less sensitive to errors than the 6 direction protocol due to a smaller net gradient amplitude. At 6 cm (coinciding with typical extent of human brain), δADC_{Th} can be as high as 0.14×10^{-3} mm^2/s for the SGSSE preparation, which is 20% of the mean diffusion coefficient in human brain parenchyma of 0.7×10^{-3} mm^2/s [77]. There is good agreement of experimental results for δADC_{Th} measured for a diffusion gradient orientation of (1,1,0) with the values predicted from Equation 2.8 for both phantom at slice positions of -10 cm to 10 cm and human brain from 0 to 10 cm (Figure 2.4b) for the SGSSE preparation. The slight overestimation of δADC_{Th} from Equation 2.8 is likely due to the assumption of a perfectly uniform magnetization profile, which does not occur in practice, and/or possibly from differing eddy current characteristics between the Stejskal-Tanner and eddy-current compensating diffusion preparations (gradient pre-emphasis mitigated this source of error). The comparable results between phantom and in-vivo human brain highlight the theoretical prediction that δADC_{Th} is sample-independent. Moreover, since the phantom and human data were acquired with pff = 1 and 3/4, respectively, the results

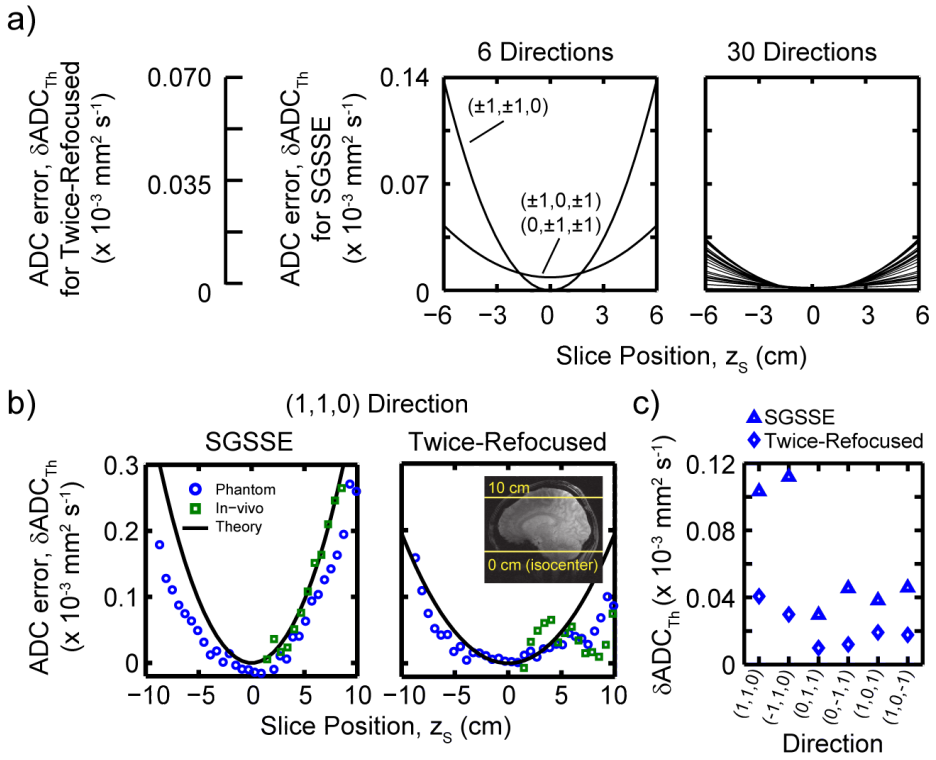

Figure 2.4: (a) Simulation results for the concomitant gradient field induced ADC error from intravoxel dephasing for axial slices (mean error over entire slice). For arguments of the sinc function close to zero in Equation 2.8, δADC_{Th} is approximately proportional to τ^2, where $\tau = 25.2$ ms for SGSSE and $\tau = 17.8$ ms for twice-refocused. Direction-dependent error worsens with distance from iso-center, with the 6 direction SGSSE representing the most severe case. The 30 direction protocol is less sensitive to errors than 6 directions due to a smaller net gradient amplitude (85 mT/m for 6 direction and 60 mT/m for 30 direction). (b) Comparison of experimentally obtained ADC error in a silicone oil phantom and human brain to theoretical prediction (Equation 2.8) for both SGSSE and twice-refocused preparations (error defined as difference from Stejskal-Tanner). Excellent agreement is observed for the silicone oil phantom for both preparations; however, for the human brain there is worse agreement to theory for the twice-refocused case due to a higher sensitivity to B_1 inhomogeneity. The position of slices for the human subject is depicted in the inset the brain was offset from iso-center to demonstrate the agreement with theory at larger offsets from iso-center. (c) ADC error in the silicone oil phantom at a slice position of 6 cm for the diffusion gradient directions of the 6 direction protocol. The trend supports the theoretical prediction in (a) that directions $(\pm 1, \pm 1, 0)$ exhibit the highest error.

highlight the lack of dependence of intravoxel dephasing error on pff. For the twice-refocused preparation, the poor in-vivo agreement with Equation 2.8 is likely due to a higher sensitivity to B_1 inhomogeneity for the twice refocused preparation compared to the SGSSE preparation. B_1 inhomogeneity is negligible in the silicone oil phantom where there is better agreement with Equation 2.8. The error is experimentally highest for diffusion directions of (1, 1, 0) (Figure 2.4c), which supports the theoretical prediction in Figure 2.4a.

2.4.3 Corrections and DTI Metrics

The experimentally measured ADC error for data acquired with and without the prospective and retrospective corrections for a human brain is shown at slice positions ranging from 0 cm to 10 cm (slice range depicted in inset of Figure 2.4b) for diffusion directions of (1,1,0) and (0,-1,1) (Figure 2.5). For both diffusion directions, it is evident that the prospective correction substantially reduces the error that arises from both in-plane and intravoxel dephasing, while the retrospective correction is only effective for mitigating the effects of in-plane dephasing. Optimal results are obtained when both corrections are used together. Similar results have been obtained for other diffusion directions.

The mean FA and MD in grey matter, the corticospinal tract, and splenium for 5 healthy volunteers are summarized in Figure 2.6 (see Figure 2.7 for example MD and FA maps). In grey matter the FA is larger for the SGSSE and twice-refocused preparations relative to Stejskal-Tanner at a slice position of 0 cm. The error is reduced with the corrections, but the FA is still higher than from Stejskal-Tanner; this residual error can likely be attributed to k-space blurring (a slice-position independent error that cannot be fully corrected with these corrections). For the slice position at 5 cm, an

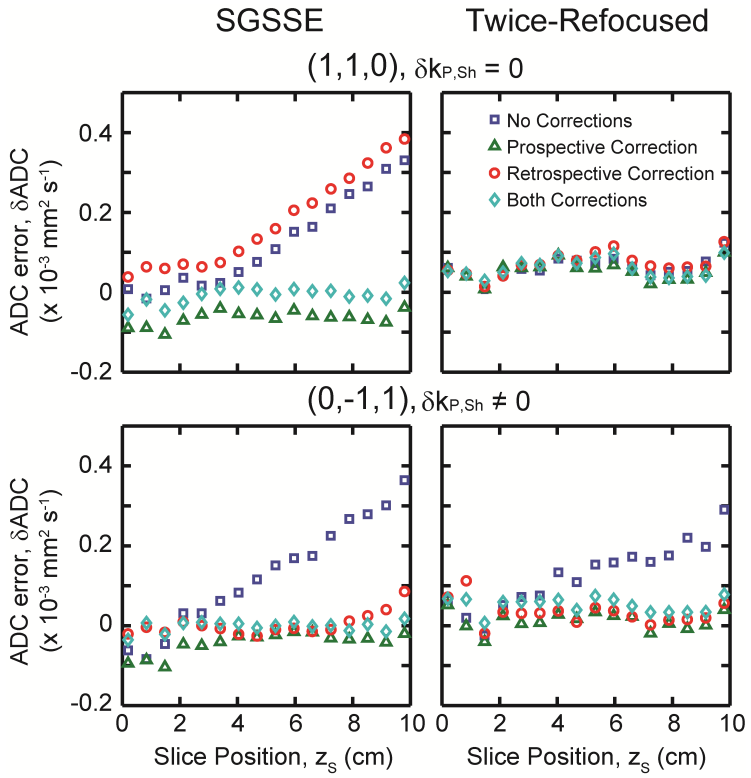

Figure 2.5: The difference in ADC (δADC) between Stejskal-Tanner and either SGSSE (left) or twice-refocused (right) diffusion preparations measured for two gradient directions at slice positions (z_S) ranging from 0 cm to 10 cm for a human brain (slice positioning in Figure 2.4b). Results are shown for no correction, only the prospective correction, only the retrospective correction, and both corrections. The (1,1,0) and (0,-1,1) diffusion gradient directions are primarily associated with intravoxel and in-plane dephasing, respectively. The retrospective correction is only effective for mitigating the effects of in-plane dephasing. For all cases where measurable error is present, the error is significantly reduced with the prospective correction. Similar results were obtained for other gradient directions and in our second human subject.

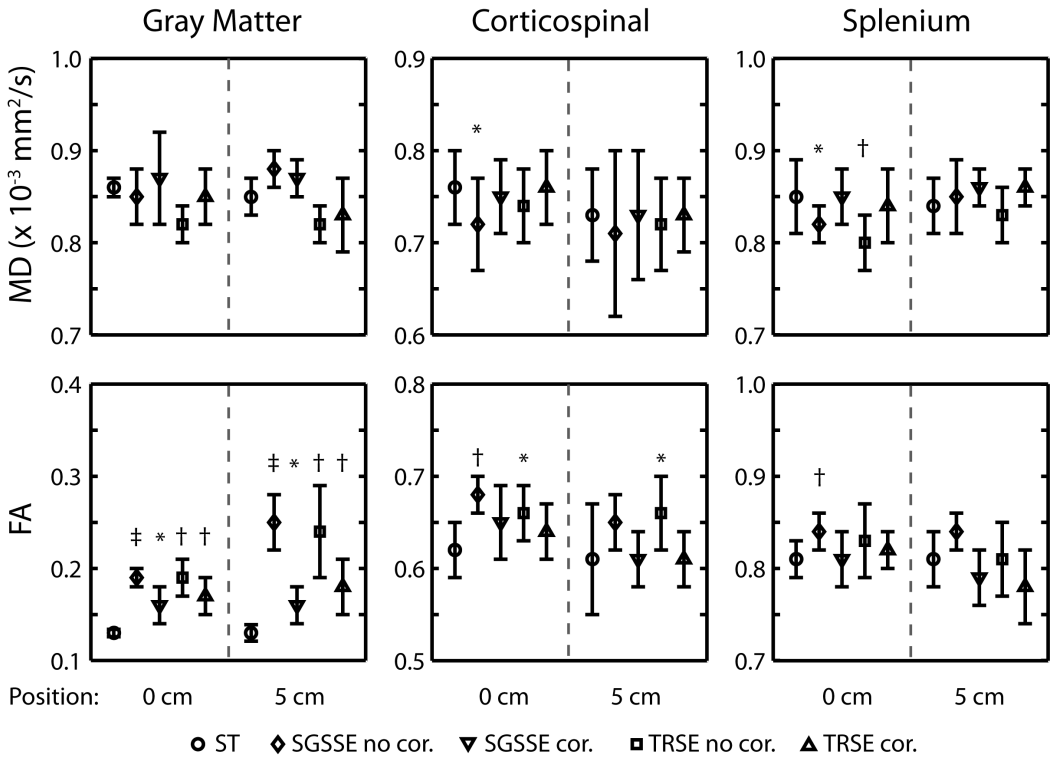

Figure 2.6: Mean FA and MD in five volunteers for the same anatomical axial slice positioned at isocenter (i.e. 0 cm) and 5 cm from isocenter (Both the patient bed and slice position were moved) with three different diffusion sensitizing schemes: ST Versus SGSSE and Reese twice refocused spin-echo (TRSE) without (no cor.) and with (cor.) retrospective and prospective corrections. Paired t-test significance (with respect to ST at the same slice position) is portrayed using * for $p < 0.05$, †for $p < 0.01$, and ‡for $p < 0.001$.

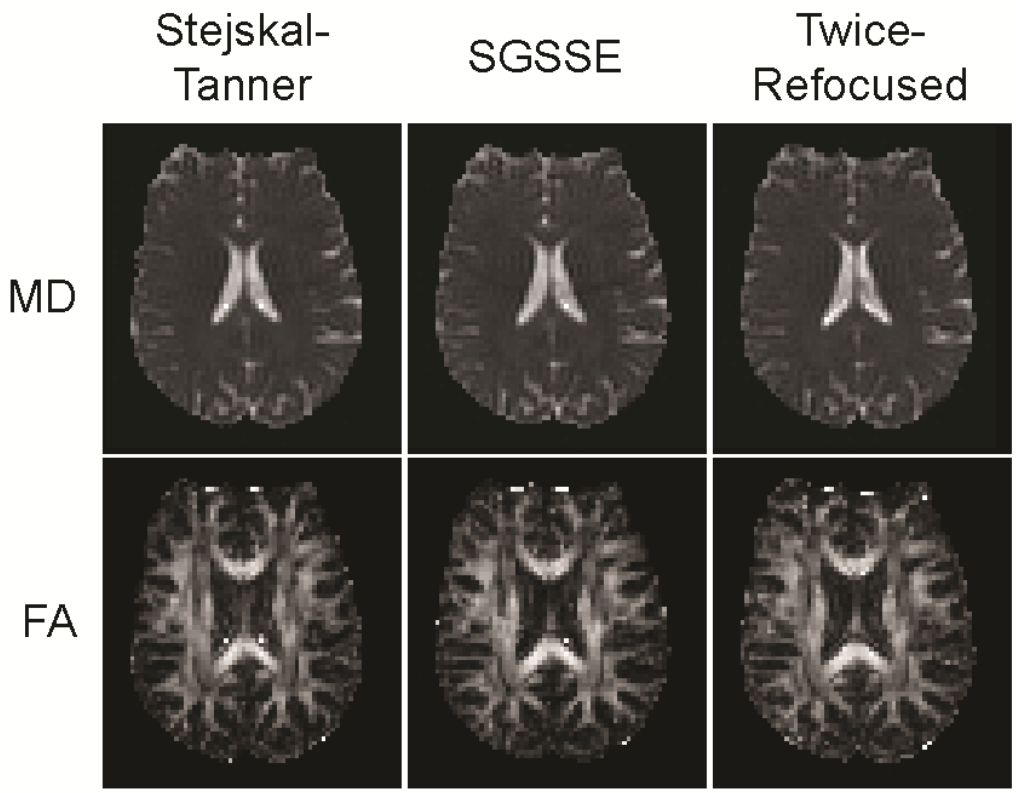

Figure 2.7: Example MD and FA for one subject at a slice position of 0 cm for the three different diffusion preparations, with both prospective and retrospective corrections.

even greater increase of FA in grey matter is observed for the SGSSE and twice-refocused preparations with respect to the Stejskal-Tanner preparation (increases of 0.12 and 0.11, respectively). This slice-dependent error is likely due to a combination of intravoxel dephasing and k-space shifting. The error is substantially reduced when the corrections are used, but again there is still a residual difference from Stejskal-Tanner. In the corticospinal tract, the FA is larger for both SGSSE and twice-refocused compared to Stejskal-Tanner and the corrections essentially bring the FA values in agreement. Few significant differences of FA were observed in the splenium, in fact only with SGSSE, which was 0.03 higher than Stejskal-Tanner at 0 cm while the corrections brought them in-line. These results suggest that structures with larger FA are proportionally less prone to error, in agreement with observations of low SNR DTI data [78]. Overall, few changes of MD were observed; only the corticospinal tract and splenium at 0 cm showed differences for uncorrected data. The overall lack of sensitivity of MD on concomitant gradients is likely because the ADC error for some diffusion directions is much smaller than for others, resulting in reduced overall error.

2.5 Discussion

In this work, it has been shown through simulation and experimental validation on phantom and human brain that concomitant gradient fields can corrupt diffusion imaging data via k-space blurring and intravoxel dephasing. A k-space shifting artefact due to concomitant gradients was confirmative of an earlier report [68] and the extension to intravoxel dephasing is a key addition here. The concomitant gradient induced dephasing can create marked errors of diffusion parameters that depend on diffusion gradient asymmetry (i.e. τ),

the gradient direction, encoding scheme, and distance from iso-center. While the effects are demonstrated at 4.7T and stronger than average gradients of 60 mT/m per axis, the use of similar strength gradients at lower static fields such as 3T will be even more problematic if using similar eddy-current minimizing diffusion encoding schemes as those depicted in Figure 2.1.

By using Equations 2.3 and 2.7 it is possible to predict the sensitivity of any set of parameters to concomitant gradient fields. To portray the sensitivity of various B_0 and gradient strength combinations that can lead to significant error from concomitant gradient fields, the predicted maximum percentage error in ADC (from intravoxel dephasing, Equation 2.7) over all diffusion directions for both SGSSE and twice-refocused diffusion preparations is shown in Figure 2.8(a-d) for both 6 and 30 direction protocols. The mean error over all directions is about half the maximum error depicted in Figure 2.8(a-d). Also note that the error is greater with increasing distance of slices from iso-center (Figure 2.8e), and with increasing τ (Figure 2.8f), which in turn varies with specific pulse sequence timings and the choice of eddy current time constants to be canceled. Nevertheless, it is evident that a clinical field strength scanner with large amplitude gradients can be prone to substantial error. For example, the ADC from a single diffusion direction can be off by as much as 25% (mean error over all diffusion directions is 13%) at 5 cm from iso-center for a 6 direction twice-refocused protocol (τ = 17.8 ms) at 1.5T equipped with 50 mT/m gradients. Note that using an increased B_0, decreased gradient strength, or 30 direction protocol with smaller net effective gradient would yield smaller errors in ADC. Also, while the simulations in Figure 2.8 show the error from intravoxel dephasing, in-plane dephasing will also contribute to the total error. For our case, in-plane dephasing effects were of similar magnitude to intravoxel dephasing effects (see Figure 2.5). Since

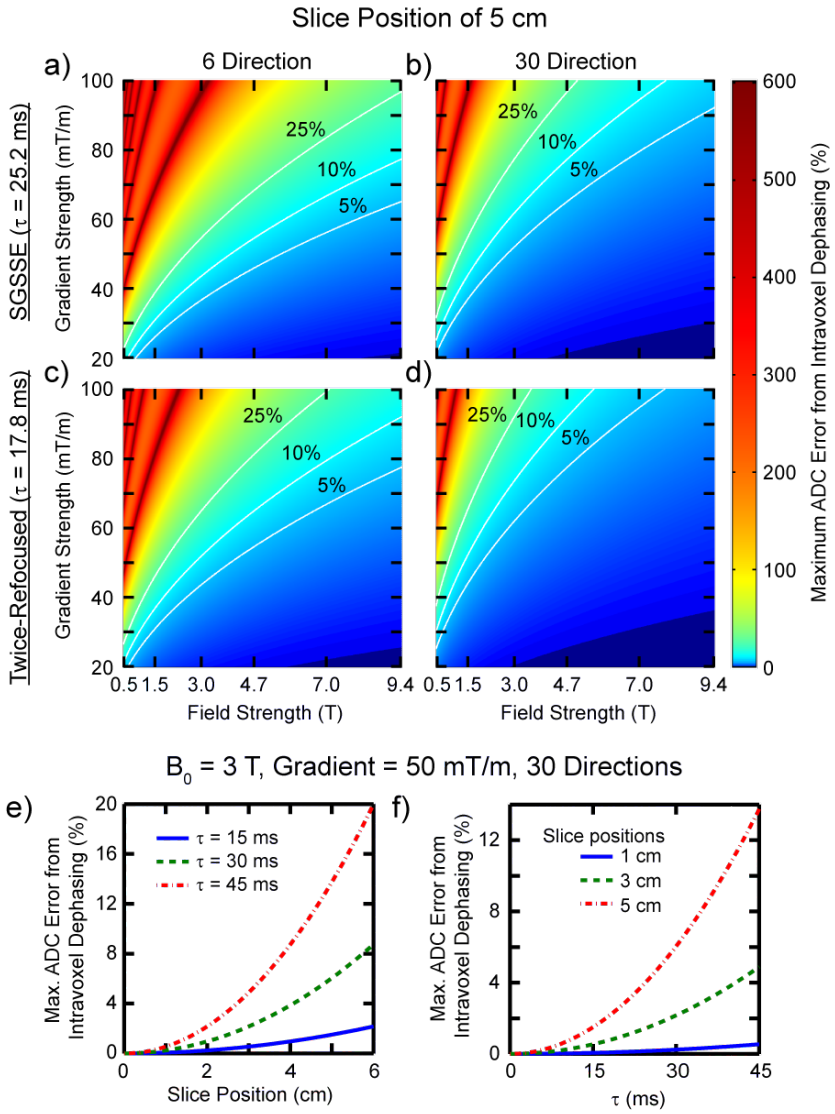

Figure 2.8: (a) - (d) Expected maximum percent-error of the ADC (over all directions of DTI protocol) for SGSSE and twice-refocused preparations for 6 and 30 direction protocols as a function of main field strength and maximum gradient strength along a single axis. The absolute intravoxel dephasing error at the center of the slice is calculated from Equation 2.7 for a 3 mm thick slice 5 cm from iso-center, and a mean diffusion coefficient of 0.7×10^{-3} mm^2/s [77] is used in the percent error calculation. All parameters except the gradient and main field strength are set equal to those used in this work. Dark bands are visible where the error is infinite due to 2π dephasing across the slice. Also shown are iso-contours for 5%, 10%, and 25% error (white lines). Notably, the error increases with slice distance from iso-center, as depicted in (e). Also, the difference between the SGSSE and twice-refocused preparations in (a)-(d) is due to the differing τ. The choice of eddy current cancellation, unique pulse sequence design, and b-value will likely affect τ; as depicted in (f), the error increases with increasing τ.

in-plane dephasing depends on in-plane voxel size (larger in-plane voxel sizes decrease the maximum extent of acquired k-space for a constant pff, causing exacerbated data loss) and intravoxel dephasing depends on slice thickness (Equation 2.7), the relative contributions from these two sources of error will vary with voxel anisotropy.

For low-field scanners with large gradients an erroneous increase in MD is likely (see Figure 2.8). This would also apply to 3 direction protocols common for clinical DWI, where net gradient amplitude is typically maximized to decrease TE. It is relevant to note that for our scanner specifications the error in a 30 direction protocol is small. However, Figure 2.8(a-d) suggests that large errors may be present for 30 direction protocols (or any high angular resolution spherical shell diffusion gradient encoding scheme) for systems utilizing large gradients (e.g. 100 mT/m "connectome" gradients). The concomitant fields do not appear to be much of an issue at 7T for any diffusion encoding scheme with currently available gradient strengths and the τ-values used here. It should be kept in mind that the errors are worse for the SGSSE method (due to a larger τ), which has the advantage of one less 180° RF pulse and can have lower TE relative to the twice-refocused method. While here we focus on the common Reese implementation of a twice-refocused diffusion preparation, other implementations of twice-refocused diffusion preparations that allow cancellation of multiple eddy current components may also have non-zero τ [79, 80], as high as 33.2 ms in Ref. [79]. In general, the twice-refocused protocol has an additional degree of freedom for timing design compared to SGSSE (via one additional gradient lobe), which may be used to minimize τ even further (or even reduce to 0, completely nullifying the effect of concomitant gradient fields) while retaining eddy current compensating qualities. Such modifications would likely have the cost of increasing TE, since the additional

degree of freedom is used to minimize TE in the original Reese implementation [35]. While to the best of our knowledge there are no studies explicitly outlining these types of modifications of the twice-refocused sequence to remove concomitant gradient effects, it appears that some studies have implemented such methods to eliminate τ [81]; note that one can verify whether such sequences with τ=0 have been implemented on a per scanner (model, software level, etc) basis. Also note that while Stejskal-Tanner is immune to such errors, care must be taken to ensure eddy current compensation (via hardware and in reconstruction) is adequate.

Because the manifestation of concomitant gradient field errors depends on position relative to iso-center, they can impart false variance to multi-subject data due to inconsistency in the position and brain size of the subjects. Furthermore, variability in scanner hardware can introduce systematic errors in diffusion parameters, thus compromising data reliability in multi-scanner or multi-center research [82]. DTI of organs such as the liver [83] or kidneys [84] will be more sensitive to errors from concomitant fields since inherently low SNR requires that relatively thick slices be used, which increases δADC_{Th} (Equation 2.8), in addition to the larger distances from iso-centre (Figure 2.8e); although one mitigating factor may be the use of smaller b-values (i.e. weaker gradients). The effects of concomitant gradient fields may also be severe for animal MRI systems, where the gradient strength can be as large a 1 T/m [85]; although the slice offsets are markedly less than for human applications. These errors may have deleterious consequences on deterministic tractography, where the increase in FA may promote voxels in grey matter to be above a fibre tracking threshold (e.g. in Figure 2.6 the FA in grey matter is increased to well beyond the common threshold of FA=0.2 for the SGSSE slice at 5 cm). The accurate detection of crossing fibres may be compromised by concomitant gra-

dient fields. High angular resolution diffusion imaging (HARDI) and diffusion spectrum imaging (DSI) techniques utilize many diffusion gradient directions to resolve multiple fibre populations co-existing in a single voxel [86–88]. Also, the higher b-values used in HARDI/DSI may necessitate larger τ or applying maximum gradient amplitude on more than one gradient channel simultaneously (not done for typical 30 direction protocol). For example, to increase b to 3000 s/mm^2 while maintaining the same eddy current cancellation, τ must increase to 35.4 ms for SGSSE (note that τ does not increase with increasing b for the Reese twice-refocused sequence). Increasing τ drastically increases the error (Figure 2.8f); thus, the direction-dependent errors from concomitant gradient fields may be particularly detrimental for these techniques, particularly for those requiring higher b-values. Moreover, we have observed that voxels with low FA in the tensor formalism, which is typical for crossing fibres, are more sensitive to error from concomitant gradient fields.

The proposed gradient correction scheme can be readily added to minimize the error and reduce its slice-position dependence. The effectiveness of the prospective correction depends on the diffusion gradients applied as well as the slice orientation (the retrospective correction does not). While the prospective correction reduces δADC_{Th} for all slice and gradient orientations, axial slices receive the most benefit (Figure 2.9). In contrast, slices with $\theta \approx 45^\circ$ contain the most residual error when the correction is implemented due to the amount of linear dephasing varying throughout the slice. Interestingly, coronal slices exhibit much higher δk than axial slices; δk can be as high as 0.5 (primarily due to k-space blurring), which may lead to signal loss even without partial Fourier undersampling. We have experimentally observed this much higher degree of k-space blurring in preliminary phantom data (not shown). Note that this simulation likely underestimated the total intravoxel

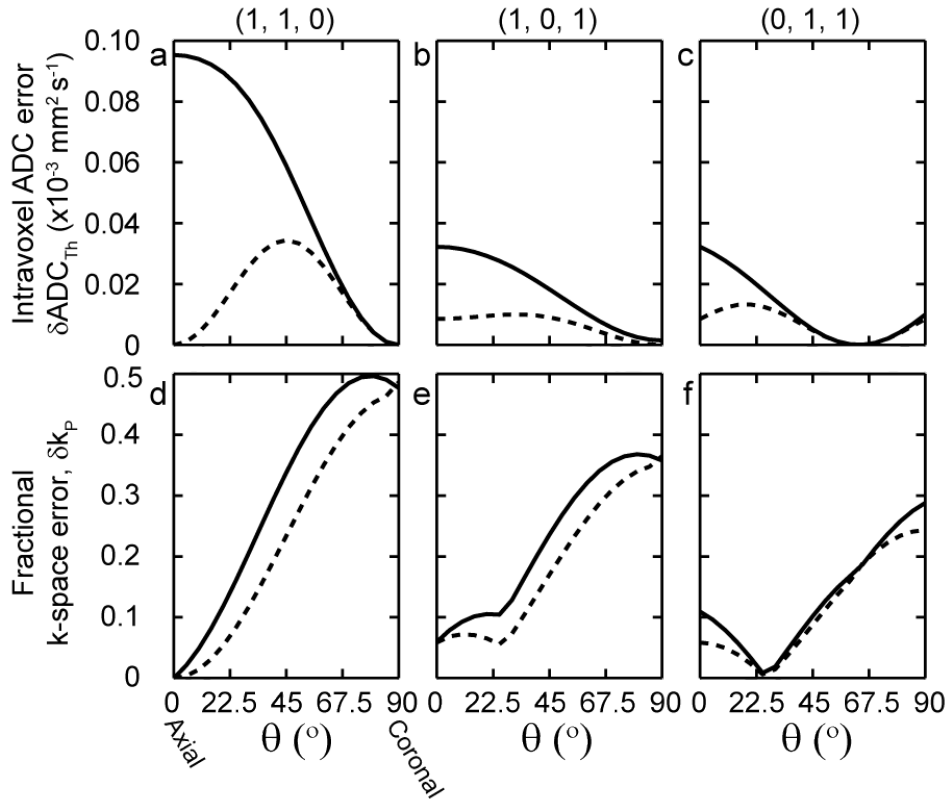

Figure 2.9: The mean δADC_{Th} (a, b, c) and δk_P (d, e, f) calculated from Equations 2.7 and 2.3, respectively, when the proposed prospective correction is (dashed) and is not (solid) implemented for a slice 5 cm from iso-center using an SGSSE diffusion preparation with no retrospective correction. All other relevant sequence parameters are the same as those used in the experiments in this work. The horizontal axis of each plot is the inclination angle, θ, of the slice from the z-axis, where $\theta = 0^\circ$ and $\theta = 90^\circ$ correspond to axial and coronal slices, respectively. Panels (a, d), (b, e), and (c, f) depict the results for diffusion gradient orientations of (1, 1, 0), (1, 0, 1), and (0, 1, 1), respectively. The effectiveness of the correction depends on the diffusion gradients applied as well as the slice orientation, with the correction being most effective for axial slices.

dephasing for coronal slices because the assumption of the dominant source of intravoxel dephasing stemming from the through-plane direction in Equation 2.7 is not as valid for coronal versus axial slices. Nevertheless, since the prospective correction does not completely remove the error for all cases, and because the retrospective correction cannot account for intravoxel dephasing, signal lost outside the acquisition window, nor signal loss from additional T_2^* decay for k-space shifted data, alternate strategies to reduce the error are recommended: minimize τ (the ideal case is Stejskal-Tanner), ensure that the anatomy of interest is located near iso-center, avoid severely oblique slices, use a larger pff when using partial Fourier undersampling, and minimize voxel size. It is relevant to note that the phase accrual imparted by B_C could, in principle, be accurately corrected using second order shims. This would require fast activating, low eddy current, and low oscillation shim coils and amplifiers.

In summary, our work suggests a "26th" pitfall for diffusion MRI to be added to the list of Jones and Cercignani [8]. Concomitant gradient fields are shown to cause phase accrual, which can lead to ADC errors as high as 20% near the periphery of the human brain (4.7T, 60mT/m gradients, SGSSE). As gradient strengths are increased to enable improved diffusion imaging, concomitant gradient fields will necessitate corrections like the one proposed here and careful parameter selection.

2.6 Results Additional to the Published Paper

While the main equations used to calculate how the concomitant fields propagate through the data to introduce error into DTI (i.e. Equations 2.3 and 2.7) used various assumptions to simplify analysis (see Theory section),

the main assumption in the Equation for B_C (Equation 2.1) and the phase accumulated by B_C (Equation 2.2) is the Taylor expansion. Accordingly, the phase accrual from concomitant fields can be quite accurately estimated from Equation 2.2, as is evident from phase experimentally measured in a phantom compared to the phase predicted from theory (Figure 2.10). Notably, no fitting

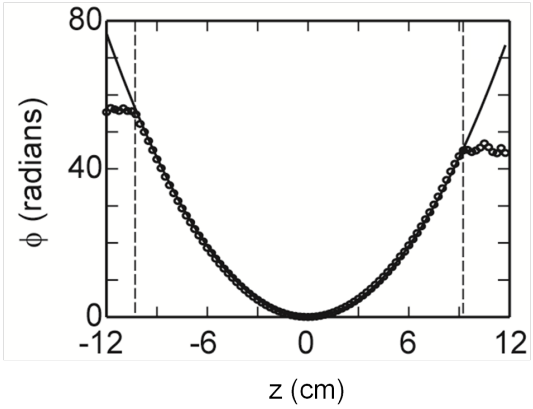

Figure 2.10: Experimentally measured phase (points), θ, along with the phase from concomitant gradient fields predicted by Equation 2.2 (line) as a function of z-position. The experimental phase values were obtained by acquiring a coronal slice in a silicone oil phantom with and without SGSSE gradients applied on the x- and y- gradient channels (using similar parameters as the SGSSE sequence described in the Methods), and calculating the phase difference between the two acquisitions to remove other sources of phase like B_0 inhomogeneity. The dotted lines identify the physical extent of the phantom.

or scaling of data was performed in Figure 2.10; the plot is simply experimental data versus the prediction from Equation 2.2.

2.7 Collaborators

The development of the theory regarding how concomitant gradient fields translated to the experimental observations was aided through discussions with Marc Lebel and Alan Wilman (Biomedical Engineering, University of Alberta).

Chapter 3

Motion Insensitive GRAPPA for Echo-Planar Imaging

3.1 Introduction

Echo-planar imaging (EPI) is essential for both fMRI and diffusion MRI due to its fast acquisition speed and insensitivity to bulk motion [89, 90]. Well known limitations of EPI are distortions from B_0 inhomogeneity and low resolution. To address these limitations, parallel imaging can be used to undersample in the phase-encode (PE) direction [91–95]. This enables faster traversal through k-space, thus decreasing accumulation of phase from B_0 inhomogeneity and lessening T_2 blurring, which reduces distortions and enables higher resolutions, respectively. Two commonly implemented options for performing parallel imaging are GRAPPA [54] or SENSE [96]; however, it has been shown that EPI acquisitions using GRAPPA are more robust against artifacts related to both motion and off-resonance [94].

Additional reference lines/scans that fully sample k-space, the auto-calibration signal (ACS), are required for GRAPPA calibration. For non-EPI applications where parallel imaging is used to decrease scan time, the ACS is

obtained by sampling the center of k-space more densely than the outer regions. However, this technique provides no benefit to EPI where GRAPPA is used to reduce distortions, because densely sampling the center of k-space introduces no k-space traversal rate increase for the low-frequency contrast generating portions of k-space [94]. Instead, the calibration data should be acquired separately from the undersampled data so that the entire extent of k-space can be sampled at a faster rate. Accordingly, for EPI the ACS is typically acquired via an interleaved EPI data set, where each shot is undersampled similarly to the fMRI or DTI data to be acquired. However, subject motion between the shots leads to miscalculation of the GRAPPA weights and ghosting, and physiological motion can lead to localized residual undersampling artifacts [94]. This work introduces and characterizes two alternative reference scans that are potentially more robust to both gross and physiological motion.

3.2 Theory

When a Cartesian k-space grid is acquired, GRAPPA is typically performed by acquiring only every Rth line of k-space, where R is the acceleration factor, as depicted in Figure 3.1a for $R = 2$. The missing lines in the undersampled data (UD) acquisition are filled in by the forward solution of

$$S_{l,k} = \sum_{l'} \sum_{k'} W_{l,l',k'} S_{l',k'} \tag{3.1}$$

where $W_{l,l',k'}$ are the GRAPPA weighting factors, l is the receiver in which the signal at k-space location k is to be determined and l' is the receiver and k' is a sampled k-space location near k. The weighting kernel (i.e. the k-space locations k' relative to the unknown k-space point k that are allowed to have non-zero weights) is designated a priori, and the calculated weights encode

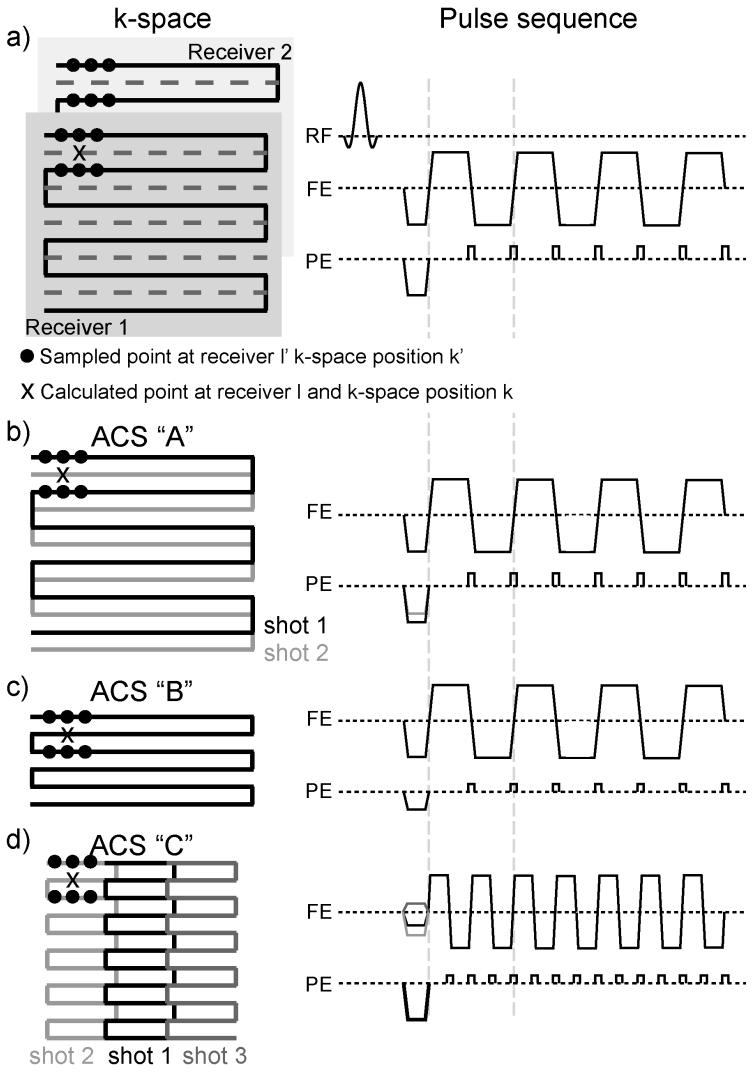

Figure 3.1: Acquired k-space and pulse sequences for (a) undersampled data, UD, and ACS methods A, B, and C (b-d) for GRAPPA rate $R = 2$. Skipped lines of k-space are shown dotted in (a), and a 3×2 GRAPPA kernel is shown. Only one receiver is shown for (b-d) for simplicity. The slice-select gradients are omitted from the pulse sequence diagrams and the spin-echo case is identical to the shown gradient echo EPI pulse sequence diagrams, aside from the addition of a 180° refocusing RF pulse and associated gradients. In contrast to methods B or C, for ACS A any position of the GRAPPA kernel includes k-space lines that are obtained from different shots (which may have subject motion between them). The smaller PE gradients for method B results in slower k-space traversal in the PE direction and worse distortions from B_0 inhomogeneity. By decreasing the duration of FE gradient lobes while simultaneously decreasing the PE gradients by a factor of R, the k-space traversal rate in method C is the same as for the UD.

the sensitivity profiles of the receiver coils. To determine $W_{l,l',k'}$, the inverse solution of Equation 3.1 must be performed using a fully sampled region of k-space (i.e. the ACS) [54]. Tikhonov regularization is often used to reduce noise, leading to the inverse least squares solution of Equation 3.1,

$$W = \left(S_{kern}^H S_{kern} + \beta I\right)^{-1} S_{kern}^H S_{lk}$$

$$S_{lk} = \begin{bmatrix} S_{1,1} & \cdots & S_{l,1} & \cdots \\ \vdots & \ddots & & \\ S_{1,k} & & S_{l,k} & \\ \vdots & & & \ddots \end{bmatrix} \qquad (3.2)$$

$$S_{kern} = \begin{bmatrix} S_{1,1} & \cdots & S_{n,1} & \cdots \\ \vdots & \ddots & & \\ S_{1,k} & & S_{n,k} & \\ \vdots & & & \ddots \end{bmatrix}$$

where β is a Tikhonov regularization weighting factor, I is an identity matrix, k encompasses all the k-space locations acquired in the ACS, l is the receiver, and $n = (l, k', l')$ are the points required to determine the signal in receiver l from ACS points located at k' in receiver l', where the choice of k' relative to k are defined by the kernel.

A set of R interleaved shots may be used to form a fully sampled k-space ACS (method A) [94]; however, motion between the shots leads to k-space inconsistencies between adjacent lines which impairs GRAPPA weight calculation because the k-space points at k and k' would correspond to different subject locations (Figure 3.1b). In order to reduce the sensitivity of the ACS to motion, it should be acquired such that adjacent lines of k-space are measured in the same shot, which causes the image position associated with k and k'

to be the same. One option to achieve this is to reduce the k-space phase encode step by a factor of R, so that a fully sampled portion of k-space is acquired in one shot (method B) (Figure 3.1c), where the only change in the pulse sequence compared to the UD scans is a reduction of the phase encode gradients. However, for this approach the ACS k-space is traversed at a slower rate along the PE direction compared to the UD, causing the distortions from B_0 inhomogeneity to be worse. Since B_0 inhomogeneity also distorts the underlying receiver sensitivity profiles that are encoded into the GRAPPA weights, the receiver sensitivity mismatch between the ACS and UD results in GRAPPA reconstruction errors.

To retain the motion insensitivity of method B while ensuring that PE distortions are equivalent for the ACS scan and UD, fully sampled bands of k-space with a shortened frequency encode extent can be acquired such that the k-space traversal speed is the same for both ACS and UD (method C) (Figure 3.1d). This requires reductions of PE gradients by a factor of R in addition to shortened frequency encode lobes to maintain the same total readout duration. While the PE k-space traversal speeds are equivalent, the ACS scan may have a slower FE traversal speed compared the UD due to slew rate constraints; however, this is expected to result in negligible errors because of the much faster FE k-space traversal rate compared to PE. Multiple overlapping bands of k-space are acquired to increase coverage of k-space, similar to readout-segmented EPI [71]. While one band may be sufficient for spin-echo (SE) EPI, using multiple bands to increase the total k-space coverage is important for gradient-echo (GE) EPI because k-space signal from regions with B_0 inhomogeneity can be shifted outside the coverage of the acquired band [97]. It is not necessary to stitch together the multiple bands of k-space when computing the GRAPPA weights; in fact, it is preferable to leave them sep-

arate because of motion-induced phase inconsistencies between them (similar to how motion between interleaved shots of ACS lines corrupts computation of weights). Rather, the k positions in Equation 3.2 should encompass all of the bands, where the k' locations corresponding to each k are only taken from within the same band; thus, Equation 3.2 determines the least squares solution of the GRAPPA weights over all the bands simultaneously.

3.3 Methods

3.3.1 Simulation

The performance of the three methods described above (i.e. A, B, and C) were investigated using simulations of k-space sampling with GRAPPA reconstruction. A modified Shepp-Logan numerical phantom was used with B_0 inhomogeneity increasing non-linearly along the phase encode direction from 0 to 1.5 PPM (parts per million) (Figure 3.2a). The B_0 offset approximates B_0 inhomogeneity near the sinuses, and 4 receiver coils were simulated. For each phase encoding step, the image phase from B_0 inhomogeneity was advanced assuming a resonance frequency of 200 MHz and acquisition delay between lines of $t_{PE} = 0.7$ ms (equivalent to experimental work) before the k-space line was sampled. The simulation algorithm for data sampling is displayed in Figure 3.3. A total matrix size of 128×64 was used (increased to 128×128 after GRAPPA reconstruction). For method A, two interleaves were sampled, where movement by 2 voxels along the phase encode direction (equivalent to ≈ 3 mm) was simulated to have occurred between the two interleaves. For method B, two identical fully sampled reference scans were acquired with the same 2 voxel motion between them, and both scans were used together in Equation 2 to calculate $W_{l,l',k'}$. For method C, three segments with 25% the width

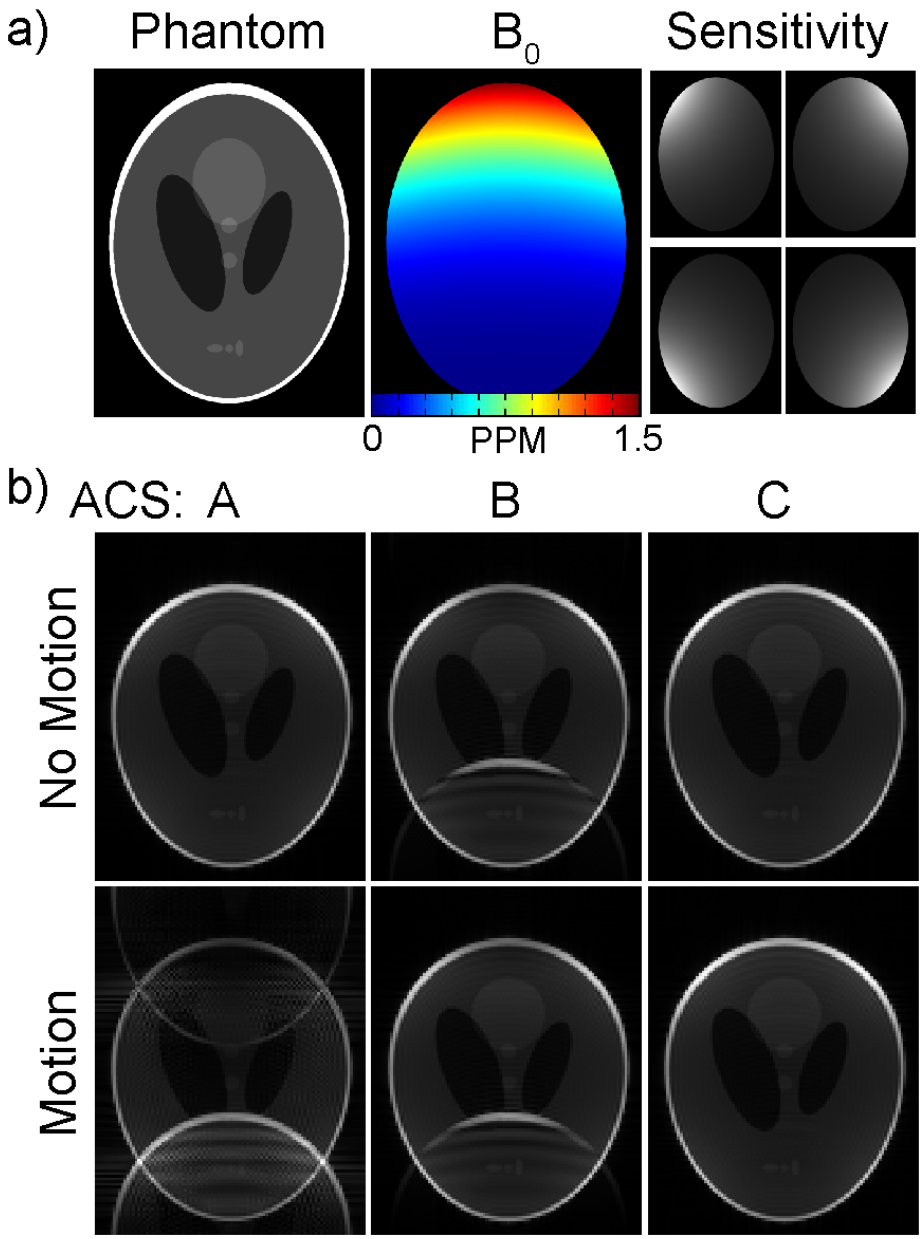

Figure 3.2: (a) Simulation of GRAPPA reconstructions were performed for a modified Shepp-Logan phantom having B_0 inhomogeneity varying from 0 to 1.5 PPM using the shown sensitivities of four receiver coils. (b) With no motion, ACS methods A and C performed identically, while method B had some residual ghosting from regions with B_0 inhomogeneity. With motion of 2 voxels during the ACS scans, severe artifacts were introduced for method A while methods B and C were almost identical to the ideal case with no motion.

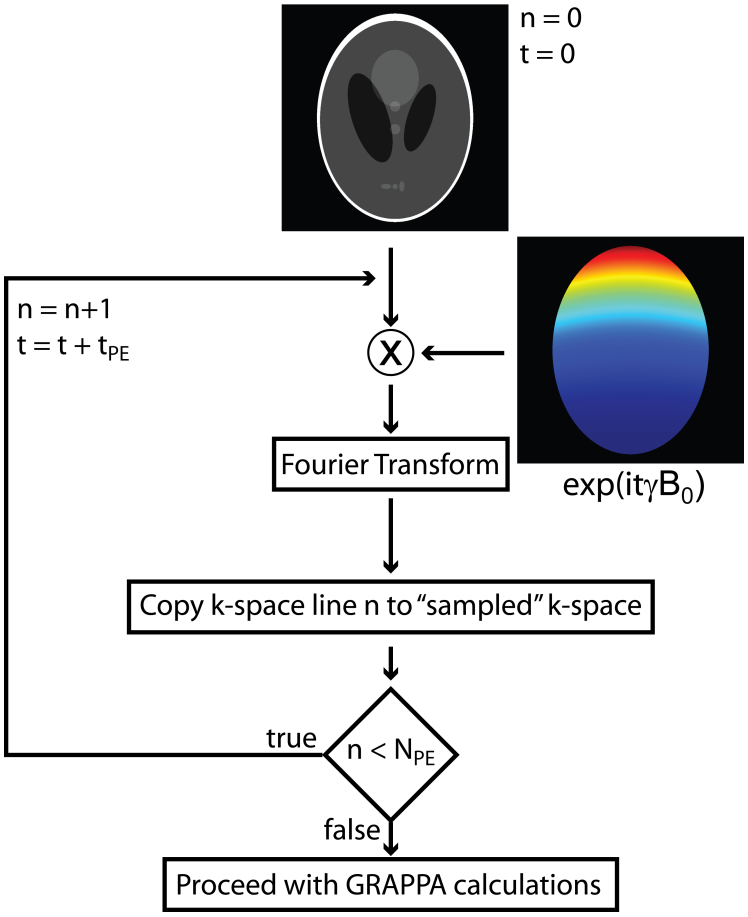

Figure 3.3: The data sampling algorithm of the simulations advanced the image phase for each phase encode line of k-space. For each phase encoding step (i.e. n), the image phase from B_0 inhomogeneity was advanced assuming an acquisition delay between lines of t_{PE} for each of the N_{PE} phase encode steps. After data sampling, GRAPPA calculations were performed identically as in the experiments.

of the nominally acquired k-space and overlapping by 8 voxels were sampled (similar to experimental work). Again, the motion of 2 voxels occurred between the sampling of the first and second segments. The three methods were also simulated without prescribing any motion. A GRAPPA kernel spanning four PE lines with five points along the FE direction was used.

3.3.2 Image Acquisition

Intentional Motion

To test the robustness of the ACS methods to extreme motion, 3 subjects were instructed to perform continuous head motion during the acquisition of one UD scan followed by 3 repetitions of each of the reference scan types (i.e. UD - (ACS_A - ACS_B - ACS_C) $\times$ 3). This scheme was performed for both spin-echo EPI (SE-EPI) and gradient echo EPI (GE-EPI). The 3 repetitions of the ACS scans were performed to reduce the effects of inconsistencies of the subjects' intentional motion. This led to a total of 9 reconstructed image volumes for each subject, where each of the 9 volumes were generated from the same UD but different GRAPPA weights. Method C used 3 segments, each with an FE width 25% of the nominally acquired k-space. While more segments could have been used to more fully fill k-space, the benefit of doing so is negligible as long as low frequency k-space information is not shifted outside the total acquired k-space by B_0 inhomogeneity, which is a concern primarily for GE-EPI. Other parameters were: $R = 2$ GRAPPA; TR = 6 s; TE = 60 ms for SE-EPI, TE = 20 ms for GE-EPI; FOV = 22×24 cm^2; resolution $2 \times 2 \times 2$ mm^3; 50 slices. The GRAPPA kernel was identical to the one used in the simulations. Nyquist ghosting was corrected using an iterative linear correction [98].

No Motion

Six subjects were instructed to remain still during the acquisition of one UD scan followed by 9 repetitions of each of the reference scan types (i.e. UD - (ACS_A - ACS_B - ACS_C) $\times$ 9) for both SE-EPI and GE-EPI. Aside from having more repeats (9 instead of 3), all acquisition parameters were identical as the above scans where intentional motion was performed. More repetitions of the ACS were collected to better characterize stability of the tissue signal with identical scanning parameters, because it was expected that the tissue signal would be less consistent between repetitions for ACS methods less robust to motion, even if the ghosting intensity outside the brain is small.

3.3.3 Image Analysis

The scans with and without intentional motion were analyzed separately. For each case, automated segmentation [99] was used to create signal masks for all the images reconstructed from the different GRAPPA weights (including all repeats and all 3 ACS methods), and the location of "true" signal free from ghosts was estimated as the voxel locations that coincided on all masks. The mean ghost intensity (I_G) over all the repeated ACS was quantified as the mean signal from the voxels outside the "true" mask minus the noise floor. The noise floor was estimated from voxels outside the extent of the object along the frequency encode direction where neither ghosting nor true signal resides. I_G values were normalized to the signal in a region-of-interest (ROI) manually placed in the internal capsule. To investigate consistency of the tissue signal in the scans with no motion, the standard deviation of signal over the images reconstructed using weights from the repeated ACS scans, normalized by the mean signal in the ROI in the internal capsule, was calcu-

lated for each of the three ACS methods and averaged over the entire brain, (I_{STD}). Statistical significance of differences of I_G and I_{STD} for ACS method C compared to methods A and B was evaluated using a paired students t-test ($P < 0.05$).

3.4 Results

3.4.1 Simulation

With no subject motion, both of ACS methods A and C performed nearly perfectly; however, method B suffered from residual aliasing from the B_0 inhomogeneity (Figure 3.2b). Almost no change was observed for methods B and C when the phantom was shifted by 2 voxels during the reference scans; however, severe artifacts were introduced for method A. For simulations with no B_0 inhomogeneity the performance of method B was similar to method C (data not shown).

3.4.2 In vivo

For subjects instructed to move their head during the entire scan, ACS method A resulted in severe ghosting artifacts for both SE and GE EPI (Figure 3.4). In contrast, both of methods B and C produced images of reasonable quality. Over all 3 subjects, method A exhibited ghosting signal a factor of 10 larger than method C for both SE and GE (Figure 3.5a). Even though method B had much lower ghosting than method A, it still had ghost signal 30% larger than method C for both SE and GE.

The performance of method A was much better for subjects instructed to remain still compared to when they moved intentionally; however, the ghost

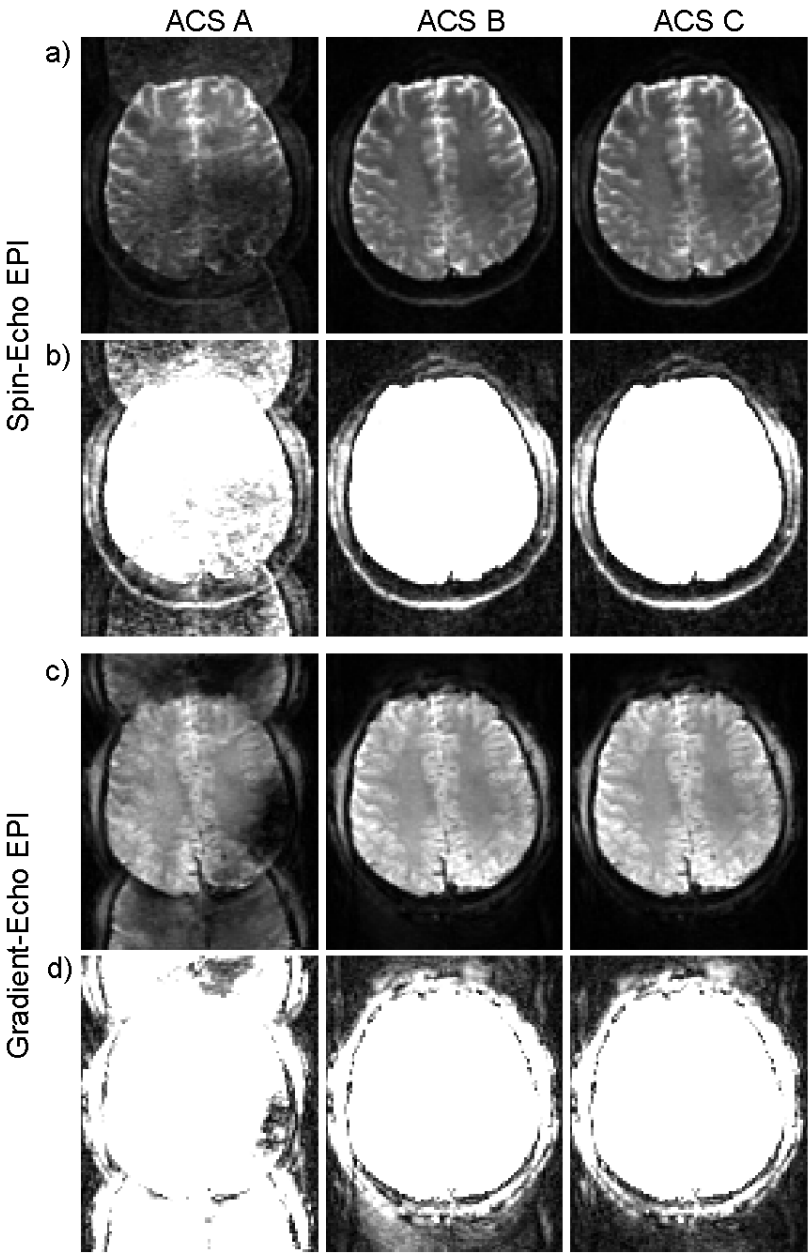

Figure 3.4: Results in one subject moving continuously throughout the entire acquisition of ACS and UD for both spin-echo (a) and gradient echo (c) EPI, where the same UD was used for all three ACS methods. The same images with low contrast are also shown to better portray the level of ghosting (b, d). Severe ghosting is observed for method A compared to method B or C. Also, method B exhibits more ghosting that method C, particularly for the gradient-echo EPI scan.

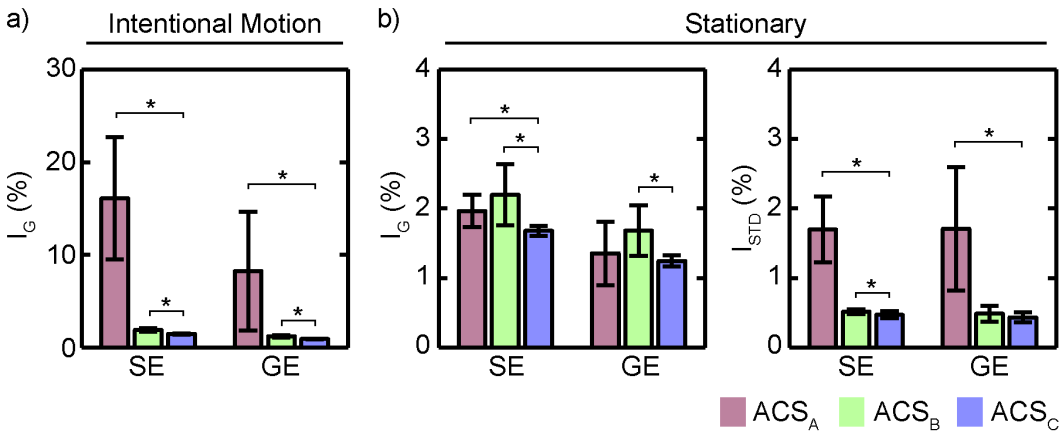

Figure 3.5: Quantitative measurements of total background ghosting (I_G) and tissue signal standard deviation (I_{STD}) over all slices in subjects moving intentionally (a) or remaining still (b). The I_G and I_{STD} values are relative to the tissue signal in the internal capsule. ACS method A exhibited extremely strong ghosting with moving subjects. While the ghosting for ACS A was reduced for the still subjects, the tissue signal still varied considerably over repeated acquisitions of the ACS (i.e. I_{STD}). ACS methods B and C show little sensitivity to subject motion; however, method B has more background ghosting than method C regardless of whether the subjects moved. Differences between methods A and B relative to method C were evaluated using a paired student's t-test (* $P < 0.05$).

signal was still 17% higher for method A compared to method C for SE (Figure 3.5b). Again, method B had approximately 30% more ghost signal compared to method C for both SE and GE. In addition, the signal variability, I_{STD}, within the brain was more than a factor of 3 larger for method C compared to method B or method C. The standard deviation of the images reconstructed from repeated ACS (i.e. voxel-wise I_{STD}) shows that eye or physiological motion in the brain causes localized ghosting artifacts for method A, but not for methods B or C (Figure 3.6).

3.5 Discussion

This work has shown that severe GRAPPA-EPI artifacts can occur from motion during the acquisition of ACS, which can be drastically reduced by

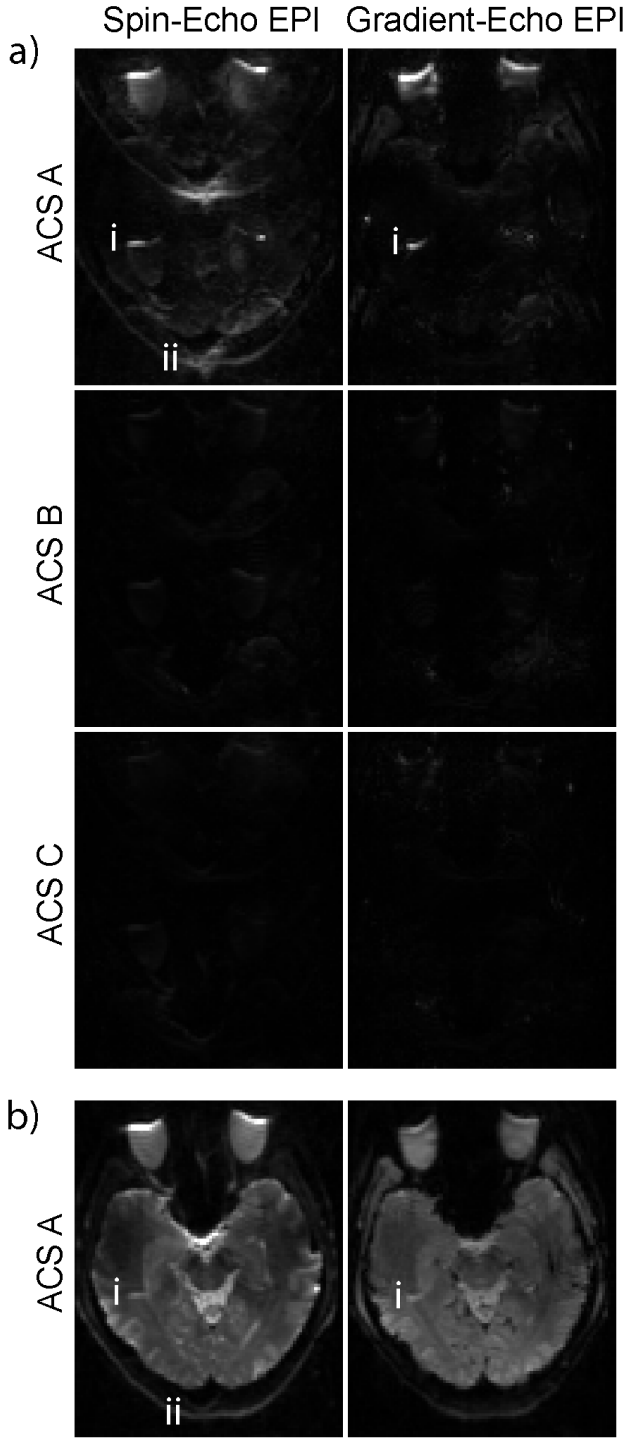

Figure 3.6: (a) The standard deviation of images reconstructed using 9 different calibration scans (i.e. voxel-wise I_{STD}) for subjects instructed to remain still. Eye (i) or physiological (ii) motion resulted in localized ghosting artifacts for ACS method A, but not for methods B or C (the images are scaled the same). (b) For reference, one of the 9 images reconstructed using method A is shown.

using a densely phase encoded (i.e. method B) or readout-segmented GRAPPA reference scan (method C). The intentional motion data represents a worst case scenario that is possible if the subject moves during the GRAPPA reference scan, which would require time-expensive re-acquisition of data if method A was used. Even though method B decreased sensitivity to motion, additional ghosting was still present compared to method C regardless of whether the subjects moved or not. The ghosting using the standard interleaved approach (i..e. method A) was not as drastic when the subjects were instructed to remain still; however, the signal varied considerably with re-acquisition of the ACS data and localized artifacts from eye or physiological motion were present. Notably, the subjects scanned were well accustomed to participating in MRI scans and likely moved less than subjects being scanned for the first time. Accordingly, even for the best case scenario, errors from motion are present when using method A.

The methods introduced here only address motion during the acquisition of the ACS, and not motion between the ACS and UD scans. It has been experimentally shown that if the subject position is different between the reference scan and UD, the impact on GRAPPA reconstruction is negligible because $W_{l,l',k'}$ (Equation 3.2) only depends on the receiver sensitivity profiles (which have not moved between ACS and UD) and not the image contrast [98]. For example, even though severe motion (through-plane and in-plane) was present between the ACS and UD in Figure 3.4, negligible ghosting is observed for method C. A caveat, though, is that the B_0 inhomogeneity may change due to a new head position and introduce some ghosting (similar to the residual ghosting for method B); however, even at the high field of 4.7 T and extreme motion investigated, this was not observed.

A limitation of method C is the increased scan time required to acquire

additional blinds (e.g. here 3 blinds were acquired for method C compared to 1 extra interleaved acquisition for method A). However, it is likely that fewer blinds are required for SE-EPI because it was found that the image quality was not degraded when only one central band of k-space was used to calculate the weights (data not shown). However, the image quality was degraded when only one band was used for GE-EPI. Also, since DTI or fMRI scans typically acquire many image volumes, the additional total scan time increase for the extra blinds would be low. For example, for an 8 minute fMRI scan with a TR of 1.5 seconds, the scan time would increase by less than 1% for method C compared to method A (for $R = 2$). A potential limitation of method C is that differing eddy currents between the ACS scan and UD scan (because of the different frequency encode gradients) may result in different image distortions for the reference scan compared to the UD scan, leading to reconstruction errors similar to method B. This can be mitigated by gradient precompensation [36, 37], which was performed for this work. Finally, measuring the ghost signal intensity only in the background may have underestimated the artifacts for method B, since B_0 inhomogeneity can result in spatially varying ghost intensity (Figure 3.2).

The results shown here were all for rate 2 parallel imaging, which is the most commonly utilized parallel imaging acceleration rate and the limit for our 4-channel receive array, and simulations with more receiver elements (e.g. 16) showed similar results as the 4-channel simulations in Figure 3.2 (data not shown). The readout-segmented method can likely be applied to higher accelerations, where the number of blinds required to adequately fill k-space would increase because the faster k-space traversal speed would necessitate narrow blinds.

In conclusion, a readout-segmented GRAPPA reference scan enables

high quality, motion-robust GRAPPA for EPI.

Chapter 4

Acquisition Strategy to Reduce Cerebrospinal Fluid Partial Volume Effects for Improved DTI Tractography [1]

4.1 Introduction

Diffusion tensor imaging (DTI) and tractography are commonly used to delineate voxels associated with specific white matter (WM) tracts which are then characterized by diffusion parameters such as fractional anisotropy (FA) and mean diffusivity (MD). Current DTI techniques are limited by their inherently low spatial resolution, leading to deleterious partial volume effects where the signal measured is a volume, relaxation, and diffusion-weighted average of the signal from each of the compartments [8–11]. One long recognized contaminating compartment is cerebrospinal fluid (CSF) which has high diffusivity,

[1] A version of this chapter has been published: Baron CA, Beaulieu C. Acquisition Strategy to Reduce Cerebrospinal Fluid Partial Volume Effects for Improved DTI Tractography. Magn Reson Med. Epub Early View DOI: 10.1002/mrm.25226

isotropic diffusion, and greater signal than tissue on the non-diffusion-weighted (b0) scans due to its long T_2 and the typical use of an echo-planar imaging (EPI) acquisition, where a long spin echo time is needed to accommodate the diffusion-sensitizing gradients. As a result, the CSF signal can overwhelm the tissue signal even when the CSF volume fraction in a particular voxel is relatively low. An improvement of spatial resolution is considerable motivation to perform DTI at higher magnetic field strengths. While improved resolution reduces partial volume effects, it may still be insufficient to overcome CSF contamination; furthermore, the move to higher fields introduces new challenges for DTI acquisition.

Since the diffusion of water is isotropic in CSF (i.e. FA near zero), the voxels containing both CSF and tissue have reduced FA compared to pure tissue voxels. Accordingly, these voxels can often be missed during tractography as they end up below the tracking FA threshold, impairing the ability to extract fiber tracts that are adjacent to CSF [100–102]. Furthermore, even if the white matter tract is delineated, the 3 to 4 fold greater MD in CSF relative to brain tissue will yield erroneously elevated diffusivity values (mean, parallel, and perpendicular), as well as reduced FA as mentioned earlier. The dependence of the diffusion metrics on the amount of partial volume of CSF will impair their interpretation relative to the underlying white matter microstructure. There is much interest in tractography of the fornix as it is the major efferent tract from the hippocampus. However, the fornix is severely impaired by CSF partial volume effects and is difficult to consistently delineate without some form of CSF signal removal [101, 103]. The fornix has been studied with DTI tractography in numerous brain disorders, including epilepsy [104–106], dementia [107, 108], schizophrenia [109, 110], aging [111–113], and multiple sclerosis [114], but removal of the CSF signal is not usually done (only

4 of these 11 example fornix studies did this).

An inversion recovery preparation that nulls signal from CSF (i.e., fluid attenuated inversion recovery, FLAIR) is the most common method for reducing CSF partial volume effects in diffusion EPI acquisitions, although there is a signal-to-noise and acquisition time penalty, the latter which often limits the brain coverage [12]. The FLAIR-DTI acquisitions have shown more accurate measures of MD and FA in human brain [12, 115–118], as well as improved tractography of tracts near CSF, such as the fornix and corpus callosum [100, 101]. While FLAIR-DTI works well at lower magnetic field strengths such as 1.5 T and 3 T, specific absorption rate (SAR) constraints preclude the practical use of FLAIR with DTI at ultra-high magnetic field strengths such as 4.7 T (in our case), 7 T, and beyond. This necessitates alternative acquisition strategies other than inversion recovery in order to minimize CSF contamination, ideally without increasing SAR or scan time. While post-acquisition strategies that model each voxel as having two signal sources have been developed [103, 119], reducing the CSF signal at the acquisition stage is of relevance since it has no dependence on any model assumptions or constraints.

In this work, an alternative acquisition method comprised of two complementary components was investigated for reducing the effects of CSF signal on DTI tractography and parameter quantification at 4.7 T. The first component is to reduce the repetition time (TR) by acquiring DTI data in smaller sets of slices to achieve the steady state effects of stronger T_1 weighting, thereby reducing the relative signal contribution from long T_1 CSF. In the second component, at least a small degree of diffusion weighting, quantified by the b-value, is applied to all scans to attenuate CSF signal with respect to brain tissue signal (i.e. do not acquire b0 images). The latter methodology has been investigated in a preliminary report using an approach requiring twice

the typical scan time [120]; however, we investigate a strategy that does not increase scan time. Short TR and non-zero minimum b-value can be used in combination to decrease the CSF signal, albeit at the expense of overall brain tissue SNR. Simulations were performed for choosing suitable combinations of TR and b-values, and the effectiveness of the techniques were experimentally evaluated for deterministic tractography of the fornix in healthy young adult volunteers. Tractography of the superior longitudinal fasciculus (SLF) was also performed as a "control" tract since it is not expected to be nearly as influenced by CSF.

4.2 Methods

4.2.1 Optimization of Parameters

A reduction of TR will attenuate the CSF signal strength relative to the tissue due to T_1 saturation given the longer T_1 of CSF ($\approx$ 4.5 s [121]) relative to brain tissue (1.1 s in WM at 4.7 T [122]). An increase of the minimum b-value, b_{min}, to a value greater than 0 s/mm^2 will further reduce the CSF signal due to dephasing of the highly diffusive CSF, whose water has an apparent diffusion coefficient (ADC) much larger than water in brain tissue ($\approx 3 \times 10^{-3}$ mm^2/s in CSF and 0.5-1.5 $\times 10^{-3}$ mm^2/s in tissue, both at an in vivo temperature of 37° C). Both of these modifications also result in an SNR decrease in the tissue, and there exists a choice of TR and b_{min} that results in maximum SNR for a given level of CSF signal suppression. Since the tissue of interest in DTI is typically WM, the level of CSF signal suppression is given by the ratio, $R_{CSF/WM}$, of the CSF signal over the WM signal. The choice of b_{min} and TR is dictated by the equations governing $R_{CSF/WM}$ and the SNR

in WM at b_{min}:

$$R_{CSF/WM} = C_R \frac{\left(1 - e^{-TR/T_1^{CSF}}\right) e^{-b_{min} ADC^{CSF}}}{\left(1 - e^{-TR/T_1^{WM}}\right) e^{-b_{min} ADC^{WM}} e^{-TE_{b_{max}}/T_2^{WM}}} \tag{4.1}$$

$$SNR_{CSF/WM} = C_{WM} \left(1 - e^{-TR/T_1^{WM}}\right) e^{-b_{min} ADC^{WM}} e^{-TE_{b_{max}}/T_2^{WM}} \tag{4.2}$$

where C_R is a constant representing the relative initial magnetizations between CSF and WM with $b = 0$ s/mm^2, C_{WM} is a constant representing the initial tissue magnetization, receiver sensitivity, and standard deviation of the noise, and $TE_{b_{max}}$ is the echo-time (dependent on the maximum b-value, b_{max}). At 4.7 T, $T_1^{WM} = 1100$ ms and $T_2^{WM} = 60$ ms [26, 122], and $T_1^{CSF} = 4500$ ms [121]. The T_2 of CSF is ignored due to its large value compared to the small changes in TE caused by changes in b_{max}. A typical diffusion coefficient of ADC^{WM} $= 0.7 \times 10^{-3}$ mm^2/s was chosen for white matter. Since it has been shown that a difference between minimum and maximum diffusion values of ≈ 1000 s/mm^2 will yield minimal error in the diffusion tensor [123, 124], a maximum b-value 1000 s/mm^2 greater than b_{min} was assumed for the determination of $TE_{b_{max}}$. $C_R = 1.8$ and $C_{WM} = 166$ were determined experimentally for this work using several b = 0 s/mm^2 scans at various TR. In summary, the only unknown parameters in Eq. 4.1 and 4.2 are SNR_{WM}, $R_{CSF/WM}$, TR, and b_{min}.

The first step in determining the SNR-optimal choice of b_{min} and TR is choosing a target CSF to white matter signal ratio. An exemplary value of $R_{CSF/WM} = 0.8$ will be used here and in the experimental work ($R_{CSF/WM}$ $= 3.5$ for standard DTI on the system used in this work). This value was chosen because it maintains a high SNR of ≈ 40 on the minimum b value

images while lowering the CSF signal to below the WM signal. For any value of $R_{CSF/WM}$, Eq. 4.1 gives b_{min} as a function of TR, as shown in Figure 4.1a for $R_{CSF/WM} = 0.8$ (i.e. b_{min} and TR are the only unknown values in Eq. 4.1). This relationship simply shows that if a small b_{min} is used, then a short TR must be utilized to achieve the desired $R_{CSF/WM}$. Thus, b_{min} as a function of TR can be substituted into Eq. 4.2 to obtain SNR_{WM} as a function of TR (i.e. eliminating b_{min} from Eq. 4.2), as shown in Figure 4.1b. A maximum SNR is clearly evident for TR = 3.0 s which, according to Figure 4.1a, requires b_{min} = 425 s/mm^2 to reach the target value $R_{CSF/WM} = 0.8$. Note that the same optimal values could have also been obtained by using Eq. 4.1 to eliminate TR in Eq. 4.2 instead of b_{min}. This results in SNR_{WM} as a function of b_{min}, as shown in Figure 4.1c, where the maximum value is unsurprisingly located at b_{min} = 425 s/mm^2. This optimization procedure can be performed for any $R_{CSF/WM}$ value; as such, the value of SNR_{WM} at the optimal choice of TR and b_{min} as a function of $R_{CSF/WM}$ is shown in Figure 4.1d. A trade-off is observed, where greater CSF suppression (i.e. lower $R_{CSF/WM}$) results in larger SNR penalties for the WM. Note that the experimental determination of C_{WM} is not strictly necessary for determining the optimal TR and b_{min} since it simply scales the plots in Figure 4.1b,c; however, it provides quantitative values of the expected SNR, which aids in determining a target $R_{CSF/WM}$ based on the trade-off with SNR (Figure 4.1d), with the caveat that for high b_{max} (e.g. $>$ 2000 s/mm^2) the accuracy of the simulations will decrease due to the non-monoexponential behaviour of diffusion in tissue [41, 125].

To investigate how the choice of $R_{CSF/WM}$ affects measured DTI parameters, MD and FA as a function of $R_{CSF/WM}$ were simulated for a voxel containing relative volumes of CSF to white matter of 20%, 50%, and 80% (Figure 4.1e,f). See Section 4.5 for a derivation of the dependence of the

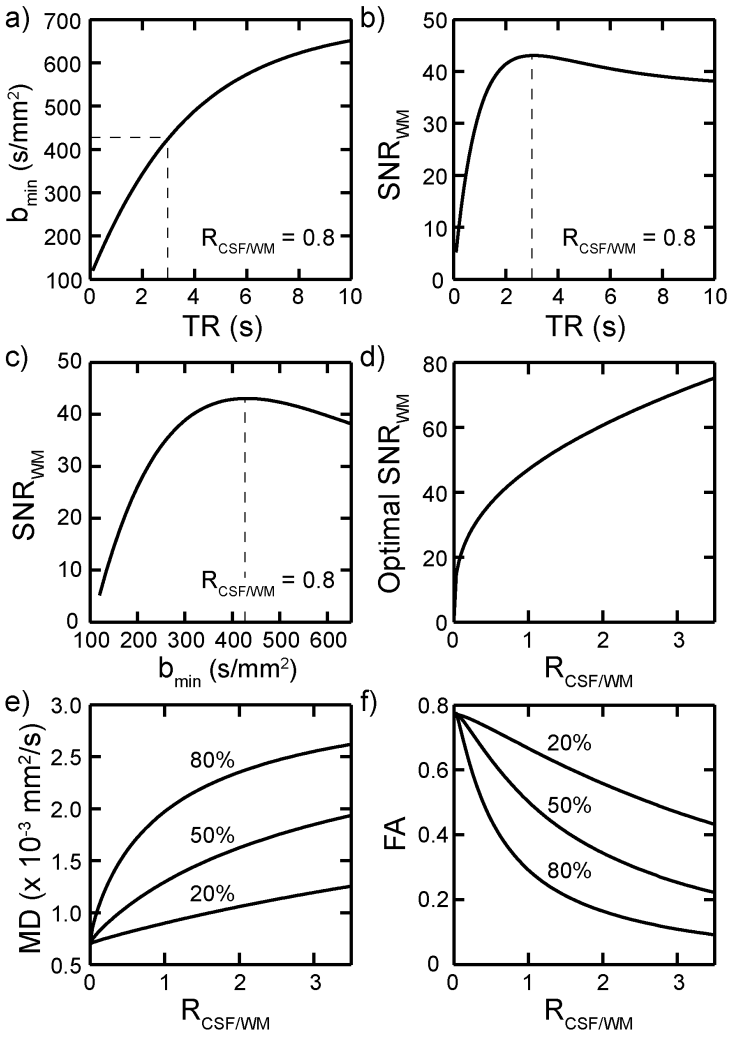

Figure 4.1: (a) Relationship between b_{min} and TR obtained by setting $R_{CSF/WM} = 0.8$ in Eq. 4.1. Using this relationship, Eq. 4.2 can be re-written to give SNR_{WM} as a function of TR (b) or as a function of b_{min} (c). The optimal TR and b_{min} (where SNR_{WM} is maximum) occurs when TR = 3.0 s and $b_{min} = 425$ s/mm^2. Panel (d) shows the SNR_{WM} at b_{min} that is obtained with the optimal choice of TR and b_{min} for various CSF to WM signal ratios, where a trade-off between CSF suppression and SNR is observed. Panels (e) and (f) show simulations of the measured MD and FA, respectively, in voxels with 20%, 50%, and 80% of the volume filled by CSF (MD $= 3 \times 10^{-3}$ mm^2/s; FA = 0). The rest of the voxel is occupied by white matter with intrinsic DTI eigenvalues of $(1.5, 0.3, 0.3) \times 10^{-3}$ mm^2/s (MD $= 0.7x10^{-3}$ mm^2/s; FA = 0.77). At $R_{CSF/WM} = 0.8$, FA and MD values are much closer to the intrinsic values in WM compared to standard DTI where $R_{CSF/WM} = 3.5$.

ADC on $R_{CSF/WM}$. The intrinsic white matter MD and FA were assumed to be 0.7×10^{-3} mm^2/s and 0.77, respectively (eigenvalues $[1.5, 0.3, 0.3] \times 10^{-3}$ mm^2/s), and for CSF an isotropic MD of 3×10^{-3} mm^2/s was assumed. All other parameters were the same as in the other simulations shown in Figure 4.1.

4.2.2 Image Acquisition

The primary experimental goal was to compare DTI with the SNR-optimal combination of both reducing TR and increasing b_{min} relative to standard DTI (i.e. long TR, b_{min}=0 s/mm^2). It was also of interest to investigate the individual effects of reduced TR and increased b_{min} to assess their relative contributions to the combined approach. Additionally, it may be possible to reduce CSF partial volume effects by increasing resolution (instead of the proposed methods), which also results in decreased SNR. As such, an acquisition with improved resolution was also compared to standard DTI.

Five Stejskal-Tanner DTI protocols were acquired in 8 healthy young adult subjects on a Varian Unity Inova (Walnut Creek, CA) 4.7 T MRI using standard DTI (DTI$_S$), standard DTI with high resolution (DTI$_{highres}$), reduced TR DTI (DTI$_{TR}$), DTI with no b0 acquisitions (DTI$_b$), and a combination of DTI$_{TR}$ and DTI$_b$ (DTI$_{TR+b}$). The differences between the five protocols are summarized in Table 4.1. All protocols used: FOV = 24 cm $\times$ 24 cm; 1 average; R=2 GRAPPA; 0.75 partial Fourier fraction. The standard resolution protocols (DTI$_S$, DTI$_{TR}$, DTI$_b$, DTI$_{TR+b}$) used a 120×120 matrix (zero-filled to 240×240) and 64 slices at a thickness of 2.0 mm. The 8 mm^3 acquisition voxel volume is common in DTI, but the differences between the standard and CSF-suppressed scans would be greater at lower spatial resolutions than those evaluated here [9]. The DTI$_{highres}$ protocol used a 148×148 matrix (zero-

Table 4.1: DTI protocols for reducing CSF signal (TR+b, TR, b) versus standard (S) and high resolution (highres) scans without any CSF suppression

	Scan time (min)	Resolution (mm)	b_{min}	b_{max}	TR	TE
DTI_S	6.7	2.00	0	1000	10	56
DTI_{TR+b}	6.7	2.00	**425**	**1425**	**2.5**	56
$DTI_{highres}$	8.1	**1.62**	0	1000	12.2	62
DTI_b	6.7	2.00	**425**	**1425**	10	60
DTI_{TR}	6.7	2.00	0	1000	**2.5**	56

Primary differences from DTI_S are in bold.

filled to 296×296) and 78 slices at a thickness of 1.62 mm. The resolution for $\text{DTI}_{highres}$ was chosen such that the SNR in white matter (WM) was similar to DTI_{TR+b} at b_{max} (where SNR is more limiting).

For standard full-brain DTI acquisitions, the minimum TR is limited by the number of slices. Therefore, to decrease the TR below this limit the acquisition was performed by acquiring multiple slabs of slices independently from each other. As portrayed in Figure 4.2, this approach does not affect the total scan time. The TR was 10 s for both DTI_S and DTI_b, while the increased

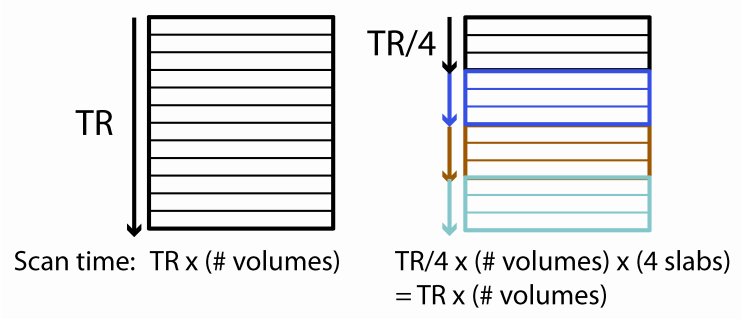

Figure 4.2: Portrayal of how total scan time is maintained when a number of slabs are acquired with a reduced TR, where the TR reduction factor is equal to the number of slabs. The shorter effective TR enables greater suppression of long T_1 compartments like CSF. All diffusion weighted images of a slab are acquired before moving to the next slab.

number of slices for $\text{DTI}_{highres}$ (to maintain total brain coverage) resulted in a TR of 12.2 s. To determine the optimal combination of TR and b for DTI_{TR+b}, a target CSF to WM signal ratio of $R_{CSF/WM} = 0.8$ was chosen because it reduces the CSF signal to below that of the WM signal while maintaining a reasonably large SNR of at least 40 on the b_{min} images (Figure 4.1d). While there may be enough SNR for additional CSF suppression, it was kept high for this study to minimize the impact of SNR differences between the five protocols. The optimal TR and b_{min} for $R_{CSF/WM} = 0.8$ are 3.0 s and 425 s/mm^2, respectively (Figure 4.1); however, to divide the CSF suppressed acquisition into 4 equally sized slabs of 16 sequential slices each and maintain total scan

time (Figure 4.2), a TR of 2.5 s was used for DTI_{TR} and DTI_{TR+b}. While this does not exactly match the design target of 3.0 s, the SNR penalty for using TR = 2.5 s instead of the optimal TR and b_{min} (for the same $R_{CSF/WM}$) is less than 1%.

For DTI_S, $\text{DTI}_{highres}$, and DTI_{TR}, 30 directions at $b_{max} = 1000$ s/mm^2 were acquired along with six $b_{min} = 0$ s/mm^2 scans. For DTI_b and DTI_{TR+b}, 6 directions at $b_{min} = 425$ s/mm^2 (optimal value for $R_{CSF/WM} = 0.8$ for DTI_{TR+b}) were acquired instead of any b0 scans along with 30 directions at $b_{max} = 1425$ s/mm^2. The set of 30 directions used at b_{max} and the set of 6 directions used for non-zero b_{min} were each uniformly distributed in space [73]. Note that the b_{min} directions need not be parallel to the b_{max} directions, which would require nearly twice the scan time for 30 directions, as in [120]; an over-determined matrix equation that solves for the diffusion tensor simply needs a good spread of directions at both b-values to provide a robust least squares fit. Also, DTI_b and DTI_{TR} are expected to exhibit lower CSF suppression than DTI_{TR+b}; their purpose is for determination of the relative contributions of each method (reduction of TR and increase of b_{min}) to the net CSF suppression observed for DTI_{TR+b}. The TE values were 56 ms for DTI_S and DTI_{TR}, 60 ms for DTI_{TR+b} and DTI_b (increased due to higher b_{max}), and 62 ms for $\text{DTI}_{highres}$ (increased due to longer EPI readout train).

The average SNR over all acquisitions at each b-value was measured in the SLF. The signal ratio of CSF (using lateral ventricles) over WM (using the SLF) was averaged amongst the 6 b_{min} acquisitions for each protocol, since CSF partial volume effects are most problematic at the minimum b-values.

4.2.3 Fibre Tracking

The fornix is a thin tract that passes directly through ventricular CSF and is thus the primary interest for assessing the mitigation of CSF partial volume effects, whereas the SLF was chosen as a "control" tract with little CSF contamination expected (assuming one avoids the sulci). ExploreDTI v4.8.2 [76] was used for deterministic (streamline) tractography using an FA threshold of 0.3 and angle threshold of 45°. Note that the fornix studies in References [104–114] that utilized deterministic tractography had FA thresholds ranging from 0.15 to 0.3. A higher FA threshold is desirable as it limits the participation of voxels corrupted by partial volume effects. Tracts were selected if they passed through a selection region halfway along the desired portion of the tract and any of two selection regions drawn at the extremes of the portion (Figure 4.3), in a similar manner to an earlier study [101]. The fornix has a high degree of curvature, and is difficult to extract without separating it into manageable sections; thus, tractography for the crura of the fornix was performed independently from tractography of the body, as shown in Figure 4.3. The SLF (our "control" tract) was refined by omitting streamlines deviating to the cortex to avoid sulcal regions with CSF (Figure 4.3). The left and right side diffusion and volumetric values were averaged for both the crura of the fornix and the SLF.

Tractography was performed separately for each protocol to determine their relative tract volumes and enable qualitative assessment of the tractography. In addition, mean, parallel, and perpendicular diffusivities and FA were measured for all five protocols in the fornix and SLF. Voxels for these measurements were chosen from the tractography masks obtained from DTI_{TR+b} and applied to the four other protocols, since DTI_{TR+b} consistently resulted

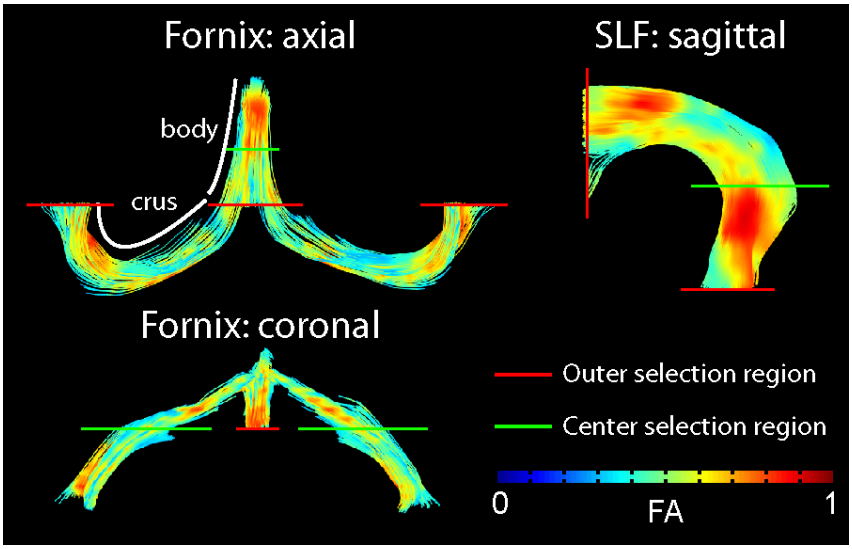

Figure 4.3: Tractography was performed separately for the body and crura of the fornix and was used to identify the core of the superior longitudinal fasciculus (SLF). Tracts were selected if they passed through a center selection region halfway along the desired portion of the tract and any of two selection regions drawn at the extremes of the portion. The cortical extensions of the SLF were excluded from the tract. The relative sizes between the fornix and SLF are not to scale, and the example shown was acquired with the DTI_{TR+b} protocol.

in the largest tract volume. For $\text{DTI}_{highres}$ the tract mask was re-sampled at the higher resolution. This approach was used instead of using each respective protocols own tracts for a mask because it ensures that the same voxel positions are queried for all the protocols, and removes FA-biasing between the different protocols that would occur due to FA being used as criteria to start/terminate tracts. Moreover, tractography was incomplete in the crus of the fornix for many the subjects when using DTI_S, precluding the use of the DTI_S tract mask to determine mean values of FA and MD. For each individual, motion between the 5 scans was corrected using rigid body translations and rotations [126] with an autocorrelation cost function. Correction between adjacent slabs within a given scan was not performed, as there was no apparent misalignment between slabs. Statistical significance of the results was evaluated with paired students t-tests for DTI_S with respect to the four other

protocols using a p-value of 0.05. Multiple comparisons were compensated using a Bonferroni correction, where each tract and variable were considered separately (i.e. there were 4 comparisons for each case).

4.3 Results

The top half of Figure 4.4 displays example raw data for b_{min} and b_{max} for one subject, SNR_{WM}, and the CSF to WM signal ratio at b_{min} for the five protocols (the numerical values are the mean from all 8 subjects). The DTI_{TR+b} method markedly reduced the CSF to WM signal ratio to 0.7, compared to the ratio of 3.5 for standard DTI (DTI_S); however, SNR_{WM} was reduced from 36 to 23 (36% reduction) at b_{max} and 71 to 40 (44% reduction) at b_{min}. In contrast, the CSF to WM signal ratio is increased to 3.8 for the high resolution approach ($\text{DTI}_{highres}$), which is due to the longer TR and TE relative to DTI_S. Similarly to DTI_{TR+b} at b_{max}, the SNR_{WM} for $\text{DTI}_{highres}$ was reduced to a value of 23 at b_{max} (71 to 47 at b_{min}). The CSF to WM signal ratio reductions to 1.3 and 2.0 for DTI_b and DTI_{TR}, respectively, indicate that both protocols significantly contributed to reducing the CSF signal. It is relevant to note that the signal ratio of 0.7 for DTI_{TR+b} is comparable to the design target of 0.8. MD maps and FA maps color-coded with principle eigenvector direction for the five protocols are shown in the bottom half of Figure 4.4. While the color-coded FA maps were similar for all 5 protocols, the MD appears globally lower for all brain tissue for both DTI_{TR+b} and DTI_b compared to DTI_S. Coronal views of the FA maps show good alignment of the slabs (similar for other subjects).

Examples of tractography of the fornix (crura and body combined) and SLF of the same subject for all five protocols are shown in Figure 4.5. For

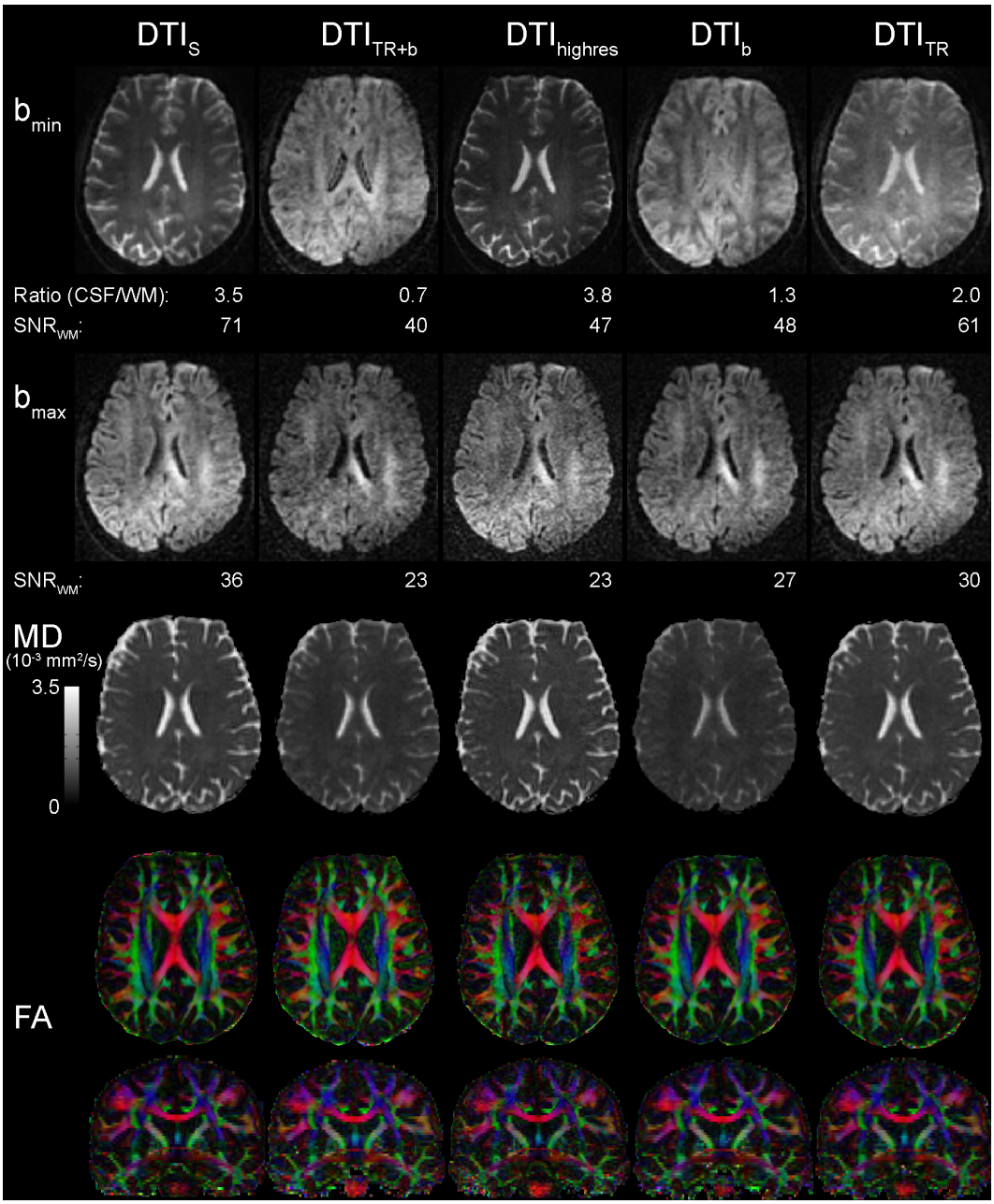

Figure 4.4: Example raw data at bmin and bmax and DTI parameter maps for one subject (raw data individually scaled for each protocol). For non-zero b_{min}, the diffusion encoding direction is $(x, y, z) = (0.1, -0.9, 0.1)$, and for b_{max} the diffusion encoding direction is $(0.1, -0.8, 0.7)$. The mean ratio of CSF to white matter (WM) signal is given for the b_{min} raw data, and the SNR in the SLF, SNR_{WM}, is given for both b_{min} and b_{max}. All numerical values are the mean from all 8 subjects. The MD maps appear to yield lower values for the DTI scans with reduced CSF signal while the direction-encoded FA maps are all similar.

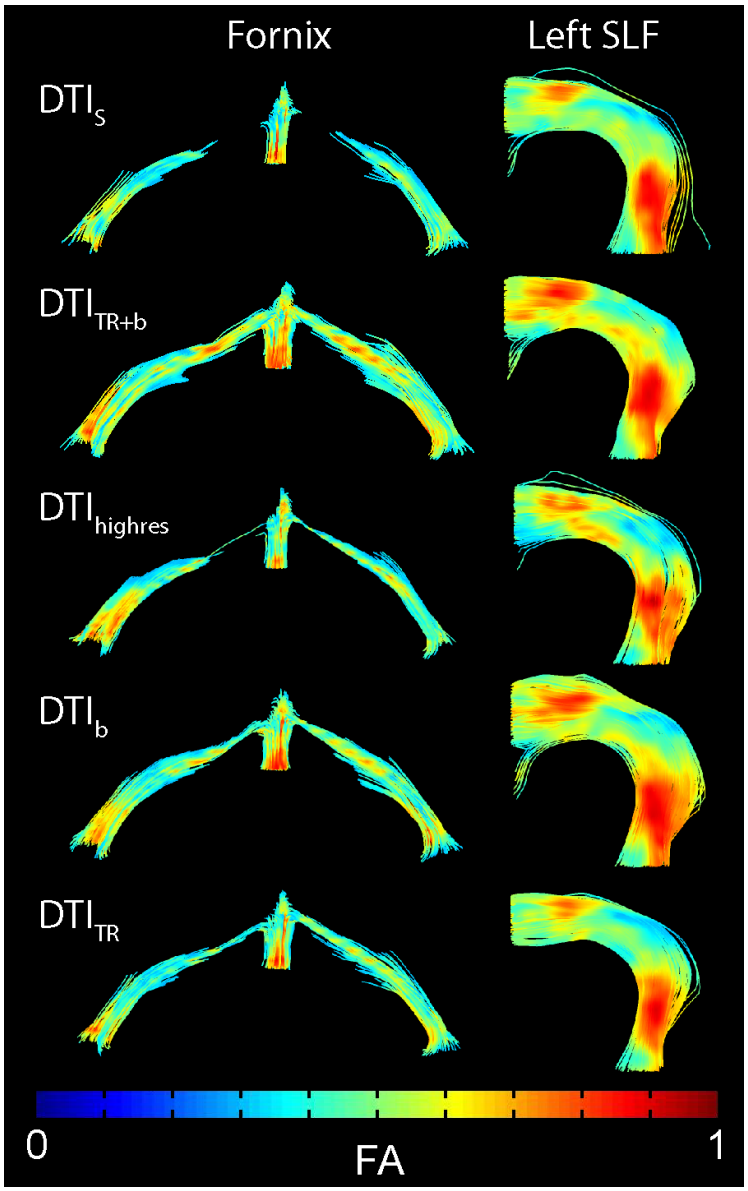

Figure 4.5: Examples of tractography of the fornix (body and crura; coronal view from front) and left superior longitudinal fasciculus (SLF; sagittal view from left) in one subject. The tractography of the crura was incomplete for DTI_S due to a reduction of FA below the tractography threshold. It was best outlined using DTI_{TR+b}, while the other protocols contained much wispier connections. Little difference is observed between the five protocols for the SLF. Similar findings were observed in the other 7 subjects. The relative sizes between the fornix and SLF are not to scale.

the example shown, the tractography of the crura was incomplete and did not connect to the body for DTI_S. The best connection in terms of thickness of tract between the bottom of the crura and body was observed for DTI_{TR+b}. Figure 4.6 shows the results of fornix tractography for DTI_S and DTI_{TR+b} for all 8 subjects, where it is evident that the DTI_{TR+b} approach resulted in consistently larger and better connected tracts in all cases. For DTI_S, tractography of the crura of the fornix was artificially disconnected for half of the subjects (who had narrow fornix crura), whereas for DTI_{TR+b} the tracts were all completely delineated (Figure 4.6). While tractography was more successful for all four of the other protocols compared to DTI_S (artificial disconnections in 25% of the subjects for $DTI_{highres}$, 12.5% for DTI_b, and 25% for DTI_{TR}), the DTI_{TR+b} approach was the only one where it was successful in all of the subjects. As seen in the example in Figure 4.5, tractography of the SLF was similar for all five protocols. Similar results were observed in the other subjects, which is likely due to the large size of the SLF and lack of CSF adjacent to it.

Figure 4.7 shows that significant increases in tract volume were observed for DTI_{TR+b} compared to DTI_S for all the tracts studied (increases of 69% in the fornix crura, 54% in the fornix body, and 14% in the SLF), which reflects that more voxels were able to overcome the FA threshold with the removal of CSF signal. This was even the case in the SLF (albeit by a smaller margin), which is not typically associated with CSF partial volume effects. There was a significant decrease in volume of the crura of the fornix for $DTI_{highres}$ relative to DTI_S, potentially because the CSF to WM signal ratio for $DTI_{highres}$ was larger than for DTI_S. Alternatively, partial volume effects may have caused the lower resolution images to over-estimate the size of the crura; however, wispy connections observed for $DTI_{highres}$ (e.g. Figure

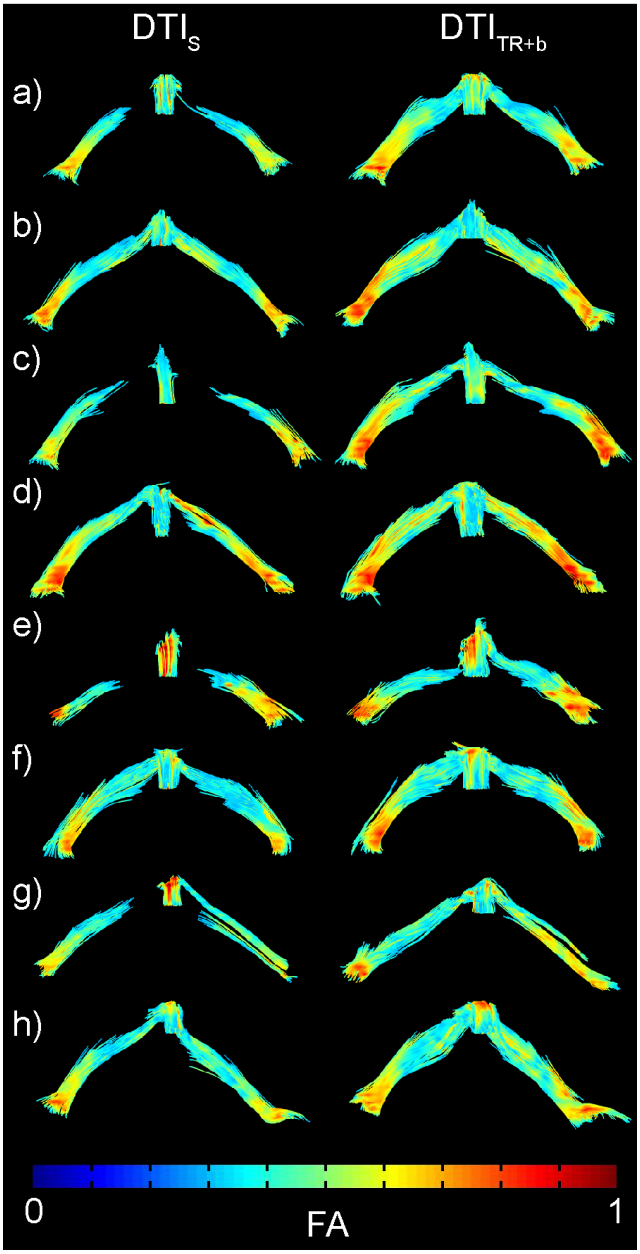

Figure 4.6: Tractography of the fornix in all 8 subjects (a-h) for DTI_S (left column) and DTI_{TR+b} (right column), where it is evident that DTI_{TR+b} consistently results in larger and better connected tracts compared to DTI_S. Artificial disconnections between the crura and body can be observed in half of the subjects (a,c,e,g) when DTI_S is utilized (no artificial disconnections for DTI_{TR+b}).

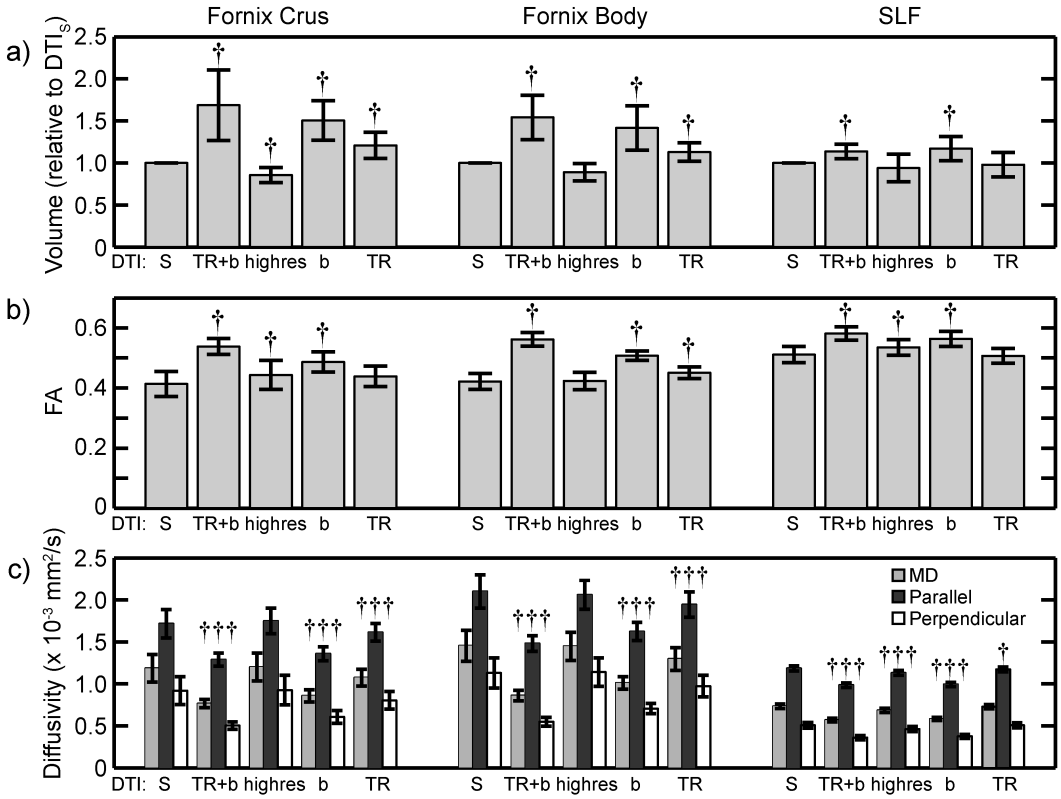

Figure 4.7: Mean (a) volume, (b) FA, and (c) mean, parallel, and perpendicular diffusivities in the fornix crura, fornix body, and superior longitudinal fasciculus (SLF) for 8 healthy subjects using the various protocols for mitigating CSF partial volume effects. Volumes are reported relative to the volumes measured using the DTIS protocol, where the mean volumes for DTI_S are 1900 mm^3 for the fornix crus (left and right combined), 900 mm^3 for the fornix body, and 3900 mm^3 for the SLF (left and right combined). Volumes were measured using tractography masks from each individual protocol, while the DTI_{TR+b} tractography mask was applied to all the other data sets to measure FA and diffusivity values (i.e. the same voxels were queried). Paired t-test significance with respect to DTI_S is portrayed using †for $p < 0.05$.

4.5) point to the former explanation. In the SLF, there was no significant change in tract volume when using $\text{DTI}_{highres}$. In all tracts the volume increased when using DTI_b; nearly to the level of that observed with DTI_{TR+b}. Volume increases were observed in the body and crura of the fornix, but not in the SLF, with DTI_{TR}.

In the fornix (body and crura), the FA and diffusivities (MD, parallel, and perpendicular) are increased and decreased, respectively, for all of DTI_{TR+b}, DTI_b, and DTI_{TR} compared to DTI_S (Figure 4.7) in the voxels defined by the DTI_{TR+b} protocol (i.e. the one that yielded the largest tracts). The highest FA values and lowest diffusivity values are observed with DTI_{TR+b} (e.g. in the crura, FA is 30% larger and MD is 36% smaller for DTI_{TR+b} with respect to DTI_S), which is consistent with reduced CSF partial volume effects. In the SLF, both DTI_{TR+b} and DTI_b resulted in increased FA and decreased MD, while no change was observed for DTI_{TR}. The $\text{DTI}_{highres}$ protocol produced similar FA and diffusivity values compared to the DTI_S protocol. Overall, the parallel and perpendicular diffusivities behaved similarly to MD; however in cases where FA increased and MD decreased relative to DTI_S, the proportional decreases in parallel diffusivity were smaller than the proportional decreases in perpendicular diffusivity, which is consistent with the FA increases.

4.4 Discussion

The results indicate that tractography of the fornix can be improved through a combination of reducing TR and using a non-zero b_{min}. The trends observed in tract volume (increased), FA (increased), and MD (decreased) are in agreement with methods that instead use FLAIR to suppress the CSF signal in the fornix [101]. Interestingly, the inter-subject variation of FA and

MD values was the lowest for DTI_{TR+b} for both the fornix and SLF, which is indicative of more reliable measurements. Since both DTI_b and DTI_{TR} resulted in improvements for tractography and changes in tract volume, FA, and MD, the marked improvements observed with DTI_{TR+b} were caused by both increasing the minimum b-value and reducing the TR. In addition, the only protocol where no artificial disconnections occurred in the fornix was DTI_{TR+b}; however, the similar tract volumes between DTI_{TR+b} and DTI_b suggest that increasing b_{min} provided a larger benefit than reducing the TR. It was also observed that using a similar SNR penalty as the DTI_{TR+b} protocol to instead improve resolution (i.e. $\text{DTI}_{highres}$) does not circumvent CSF partial volume effects as well; an artificially disconnected fornix still occurred in two of the eight subjects (none for DTI_{TR+b}) and FA values were not increased by as much, nor MD values decreased, as for DTI_{TR+b}. It is noteworthy that in single shot techniques, as was the case here, increasing the resolution has diminishing returns due to worsening T_2 blurring of the image. The results here used a relatively high FA threshold of 0.3 for deterministic tractography. A lower FA threshold of 0.2, as used in other studies of the fornix, results in similar relative differences in tract volume, FA, and MD between the protocols, but causes globally lower measures of FA, higher tract volumes, and lower rates of artificial disconnection. While reduced artificial disconnection of tracts improves the ability to extract the tract, a globally decreased FA suggests increased corruption by partial volume effects.

Reliable DTI tractography using a low SAR approach is desirable given the shift to increasing magnetic field strengths and their associated SAR limitations, particularly for high SAR sequences like FLAIR. Moreover, while the combined approach proposed here results in a 36% SNR loss, FLAIR also results in an SNR loss that can be as large as 28% [101], and while FLAIR

requires longer scan times, the proposed method does not. This time savings also makes the proposed methods attractive for low field application. While post-acquisition corrections have also been reported for mitigating CSF partial volume effects and improving tractography of the fornix [103, 119], these use model assumptions (e.g. Gaussian diffusion) and constraints (e.g. smoothness) that may not work as well as minimizing CSF signal in the first place during acquisition; however, a direct comparison was not demonstrated here and is beyond the scope of this work. Additionally, it may be beneficial to combine the post-acquisition techniques with the acquisition strategies introduced here to mitigate partial volume effects stemming from any remaining CSF signal as well as allow the estimation of the amount of partial volume initially.

Even in the SLF "control" tract, FA values increased and MD values decreased using DTI_{TR+b} (which could be from sampling at higher b-values where the signal decay curve is deviating from exponential); however, tractography itself was not greatly impacted. Therefore, the SNR penalty from DTI_{TR+b} is likely not worthwhile for the SLF and other tracts that are not substantially impacted by CSF partial volume effects. Instead, the techniques introduced here may be best suited for targeting a problem area like the fornix. The approach of reducing TR by using smaller slabs of slices may be well suited to this type of usage, since only a single slab may be required for the specific tract of interest.

While the $R_{CSF/WM}$ chosen here for exemplary purposes was 0.8, the value chosen for other applications would depend on the specific goals. Here, the value was chosen to attenuate the signal of CSF below WM (rather than being 3.5 times brighter) and still maintain a high SNR_{WM}, mitigating any differences in our results that could have stemmed from different SNR between the five scan protocols. This $R_{CSF/WM}$ value does not eliminate the effect of

partial volume on the quantitative parameters, as is evident in Figure 4.1e,f, but does result in a marked improvement. For example, for $R_{CSF/WM} = 0.8$, the FA is higher than a typical tractography threshold of 0.3 even in voxels 80% filled with CSF; however, for the standard case of $R_{CSF/WM} = 3.5$, voxels with 50% CSF do not surpass FA = 0.3. A much lower $R_{CSF/WM} = 0.15$ could have been chosen while maintaining $SNR_{WM} > 20$ at b_{min}. It is clear from Figure 4.1e,f that DTI parameters would be fairly accurate even for voxels with CSF occupying 80% of the volume; however, for this case the optimal minimum b-value turns out to be 1100 s/mm^2. Coupled with a required second b value of 2100 s/mm^2 (keeping with a 1000 s/mm^2 separation between b values), ADC values would be much lower than the expected CSF-suppressed values because of non-Gaussian behaviour [41, 125]. Since only the few voxels with very high CSF volume fractions are affected when moving to such a low $R_{CSF/WM}$, it may be more desirable to target a higher $R_{CSF/WM}$ like 0.8 and use the remaining "extra" SNR to increase spatial resolution. This is demonstrated in Figure 4.8, where a small 3.25 cm slab covering the fornix has been acquired at an isotropic resolution of 1.62 mm (4.3 mm^3) in 3.8 min using $R_{CSF/WM} = 0.8$.

Given that all diffusion directions were acquired for one slab before moving to the next, there is potential for slab misalignment due to subject motion. This was not observed in the experienced volunteers recruited for this work (see coronal images in Figure 4.4); however, if problematic for a certain patient group it could likely be corrected via registration of partially overlapping slabs. Also, cardiac gating was not used here, but its implementation would require additional considerations. First, cardiac gating decreases scan efficiency, meaning that fewer slices could be acquired within a desired TR; thus, more slabs would be required for the same brain coverage. Second, variations in heart rate could cause TR variations that would introduce CSF

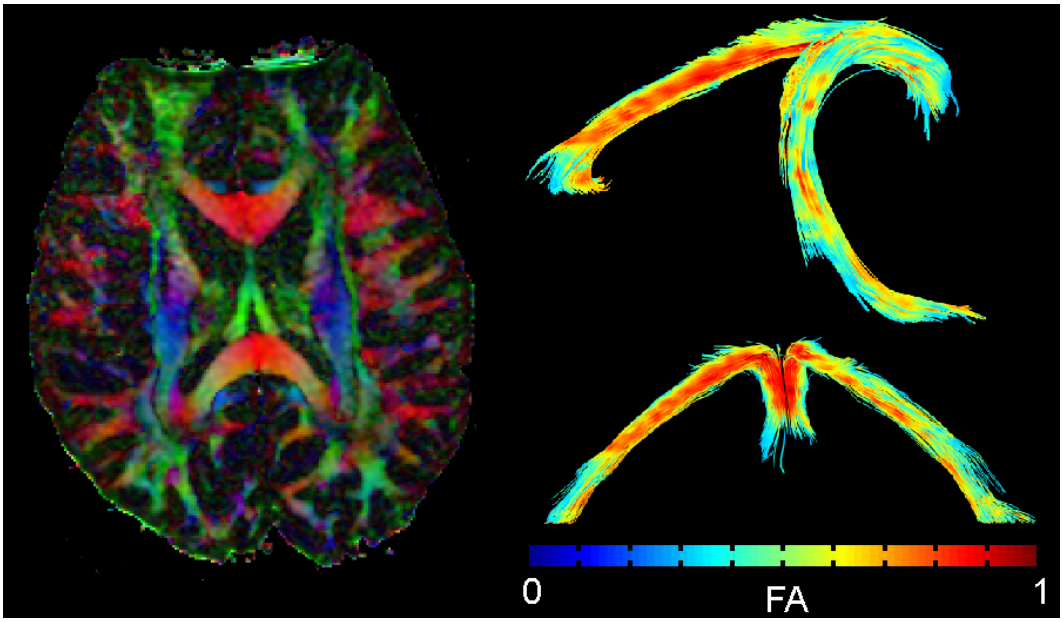

Figure 4.8: A color-coded FA map of an axial slice acquired with 1.62 mm isotropic resolution and the fornix identified by streamline tractography using the DTI_{TR+b} approach with $R_{CSF/WM} = 0.8$. A small 3.25 cm slab (20 slices) spanning the fornix was acquired in 3.8 min.

signal inconsistencies between different diffusion weightings.

Changes in the diffusion parameters with the use of a non-zero b_{min} and a higher b_{max} likely arose not only from the suppression of CSF, but also from non-Gaussian diffusion in tissue. In free liquids (e.g. CSF), signal amplitude scales exponentially with b-values. In contrast, signal amplitudes measured in brain tissue tend to decrease more slowly with increasing b-value [41, 125], because the diffusion is hindered by cell membranes and myelin. Accordingly, decreased ADC and MD values are measured at higher b-values. This was investigated by acquiring 30 direction data sets with b-values ranging from 0 s/mm^2 to 2500 s/mm^2 in 500 s/mm^2 increments in one healthy volunteer (one scan session; all sequence parameters identical for all b-values; Figure 4.9). Non-Gaussian diffusion characteristics were observed in an ROI placed in the SLF, and ADC values decreased if either the minimum or maximum b-value used in the two-point fit was increased. For b-values of {0,1000} s/mm^2

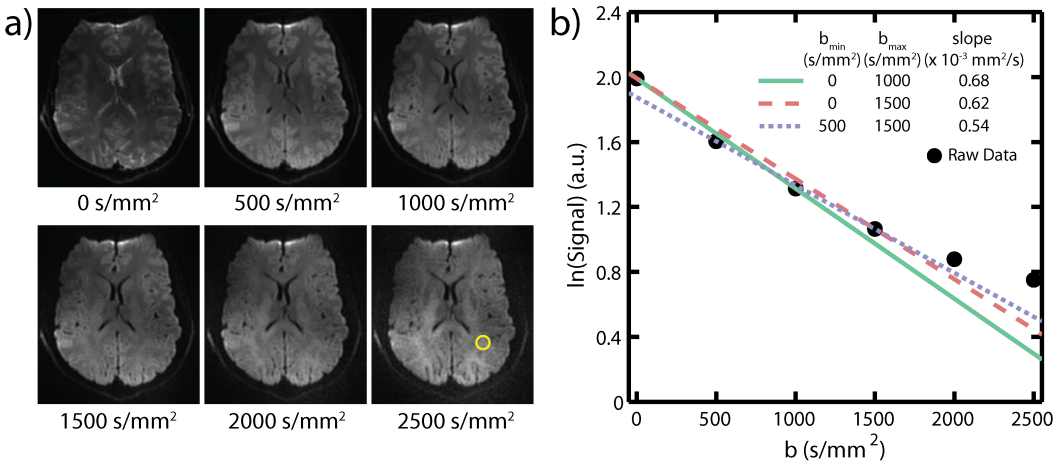

Figure 4.9: (a) Mean diffusion weighted images (averaged over 30 directions) for b-values ranging from 0 s/mm^2 to 2500 s/mm^2. (b) Natural logarithm of the mean signal in an ROI in the SLF (circle in a), with linear fits calculated using two points at b = 0 s/mm^2 and b = 1000 s/mm^2 (solid), b = 0 s/mm^2 and b = 1500 s/mm^2 (dashed), and b = 500 s/mm^2 and b = 1500 s/mm^2 (dotted). The slopes of the fits gives the mean ADC which, as a result of the non-Gaussian nature of diffusion in tissue at large b-values, decreases substantially as either the minimum or maximum b-value is increased.

compared to {500,1500} s/mm^2, the ADC decreased from 0.68×10^{-3} mm^2/s to 0.54×10^{-3} mm^2/s (21%), which is similar to the drop in MD observed in the SLF for DTI$_{TR+b}$ and DTI$_b$ compared to DTI$_S$ (22%). Thus, the decrease of MD in the SLF was likely due to the higher b-values, while the larger decreases of 41% and 36% in the body and crura of the fornix, respectively, are likely due to reduced partial volume effects in addition to increased b-value. Assuming a 22% decrease of MD in the fornix from the higher b-value, the MD decreases from partial volume effects alone were approximately 24% (body) and 17% (crura).

Enhanced suppression of CSF signal near the ventricle walls was observed with non-zero b_{min} (e.g. b_{min} for DTI$_{TR+b}$ in Figure 4.4). This exaggerated signal reduction varied (or disappeared entirely) depending on the diffusion gradient orientation, which suggests it was likely due to incoherent flow in the CSF arising from intra-ventricular pulsation.

It is evident from the parameter optimization results (Figure 1b,c) that one could obtain the same design target of $R_{CSF/WM} = 0.8$ by using b = 650 s/mm^2 and TR = 10 s, which avoids the necessity a multi-slab approach. This may be preferable in some situations; however, the disadvantage of doing so is a 12% decrease in SNR relative to the optimal combination of TR and b_{min} (Figure 4.1b,c), and even more reduction in measured ADC values from sampling at higher b-values. It is also important to note that the optimal parameters to achieve a desired $R_{CSF/WM}$ will vary with different MRI systems, because the CSF to WM signal ratio depends on TE (which changes with maximum gradient strength) and T_2 (which changes with field strength). In addition, while the multi-slab slice re-organization used here provides a simple, easily implemented method for the reduction of TR, an alternative (or complimentary) method may be simultaneous multi-slice EPI [127, 128].

In conclusion, it has been demonstrated that CSF partial volume effects in DTI can be effectively mitigated through a combination of reduced TR and a non-zero minimum diffusion weighting. While these techniques decrease the overall tissue SNR, they have the advantage of having no impact on scan time or SAR. The lack of SAR increase is attractive for DTI at high field strengths, where RF power deposition must be carefully considered, while the scan time benefit over FLAIR may be attractive for any field strength. The effective reduction of confounding CSF partial volume effects may have a particular benefit in studies where one needs to mitigate the confound from variable CSF, such as in aging.

4.5 Addition to the Published Paper

To show how the partial volume effect depends on the choice of both the low and high b-value, the formula for the ADC measured in a voxel containing partial volumes of CSF and white matter will be investigated. The calculation of ADC along a single direction will be assumed, where p is the fractional volume of the voxel occupied by CSF. For standard DTI that uses $b = 0$ s/mm^2 and some non-zero b-value, b_{high} (typically 1000 s/mm^2), the measured ADC in a voxel with partial volume is given by:

$$ADC = -\ln\left(\frac{pS_{CSF}e^{-b_{high}D_{CSF}} + (1-p)S_{WM}e^{-b_{high}D_{WM}}}{pS_{CSF} + (1-p)S_{WM}}\right)/b_{high} \qquad (4.3)$$

where S_{CSF} and S_{WM} are the signal strengths of CSF and white matter, respectively, at $b = 0$ s/mm^2 for the given TE and TR (i.e. the signal values received if there was no partial volume), and D_{CSF} and D_{WM} are the "real" ADC's of CSF and white matter, respectively (again, the values without partial volume). The equation can be rearranged to show that the partial volume effect depends on the relative net signal levels of CSF and WM at b0:

$$ADC = -\ln\left(\frac{\frac{S_{CSF}}{S_{WM}}pe^{-b_{high}D_{CSF}} + (1-p)e^{-b_{high}D_{WM}}}{\frac{S_{CSF}}{S_{WM}}p + (1-p)}\right)/b_{high} \qquad (4.4)$$

and thus for non-zero p (proportion of CSF), one must reduce S_{CSF} in order for the ADC to primarily reflect the white matter.

If the low b-value is increased by b_1 and the high b-value is increased by $b_2 = b_1 + \Delta b$ (assuming $b_{high} + \Delta b > 0$ to keep the high b-value larger than

the low b-value), the equation becomes:

$$\begin{aligned} ADC = & -\ln\left(\frac{e^{-b_2 D_{CSF}}\frac{S_{CSF}}{S_{WM}}pe^{-b_{high}D_{CSF}} + e^{-b_2 D_{WM}}(1-p)e^{-b_{high}D_{WM}}}{e^{-b_1 D_{CSF}}\frac{S_{CSF}}{S_{WM}}p + e^{-b_1 D_{WM}}(1-p)}\right) \\ & /((b_{high}+b_2)-b_1) \\ = & -\ln\left(\frac{\frac{S_{CSF}e^{-b_2 D_{CSF}}}{S_{WM}e^{-b_2 D_{WM}}}pe^{-b_{high}D_{CSF}} + (1-p)e^{-b_{high}D_{WM}}}{\frac{S_{CSF}e^{-b_1 D_{CSF}}}{S_{WM}e^{-b_1 D_{WM}}}p + (1-p)}\right)/(b_{high}+\Delta b) \\ = & -\ln\left(\frac{R_{CSF/WM}\frac{e^{-\Delta b D_{CSF}}}{e^{-\Delta b D_{WM}}}pe^{-b_{high}D_{CSF}} + (1-p)e^{-b_{high}D_{WM}}}{R_{CSF/WM}p + (1-p)}\right) \\ & /(b_{high}+\Delta b) \end{aligned} \tag{4.5}$$

The above equation sheds some light on how the choices of increases of b will affect the partial volume effect:

1. The ADC that is measured will become the true ADC in white matter (i.e. D_{WM}) if $R_{CSF/WM}$ is close to 0.

2. When both the high and low b-values are increased by the same amount (i.e. $b_1 = b_2$ and $\Delta b = 0$), as was the case in our work, the reduction of the partial volume effect via increased b-values depends only on $R_{CSF/WM}$.

3. For a larger b_2 compared to b_1 (i.e. $\Delta b > 0$), the ADC will be closer to D_{WM} for the same $R_{CSF/WM}$.

4. For a smaller b_2 compared to b_1 (i.e. $\Delta b < 0$), the ADC will be farther from D_{WM} for the same $R_{CSF/WM}$.

Therefore, the partial volume effect depends on the separation of the b-values in addition to the common increase of b at both the low and high

b-values. However, for the case where $b_1 = b_2$, which maintains the optimal separation of low and high b-values of 1000 s/mm^2 [123, 124], the reduction of partial volume error of ADC depends directly on $R_{CSF/WM}$.

Chapter 5

Oscillating Gradient Spin-Echo (OGSE) Diffusion Tensor Imaging of the Human Brain[1]

5.1 Introduction

The apparent diffusion coefficient (ADC) measured using diffusion tensor imaging (DTI) depends on the time allowed for diffusing water molecules to probe the local environment; namely, the effective diffusion time (Δ_{eff}). If, during the diffusion time, most molecules do not travel far enough to interact with any obstacles, the measured ADC will be equivalent to the intrinsic diffusion coefficient [42, 43]. For increasing diffusion times, the molecules will interact with more barriers and the ADC will decrease, eventually reaching an asymptotic lower value; thus, measuring diffusion time dependence of ADC values may give insight into the microstructure [129].

DTI is typically performed using pulsed gradient spin-echo (PGSE)

[1]A version of this chapter has been published: Baron CA, Beaulieu C. Oscillating Gradient Spin-Echo (OGSE) Diffusion Tensor Imaging of the Human Brain. Magn Reson Med. Epub Early View DOI: 10.1002/mrm.24987

diffusion encoding [32], which has an inherently large Δ_{eff}, typically greater than 30 ms for in-vivo human studies. The minimum diffusion time attainable while maintaining a desired level of diffusion sensitization (i.e. b-value) is limited by the maximum gradient strength. Early investigations utilizing strong insert gradients demonstrated the dependence of ADC on Δ_{eff} in various excised nerves [39, 130–132] and rodents [133]. The minimum Δ_{eff} ranged from 1-4 ms and yielded increases of approximately a factor of 2 in perpendicular diffusion coefficients for short relative to long Δ_{eff} [39, 130–132]. While no changes in parallel diffusion coefficients were observed in one case [39], increases in parallel ADC by approximately a factor of 1.5 were observed in other studies [130, 131]. Lower diffusion anisotropy with decreasing Δ_{eff} was also reported in general [39, 130, 131]. In contrast, there have been no findings of Δ_{eff}-dependence (with constant b-value) in human brain using PGSE or combinations of bi-polar pulsed gradients with Δ_{eff} ranging from 8 ms to 256 ms [134–136]. The equivalent diffusion distances in water at body temperature for these diffusion times ranges from 7 - 39 μm and, given that axon diameters in the human corpus callosum range from 0.5 - 3 μm [137, 138], most axons in these studies were likely in a restricted regime for all Δ_{eff}. Therefore, shorter diffusion times, as shown in the pre-clinical studies mentioned above, are presumably necessary to observe the onset of diffusion restriction in the human brain.

The oscillating gradient spin-echo (OGSE) method enables reduced Δ_{eff} by employing a succession of short diffusion weighting periods [4–6]. The use of bipolar gradient pulses to achieve small Δ_{eff} in some earlier studies was similar [39, 133, 135]; however, OGSE theory additionally considers the frequency content of the diffusion gradients, which enables the design of optimal gradient waveforms. Moreover, OGSE waveforms enable the measurement

of MRI signal with unique dependencies on intracellular properties [139], and may provide a means of quantitative measurements of cell characteristics, such as nuclear size and surface to volume ratios [140, 141]. A recent study in an in-vivo rat model reported increases of mean ADC in cortical and subcortical grey matter as diffusion time decreased from 9.75 ms to 0.38 ms [142]. Another study in an in-vivo mouse brain with diffusion times ranging from 15 ms to 1.67 ms observed enhanced tissue contrast between different cell layers in the hippocampus at the shortest diffusion times [143]. The same study also showed increases in diffusion tensor eigenvalues (parallel and perpendicular) and decreases in fractional anisotropy (FA) in various white and grey matter regions with a reduction of Δ_{eff}. Similar OGSE DTI results in both white and grey matter have been observed in the in-vivo rat brain with Δ_{eff} ranging from 7.5 ms to 1.88 ms [144]. The additional specificity to intracellular structure provided by OGSE may provide insight into pathology. For example, the aforementioned study of the rat brain observed that the mean ADC decrease observed after a global ischemic event was approximately 50% lower for a Δ_{eff} of 0.5 ms compared to 9.75 ms, which suggests that half of the ischemic ADC decrease is from microstructure sensitive to diffusion times shorter than 0.5 ms [142]. A recent study examining ADC characteristics in a rat glioma cell culture upon ischemia (Δ_{eff} ranging from 40 ms to 0.83 ms) concluded that at long diffusion times ischemia-induced ADC decreases in intracellular water result from changes in cell size and cellular volume fraction, while at short diffusion times ADC decreases are from changes in the intrinsic properties of the intracellular water [145]. Additionally, it has been proposed that sensitivity to cell nuclear size may make OGSE useful in the monitoring of tumors [140, 146, 147].

The exploration of Δ_{eff}-dependence of diffusion in the human brain

could enable greater insight into the mechanisms behind disease and their progression. First, though, an understanding of diffusion time dependence of DTI measurements is required in the healthy human brain. There has been one publication reporting Δ_{eff}-dependence of ADC measurements at constant b-value in humans, utilizing OGSE gradients with a tetrahedral-encoding scheme and b = 200 s/mm^2 [53]. The mean ADC in the corpus callosum showed a tendency to increase in 4 subjects with Δ_{eff} from 20 to 4 ms. The purpose of this work is to investigate the Δ_{eff} dependence of the full diffusion tensor in white and grey matter regions of healthy subjects by comparing OGSE and PGSE DTI with b = 300 s/mm^2 and Δ_{eff} ranging from 4 - 40 ms.

5.2 Theory

The OGSE method utilizes the multiple application of short duration diffusion sensitizing periods (i.e. multiple bipolar pulses of gradients) to achieve a low Δ_{eff}, as shown in Figure 5.1(a-d). Since the individual diffusion weighting periods are adjacent to each other, they cannot be considered independent. As such, the diffusion time for OGSE is better understood by recasting the diffusion tensor to a frequency-dependent form, $D(f)$, where the signal attenuation, S/S_0, is described by [4, 48]

$$\ln(S/S_0) = -\int F(f)D(f)F(f)df \tag{5.1}$$

$F(f)$ characterizes the frequency content of the diffusion sensitizing gradients, G, and is given by

$$F(f) = -\int_0^\infty \left(\int_0^t \gamma G(\tau)d\tau\right) e^{i2\pi ft}dt \tag{5.2}$$

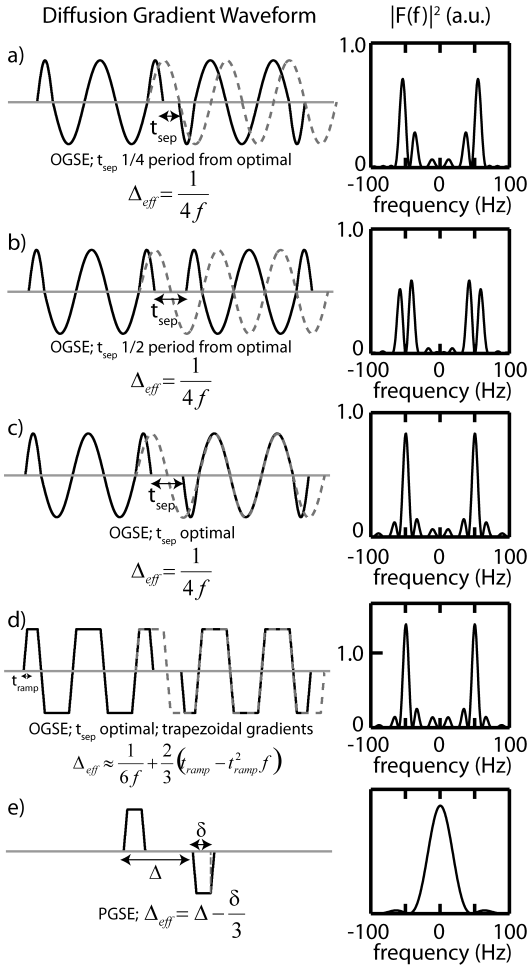

Figure 5.1: Diffusion gradient waveforms and gradient modulation power spectra, $|F(f)|^2$, for OGSE (a-d) and PGSE (e). The polarity of the second gradient waveform has been reversed from what is actually played out to account for the 180° RF pulse that is between the gradient waveforms (RF pulses omitted from diagrams), and $|F(f)|^2$ is numerically calculated directly from the time-domain waveforms. The OGSE waveforms are cosine-modulated, with the start and end quarter-periods replaced with a twice-frequency sinusoid lobe. The separation between gradient waveforms, t_{sep}, is required to accommodate the 180° RF pulse. In (a-d), the dashed lines show that if t_{sep} is a value that allows a continuous single frequency oscillating gradient to be drawn between the two waveforms, narrower $|F(f)|^2$ are obtained. It is evident in (c-d) that trapezoidal gradients result in a negligible change in the shape of $|F(f)|^2$ relative to the sinusoidal gradients; however, it does increase the relative spectral amplitude enabling larger b-values. The duration of the shorter lobes in the trapezoidal case are increased by half the gradient ramp time, tramp, to ensure zero cumulative gradient area. The relationship for Δ_{eff} depends on the gradient shape, and is shown below each gradient waveform.

where γ is the gyromagnetic ratio. $F(f)$ can be intuitively understood as the Fourier transform of the wave number, k. It is clear from Equations 5.1 and 5.2 that the signal attenuation is only sensitive to frequency components that are present in $F(f)$. It has been shown that cosine gradients apodized with sinusoidal lobes at twice the target frequency produces a gradient modulation power spectra, $|F(f)|^2$, that is narrow around the desired frequency [48, 142]. For such a gradient waveform the diffusion time is given by $\Delta_{eff} = 1/(4f)$.

Additionally, the separation and polarity between the two gradient waveforms before and after the 180° RF pulse affects the diffusion frequency spectra [53]. Figure 5.1a-c shows that a separation, t_{sep}, which allows a continuous, unbroken sinusoid to be drawn across the two waveforms results in the most narrow spectral shape. Since sinusoids are not efficient for achieving large b-values, trapezoidal gradient waveforms are used in this work to enable an increase in b-value by 67% over the sinusoidal variant [53, 148]. There is almost no difference in the shape of $F(f)$ for the trapezoidal case (Fig. 5.1c,d), because integrating the gradient before performing the Fourier transform in Equation 5.2 results in a very similar spectra for the two waveform types; however, the amplitude of the trapezoidal $|F(f)|^2$ at the desired frequency is 69% larger than the sinusoidal version, reflecting it's increased b-value. As with the sinusoidal shape, for the trapezoidal gradient shape there is an optimal t_{sep} where a continuous oscillating trapezoidal gradient can be drawn across the waveforms (Fig. 5.1d). Using the same procedure as Gross [4] and Parsons [48], the relationship between Δ_{eff} and f for the trapezoidal waveform is

derived to be (see Section 5.6)

$$\begin{aligned}\Delta_{eff} &= \frac{1}{6f} + \frac{2}{3}t_{ramp} - \frac{t_{ramp}^2}{6\left(0.25/f - t_{ramp}/2\right)} + \frac{(2N+1)t_{ramp}^3}{120N\left(0.25/f - t_{ramp}/2\right)} \\ &\approx \frac{1}{6f} + \frac{2}{3}\left(t_{ramp} - t_{ramp}^2 f\right)\end{aligned} \tag{5.3}$$

where t_{ramp} is the gradient ramp time from zero gradient to the maximum gradient value and N is the total number of periods in both the gradient waveforms combined. Interestingly, the trapezoidal gradients are characterised by smaller diffusion times than the original cosine shape (for the same oscillation frequency) because of the larger b-values that are attained. The b-value is given by $b = 2N\gamma^2G^2(0.25/f - t_{ramp}/2)^2\Delta_{eff}$, where G is the maximum gradient amplitude. For PGSE, $F(f)$ is broad and centered at a frequency of zero and the diffusion time is given by $\Delta_{eff} = \Delta - \delta/3$ (Fig. 5.1e).

5.3 Methods

5.3.1 Image Acquisition

Four DTI protocols were acquired per session in 7 healthy human subjects (4 male / 3 female; age 28 ± 4 years) on a Varian Unity Inova 4.7 T MRI using Δ_{eff} = 4.1 ms (OGSE 50 Hz), 7.4 ms (OGSE 25 Hz), 20 ms (PGSE), and 40 ms (PGSE). The protocol parameters are summarized in Table 5.1. All protocols used b = 300 s/mm^2 with 6 diffusion encoding directions. Note that for low b-values, such as the case here, OGSE and PGSE gradient waveforms with the same Δ_{eff} have been shown to provide similar measurements of ADC [149]. The 6 direction diffusion encoding scheme permits maximum gradient amplitude on two channels simultaneously that allows for b-values

Table 5.1: DTI Protocols

Δ_{eff} (ms)	f(Hz)	Type	δ (ms) [a]	Periods [b]	b (s/mm^2)	Scan Time (min)
4.1	50	OGSE	4.4	2	300	10
7.4	25	OGSE	9.7	1	300	10
20	0	PGSE	5.7	-	300	10
40	0	PGSE	3.9	-	300	10

[a] For OGSE, the effective gradient pulse width is given by $\delta = 0.25f - t_{ramp}/2$
[b] The number of periods on each side of the 180° pulse.

2 times larger than from schemes with many directions (e.g. 30 directions). The 50 Hz OGSE protocol utilized 2 periods per gradient waveform with a maximum gradient of 57.5 mT/m per channel, while the 25 Hz OGSE protocol utilized 1 period per gradient waveform with a maximum gradient of 28.1 mT/m, thereby maintaining an equal total diffusion gradient time and b-value compared to the 50 Hz protocol. The number of periods are limited to prevent excessively long TE. For the 50 Hz scan t_{sep} was 1/8 of a wavelength from the optimal value (the closest possible while maintaining the shortest possible TE), while t_{sep} was optimal for the 25 Hz scan. A conservative net slew rate of only 70 T/m/s was used to avoid peripheral nerve stimulation. Both PGSE protocols used a maximum gradient amplitude of 57.5 mT/m per channel, and used δ = 3.9 ms and Δ = 41.3 ms for the Δ_{eff} = 40 ms scan, and δ = 5.7 ms and Δ = 21.9 ms for the Δ_{eff} = 20 ms scan. Other single-shot EPI imaging parameters were as follows: TR = 12.5 s; TE = 110 ms; FOV = 24 cm; 2 mm x 2 mm acquired in-plane resolution (zero-filled to 1 mm x 1 mm resolution); 40 slices, thickness 2.5 mm; 6 averages; R=2 GRAPPA; scan time 10 min per protocol. Note that the TR (and scan time) was slightly lengthened to mitigate gradient heating that occurs due to the high duty cycle of the OGSE gradients.

A potential concern for this study was differing eddy currents for each diffusion gradient scheme; however, this was mitigated by utilizing gradient pre-compensation [36, 37]. Any remaining eddy currents were evaluated by measuring them directly using a signal point source [2]. The maximum gradient from any eddy current in any of the four protocols was less than 35 μT/m (0.1% of frequency encode gradient) at the beginning of the data readout, and exponentially decayed to less than 5 μT/m at TE (0.02% of frequency encode gradient). Thus, eddy current induced gradients were not expected to impact any findings from this study. Conversely, a transient B_0 eddy current ($\approx$ 1 ppm at beginning of data readout and 0.03 ppm at TE for OGSE 50 Hz; all other scans had a smaller B_0 eddy current) was found to degrade image quality if not accounted for. The phase imparted by the B_0 eddy current was found to be consistent with repeated acquisitions, and it was modelled by applying a least squares exponential fit to the phase accrual directly measured using a small 3 mm diameter probe sample. Then, the phase accrual was subtracted from the phase of the raw subject data before EPI image reconstruction. The effectiveness of the correction is shown in Fig. 5.2.

5.3.2 Fiber Tracking and Statistical Analysis

ExploreDTI used an FA threshold of 0.2 and angle threshold of 30° for tractography of the body (bCC), splenium (sCC), and genu (gCC) of the corpus callosum, corticospinal tracts (CST), cingulum (CG), inferior fronto-occipital fasciculus (IFO), superior longitudinal fasciculus (SLF), and inferior longitudinal fasciculus (ILF) bilaterally. Examples of tractography and the regions used for diffusion parameter analysis are shown in Figure 5.3. Only

[2]The measurements of eddy currents were performed by Robert Stobbe, Research Associate, Biomedical Engineering, University of Alberta.

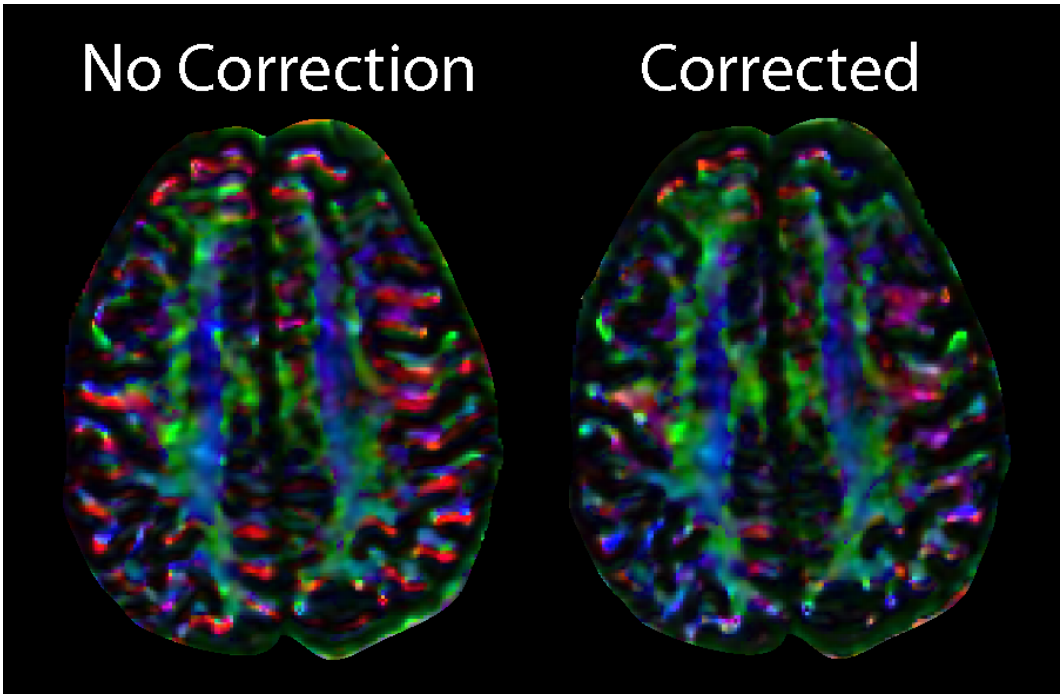

Figure 5.2: FA color coded with principal eigenvalue direction with and without the phase correction for a transient B_0 eddy current, which causes non-uniform image shifts that vary with diffusion gradient direction. By applying a phase correction in k-space, incorrect directionality is ameliorated in the periphery.

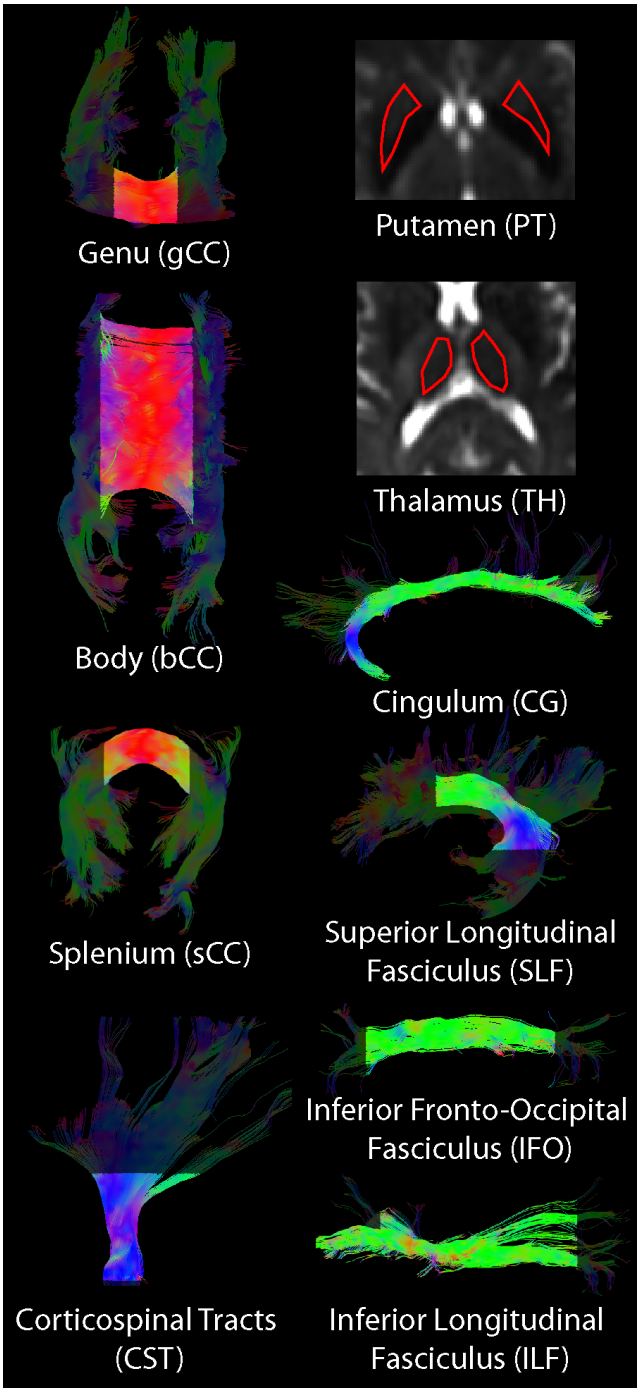

Figure 5.3: Examples of tractography for eight white matter tracts using the $\Delta_{eff} = 40$ ms scan, where tracts are color-coded with principal eigenvector direction, and ROI placement for the thalamus and putamen in one subject. The thin tract portions extended into the cortical areas (semi-transparent portions of the shown tracts) were excluded from analysis to minimize partial volume effects.

central core regions were used for analysis to reduce errors that can occur from mis-registration of the 4 scans due to bulk patient motion and partial volume effects for the narrow tract extensions into the cortex (Fig. 5.3). The thalamus (TH) and putamen (PT) were delineated using manual region-of-interest (ROI) placement on multiple axial slices on the b = 0 s/mm^2 (b0) images. ROI's were placed on all slices that the TH or PT could be clearly identified; as such, the number of slices used varied with each subject. The data from the 4 scans were rigid-body motion corrected relative to each other using in-house auto-correlation based registration software. Voxels for analysis were chosen using the tract mask (or volumetric ROI for grey matter) obtained from the Δ_{eff} = 40 ms scan to yield parallel ($\lambda_{||}$) and perpendicular ($\lambda_{\perp}$) eigenvalues and fractional anisotropy (FA). A potential limitation was misalignment of the tract voxel mask across the 4 scans. Since eddy currents were effectively mitigated using gradient pre-compensation and correction methods, differences in eddy current distortions between the scans were not observed. Also, rigid body motion was corrected using registration and proper alignment of the data sets was confirmed before analysis for each subject. The scans and DTI analysis were performed on four different occasions for a 22° C, 14 cm diameter water phantom doped with $CuSO_4$ to evaluate diffusion parameter consistency over the four DTI protocols in a homogeneous, unrestricted environment. Statistical significance of overall Δ_{eff}-dependence was evaluated using a repeated measures ANOVA, and changes with respect to the Δ_{eff} = 40 ms scans were evaluated using paired t-tests if the ANOVA reported a p-value less than 0.05.

The relatively small b-value of 300 s/mm^2 (b300) could potentially result in low quality data because the signal difference between the b0 and diffusion weighted images is smaller compared to typical b = 1000 s/mm^2 (b1000) DTI and, thus, is more susceptible to errors from noise and residual

Nyquist ghosting. To investigate this, the $\Delta_{eff} = 40$ ms scan was performed at b-values of 300 and 1000 s/mm^2 in two subjects with all other imaging parameters identical (data not shown in paper; see Figure 5.10). Note that the $\Delta_{eff} = 40$ ms, b300 scan had large durations where no gradients were played out in order for it to have the same TE as the OGSE scans (i.e. the TE was limited by the OGSE scans); therefore, it was possible to increase the diffusion gradient duration from 3.9 ms (Table 5.1) to 7.4 ms and change Δ_{eff} from 40 ms to 39 ms to attain b1000 without changing any other parameters in the pulse sequence. While the FA maps colour coded with principal eigenvector direction had a similar qualitative appearance for the two scans, b300 generally resulted in smaller tracts and was more prone to false tracking than b1000. Nevertheless, tractography at b300 was capable of delineating the 8 major white matter tracts that were investigated in this study. The two scans did not have noticeably different eddy current distortions (due to effective gradient pre-compensation - see above), and the extraction of DTI values within the tracts was evaluated by applying the tract masks obtained with b300 to both co-registered scans. Over all 10 regions, $\lambda_{||}$ changes ranged from 15% to 30% and $\lambda_{\perp}$ changes ranged from -19% to 29% for b300 relative to b1000. A -19% change in $\lambda_{\perp}$ in the genu was the only negative change, and it arose due to a Gibbs ringing artefact that was most severely present in that tract. While the artifact varied with b-value, it was consistent with different Δ_{eff} at the same b-value. FA changes ranged from -4% to 10% in the 8 white matter tracts. The consistent overall increase in ADC values is likely a result of the non-Gaussian nature of diffusion in brain tissue, where ADC values decrease for increasing b-values [150], while the small changes in FA are likely due to the greater sensitivity of the lower b-value data to noise; for example, in the CST the mean signal drop compared to b0 was 13% for b300 (mean SNR =

31) and 39% for b1000 (mean SNR = 21). Nevertheless, the results suggest that the smaller b-value did not have a large impact on the data quality within the regions studied, aside from a uniform shift in ADC values (perhaps with the exception of $\lambda_\perp$ in the genu).

5.4 Results

The b = 0 s/mm^2 and b = 300 s/mm^2, as well as the diffusion parametric maps of mean diffusivity (MD, the average of the three eigenvalues) and FA, had similar qualitative appearance in the brain tissue over all four diffusion times (Fig. 5.4). Additionally, $\lambda_{||}$ and $\lambda_\perp$ appear qualitatively similar for Δ_{eff} = 4.1 ms compared to Δ_{eff} = 40 ms where difference images between the two diffusion times shows widespread increases in eigenvalues in brain tissue for the shorter diffusion time (Fig. 5.5). Even with a low b-value of 300 s/mm^2 the DTI images were of reasonable quality over much of the brain (Fig. 5.6), presumably due to the high SNR of greater than 50 (in the splenium) on b0 images for all the protocols.

In the water phantom, no significant variation of eigenvalues or FA was observed with respect to Δ_{eff}, and the very low FA of ≈ 0.03 suggests high data quality (Fig. 5.7). In contrast, statistically significant variations of $\lambda_{||}$, $\lambda_\perp$, and FA were observed in the 7 healthy volunteers. For all white matter regions aside from $\lambda_{||}$ in the bCC, both eigenvalues increased significantly at the shorter OGSE diffusion times relative to the Δ_{eff} = 40 ms PGSE scan (Fig. 5.8). Very large proportional changes in ADC occurred in the SLF, with a 35% increase in $\lambda_\perp$ and 20% increase in $\lambda_{||}$ for Δ_{eff} = 4.1 ms relative to Δ_{eff} = 40 ms (Table 5.2). The other association tracts (CG, IFO, and ILF) had much smaller increases, near 10% for $\lambda_\perp$ and 15% for $\lambda_{||}$. In the

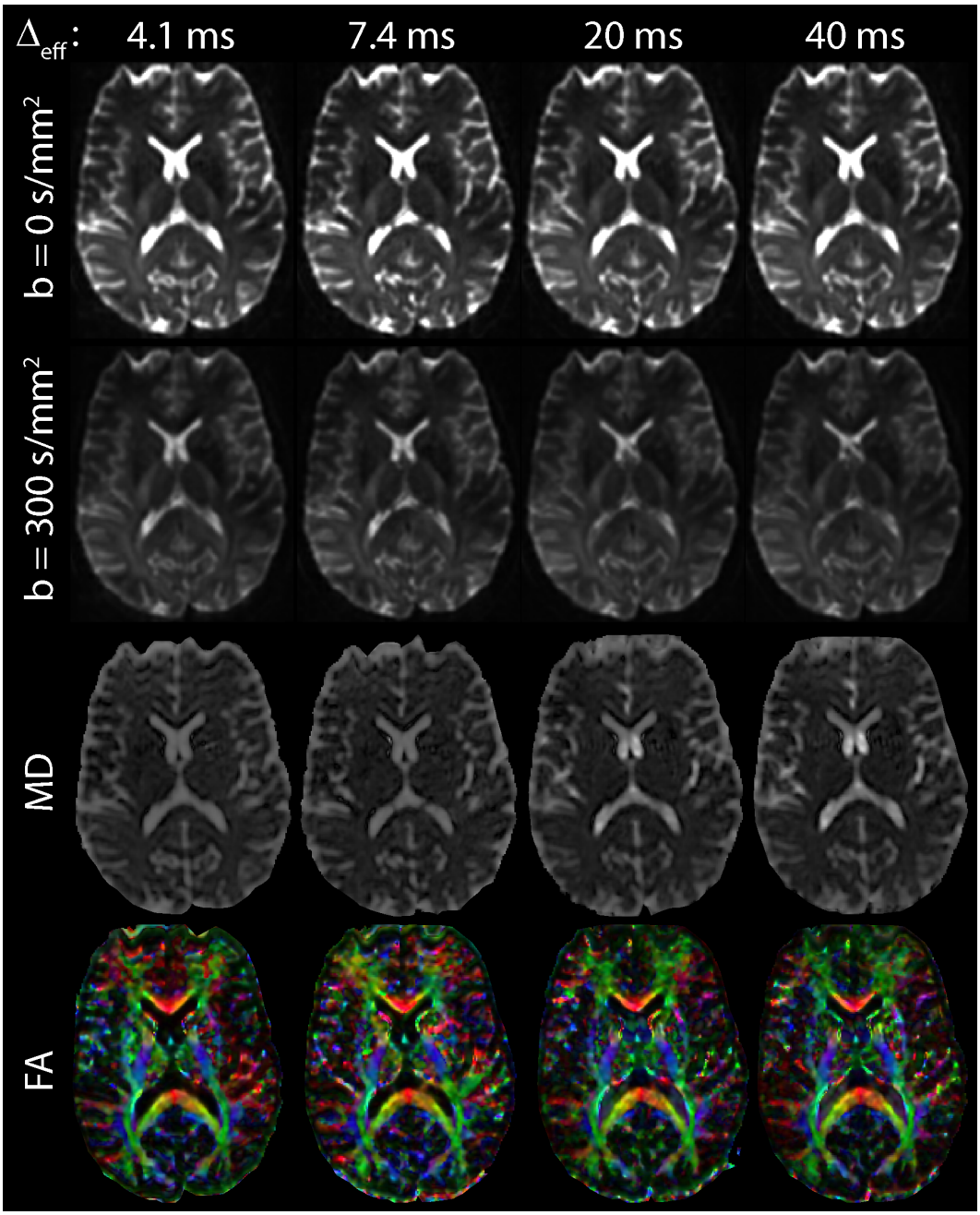

Figure 5.4: Example raw data at b = 0 s/mm^2 and 300 s/mm^2 along with MD and FA (computed from the same data) color-coded with principal eigenvector direction for one subject. The images from the four diffusion times (4.1 ms OGSE, 7.4 ms OGSE, 20 ms PGSE, and 40 ms PGSE) are displayed using the same scale.

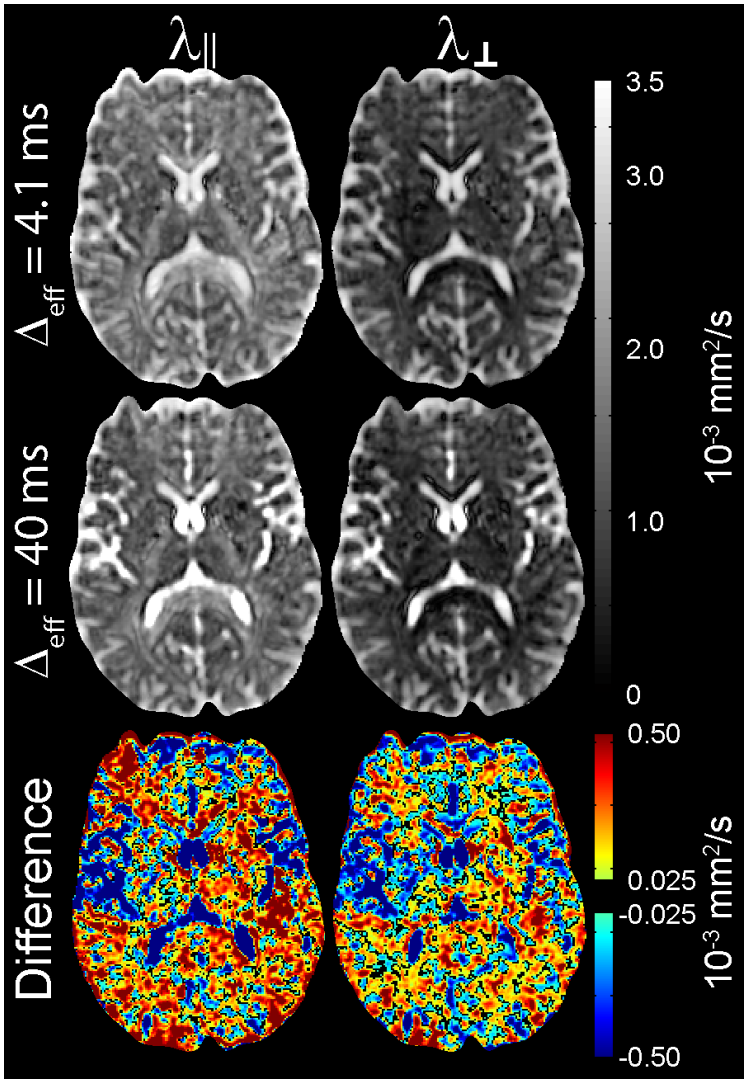

Figure 5.5: Eigenvalue maps for the shortest (4.1 ms OGSE) and longest (40 ms PGSE) diffusion times (Δ_{eff}) and their difference (OGSE 4.1 ms PGSE 40 ms). Widespread increases for both parallel and perpendicular eigenvalues are observed throughout the brain tissue as the diffusion time is reduced. Large ADC differences in the opposite direction are observed in CSF, particularly the lateral ventricles, due to elevated values (greater than free water at 37° C) in the 40 ms PGSE scan presumably due to flow.

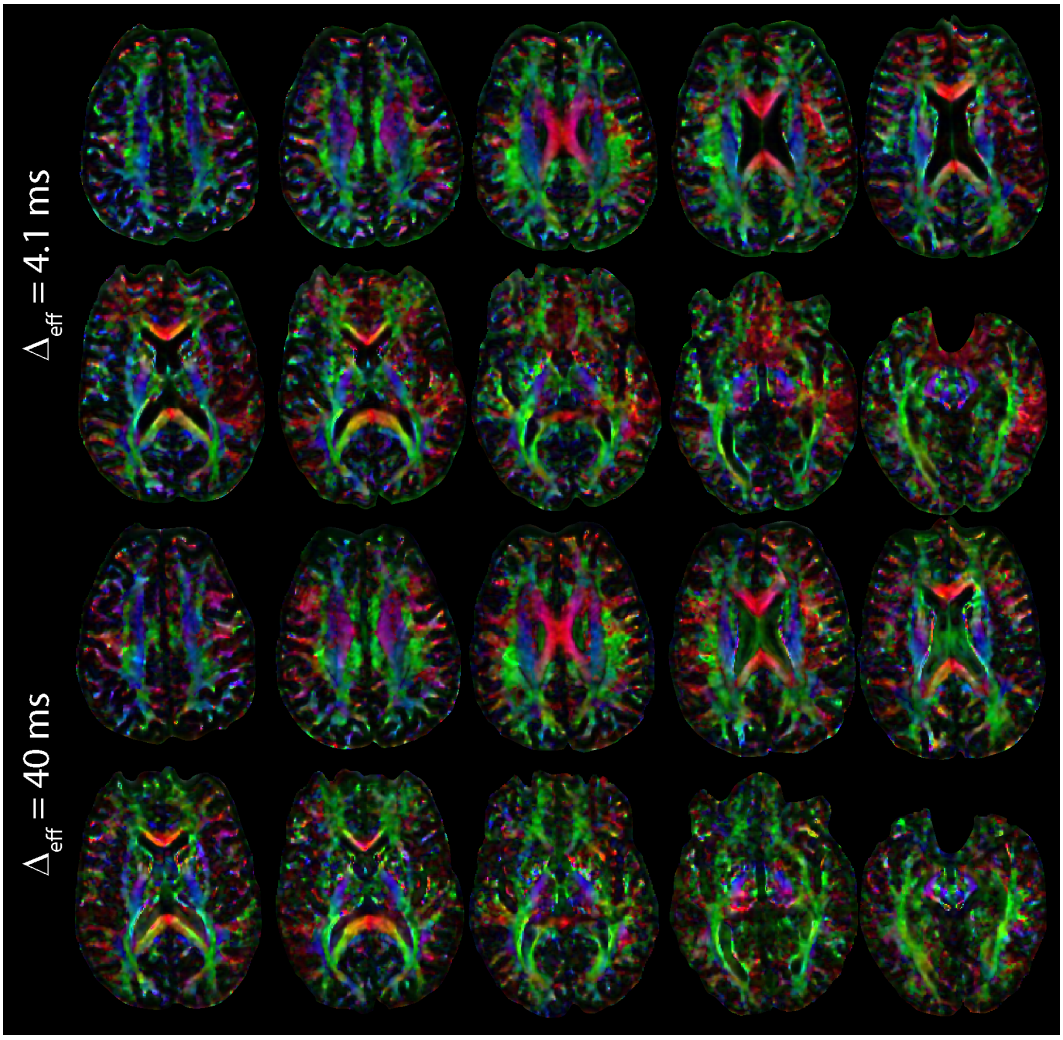

Figure 5.6: Example data showing FA color-coded with principal eigenvector direction for one subject at diffusion times of 4.1 ms (OGSE) and 40 ms (PGSE). The images are very similar, particularly within the major white matter tracts that were of interest in this work.

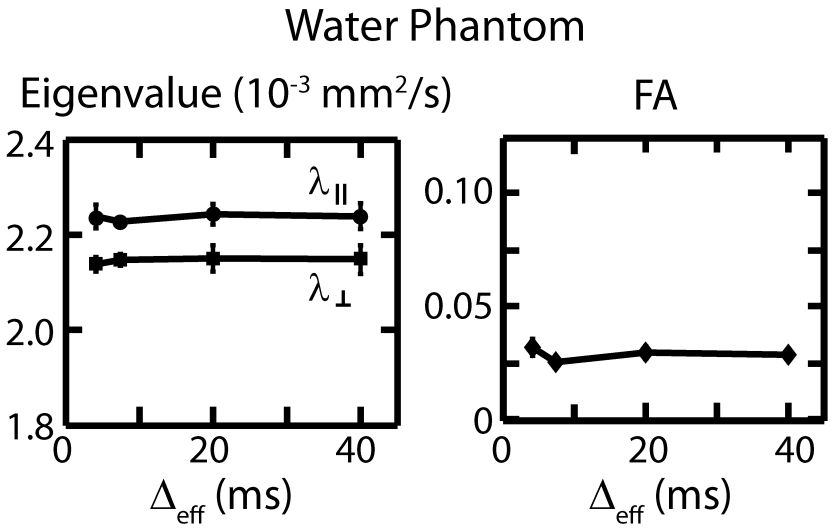

Figure 5.7: Measurements of DTI eigenvalues and FA, which are very low at ≈ 0.03, showing consistency in a $CuSO_4$ doped water phantom (N=4) at room temperature (22° C) as a function of diffusion time, Δ_{eff}.

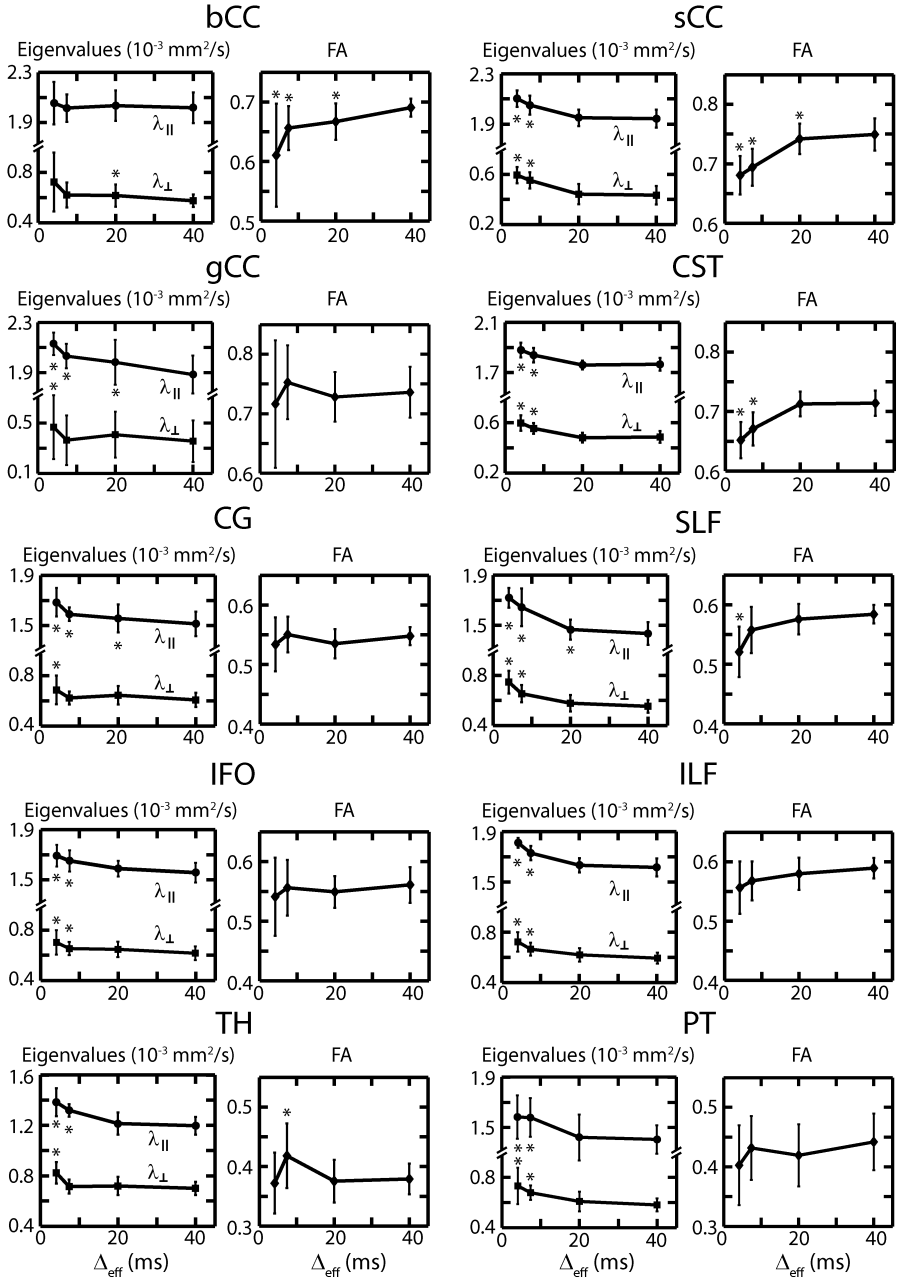

Figure 5.8: Mean ± standard deviation of DTI eigenvalues and FA in 7 healthy human volunteers as a function of diffusion time, Δ_{eff}, for Δ_{eff} values of 4.1 ms (OGSE), 7.4 ms (OGSE), 20 ms (PGSE), and 40 ms (PGSE). Statistical significant deviations from the $\Delta_{eff} = 40$ ms scan determined using a paired t-test are denoted with * ($p < 0.05$). Increasing parallel ($\lambda_{||}$) and perpendicular ($\lambda_{\perp}$) eigenvalues for reduced Δ_{eff} are observed in all white matter regions except the bCC, while decreasing FA for reduced Δ_{eff} is observed only in the bCC, sCC, CST, and SLF. In the deep grey matter (TH and PT), both eigenvalues increase with decreasing Δ_{eff}; however, there is no clear trend of FA. Region abbreviations are as in Figure 3.

Table 5.2: Mean percent change (± standard deviation) of $\lambda_{||}$, $\lambda_{\perp}$, and FA for diffusion times of 4 ms (OGSE) relative to 40 ms (PGSE) in seven healthy subjects

	$\lambda_{\|\|}$ (%)	$\lambda_{\perp}$ (%)	FA (%)
bCC	2 ± 3	24 ± 29	-12 ± 12 *
sCC	8 ± 4 *	40 ± 22 *	-9 ± 4 *
gCC	14 ± 10 *	32 ± 21 *	-3 ± 10
CST	6 ± 3 *	23 ± 9 *	-9 ± 4 *
CG	11 ± 2 *	13 ± 11 *	-3 ± 7
SLF	20 ± 4 *	35 ± 14 *	-11 ± 8 *
IFO	9 ± 6 *	14 ± 13 *	-4 ± 8
ILF	12 ± 5 *	22 ± 16 *	-6 ± 6
TH	16 ± 6 *	18 ± 10 *	-2 ± 12
PT	16 ± 8 *	26 ± 26 *	-8 ± 18

Values with statistical significance using a paired t-test ($p < 0.05$) are denoted by *.

sCC, gCC, and CST, ADC increases near 30% and 10% were observed for $\lambda_{\perp}$ and $\lambda_{||}$, respectively. Additionally, statistically significant decreases of FA to approximately -10% for diffusion times decreasing to 4.1 ms were observed in the bCC, sCC, CST, and SLF. Notably, FA reductions occurred because $\lambda_{\perp}$ increased by a larger proportion compared to $\lambda_{||}$ (Table 5.2). In the TH and PT, large increases in $\lambda_{||}$ and $\lambda_{\perp}$ of 16% and 18%, respectively (TH), and 16% and 26%, respectively (PT), were observed. The similar changes for $\lambda_{||}$ and $\lambda_{\perp}$ resulted in no clear trend in FA, and contrast the observations in half of the white matter tracts. While an FA increase was observed in the TH for $\Delta_{eff} = 7.4$ ms, the variation in FA in that region was high and more prone to error due to its low value [151].

5.5 Discussion

This work demonstrates that OGSE DTI is feasible in the adult human brain and that a b-value of 300 s/mm^2 can yield adequate diffusion tensor parameterization for major white matter tracts and deep grey matter, provided that the SNR is sufficient. This is partially enabled by a trapezoidal gradient design, for which the equation for diffusion time has been introduced here. The key finding is that the diffusion tensor in human brain depends on diffusion time for Δ_{eff} as low as 4 or 7 ms in many white matter tracts and in deep grey matter. A diffusion time of 7 ms corresponds to a characteristic diffusion length of 4.6 μm, which defines a threshold of length scales where diffusion begins to become unrestricted [152]. Given that typical axon dimensions in the human corpus callosum range from 0.5 to 3 μm, with a small number of axons as large as 10 μm [137, 138], much larger changes in eigenvalues and FA may be observed for even smaller diffusion times because many more molecules would become unrestricted. That being said, cells other than axons likely contributed to the changes observed, such as the oligodendrocytes. These findings may explain the lack of Δ_{eff}-dependence observed previously [134–136], where the diffusion measurements used a larger minimum Δ_{eff} of 8 ms. Moreover, since the diffusion gradients contained spectral components at $f = 0$, in contrast to the cosine-like gradient waveforms used in this work, the previous PGSE experiments were not performed in a high-frequency regime [153]. Notably, this work agrees with and expands upon the recent OGSE findings that suggested an increase of mean ADC in the splenium and genu of the human corpus callosum ranging from 5% to 50% for a diffusion time of 4 ms compared to 20 ms [53], compared to the increases of mean ADC found in the splenium (17%) and genu (18%) in this work (mean ADC, i.e. MD, not

shown here, but readily calculated from the eigenvalues).

The overall finding in white matter that both $\lambda_\perp$ and $\lambda_{||}$ increase and FA decreases with substantially reduced Δ_{eff} agrees with some early findings in ex-vivo nerve [130, 131] and white matter of in-vivo mouse [143]. Using bipolar gradient pulses, one early study in excised frog sciatic nerve did not observe a change in $\lambda_{||}$ as diffusion time was reduced from 28 ms to 2 ms [39]. Moreover, over the same OGSE frequency range as here (0 to 50 Hz), $\lambda_\perp$ and $\lambda_{||}$ increases of approximately 30% and 10%, respectively, and FA decreases of 5% were observed in mouse white matter *in vivo* [143], which is comparable to our findings. The Δ_{eff} for which ADC values approach an asymptotic value defines a transition to a regime where the free water diffusion distance is several times larger than the surrounding tissue microstructure. Therefore, since the FA decreased for short Δ_{eff} in the bCC, sCC, CST, and SLF, it is probable that more molecules transitioned from a restricted to unrestricted regime in the perpendicular direction compared to the parallel direction as the diffusion time was decreased, likely because the perpendicular direction had more molecules in a restricted regime to begin with. This rationale coincides with the observations of larger eigenvalue changes in the perpendicular direction compared to the parallel direction. This is appropriate given the highly anisotropic microstructural dimensions of white matter. The FA only decreased for smaller Δ_{eff} in half of the white matter tracts, as it did not significantly change in the ILF, IFO, gCC, and CG, since the proportional increases in $\lambda_\perp$ and $\lambda_{||}$ were similar. This finding suggests that the anisotropy in these tracts stems from smaller length scales than those accessed by the minimum diffusion time of 4 ms. This may suggest smaller axon diameters compared to the other tracts. This finding agrees with histological findings in the corpus callosum, where the axons in the genu are smaller than in the

body and splenium [137]. The finding of similar increases of both $\lambda_{\perp}$ and $\lambda_{||}$ with decreasing Δ_{eff} in the thalamus and putamen agrees with observations of deep grey matter in rodents [142, 143]. Thus, there were no changes of FA, which is consistent with "isotropic" length scales of microstructure (averaged over each voxel) expected in grey matter. Also, the increases in mean ADC of approximately 10 - 15% that were observed in the rodent deep grey matter for OGSE frequencies from 0 to 50 Hz are comparable to our findings.

Geometric dispersion of axons (i.e. fanning), particularly in the association tracts, may have contributed to differences in the eigenvalues and FA with Δ_{eff}. The degree of axon dispersion varies for different white matter tracts [154], but is less plausible to have affected the results for the central portions of the genu and splenium of the corpus callosum. The axon dispersion effectively creates some mixing of perpendicular and parallel diffusion. Note that crossing fibers would result in a similar effect. This may also explain why changes in parallel eigenvalues were observed here for most tracts, but not previously in an excised frog sciatic nerve which has highly ordered axons and presumably little dispersion [39]. However, excised nerves have other underlying microstructural differences (e.g. edema) relative to in vivo. Another alternative explanation is that changes in parallel eigenvalues at short diffusion times may be due to restriction effects of water in isotropic cells, such as oligodendrocytes, in the white matter. Another potential consideration in the interpretation of these results are the effects of different diffusion gradient pulse durations for the different scans (Table 5.1), where longer gradient pulses can lead to an apparent narrowing of restricted geometry and reduction of the signal drop expected from diffusion [155]. This effect has been shown to decrease with b-value, and for b-values of 1000 s/mm^2 it was negligible in a rat sciatic nerve with gradient durations ranging from 2 to 32 ms [156]. As

such, at the very low b-value of 300 s/mm^2, it is unlikely that this phenomenon affected the results.

It was evident in the processed diffusion maps that the MD and FA for water in the CSF became elevated beyond expected values and less uniform for the PGSE scans with longer Δ_{eff} (Fig. 5.4-5.6). The origin of this is likely turbulent flow of CSF, which would have long effective "diffusion" distances and, thus, only the long Δ_{eff} PGSE scans with gradient frequency components (i.e. $F(f)$ in Equation 5.2) equal to zero are sensitive to it. Moreover, the OGSE waveform used is inherently velocity-compensated [53], which reduces first order flow effects. Non-uniform MD and FA in CSF is not observed in typical PGSE DTI acquisitions because the much larger b-values (1000 s/mm^2 instead of 300 s/mm^2) are not as sensitive to flow. Averaging over all the ventricular space in all subjects, this flow-sensitivity led to higher $\lambda_\perp$ of 5% (OGSE $(2.9 \pm 0.09) \times 10^{-3}$ mm^2/s, PGSE $(3.0 \pm 0.2) \times 10^{-3}$ mm^2/s), $\lambda_{||}$ of 19% (OGSE $(3.22 \pm 0.02) \times 10^{-3}$ mm^2/s, PGSE $(3.8 \pm 0.4) \times 10^{-3}$ mm^2/s), and FA of 115% (OGSE 0.07 ± 0.02, PGSE 0.15 ± 0.03) for PGSE ($\Delta_{eff} =$ 40 ms) relative to the OGSE ($\Delta_{eff} = 4$ ms) in CSF, which is in the opposite direction to the diffusion parameter changes seen in brain tissue. The above values also demonstrate that the flow effects were highly subject dependent. Notably, diffusion time dependence of ADC in CSF with very large inter-subject variation has been mentioned for in-vivo rat brain measured with low b-value of 400 s/mm^2 [142].

The primary limitation of the OGSE methodology for human in-vivo applications is the long TE of 110 ms required to yield a minimally acceptable b-value of 300 s/mm^2 given our single axis gradient strength of 60 mT/m. At this long TE, particularly at 4.7 T, the SNR in some regions with or near high concentrations of iron was not sufficient for analysis, such as in the basal

ganglia (note: this problem will be worse at 7 T and higher). The long TE also resulted in very high CSF signal, which exacerbated Gibbs ringing and partial volume effects adjacent to the ventricles and cortex; as such this precluded tractography in small tracts near CSF, such as the fornix, and measurements in the cortex (also limited by spatial resolution).

The ability to accurately identify the onset of Δ_{eff}-dependence may provide insight into microstructure changes that occur in pathology. With recent advances in hardware enabling gradients as large as 100 or 200 mT/m on custom-built human MRI scanners, higher b-values and/or OGSE frequencies (i.e. lower diffusion times) will be achievable with OGSE. For example, a frequency as high as 100 Hz at a b-value of 1000 s/mm^2 could be possible with 200 mT/m gradients; however, slew rate constraints would have to be carefully considered. Given that the minimum diffusion time of 4 ms in this work is likely only small enough to circumvent restricted diffusion in larger axons, much larger changes in DTI parameters will likely occur with shorter minimum diffusion times (and higher frequencies), as shown in the animal models. Further, a larger range of Δ_{eff} may enable quantitative measurements such as nuclear size or surface to volume ratios in the in-vivo human brain, which may give new understanding into the mechanisms underlying tissue changes observed in disease, such as the still not well understood ADC decreases observed in ischemic stroke.

In conclusion, this work has demonstrated the feasibility of acquiring OGSE DTI in the human brain, and that DTI eigenvalues and FA depend on the diffusion time over 4 to 40 ms in both white matter tracts and deep grey matter. The ability to target different length scales via the diffusion time may improve specificity to changes in tissue microstructure associated with particular pathologies.

5.6 Additional Content to the Published Paper

5.6.1 Derivation of Diffusion Time for Trapezoidal Gradients

The first step to derive the diffusion time, Δ_{eff}, for any diffusion gradient waveform is to derive the b-value. For a trapezoidal OGSE gradient waveform $G(t)$, there are two types of diffusion "blocks" where $k(t)$ is zero at the start and end of the block: the blocks at the start and end of the gradient waveform (type A) and the blocks in the middle (type B) (Figure 5.9). For

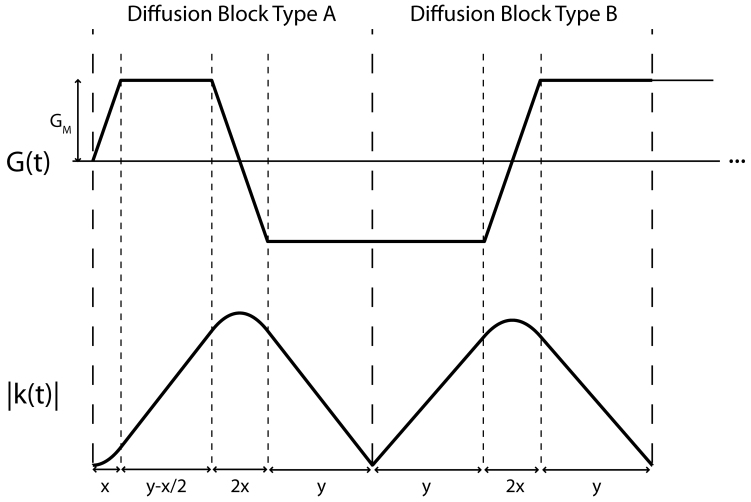

Figure 5.9: The trapezoidal OGSE gradients, $G(t)$, consist of two types of b-value generating "blocks" that have a net k-space accumulation of zero. Block type A occurs at the beginning and end of each OGSE waveform, and block type B occurs for additional periods in the middle of the waveform. The net b-value can be computed from the sum of the individual b-value contributions from each block.

each block, the analytical form of $|k(t)|$ can be computed through integration of $G(t)$ (Figure 5.9). As discussed in Section 1.5.1, $b = 4\pi^2 \int |k(t)|^2 dt$. Because $k(t)$ returns to zero at the end of each block, the net b-value is just the

sum of the contributions from each block. The contribution to b from block type A is

$$\begin{aligned} b_A =& \gamma^2 G_M^2 \left[\int_0^x \frac{t^4}{4x^2} dt + \int_0^{y-x/2} \left(t^2 + xt + \frac{x^2}{4} \right) dt + \right. \\ & \int_0^{2x} \left(\frac{t^4}{4x^2} + t^2 + y^2 - \frac{t^3}{x} - \frac{yt^2}{x} + 2yt \right) dt + \\ & \left. \int_0^{y} \left(t^2 - 2yt + y^2 \right) dt \right] \\ =& \gamma^2 G_M^2 y^2 \left(\frac{2y}{3} + 2x + \frac{4x^2}{3y} + \frac{11x^3}{40y^2} \right) \end{aligned} \tag{5.4}$$

where G_M is the maximum gradient, x is the duration required to ramp from a gradient of 0 to G_M, and y is the duraction spend at G_M (Figure 5.9). The four integrals in Equation 5.4 correspond to the initial gradient ramp up of duration x, the constant gradient at G_M for a duration $y - x/2$, the ramp down to a negative gradient of $-G_M$ for duration $2x$, and the final constant gradient portion of duration y, respectively. The contribution to the net b-value is computed similarly for block type B to obtain

$$b_B = \gamma^2 G_M^2 y^2 \left(\frac{2y}{3} + 2x + \frac{4x^2}{3y} + \frac{4x^3}{15y^2} \right) \tag{5.5}$$

For a total of N periods of oscillation, with half of the periods on each side of a 180° RF pulse, the net b-value is $b = 4b_A + (2N - 4)b_B$, which yields

$$b = 2N\gamma^2 G_M^2 y^2 \left(\frac{2y}{3} + 2x + \frac{4x^2}{3y} + \frac{4x^3}{15y^2} + \frac{x^3}{60Ny^2} \right) \tag{5.6}$$

To determine the effective diffusion time, the equation for b must be recast into a form $b = R\gamma^2 G_M^2 \delta^2 \Delta_{eff}$, where R is the number of times a bipolar gradient pair is repeated (= 2N for this case) and $\gamma\delta G_M$ is the maximum k-space value

attained by a single gradient lobe [4, 48]. Relating these requirements to Equation 5.6 yields

$$\begin{aligned} \delta &= y + x/2 \\ \Delta_{eff} &= \frac{2\delta}{3} + x - \frac{x^2}{6\delta} + \frac{x^3}{60\delta^2} + \frac{x^3}{60N\delta^2} \end{aligned} \tag{5.7}$$

For OGSE it is instructive to portray the diffusion time as a function of oscillation frequency, and by making the substitution $f = 1/4(\delta + x/2)$, Equation 5.3 is obtained.

5.6.2 Comparing b300 to b1000

The data from 2 subjects comparing eigenvalues and FA for b-values of 300 s/mm^2 and 1000 s/mm^2 (see Methods section) is shown in Figure 5.10.

5.6.3 Potential Impact of Perfusion

Because of the low b-value of 300 s/mm^2, it is possible that perfusion may have had a larger effect on results compared to DTI at a b-value of 1000 s/mm^2. However, the comparison between b300 and b1000 shown above and the high quality color coded FA maps (Figure 5.4) suggests that the impact on measured DTI parameters was low.

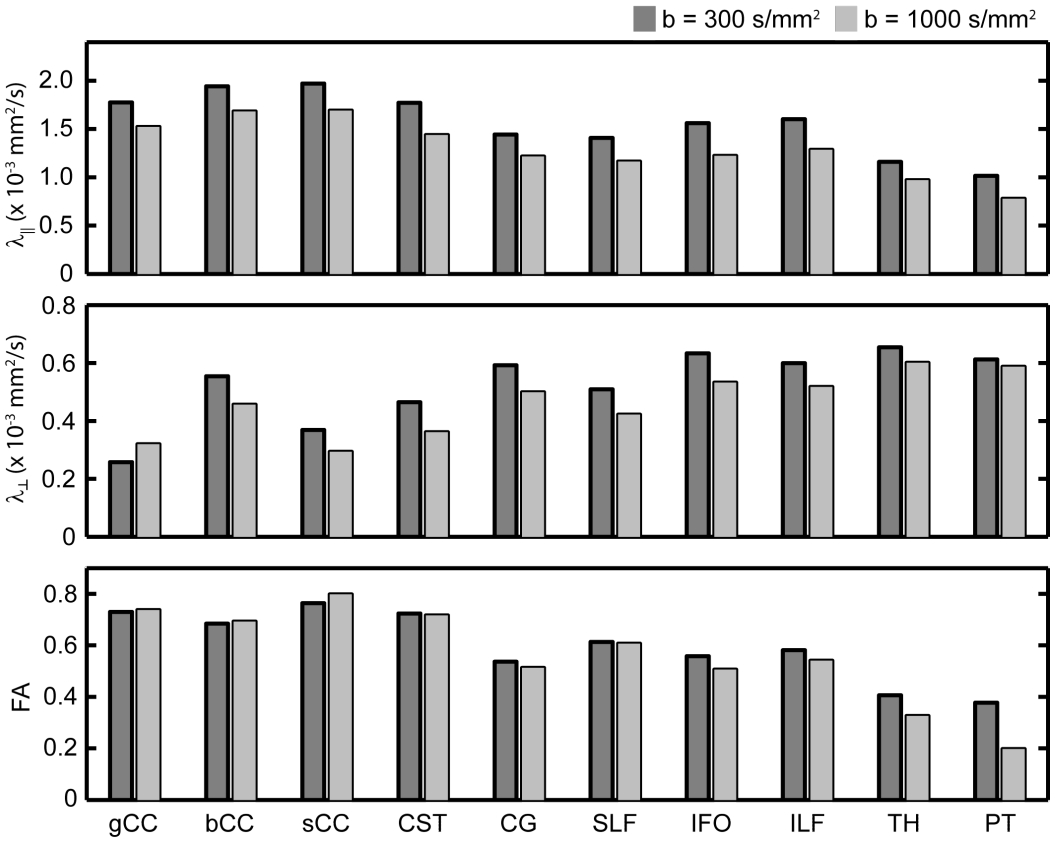

Figure 5.10: Mean values of DTI eigenvalues and FA in 2 healthy human volunteers for b values of 300 s/mm^2 and 1000 s/mm^2 ($\Delta_{eff} \approx 40$ ms for both). Generally increased eigenvalues for all regions and increased FA in gray matter is observed for b = 300 s/mm^2 compared to 1000 s/mm^2. Region abbreviations are as in Figure 3.

Chapter 6

Oscillating Gradient Spin-Echo (OGSE) Diffusion Tensor Imaging Yields Mechanistic Insights in Acute Human Stroke

6.1 Introduction

The measurement of mean apparent diffusion coefficients of water (MD) using diffusion weighted MRI is a sensitive marker of acute ischemic attack. Although it was discovered 24 years ago that the MD markedly decreases in the infarct within minutes after an ischemic event [13], the underlying biophysical mechanisms are still not well understood. Upon ischemia, glucose and oxygen deprivation results in the failure of Na^+/K^+ ion pumps in cell membranes, leading to an osmotic shift of water and swelling (i.e. cytotoxic edema). Accordingly, the long-standing hypothesis is that this shift of water from highly diffusive extracellular space to a more restrictive intracellular space is the underlying mechanism for the MD changes [157–159]. However,

the models based on cell swelling alone cannot explain that the *intracellular* MD of metabolites decreases after global ischemia, which has been determined from diffusion weighted spectroscopy in rat brain for many different intracellular metabolites including choline, creatine, N-acetylaspartate (NAA), taurine, glutamate, myo-inositol, and Cs^+ [160–164]. Similar findings have been observed in the acute stage of stroke in human brain for NAA, creatine, and choline [165, 166]. Recent simulations and pre-clinical models implicate that cytotoxic edema causes the formation of enlargements and constrictions in neuronal membranes (i.e. "beading"), which introduces barriers along neural fibers that restrict water mobility and may account for the MD decreases observed in acute stroke (Figure 6.1) [167]. Beading is a generalized property of

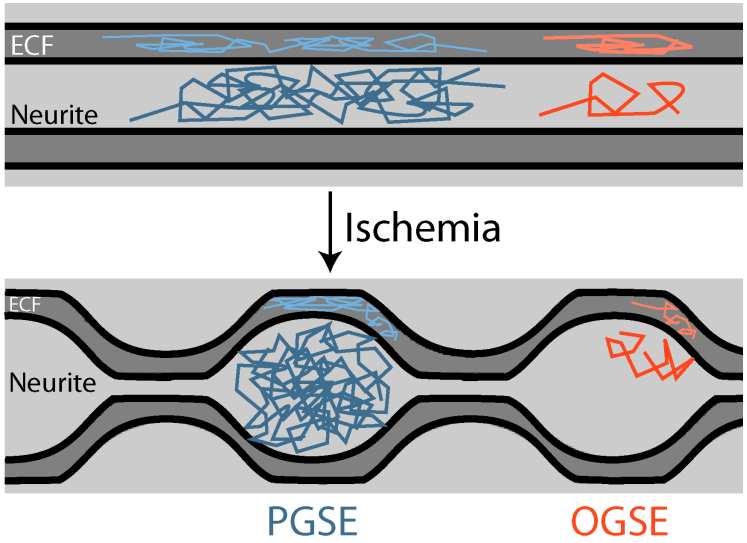

Figure 6.1: Upon ischemia, neurites (e.g. axons - depicted above, dendrites) swell non-uniformly (i.e. "beading"). This inhibits the ability of water to diffuse along the length of the axon and increases tortuosity in the extracellular fluid (ECF), making it a plausible mechanism for the marked decrease of the overall apparent diffusion coefficient (MD) of water within a lesion after stroke observed using diffusion-weighted MRI.

axons and dendrites that occurs after injury such as depolarization or stress [168, 169]. This beading hypothesis has yet to be evaluated in human acute ischemic stroke given the technical limitations of routine diffusion MRI.

The beading in white matter occurs with length scales on the order of the axon diameters, and adjusting the length scale sensitivity of the diffusion MRI experiment may shed light on changes that occur upon stroke. Different microstructure length scales can be probed by varying the "diffusion time", Δ_{eff}. If, during the diffusion time, most molecules do not travel far enough to interact with any obstacles, the measured ADC is equivalent to the intrinsic diffusion coefficient [42, 43]. For increasing diffusion times, the molecules interact with more barriers and the ADC decreases. As described in Chapter 5, this has been observed in several ex vivo investigations using strong gradient inserts, where increases in MD and decreases in anisotropy were observed for shorter Δ_{eff} (< 5 ms) [39, 130–132]. The oscillating gradient spin-echo (OGSE) method enables shorter Δ_{eff} compared to PGSE, which grants sensitivity to diffusion restriction/hindrance over smaller length scales [4–6] (Figure 6.1). In a rat model of global ischemia, the mean ADC decrease in cortical grey matter observed after a global ischemic event was approximately 50% lower for a Δ_{eff} of 0.5 ms compared to 9.8 ms, which suggests that the MD decreases observed during ischemia are due to structural changes (i.e. not permeability or viscosity changes) because moving to shorter length scales can mitigate the MD decrease [142, 170]. OGSE has only recently been applied to healthy human brain [53, 171] (Chapter 5) where, similar to the early ex vivo work, increases in MD and decreases in anisotropy were observed for shorter Δ_{eff}. However, OGSE has not yet been applied to human stroke and OGSE diffusion tensor imaging (DTI), which may shed light on directional dependencies of the length scales of diffusion, has been applied neither for the study of human nor animal ischemia. This work aims to determine the dependencies of DTI eigenvalues and anisotropy on Δ_{eff} in human stroke, and test whether any changes are consistent with cellular beading using simulations.

6.2 Methods

6.2.1 Subjects

Participants included 11 male patients recently diagnosed with ischemic stroke (age 51 ± 12 years, range 25-67 years), who were recruited from the University of Alberta Hospital stroke unit. The patients were scanned 46 ± 31 hr after symptom onset (range 13-106 hr), National Institute of Health Stroke Scale (NIHSS) Scores at presentation were 4.0 ± 2.5 (range 1-10), and the mean total lesion volume was 9 ± 20 mL (0.2 - 69 mL). Lesions in white and grey matter were outlined with separate regions of interest (ROI), and a total of 20 lesions (9 white matter; 6 cortical grey matter, 5 deep grey matter) were located in vascular territories of the middle cerebral artery (9), basilar artery (2), lateral lenticulostriate arteries (2), posterior cerebral artery (2), and anterior choroidal artery (2).

6.2.2 MRI Acquisition

MRI acquisition was performed in one scan session on a Varian Unity Inova 4.7 T. A b = 1000 s/mm^2 (b1000) DWI protocol with 3 orthogonal diffusion encoding directions was used to locate the lesion(s). The single-shot EPI parameters were: TR = 10 s; TE = 60 ms; FOV = 24 x 19 cm^2; 1.5 mm x 1.5 mm acquired in-plane resolution (zero-filled to 0.75 mm x 0.75 mm resolution); 80 slices, thickness 1.5 mm; 4 averages; R=2 GRAPPA; scan time 3.5 min. Two DTI protocols were acquired using Δ_{eff} = 4.1 ms (OGSE 50 Hz) and 40 ms (PGSE) with identical parameters as in Chapter 5 (Figure 6.2). Both protocols acquired a 5 cm slab that was centered on the lesion, and used b = 300 s/mm^2 with 6 diffusion encoding directions. Both scans used a

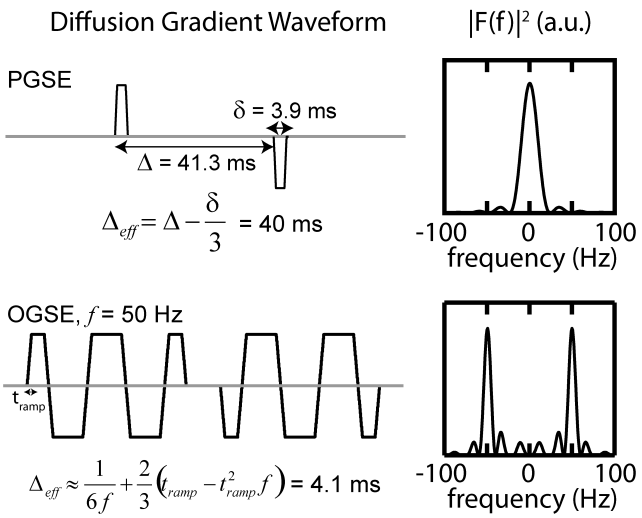

Figure 6.2: Diffusion gradient waveforms and gradient modulation power spectra, $|F(f)|^2$, for PGSE and OGSE. The polarity of the second gradient waveform has been reversed from what is actually played out to account for the 180° RF pulse that is between the gradient waveforms (RF pulses omitted from diagrams). The relationship for Δ_{eff} depends on the gradient shape, and is shown below each case.

maximum gradient amplitude of 57.5 mT/m per channel. Other single-shot EPI imaging parameters were: TR = 12.5 s; TE = 110 ms; FOV = 24 x 24 cm^2; 2 mm x 2 mm acquired in-plane resolution (zero-filled to 1 mm x 1 mm resolution); 20 slices, thickness 2.5 mm; 6 averages; R=2 GRAPPA; scan time 5 min per protocol. Confounding effects from eddy currents were mitigated using a combination of gradient pre-compensation and post-acquisition phase correction, as in previous work (Chapter 5).

6.2.3 MRI Analysis

For each individual, motion between the OGSE and PGSE scans was corrected using rigid body translations and rotations [126] with an autocorrelation cost function. The b1000 DWI scan was re-sampled to be the same resolution as the OGSE and PGSE scans, and aligned to them using the same rigid body motion correction algorithm. The lesions were outlined on the b1000

DWI on all slices where they were visible using a semi-automated region-of-interest (ROI) tool that defines the boundary of the ROI where the DWI signal intensity is halfway between a value manually selected in the lesion and a value in nearby healthy tissue (Appendix B). ROIs were also manually drawn in the contralateral healthy tissue. Portions of the lesions or contralateral healthy tissue within grey (GM) or white matter (WM) were differentiated with the aid of the b1000 DWI, which had strong grey-white matter contrast, and PGSE fractional anisotropy (FA) maps.

DTI eigenvalues, MD, and FA were computed for the PGSE and OGSE scans using ExploreDTI v4.8.3 [76]. The regions identified using the DWI scan were applied to the PGSE and OGSE DTI parameter maps to measure MD in the GM lesions (n=11) and parallel ($\lambda_{||}$) and perpendicular ($\lambda_{\perp}$) eigenvalues and MD in the WM lesions (n=9). Statistical significance was evaluated using paired t-tests for OGSE relative to PGSE ($P < 0.01$).

6.2.4 Monte Carlo Diffusion Simulations

Simulations of the diffusion weighted MRI experiment for various geometrical surfaces [167] were performed using the Camino diffusion toolkit [172] [1]. Three-dimensional mesh surfaces were generated in Matlab and consisted of cylinders arranged in a hexagonal lattice with a uniform initial radius and intracellular volume fraction. Beaded axons were modeled as axisymmetric three-dimensional unduloids with a degree of undulation (A) scaling from 0 (cylinder) to 1 [167].

The dynamics of the simulation consisted of a random walk of 20000 magnetic spins. The initial position was random but consistent with the intra-

[1] All simulations were performed by collaborator Matthew Budde, Assistant Professor, Neurosurgery, Medical College of Wisconsin.

and extracellular volume fractions of the geometrical surfaces. At each of 1000 time-points, spins moved a distance equivalent to a "free" diffusivity of 1.7×10^{-3} mm^2/s, which was chosen from the $\lambda_{||}$ measured in healthy white matter tissue using OGSE. Boundaries were impermeable, and spins that intersected a boundary were elastically reflected. The diffusion gradient waveforms replicated those of the in vivo experiments, including identical diffusion gradient waveforms, diffusion times, and b-values. The spin phase was updated at each time step with the total signal equal to the phase-sensitive average of all spins at the final time-point. The effects of T_2 relaxation were ignored.

To fully investigate the effects of axonal diameter, volume fractions, and beading amplitude on the resulting DTI measures and differences between OGSE and PGSE, simulations were performed using all possible combinations of initial diameters of $\{1, 2, 3, 4, 5, 6, 7, 8\}$ μm, volume fractions of $\{0.4, 0.5, 0.6, 0.7, 0.79\}$, and beading amplitudes of $\{0, 0.2, 0.4, 0.6, 0.73\}$. The resultant DTI eigenvalues were interpolated to 100 points for each of the 3 independent variables using cubic spline interpolation. The simulation parameters that resulted in DTI eigenvalue percent changes (pre-beading versus post-beading) with the smallest root mean squared difference from the experimental results was determined from all possible combinations of the interpolated simulation parameters.

6.3 Results

DWI lesions were clearly observed in the b1000 scans, as in the examples in Figure 6.3; however, while the lesions are hypointense in the PGSE MD maps, they are not as clearly visible in the OGSE MD maps.

Over all the subjects, this translated to very little MD change in white

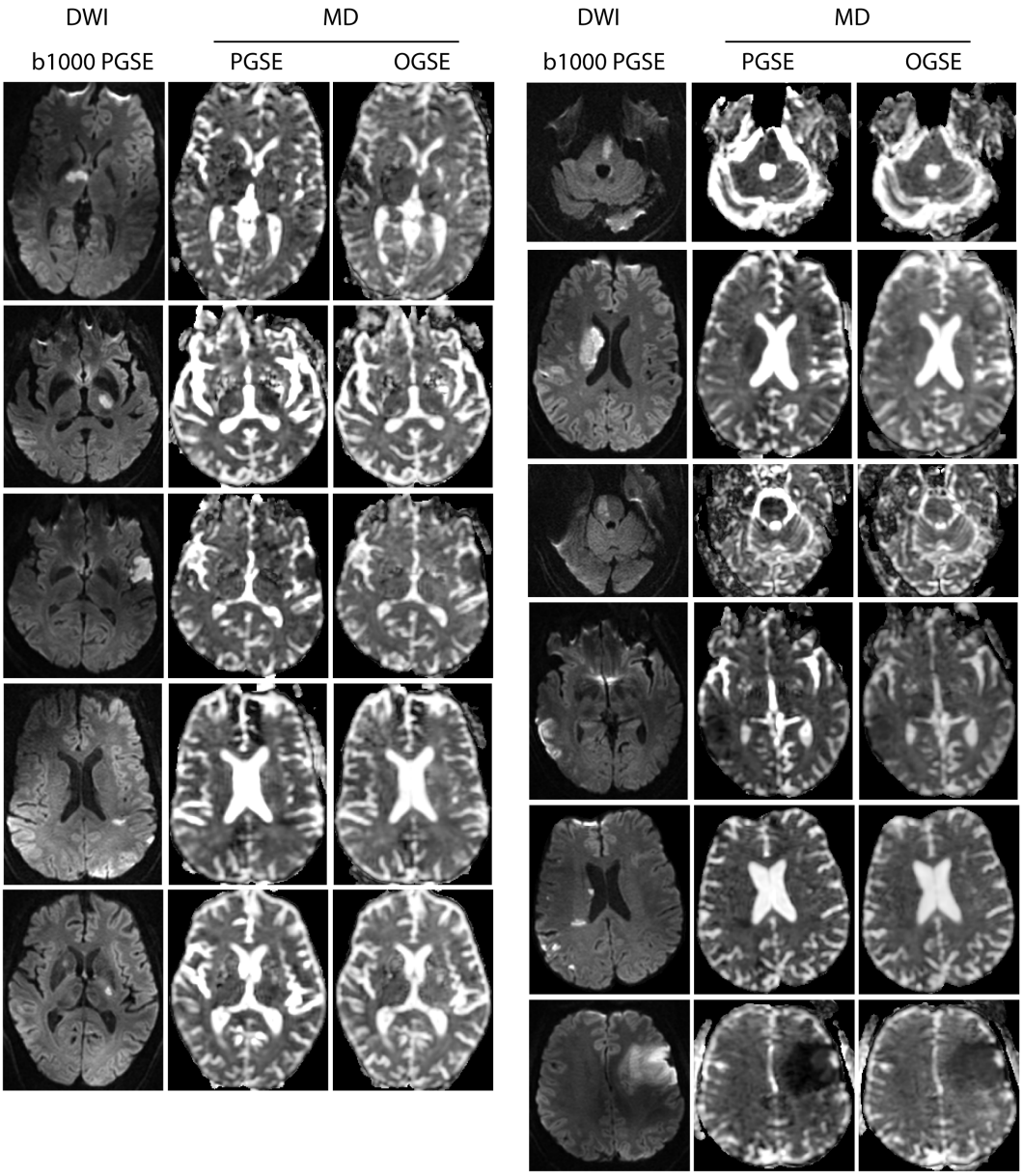

Figure 6.3: Hyper-intense lesions were observed in a standard DWI scan (b1000). While the MD was hypo-intense in the lesions for PGSE, the lesions show far less diffusion change in the OGSE MD maps acquired with much shorter diffusion time.

matter lesions for OGSE ($-8 \pm 18\%$) compared to the normal decrease of $-37 \pm 15\%$ for PGSE (Figure 6.4a). Moreover, $\lambda_{||}$ and $\lambda_{\perp}$ were reduced in the lesions compared to healthy tissue for PGSE ($\lambda_{||}$: $-42 \pm 12\%$; $\lambda_{\perp}$: $-30 \pm 21\%$), which is typical, but notably, $\lambda_{||}$ did not reduce nearly as much for OGSE ($-22 \pm 12\%$), while $\lambda_{\perp}$ even increased ($7 \pm 26\%$) (Figure 6.4b). In the grey matter, a similar MD decrease in the lesion was observed for both PGSE ($-32 \pm 18\%$) and OGSE ($-25 \pm 12\%$).

The Monte Carlo simulations performed at a range of axonal diameters, volume fractions, and beading amplitudes provides insight into the dependencies of OGSE and PGSE measurements (Figure 6.5). In general, volume fraction had little impact on OGSE-PGSE differences for $\lambda_{||}$, but higher VF decreased $\lambda_{\perp}$. Alternatively, increasing the beading amplitude resulted in decreased $\lambda_{||}$ and increased $\lambda_{\perp}$. There was little difference between OGSE and PGSE for axon diameters smaller than 3 μm, which is a limitation of the experimental diffusion time (shorter diffusion times would increase the differences for smaller axons).

A simulated cellular swelling from an axonal volume fraction of 0.58 to 0.74 (similar to expected from edema) along with beading of the axonal membrane (amplitude 0.6) for 5.5 μm diameter axons most closely approximated both the direction and percentage change in the *in vivo* DTI parameters (Figure 6.6a). The simulations with swelling or beading alone help to expose the mechanisms behind the diffusion changes (Figure 6.6b). The experimental finding of a smaller decrease in $\lambda_{||}$ for OGSE compared to PGSE in white matter was only mirrored in the simulations when beading was present (with or without swelling). In contrast, the experimental finding of a small increase in $\lambda_{\perp}$ for OGSE compared to a decrease for PGSE was only mirrored in the simulations when both beading and swelling occurred. The root

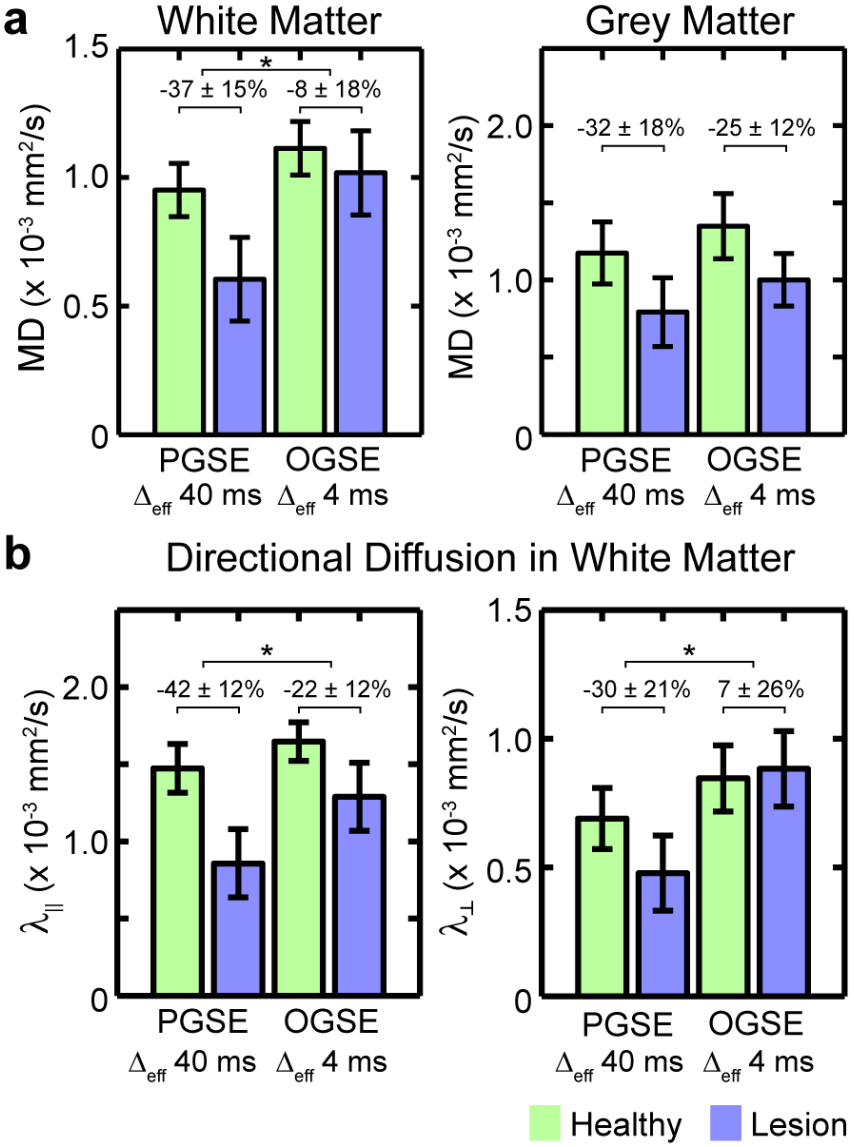

Figure 6.4: (a) The MD reductions in white matter lesions (n = 9) observed using PGSE was almost eliminated when using OGSE, but the MD reductions in grey matter lesions (n = 11) were similar for both acquisitions. (b) More insight can be gained from the directional ADCs in white matter, where a smaller decrease (lesion versus healthy) in parallel diffusivity was observed for OGSE compared to PGSE, while the change of perpendicular diffusivity was opposite for OGSE compared to PGSE. The average percent changes are were compared using a paired students t-test (* $P < 0.01$).

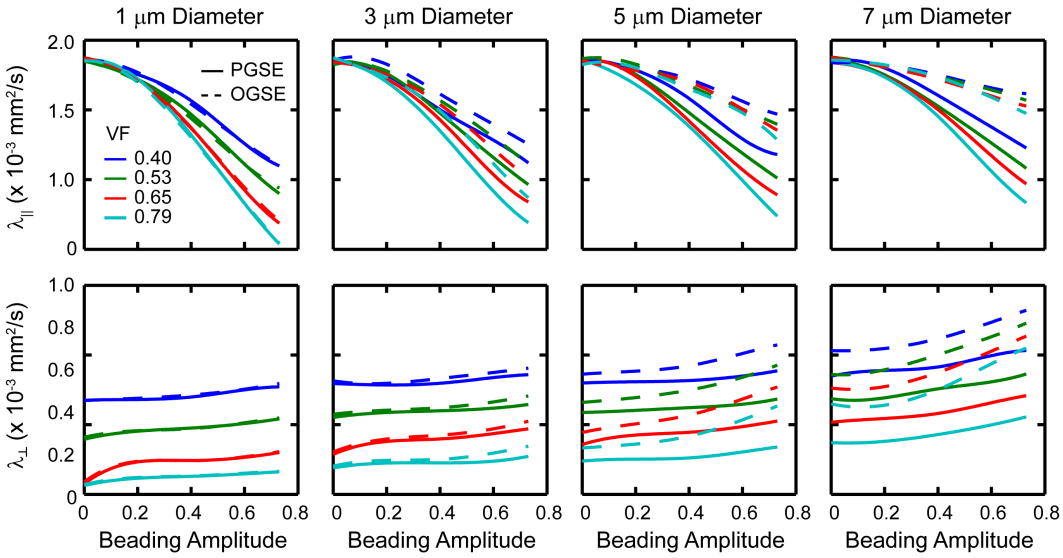

Figure 6.5: Parallel ($\lambda_{||}$) and perpendicular ($\lambda_{\perp}$) apparent diffusion coefficients obtained from Monte Carlo simulations of diffusion tensor MRI of beaded cylinders for a range of axonal diameters, beading amplitudes, and axonal volume fractions (VF) for long diffusion time PGSE (solid lines) and short diffusion time OGSE (dashed lines). Volume fraction had little impact on OGSE-PGSE differences for $\lambda_{||}$, but higher VF decreased $\lambda_{\perp}$. Additionally, increasing beading amplitude decreased $\lambda_{||}$ and increased $\lambda_{\perp}$. There was little difference between OGSE and PGSE for axon diameters smaller than 3 μm, which is a limitation of the experimental diffusion time (shorter diffusion times would increase the differences for smaller axons).

mean squared difference between simulation and experiment for the ischemic to healthy tissue percent-changes (over both $\lambda_{\perp}$ and $\lambda_{||}$ for each of PGSE and OGSE) was a smoothly varying function with a well-defined global minimum at the aforementioned "best-fit" simulation parameters with no other local minimums (Figure 6.7).

6.4 Discussion

In healthy tissue, eigenvalues and MD were larger for OGSE compared to PGSE, which agrees with previous in-vivo [53, 171] and rodent [142, 143] work. Only one other study has investigated ADC changes during ischemia

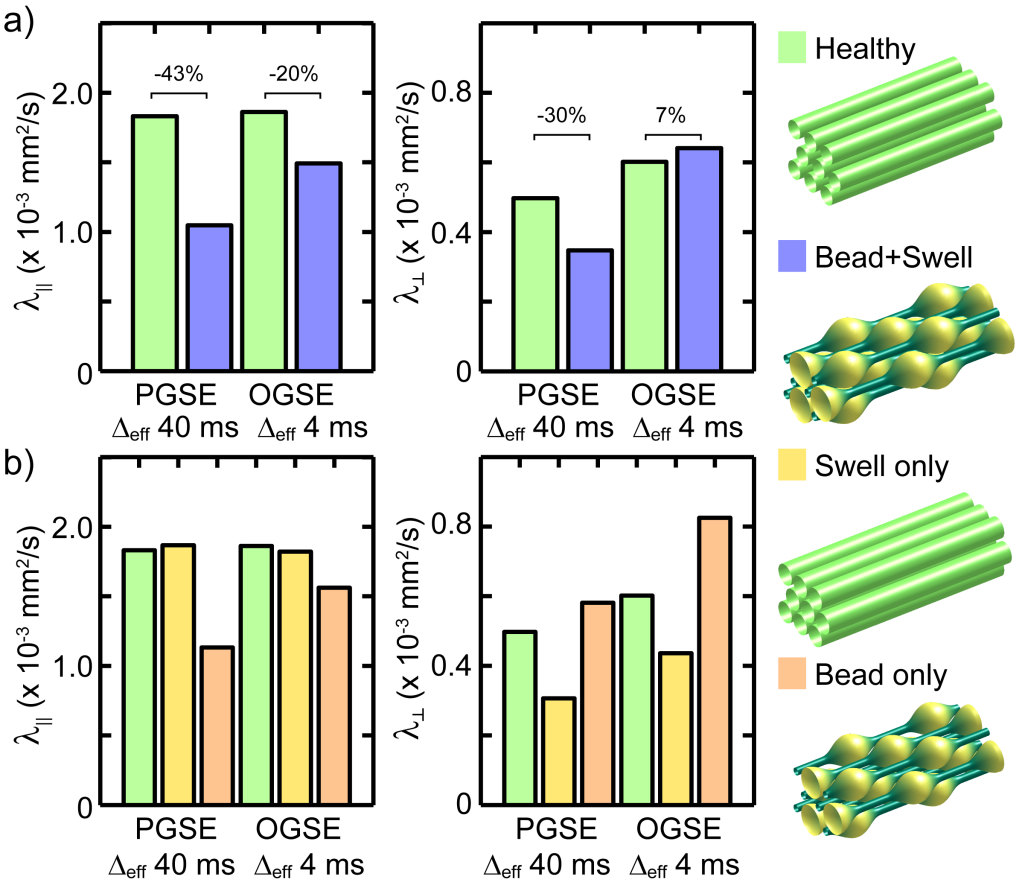

Figure 6.6: (a) In Monte Carlo simulations of beaded cylinders, changes in parallel ($\lambda_{||}$) and perpendicular ($\lambda_{\perp}$) diffusivities mirrored the in vivo white matter results in Figure 6.4b when beading (amplitude 0.6) and swelling from an axon volume fraction of 0.58 to 0.74 occurred in 5.5 μm diameter axons. (b) Swelling or beading alone could not replicate the experimental results because swelling alone had no affect on $\lambda_{||}$ for both OGSE and PGSE and had the wrong direction of change for OGSE $\lambda_{\perp}$, while beading alone resulted in the wrong direction of change for PGSE $\lambda_{\perp}$.

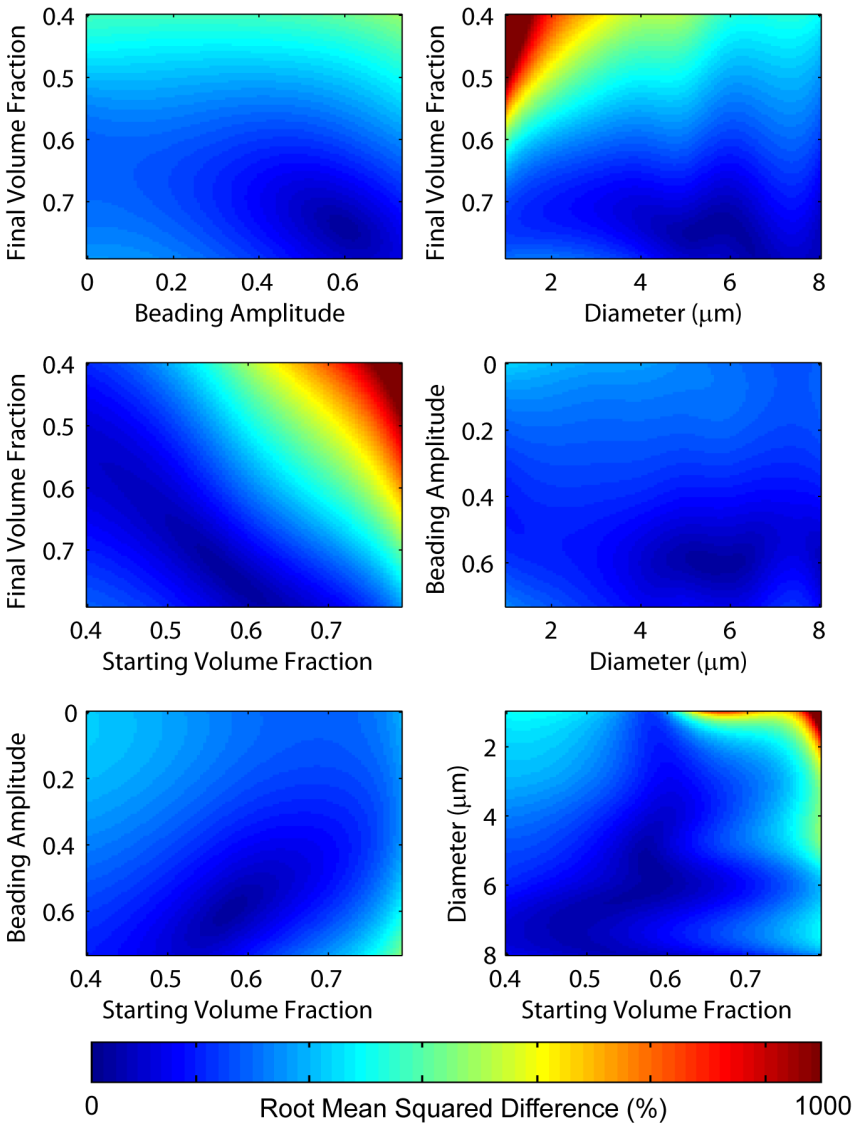

Figure 6.7: The determination of the simulation parameters (axonal volume fraction before stroke, axonal volume fraction after stroke, axon diameter, and beading amplitude) that resulted in DTI eigenvalue changes that most closely matched the experimental findings were determined by finding the set of parameters with the smallest root mean squared difference between experiment and simulation. The root mean squared difference surfaces for the 6 possible combinations of the 4 fitted parameters is shown, where a smoothly varying function with a well-defined global minimum is observed in all cases.

using OGSE, where the MD was measured in the cortex of rats before and after death (i.e. global ischemia) for OGSE frequencies ranging from 0 to 500 Hz [142]. Smaller ischemic decreases in MD were observed for larger OGSE frequencies (17% decrease at 500 Hz ($\Delta_{eff} \approx 0.5ms$) compared to 32% at 0 Hz), which was not observed with statistical significance in the grey matter in this work. This is likely due to the much smaller OGSE frequency of 50 Hz used here and the fact that much shorter diffusion times (i.e. higher frequencies) would be needed to circumvent beading in dendrites that are smaller than axons. Notably, the MD decrease in the aforementioned rat study was 27% at 50 Hz, which is similar to the 32% decrease they observed at 0 Hz. In addition, the difference could have stemmed from anatomical differences between human and rat, or the difference between an in-vivo system and postmortem model.

This is the first OGSE study of ischemic white matter. Only a small difference between OGSE and PGSE is observed in the healthy tissue. The smaller decrease of $\lambda_{||}$ in the lesion for OGSE vs PGSE, along with evidence from measurements of diffusion kurtosis [173], suggests the introduction of parallel barriers upon ischemia (i.e. greater reductions at long diffusion times). As shown by the simulations, neurite beading is sufficient to create parallel barriers that result in $\lambda_{||}$ changes that mirror the experimental results. In addition, the simulations suggest that the increase in $\lambda_{\perp}$ for OGSE stems from beading, which likely stems from fewer molecules interacting with the walls in the beads (because they have a higher effective diameter than the healthy axons) for the short diffusion time OGSE. In contrast, the simulations suggest that the decrease in $\lambda_{\perp}$ for PGSE stems from cell swelling, which likely results from the reduced diffusion lengths and increased tortuosity in the ECF. Since neither the decreases in $\lambda_{||}$ for OGSE and PGSE nor the increase in $\lambda_{\perp}$ for OGSE was replicated with swelling alone (Figure 6.6), these findings argue

against the long-held belief that swelling alone is responsible for MD decreases in stroke [13]. Rather, the results implicate beading as the primary source of MD decreases. These findings also argue against the MD decreases stemming from changes in intracellular viscosity or cytoplasmic streaming because the diffusion measurements would not depend on the diffusion time.

Interestingly, while we did not observe a statistically different MD in the grey matter for OGSE compared to PGSE, the changes of MD in white matter are similar to the changes in MD observed in the cortical grey matter in the global ischemia rat study [142]. It is likely that with shorter diffusion times where diffusion distances are on the order of the size of dendrites, human grey matter would show similar behaviour. However, partial volume effects may have had a larger effect in cortical GM (5 of the 9 GM data points) due to its proximity to cerebrospinal fluid, and the SNR was low in some deep GM regions.

The mean diameter of axons in the human corpus callosum are around 1-2 μm with decreasing populations for sizes increasing to 10 μm [137]. However, the in vivo findings were most closely replicated by simulations with 5.5 μm diameter axons because the OGSE parameters only provide sensitivity to the largest axons (as shown in Figure 6.5). Notably, though, even a small number of large axons may significantly contribute to the MRI signal given that the volume scales with the square of diameter. While infeasible with most current human MRI systems, shorter diffusion times would improve sensitivity to smaller axons and dendrites.

The primary limitation of the OGSE methodology for human in-vivo applications is the long TE of 110 ms required. At this long TE, particularly at 4.7T, the SNR is low in regions with high concentrations of iron (e.g. basal ganglia). The long TE also resulted in very high CSF signal, which exacerbated

Gibbs ringing and partial volume effects adjacent to the ventricles and cortex. The high CSF signal could potentially be reduced by using a lower TR, as in Chapter 4; however, this would decrease the tissue signal and require more averages and longer scan times. The b-value increase suggested in Chapter 4 is not feasible here where the OGSE waveforms can only achieve even the modest b-value of 300 s/mm^2. Also, geometric dispersion (i.e. fanning) of axons and crossing fibers may have contributed to differences in the eigenvalues and FA between PGSE and OGSE in the white matter. These phenomena effectively create some mixing of perpendicular and parallel diffusion; thus, the changes in perpendicular diffusivity may have resulted from some locally parallel changes erroneously being mapped to the perpendicular eigenvalues or vice versa. In addition, non-axonal features of white matter, such as glial cells, were not modeled and may have also contributed to the diffusion measures.

Recent studies using in vivo microscopy have demonstrated that beading as a consequence of acute ischemia is caused by the combination of oxygen-glucose deprivation (OGD) with depolarization [169]. Since transient MD changes of 30% to 40% and cellular swelling have been observed with non-ischemic spreading depression (SD) [174], these results implicate that transient reversible beading may underpin SD or acute neurological injuries where MD decreases and/or cellular swelling is observed.

In conclusion, OGSE has demonstrated diffusion time dependencies of MD and parallel and perpendicular diffusivities white matter for the first time in human acute ischemic stroke. Simulations of cellular beading showed diffusion tensor changes nearly identical to the in vivo results for physiologically plausible parameters. Accordingly, these results support the hypothesis that MD reductions during stroke are primarily due to cellular beading.

6.5 Collaborators

Patient recruitment was supported by Mahesh Kate (Neurology; University of Alberta), Laura Gioia (Neurology; University of Alberta), Ken Butcher (Neurology; University of Alberta), and Derek Emery (Radiology; University of Alberta). The simulations were performed by Matthew Budde (Neurosurgery, Medical College of Wisconsin).

Chapter 7

High Resolution Diffusion Weighted Imaging of Stroke

7.1 Introduction

Diffusion weighted imaging (DWI) is the gold standard for the detection of the infarct core after ischemic stroke. Current DWI protocols for stroke strive to collect the images as fast as possible (≈1 min) by using thick slices of 5 - 7 mm, often with a gap of up to 2 mm. While the in-plane resolution is generally higher (e.g. 1.7×1.7 mm^2), spatial averaging caused by thick slices reduces the visibility of small lesions. In acute ischemic stroke, 2-3x as many lesion have been observed for a slice thickness of 3.5 mm compared to 7 mm [14], and 20-30% of transient ischemic attack (TIA) patients have lesions detected on thin-slice DWI (3 mm) when no lesions are detected on the thick slices (6 mm) [15, 16]. The latter finding has large implications for patient care, since according to the 2009 American Heart Association guidelines any suspected TIA patient with a DWI lesion of any size is now diagnosed with acute stroke [175].

While increased detection of small lesions has been reported by the

above studies when the slice thickness was decreased, little insight into the differences in quantitative metrics like lesion volume or mean diffusivity (MD) has been provided. A number of studies have implicated that lesion volume [176–181] and MD [177, 179, 181] correlate with patient outcomes; however, it has been reported that neither estimated volumes nor MD provide predictive value beyond clinical variables (e.g. stroke symptom severity and age) [182, 183]. A low added predictive value of quantitative DWI measurements may be due to poor resolution (i.e. thick slices). For example, when only a portion of the ischemic core of a stroke resides within long and narrow voxels, the estimate of lesion volume can either be increased or decreased with respect to the true volume depending on whether the voxels are included or not (Figure 7.1). Accordingly, using a large slice thickness increases the uncertainty of an estimate of lesion volume. The fractional uncertainty in lesion volume can by estimated from the number of voxels that contain both infarct and healthy tissue multiplied by the proportion of volume of a single voxel that needs to be filled by infarct for an observable MD decrease (ν_{see}). This leads to an uncertainty of

$$\sigma_V \approx \nu_{see} \frac{w}{\sqrt[3]{V}} \tag{7.1}$$

where w is the thickness of the slice, and V is the true volume of the lesion. In addition, the inclusion of voxels only partially filled with infarcted tissue generally results in an increase of MD measurement since non-compromised tissue would be included in some voxels (Figure 7.1).

The aim of this work was to investigate the uncertainty in lesion volume and MD measurement error by performing DWI in acute and sub-acute stroke patients using a 1.5 x 1.5 x 1.5 mm^3 resolution with no gap between slices (3.4 mm^3) compared to a typical resolution of 1.7 x 1.7 x 5 mm^3 with a 1 mm gap between slices (17.3 mm^3).

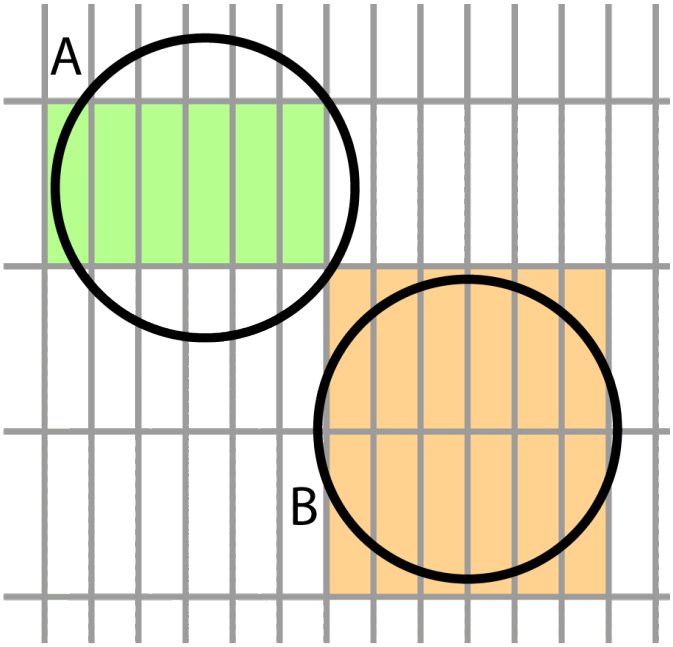

	Volume	MD in Lesion
Actual:	9 voxels	0.42 x 10^{-3} mm^2/s
Position A:	6 voxels	0.44 x 10^{-3} mm^2/s
Position B:	12 voxels	0.49 x 10^{-3} mm^2/s

Figure 7.1: When thick slices are used, lesion volumes can be either under-estimated (A) or over-estimated (B) depending on the position of the lesion relative to the slices. As in the shown example, this can result in a 50% uncertainty in measured volume for lesions with dimensions comparable to twice the slice thickness. In addition, MD measurements are generally lower due to partial volume effects with the healthy tissue. The MD measurements were simulated for the shown scenarios assuming a healthy tissue MD of 0.7×10^{-3} mm^2/s.

7.2 Methods

7.2.1 Subjects

Participants included 13 patients (11 male) diagnosed with ischemic stroke (age 56 ± 13 years, range $25 - 76$ years), who were recruited from the University of Alberta Hospital stroke unit. The patients were scanned 39 ± 32 hr after ictus (range $6 - 106$ hr), and National Institute of Health Stroke Scale (NIHSS) Scores at presentation were 3.2 ± 2.6 (range $0 - 10$).

7.2.2 MRI Acquisition

MRI acquisition was performed in one scan session on a Varian Unity Inova 4.7 T. High resolution (HR) DWI was performed with an acquired voxel size of 1.5 x 1.5 x 1.5 mm^3 (zero-filled to 0.75 x 0.75 x 1.5 mm^3) with no inter-slice gap in a scan time of 3.5 min (4 averages). Full brain coverage with this resolution was the highest the system could achieve due to console memory limitations. 80 slices were acquired with TR = 10 s and TE = 60 ms. The typical resolution (i.e. low resolution, LR) DWI was performed with an acquired voxel size of 1.7 x 1.7 x 5 mm^3 (zero-filled to 0.85 x 0.85 x 5 mm^3) with an inter-slice gap of 1 mm. The scan time was kept the similar to the high resolution scan by increasing the number of averages to 16 (only 1 average is normally required). 20 slices were acquired with TR = 3 s and TE = 53 ms. Both sequences used single-shot echo-planar imaging with R=2 GRAPPA [54], FOV = 24 x 19 cm^2, and Stejskal-Tanner diffusion encoding [32] with b = 1000 s/mm^2 along 3 orthogonal directions.

7.2.3 MRI Analysis

Regions of interest (ROIs) were drawn around all hyperintense lesions with a semi-automated ROI tool (developed in-house, see Appendix B) and with manual ROI drawing in the contralateral healthy tissue using the mean DWI image for both the LR and HR scans independently. Within each ROI the infarct core was defined to include only voxels where the MD was reduced by at least 20% compared to the MD in the ROI around the contralateral healthy tissue. The lesion volume was estimated by multiplying the number of voxels in the infarct core by the voxel volume (including any inter-slice gaps), and the mean MD in the infarct core was measured. The relative MD of each lesion compared to the contralateral healthy tissue (rMD) was calculated. Differences in rMD were evaluated using a students paired t-test ($P < 0.001$).

7.3 Results

Small lesions were much more readily visible on the HR DWI compared to LR, with some not appearing on the LR DWI at all (Figure 7.2). The sagittal and coronal views of the LR scan are poor quality and demonstrate spatial averaging that occurs due to the thick slices. In contrast, the corresponding views on the HR DWI provide accurate depictions of the lesions. The loss of information for LR compared to HR is particularly evident around the cortical gyri. Overall, 13 out of the 43 infarcts detected on the HR scans were not detected on the LR scans.

The uncertainty in lesion volume that is realized by the thick slices is evident via the percent volume difference between the LR scans as a function of the lesion volume on the HR scan (Figure 7.3a). With the assumption that the HR scan gives a good estimate of lesion volume, it is observed that the

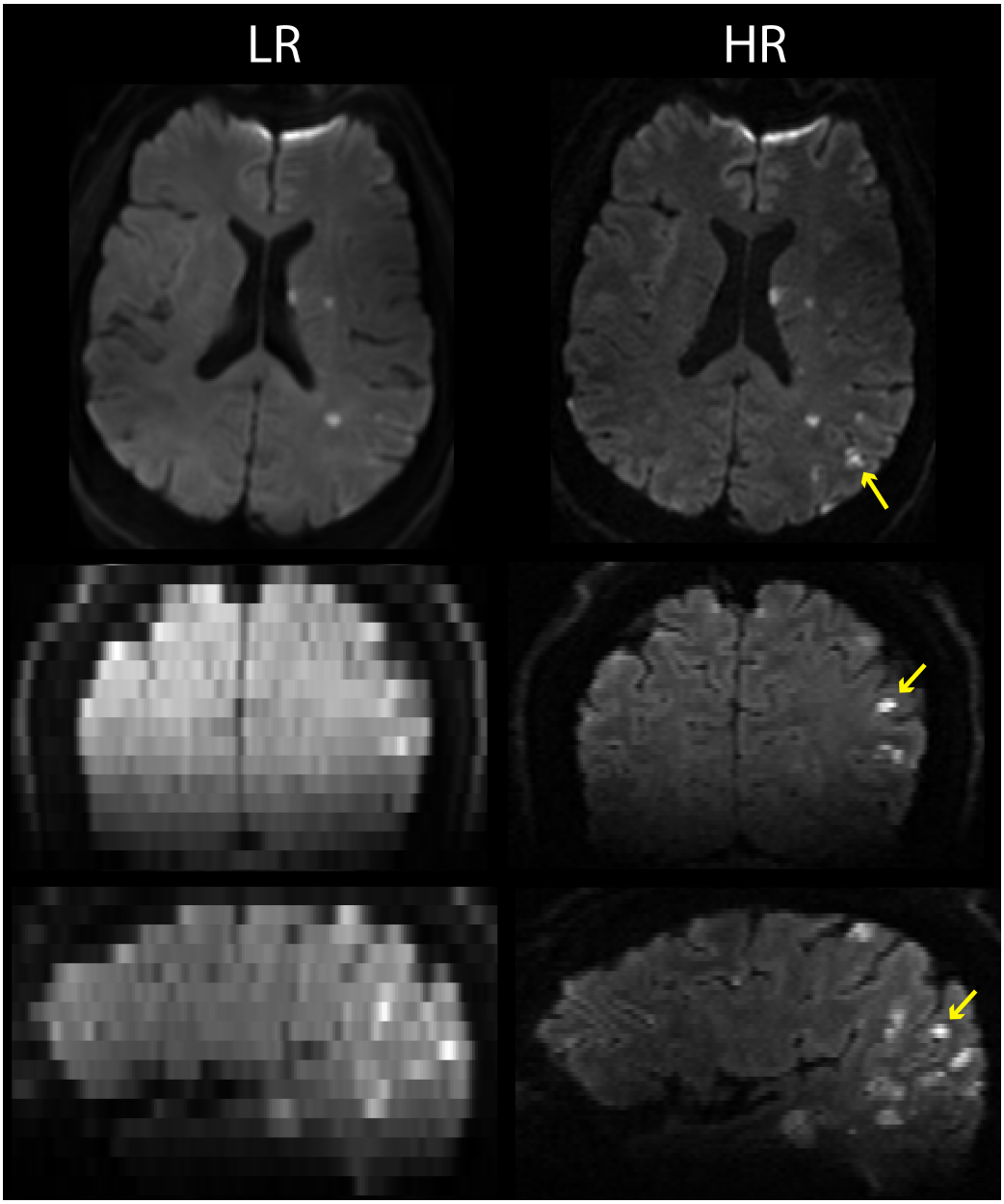

Figure 7.2: Example images from low (LR) and high (HR) resolution DWI in a subject scanned 27 hr after symptom onset. The lesion identified by the arrow is not visible on the LR scan.

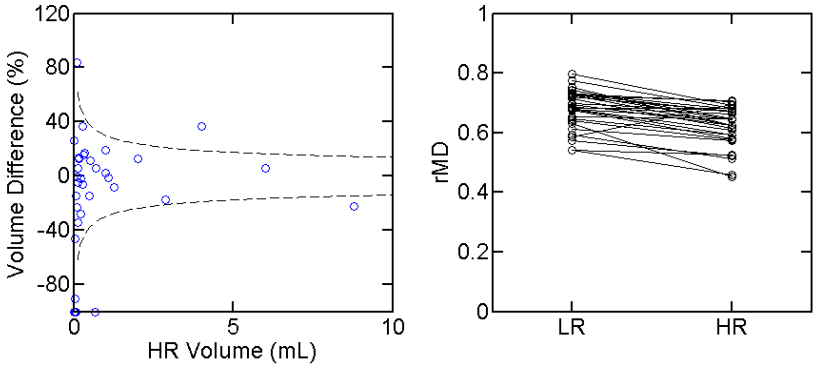

Figure 7.3: (a) The percent difference between lesion volumes measured using the low resolution (LR) and high resolution (HR) DWI scans increased for smaller HR lesion volumes. The results agree with the expected uncertainty estimated by Equation 7.1 (dashed line). (b) The MD measured in the lesion compared to contralateral healthy tissue (rMD) was smaller for HR (mean 0.62) compared to LR (mean 0.68) ($P < 0.001$).

volume error increases for smaller volumes. This trend is captured by Equation 7.1, which is also plotted in Figure 7.3a for $\nu_{see} = 0.25$ (set by assuming that the true MD drop is 40% [184], compared to the threshold of 20% described in the Methods). Interestingly, even the larger lesions with volumes greater than 5 mL still have a magnitude of volume difference as large as 20%, and the overall root-mean-squared (RMS) volume difference over all the lesions was 60%. Notably, a variance metric like RMS for volume difference is more appropriate to quantify volume error compared to a mean difference because the larger voxel volume increases the *uncertainty* of the measurement, as shown in Figure 7.1 (i.e. the difference can be positive or negative, and the mean difference is close to 0). The larger voxel size of the LR scan also resulted in an increase in rMD from $62 \pm 7\%$ to $68 \pm 7\%$ ($P < 0.001$) compared to the HR scan (Figure 7.3b). Of the 30 lesions detected on the LR scan, 29 of the corresponding lesions on the HR scan had a smaller rMD. Note that the MD in contralateral healthy tissue was similar for LR ($0.76 \pm 0.06 \times 10^{-3}$ mm^2/s) and HR ($0.77 \pm 0.06 \times 10^{-3}$ mm^2/s).

7.4 Discussion

The HR DWI protocol resulted in the detection of 43% more lesions compared to a typical DWI protocol (i.e. LR), and in lesions that were detected by both scans the rMD was 10% higher for LR compared to HR. Therefore, even if lesions are visible the smaller MD drops would likely decrease diagnostic certainty. Overall, the estimates of lesion volume differed from the high resolution estimate by 60% RMS. The corruption of volume and MD measurements by partial volume effects would likely impair studies investigating correlations of these measurements with clinical metrics like symptom severity, time of onset, lesion location, or patient outcome. For example, several studies have reported correlations of lesion volume with outcome for volumes greater than 10 mL [176–181], but very little has been reported for smaller lesions where the volumes are more uncertain.

Another advantage of the HR protocol is that with an effective 4x smaller slice thicknesses, any particular lesion is visible in 4x more slices. This would improve diagnostic confidence because a small lesion residing in 2-4 slices instead of only 1 slice would help to rule out artifacts (e.g. B_0 inhomogeneity) as the source of the apparent lesion.

While large improvements in resolution were primarily obtained by decreasing the slice thickness in this work, improving the in-plane resolution for single shot EPI has diminishing returns due to a wide point spread function from T_2 signal decay (see Section 1.4.4). While multi-shot EPI techniques could potentially reduce this issue [71, 185], they are associated with large scan time increases of at least a factor of 2.

The scan time of the LR scan was kept similar to the HR scan by increasing the number of averages to ensure that time spent to acquire an HR

DWI would not be better spent acquiring more averages with LR parameters. Considering the much higher lesion visibility for the HR scan, this was not the case. Nevertheless, a limitation of high resolution DWI is the increased scan time required. While the LR scan could be completed in less than 30 seconds (only 1 average), the HR scan was 3.5 min (4 averages with a longer TR). Accordingly, patients may be best served by a LR scan, where a subsequent HR DWI is performed if no lesions are detected on the LR DWI. Further, this work suggests that research protocols that may be searching for statistical correlations should use HR DWI to reduce uncertainty in measured parameters. It should be noted, though, that with only two averages in the HR protocol the images are still of reasonable quality (Figure 7.4), which would only necessitate a 2 min scan time. Also, while this work was performed at 4.7 T,

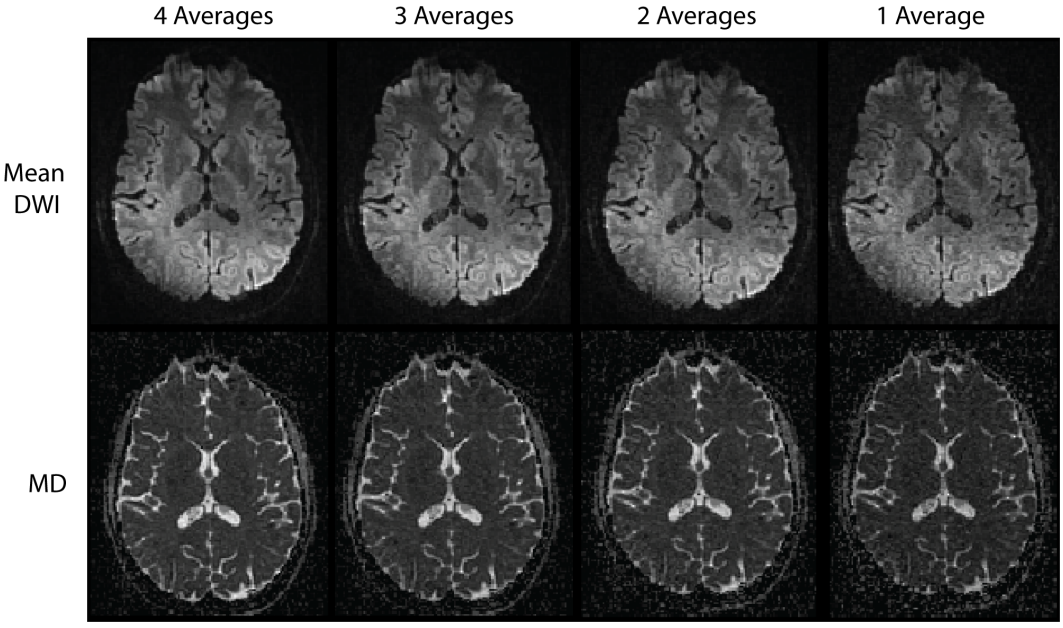

Figure 7.4: The quality of the mean diffusion weighted images (DWI) and mean diffusivity (MD) decreases for the use of a decreasing number of averages; however, reasonable image quality is still observed for only two averages.

the HR protocol could also be performed at 3.0 T or 1.5 T (Figure 7.5) with reasonable scan times ($\approx$ 5.5 min and $\approx$ 10 min, respectively).

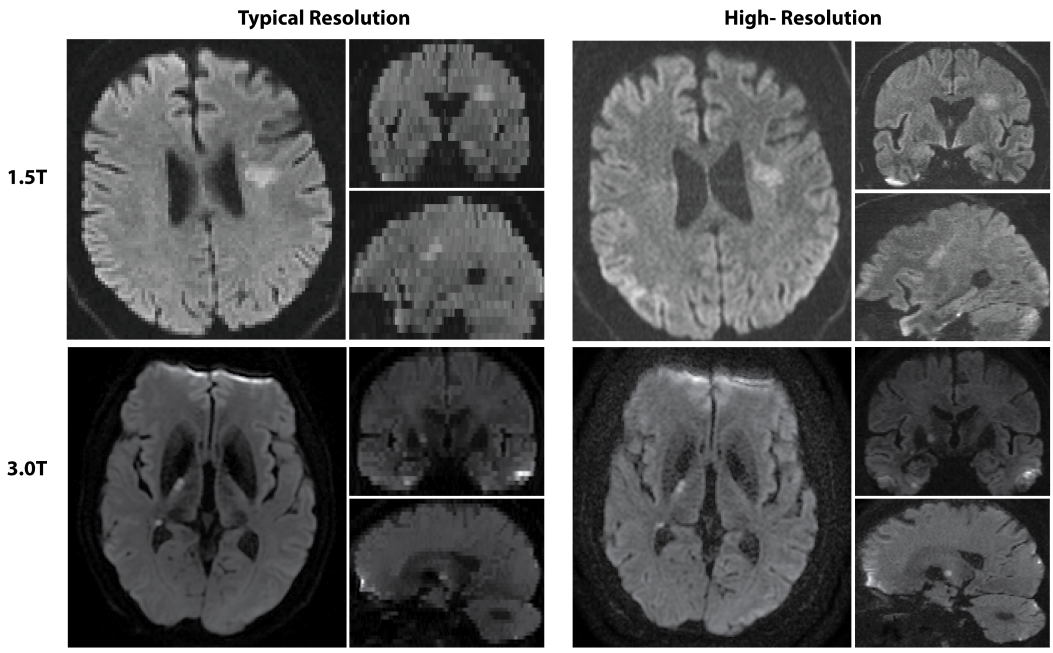

Figure 7.5: Preliminary diffusion weighted images acquired at 1.5 Tesla (University of Alberta) and 3.0 Tesla (University of Calgary - images acquired by Dr. Shelagh B. Coutts, Department of Radiology) at a typical resolution (1.7 mm x 1.7 mm x 6 mm for 1.5 T; 1.9 mm x 1.9 mm x 3 mm for 3 T) and high resolution (1.5 mm isotropic) show that the same resolution as the HR protocol can be implemented at typical field strengths.

This work was performed in patients with relatively minor stroke severity (mean NIHSSS = 3.2) and small lesion volumes (< 10 mL). The volume and MD error may be lower for larger lesions because fewer voxels would contain both infarcted and viable tissue together; however, large lesions with complex shape and high surface to volume ratios would still have a large proportion of voxels only partially filled with infarcted tissue.

In conclusion, thick slice DWI decreases the rate of detection of small lesions, introduces uncertainty in measured lesion volumes on the order of 60% for lesions smaller than 10 mL, and results in increased MD in lesions with respect to healthy tissue by 10% compared to high resolution DWI with isotropic voxels. These findings suggest that high resolution isotropic voxels should be used for accurate quantitative DWI measurements in stroke lesions.

7.5 Collaborators

Patient recruitment was supported by Mahesh Kate (Neurology; University of Alberta), Laura Gioia (Neurology; University of Alberta), Ken Butcher (Neurology; University of Alberta), and Derek Emery (Radiology; University of Alberta).

Chapter 8

Discussion and Conclusions

While each Chapter of this thesis describes the main limitations specific to itself, there are several broad limitations that affected most of the work. Following the discussion of limitations, some overarching conclusions and future directions will be discussed.

8.1 Limitations

8.1.1 Partial Volume Effects

As discussed in Chapter 4, partial volume effects of cerebrospinal fluid (CSF) with tissue voxels introduces error into quantitative DWI and DTI measurements. While the CSF-suppressing sequence introduced in Chapter 4 was not used in other work in this thesis (due to timing of work being completed and incompatibility of the method with OGSE), no measurements in regions with high CSF contamination (e.g. fornix) were performed in any of the other chapters. In addition, partial volume effects between tissue from different brain structures introduce error [9]. This may have introduced some uncertainty in measured values in any of the Chapters of this thesis. Notably,

the technique of only using the core region of white matter tracts for the analysis of OGSE data in Chapter 5 likely mitigated this source of error.

8.1.2 Magnetic Field Inhomogeneity

Even though the distortions from B_0 inhomogeneity were reduced by using parallel imaging, there were still some distortions remaining. This generally decreased data quality near the sinuses and temporal lobes (e.g. Figure 8.1), which precluded analysis of some tracts in those regions (e.g. the uncinate fasciculus in Chapter 5).

8.1.3 Receiver Array Sensitivity

Most work in this thesis used the same 4-element receive array. While the receiver array provided good signal strength in central brain regions (similar to a birdcage coil), the sensitivity quickly decreased in inferior regions of the brain and in the temporal lobes (Figure 8.1). This resulted in non-uniform signal intensities, which may have impaired stroke lesion detection in DWI's, particularly near the base of the brain. Also, the lower SNR may have increased uncertainty in quantitative DTI measurements near the base of the brain; however, most brain regions investigated were in high sensitivity regions of the receiver array.

8.1.4 SAR Monitoring

The RF power monitoring equipment only measured the transmitted RF power; however, reflected RF power does not contribute to tissue heating and SAR. By measuring the reflected power and subtracting it from the transmitted power, more accurate SAR measurements could have been estimated.

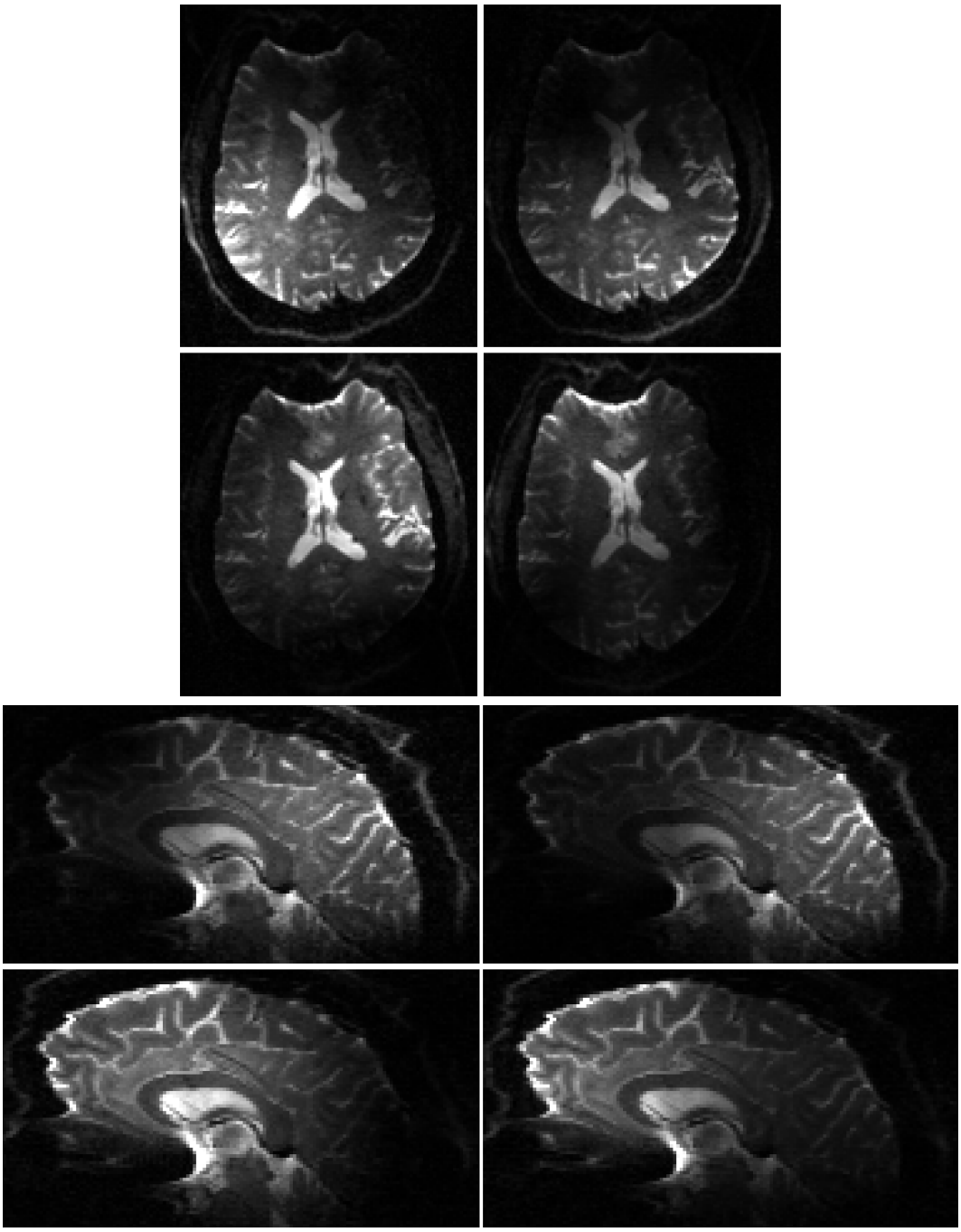

Figure 8.1: The signal from the 4 receivers had non-uniform intensity that quickly diminished toward the base of the brain. Distortions from B_0 inhomogeneity are also visible in the images, which are the non-diffusion weighted images acquired using the high resolution DWI protocol from Chapter 7.

This could have allowed shorter TR (and scan times) in some cases, as well as shortening of RF pulse lengths resulting in shorter TE. However, it was generally non-DTI pulse sequences that were most SAR limited (e.g. fast-spin echo). Nevertheless, because of the SAR limitations of the other sequences in a protocol, the birdcage transmit RF coil was often not lowered all the way down towards the shoulders of the subjects because this caused excitation of the shoulders and higher RF power requirements. This decreased B_1 field strengths near the base of the brain and exacerbated the receiver sensitivity issue described above for all sequences, including DTI. With more accurate SAR monitoring, this issue could have been mitigated.

8.1.5 Data Bottlenecks

A particularly limiting aspect of the hardware was a data flow bottleneck that limited the number of points that could be acquired per unit time. More specifically, the "First In First Out" (FIFO) data buffer in the Inova console is only 64 MB, and if it is filled up faster than it can send data out the scan will terminate early with an error. The conditions where this error can occur are not easily predicted, and whether a pulse sequence is susceptible to it or not is most easily determined through trial and error. This issue was most limiting for the high resolution DWI scan in Chapter 7, where the TR was actually limited by the data flow bottleneck and not SAR. Without this hardware issue, scan times could have been decreased by 10 to 20%. The bottleneck also resulted in long times required for the console to save the data after the sequence was completed (i.e. the hardware had to catch up because it was consistently falling behind during the scan), which is lost time where no other scanning can be performed. For the high resolution DWI sequence, the scan time was 3.5 minutes while the saving time afterward was approximately

3 minutes.

8.1.6 Gradient Duty Cycle

Because of heating, the gradient duty cycle must be kept within certain limits. The temperature of the gradients and cooling water was monitored to ensure that temperatures did not approach the gradient epoxy melting temperature. This issue was most limiting for the OGSE work, where the TR was gradient duty cycle limited. With a higher permissible duty cycle, the TR (and scan time) could have been decreased by 30 to 40%.

8.1.7 Contraindications

This work was performed at the unique field strength of 4.7 T. However, there is no safety data regarding safe metallic foreign bodies at this field strength (or higher). While certain metallic objects in the body are likely safe at 4.7 T, to prevent any unforeseen issues a zero-tolerance policy regarding metal in the body was adhered to. This greatly reduced patient yield for the stroke work, as many individuals at ages typical for stroke have had procedures done. In particular, this problem reduced the yield of women because many have had tubal ligations, where there is a reasonable chance that a metallic clip was used.

8.1.8 Scanning Preparation

Most of the pulse sequences on the 4.7 T scanner have been developed in house, and the selection of preloaded sequences is small. As such, there is not consolidated "preparation" sequence that performs frequency offset calibration, power calibration, and rough shimming. Rather, these steps

are performed manually by the operator using 3 separate protocols, which typically takes 5 to 10 minutes. This represents an unnecessary increase in scan time as the consolidated preparation protocol on new clinical scanners typically requires less than 1 minute.

8.1.9 Sample Size and Subjects

Most of the healthy volunteers in this work were local graduate students. While this subject population can serve to demonstrate improvements gained by new techniques (Chapters 2-4), they do not accurately reflect the general population for work that investigates quantitative parameters in the normal healthy brain, such as Chapter 5. Also, the total size of subject groups was generally small (≈ 10). While large effect sizes can result in statistically significant observations, the data may be subject to skew. Accordingly, the results should be considered a proof of concept of methods that should be investigated in larger and more diverse populations (e.g. Chapters 5, 6, and 7).

8.1.10 Portability

All of the pulse sequence development was on a 12 year old Varian console, which is quite rare for human MRI systems. As such, the pulse sequences that were developed are not easily ported to other systems, which limits the ability to expand the work to other centers.

8.2 Conclusions and Future Directions

The work performed in this thesis explored some challenges with dMRI using large field strengths and gradients (Chapters 2-4), and explored appli-

cations that exploited the unique system capabilities (Chapters 5-7). dMRI publications at field strengths beyond 3 T are sparse, with very few focusing on application in patients. This work establishes that dMRI can be performed at a high field of 4.7 T using fairly standard techniques, and represents some of the first high field dMRI studies in patients.

The characterization of concomitant gradient fields for DTI in Chapter 2 has implications for many new MRI systems that are now equipped with gradients having strengths up to 80 mT/m, which is 25% higher than on the system in this work. This higher gradient field is advantageous for DTI because it allows for a 56% larger b-value at the same TE, or a reduced TE at the same b-value. Combined with the lower field of new systems (e.g. 3 T) compared to the this work at 4.7 T, uncontrolled accumulation of phase from concomitant gradient fields may have disastrous effects. In addition, the proliferation of large gradient systems may merit investigation into concomitant fields associated with the imaging gradients. An extension of the work presented in this thesis may be to design diffusion preparations that are immune to concomitant gradients while simultaneously mitigating eddy currents, or the development of fast switching shim coils that could be used to counter-act the phase from concomitant fields.

The development of parallel imaging methods for EPI that are robust to motion is particularly important for patient populations where the subjects are likely unaccustomed to MRI and there is not time to reacquire corrupted data. Also, in certain patient groups there is persistent involuntary motion (e.g. parkinson's disease) that must be accounted for. While the methods in Chapter 3 mitigate motion effects for future studies, it requires pulse sequence programming that many centers may not be equipped for. Therefore, future work on this topic might involve the development of post-acquisition

motion correction algorithms that can be applied to existing pulse sequence implementations.

Contamination of signal from CSF partial volume effects makes DTI measurement in structures near CSF, like the fornix, fraught with difficulty. Using tractography to extract the position of the fornix in the first place often fails, and even if it's extracted values measured are erroneous. While these issues were overcome at typical field strengths using FLAIR, the high SAR inversion pulses required for FLAIR are not easily translatable to higher field strengths. The high field compatible methods for the reduction of CSF partial volume effects in Chapter 4 thus satisfy the need for accurate DTI of structures near CSF at high field strengths. However, the proposed methods do not completely remove the CSF signal, and a small degree of partial volume contamination of measurements may remain. Therefore, future work may be to combine the proposed methods that work at the pulse sequence level with post-processing methods that use modeling in an attempt to remove the signal contribution from CSF.

Diffusion MRI using the OGSE method had been exclusively in animal models on small bore systems prior to the start of the work in this thesis. While the results that generally showed increasing MD and decreasing FA with shorter diffusion times (i.e. higher OGSE frequencies) were intriguing, translation of the experiments to a human population was still required. The work performed by Van *et al* [53] was published while the work in this thesis was actively being pursued, and represented the first report of OGSE measurements in the human brain. While tantalizing, the results were in 4 subjects with no statistical significance reported, and only MD was measured. The work in Chapter 5 of this thesis was the first report of statistically significant diffusion time dependencies of DTI eigenvalues (which MD stems from) and fractional

anisotropy in the human brain. However, the minimum diffusion time of 4 ms was only short enough to barely start to see changes of the DTI parameters with diffusion time; accordingly, there is a need to move to higher OGSE frequencies (i.e. lower diffusion times) to allow characterization of tissue microstructure in different regions of the brain. In addition, OGSE sequences with shorter TE are required to obtain accurate measurements in deep gray matter regions rich in iron. Likely, higher gradient strengths on new systems will enable these investigations.

While it has been known for over 20 years that ischemic stroke results in a marked acute decrease in apparent diffusion coefficients (ADC) measured using dMRI, the mechanisms underlying the ADC drop are still uncertain. Evidence from histology and diffusion spectroscopy has suggested that the most popular hypothesis of cytotoxic edema with rapidly diffusing extra-cellular water moving to a more restricted intra-cellular space may not be correct (see Chapter 6). The OGSE findings in ischemic stroke patients in Chapter 6 adds to this body of evidence, and supports the hypothesis of ADC drops caused by barriers introduced by neurite beading. However, more work needs to be done to firmly establish a physiological link to the experimental observations. There is a need to establish whether the preliminary results are maintained in a larger cohort of patients with a diverse range of stroke severity, location, and onset time.

The investigations in Chapter 7 showed that improving the resolution of DWI for stroke results in the detection of more lesions and presumably more accurate measurements of lesion volumes and mean diffusivity (MD). While more lesions were generally detected in patients where the low resolution DWI still detected at least one other larger lesion, it is not clear how many patients would be promoted from a negative to positive finding of DWI

lesions. Whether or not this is the case has large implications for patient care as a positive DWI would direct the patient towards more rigorous stroke treatment and preventative care for future strokes. Answering of this question would require a larger number of patients and follow-up MRI with T_2 scans to confirm the presence of necrosis that would confirm the earlier presence of the hyper-acute lesion. Also, the finding of high uncertainty in lesion volumes and MD merits re-visiting correlational studies of these measurements with other clinical metrics and outcomes using higher resolution DWI that takes advantage of modern MRI technology.

Overall the thesis research involved the development and application of 2D EPI based techniques for dMRI on a high field and large gradient system. The strategies developed/used in this work for dMRI at high field could in principle be implemented at higher field and/or gradient strengths than those utilized here (4.7 T and 60 mT/m).

Appendices

A Common Methods

A.1 The Diffusion Weighted Echo-planar Imaging Pulse Sequence

The echo-planar imaging (EPI) pulse sequence that was used is shown in Figure A.1. Some specific characteristics of the pulse sequence are de-

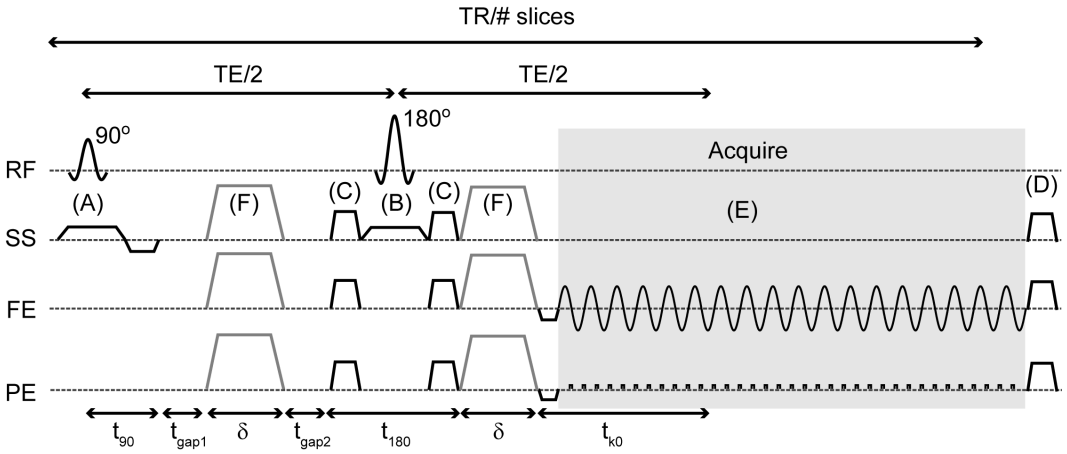

Figure A.1: (a) The pulse sequence for echo-planar imaging (EPI), where the application radiofrequency (RF) pulses, slice select (SS) gradients, frequency encode (FE) gradients, and phase encode (PE) gradients are shown as a function of time. The spin-echo at TE occurs at the center of k-space, and the TR is the total time to repeat the pulse sequence for all slices. The main features are (A) slice selective excitation, (B) refocusing, (C) crusher gradients, (D) spoiler gradients, (E) EPI readout, and (F) diffusion gradients. The durations of key components are shown under the pulse sequence.

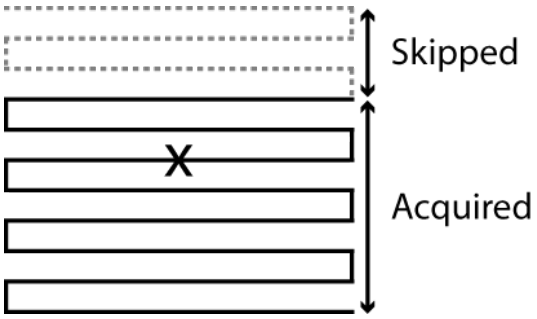

Figure A.2: With partial Fourier undersampling, acquisition of a high spatial frequency portion of k-space is skipped.

scribed below.

1. *Partial Fourier Undersampling*

   The center of k-space occurs at the spin-echo (i.e. TE). To decrease the TE (thus increasing SNR), k-space can be partially sampled (Figure A.2) which causes t_{k0} to be shorter (Figure A.1). Recovering the skipped portion of k-space can be performed by exploiting prior information about the signal acquired, which is described in more detail in Section A.2. A typical partial Fourier fraction was 7/10.

2. *Calculation of b-value*

   The design of the pulse sequence for a particular b-value was performed by solving a system of equations that attain the desired b-value (ignoring imaging gradients) with minimum TE. The minimum TE will occur for a Stejskal-Tanner diffusion preparation with $t_{gap1} = 0$ (Figure A.1) because it allows all the "dead" time in the pulse sequence where no gradients or RF pulses reside (required to have the spin-echo at the center of k-space) to contribute to growing the b-value (via t_{gap2}). Therefore, to determine sequence timing for a desired b-value the only unknown parameters are

δ and t_{gap2}, which can be solved through the system of equations

$$b = \gamma^2 G^2 \delta^2 \left(\frac{2}{3}\delta + t_{gap2} + t_{180} \right) \tag{A.1}$$

$$t_{90} + t_{gap2} = t_{k0} \tag{A.2}$$

where t_{90} and t_{180} are known timings required for slice section and t_{k0} is the time where the center of k-space is reached (Figure A.1). Equation A.1 is the b-value equation for a Stejskal-Tanner diffusion preparation, while Equation A.2 must be satisfied to have the spin-echo at the center of k-space. After determining the sequence timing, the true b-value including all imaging and slice selection gradients was determined by numerically solving the b-tensor equation, $b_{l,m} = \gamma^2 \int_0^{TE} \left(\int_0^t G_l(t') G_m(t') dt' \right) dt$, where l, m correspond to different pairings of the x, y, and z gradient channels (see Section 1.5.1).

3. *Spoiling*

   Spoiling for dMRI consists of spoiling gradients at the end of the pulse sequence to eliminate the transverse magnetization for the next TR (D in Figure A.1). However, with short enough TR stimulated echoes can occur if the spoiler gradients are identical every TR; fortunately the TR for most dMRI is too long for this to be a consideration. Because the work in Chapter 4 involved using shorter than typical TR for dMRI, spoiling was performed more carefully. To eliminate any potential stimulated echoes, RF spoiling and variation of the spoiling gradient heights between repetitions was utilized [20].

4. *Timing "tweak"*

To calibrate the sequence, a short "tweak" version of it that only acquires a single imaging volume was used. The tweak turns off the phase encode imaging gradients so that the same frequency encode line of k-space is acquired repeatedly. After the tweak scan finishes, the offsets between the k-space peaks for odd and even lines are measured, which allows estimation of the net gradient timing delay (caused by eddy currents and hardware delays). This delay is then accounted for with a tweak delay within the pulse sequence (typically $\approx 40\mu$s).

5. *Pre-imaging Volumes*

   Several extra imaging volumes were acquired before the acquisition of any $b = 0$ or diffusion weighted images: 1. a "dummy" excitation that is discarded so that the longitudinal magnetization gets closer to steady-state before acquisition of useful data; 2. Nyquist ghosting reference volume (see Section A.2); 3. GRAPPA reference volume (see Chapter 3). Only one dummy acquisition is required because of the typically long TR used for dMRI.

A.2 Echo-planar Imaging Reconstruction

The pipeline for reconstruction of the raw data obtained from the scanner is described below. All reconstruction steps were performed in Matlab in the order shown, and were written by the thesis author unless otherwise stated.

1. *Nyquist Ghost Correction*

   The back and forth nature of progression through k-space via positive and negative frequency encode gradient lobes (see Section 1.4.4) can result in an artifact known as Nyquist ghosting. The artifact generally stems from fairly short time constant eddy currents that cause two ef-

fects: 1. a gradient time delay that results in misalignment of the start of the gradient readout and the start of data sampling; 2. accumulation of phase from eddy currents that reverses polarity with the reversed gradient direction. The first effect results in misalignment of the gradient echoes for the odd and even phase encode lines of k-space, while the second effect results in a phase difference between the odd and even lines. The net result of the image is partial ghosting by half the FOV (Figure A.3a). These effects can be experimentally measured by setting the phase encode gradients to zero, which results in a k-space image where the shifted odd and even lines are clearly visible (Figure A.3b). While the misalignment can be estimated by measuring the differences between k-space peak locations, more accurate results are obtained if a 1D Fourier transform is applied along the frequency encode direction, which transforms the shift into a linear phase ramp (see Section 1.4.3). Then, subtracting the phase of the even lines from the odd lines results in a phase profile that is approximately linear, with a slope (effect 1) and DC offset (effect 2) that can be calculated from a least squares linear fit. Also, it has been observed that minimizing the Nyquist ghosting also minimizes the image entropy, which allows the determination of the phase ramp and offset using iterative methods that minimize entropy [98].

With the above considerations, the pipeline to correct Nyquist ghosting was to first estimate the phase ramp and offset between odd and even k-space lines using a reference scan as described above and subtract it from the phase of the even lines of k-space on the rest of the acquired volumes. Second, the phase correction was refined using iterative meth-

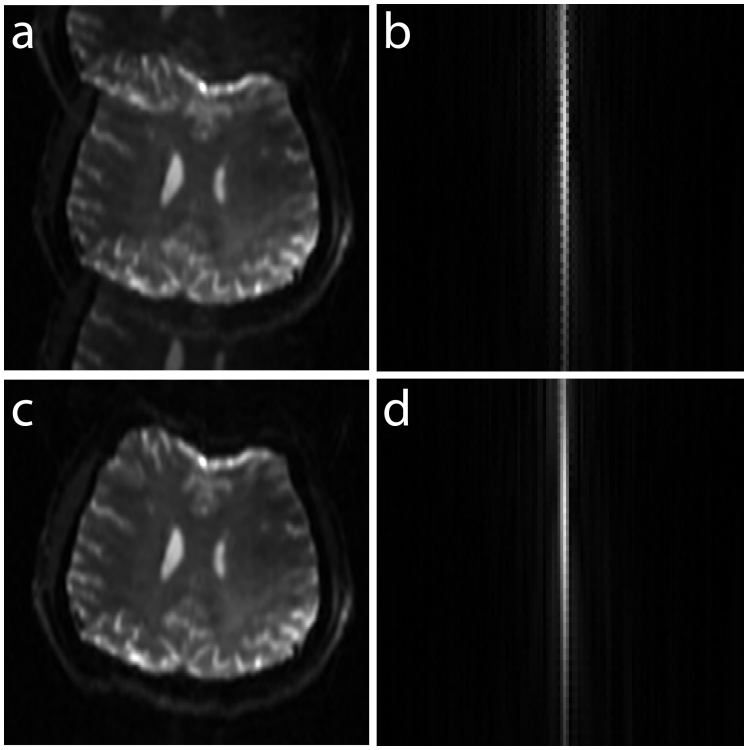

Figure A.3: Time delay and phase accumulation from eddy currents results in Nyquist ghosting (a) and misalignment of gradient echoes in k-space for a reference scan where the phase encode gradients are disabled (b). By using the reference scan in (b) to correct for the phase and timing error, the ghosting is removed (c) and the gradient echoes become aligned (d).

ods similar to those in reference [98]. While it is possible to determine the correction phase from the iterative method alone, using the phase estimated from the reference scan as an initial guess greatly sped up convergence and improved robustness of the iterative approach. The results of the correction are portrayed in Figure A.3(c,d).

Notably, it is important to perform Nyquist ghost correction before resampling the data onto a Cartesian k-space grid. Because the phase ramps correct for a time delay, the *temporal* spacing between samples should be uniform. Resampling to a Cartesian grid first causes the time spacing between k-space points to become non-uniform, which results

in the phase ramp being incorrect for samples far from the center of k-space.

2. *Resampling to Cartesian Grid* The non-uniform sampling from the sinusoidal frequency encode gradients was accounted for by resampling the k-space data onto a uniform grid using an inverse sinc interpolation method [24]. While gridding using a Kaiser-Bessel kernel is often used to approximate the optimal sinc kernel to save computation time [23], this case only requires resampling in one-dimension (along the frequency encode direction) which reduced the computational complexity enough to use a sinc method.

3. *Calculate GRAPPA Weights from Reference Data* Most of the work in this thesis utilized a GRAPPA reference scan where the phase encode step was halved, which corresponds to method B in Chapter 3. While method C was found to yield better performance, development of method C did not occur until late in the PhD program. Recall from Chapter 3 that the GRAPPA weights are calculated through the equation

$$W = \left(S_{kern} S_{kern}^H + \beta I\right)^{-1} S_{kern}^H S_{lk} \tag{A.3}$$

where S_{kern} is the signal at the points in the GRAPPA kernel relative to the signal at central kernel positions $S_{l,k}$, β is the Tikhonov regularization weighting factor, and I is the identity matrix. A value of $\beta = 0.01 \times \left\|\mathbf{S_{kern}} \mathbf{S_{kern}^H}\right\| / N$ was typically used, where $\left\|\mathbf{S_{kern}} \mathbf{S_{kern}^H}\right\|$ and N are the Frobenius norm and matrix size of $S_{kern} S_{kern}^H$, respectively. The value $\beta = 0.01$ was empirically chosen to minimize noise propagation while maintaining good GRAPPA performance.

4. *Fill Missing Lines on Undersampled Data using GRAPPA Weights* Missing k-space lines were filled using GRAPPA (see Chapter 3 and Reference [54]) with a kernel typically 5 points wide in the frequency encode direction and covering 4 phase encode lines.

5. *Shift Image Based on Prescribed Slice Offsets* When the user selects the in-plane position of the slice, the pulse sequence does not change. Rather, parameters signifying the position of the center of the slice with respect to isocenter is saved so that the slice can be shifted during reconstruction. The shifting of the slice is trivially performed by applying the appropriate phase ramps in k-space.

6. *Partial Fourier Undersampling Reconstruction* Partial Fourier undersampling works by recognizing that 1. real-valued images have conjugate symmetric k-space and 2. the phase in images that removes conjugate symmetry is typically slowly varying in space (i.e. is almost completely described by k-space data near the center of k-space). Therefore, a central band of k-space can be acquired to get all the necessary information about the image phase, and only one side of the rest of k-space needs to be acquired to get the high resolution information because of the ability to exploit conjugate symmetry. The work for most of the Chapters in this thesis used a variant of homodyne reconstruction [74] to fill the portion of k-space missing due to partial Fourier undersampling. Homodyne reconstruction works best when the image phase is small, and as discussed in Chapter 2, the low frequency phase in the image was removed prior to exploiting conjugate symmetry to help account for large phase variations imparted by any motion during the diffusion gradients. Later work (namely Chapter 3) utilized the projection

onto convex sets (POCS) algorithm [186] because of its better performance for larger undersampling factors. The POCS Matlab code was obtained from the Matlab File Exchange and was written by Michael Volker (http://www.mathworks.com/matlabcentral/fileexchange/39350-mri-partial-fourier-reconstruction-with-pocs).

7. *Receiver Combination* Receiver combination was performed using the Summation Using Profiles Estimated from Ratios for Diffusion (SUPER-D) algorithm [187]. The most basic form of receiver combination is sum of squares (SOS), which causes the receiver with the highest signal in a particular voxel to contribute more to the net signal compared to the other receivers (compared to a linear summation). This property is desirable as the receiver with the highest SNR is given priority. It turns out that the sum of squares method implicitly assumes that the receiver sensitivity is given by the actual image intensities from the receiver (noise included). The SUPER method [188] overcomes this limitation by using a low pass filtered version of the signal as the receiver sensitivity, which decreases the of high frequency noise in the final receiver combined image. The SUPER-D method is an extension of SUPER for dMRI where only the non-diffusion weighted images (i.e. b = 0) are used to estimate the receiver sensitivities since they have higher SNR than the diffusion weighted images. Also, low frequency phase variations in the diffusion weighted images are filtered out with SUPER-D, which is important for the complex average combination described below (note that the SUPER and SUPER-D algorithms produce complex valued images). Notably, the noise correlation between receiver elements should be considered for SNR-optimal combination of receivers [187, 189]. While the gold standard for calculation of the noise correlation matrix involves finding the

correlation matrix of noise voxels using a zero flip angle RF excitation pulse, in this work the correlation matrix was estimated by using voxels outside the brain in the frequency encode direction (where residual Nyquist ghosting does not occur). Similarity between the approach used and the gold standard was validated in a phantom and human brain.

8. *Filter for Gibbs Ringing* Gibbs ringing occurs because only a finite region of k-space is sampled, which results in a sinc shaped point spread function (PSF). When the sinc PSF is convolved with the "true" image, signal ringing occurs near regions with sharp contrast variations. A Kaiser-Bessel filter was applied to k-space to convert the box shaped finite sampling window to something with a smoother transition to zero. A Kaiser-Bessel function was used because it has a relatively narrow PSF with little sidelobe energy [23].

9. *Motion Correction of Averages* While EPI is robust to subject motion during the acquisition on any particular slice, subject motion between repeated acquisitions (i.e. averages) should be accounted for before the averages are combined. All averages were motion corrected relative to the first average acquired (note that all diffusion directions were typically acquired before moving to the next average). Alignment was performed using iterative rotations and translations of the image volumes until the squared difference between the two was minimized [126].

10. *Combine Averages* After motion correction, the complex mean of the averages was taken. Notably, the complex average should only be performed if the low frequency phase of diffusion weighted images is removed (both the homodyne and SUPER-D algorithms do this), because the phase can vary between averages because of different physiological

motion during the diffusion gradients (which would cause artifacts upon complex averaging). It is important to perform a complex average rather than an average of the image magnitudes because averaging the magnitudes results in a larger noise floor. In other words, with an infinite number of averages the noise floor would become zero for complex averaging, but would remain non-zero for magnitude averaging.

11. *Zero-filling* The last reconstruction step is zero-filling k-space by a factor of 2, which is important to properly resolve small image features [190]. This is shown via simulation in Figure A.4, where small features of a numerical phantom are only properly resolved if some zero-filling is performed.

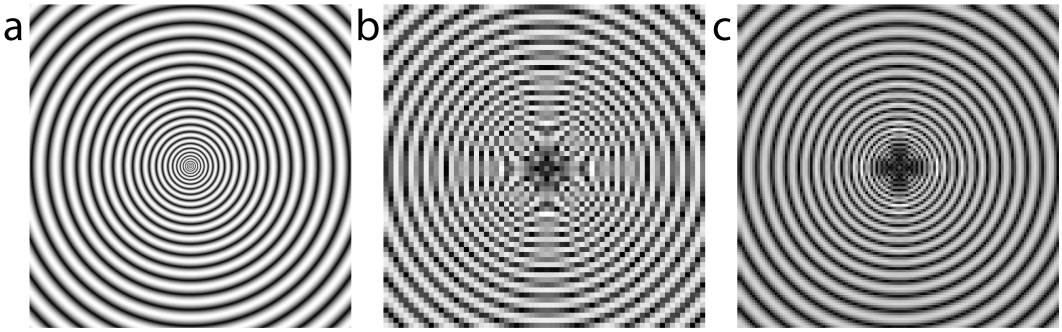

Figure A.4: For a bulls-eye numerical phantom (a), sampling of a 64×64 grid of k-space with no zero-filling results in a poor representation of the phantom (b), particularly along the diagonal directions. By zero-filling to increase k-space to a 128×128 grid, the smaller features are much more accurately represented (c).

A.3 Diffusion Imaging Calculations and Analysis

Diffusion Weighted Imaging

Further analysis for diffusion weighted imaging consisted of two additional steps beyond the basic image reconstruction: 1. motion correction between $b = 0$ and diffusion weighted images and 2. calculation of the mean

DWI and MD. Motion correction used the same Matlab code as for motion correction of averages, with the only difference being the cost function. The mean squared difference cost function does not perform well when the contrast between two images is different, as is the case for the different diffusion weighted images. Therefore, a joint histogram cost function was used [191] [1]. The mean DWI was simply the average of all the diffusion weighted images, while the MD was calculated through the equation

$$MD = -\sum_{n=1}^{N} \ln\left(\frac{S_n}{S_0}\right)/b \tag{A.4}$$

where N is the number of diffusion weighted images (typically 3), S_n is the n'th diffusion weighted image, and S_0 is the $b = 0$ image.

Diffusion Tensor Imaging

All diffusion tensor analysis, including motion correction between diffusion weighted images, eddy current distortion corrections, diffusion tensor calculations, and tractography were performed using ExploreDTI by Alexander Leemans [76].

[1] While at first I wrote my own joint histogram function, a more computationally efficient Matlab function, jointhist.m, was later obtained from http://www.maths4medicalimaging.co.uk/material/Maths4MedicalImaging/matlab/tools/. Both versions of the function produced identical results.

B Lesion Delineation Tool

Stroke lesions were delineated by a semi-automated ROI tool developed in Matlab. The user selects a position within the hyperintense lesion on the mean DWI image, and another point in nearby healthy tissue. This defines an image intensity threshold equal to the mean intensity of the two points. The tool then searches for connected voxels that have intensity above the threshold (all within the same slice), starting from the first within-lesion position selected by the user. The portion of the lesion in adjacent slices is defined by the same two position selection by the user until the entire lesion is accounted for. A typical ROI and the two points defined by the user is shown in Figure A.5.

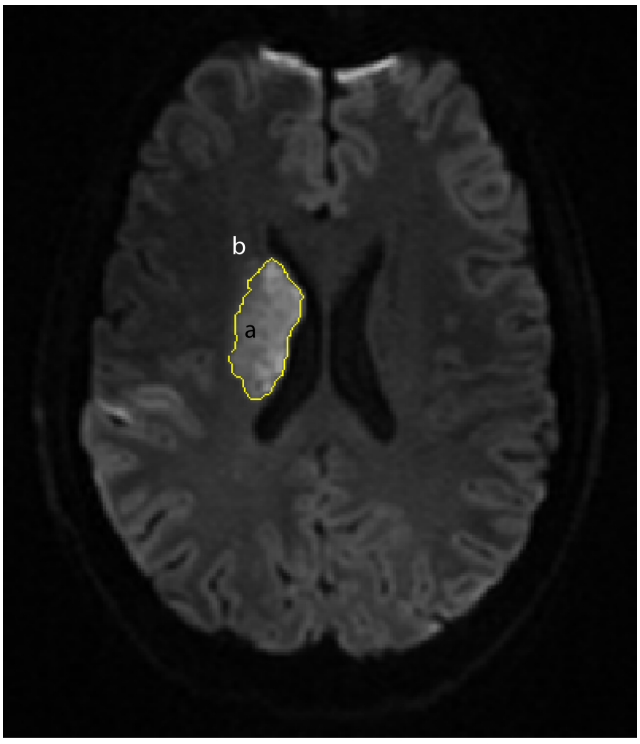

Figure A.5: After manual selection of positions within (a) and in healthy tissue nearby (b) the lesion on a mean DWI image, the ROI tool automatically outlines the lesion for further analysis.

References

[1] S. Yoshida, K. Oishi, A. Faria, and S. Mori. Diffusion tensor imaging of normal brain development. *Pediatric Radiology*, 43(1):15–27, 2013.

[2] I. Stepan-Buksakowska, J. Keller, J. Laczo, A. Rulseh, J. Hort, J. Lisy, F. Charvat, M. Rocek, and D. Horinek. Diffusion tensor imaging in alzheimer disease and mild cognitive impairment. *Neurol Neurochir Pol*, 46(5):462–71, 2012.

[3] D. W. Gross. Diffusion tensor imaging in temporal lobe epilepsy. *Epilepsia*, 52 Suppl 4:32–4, 2011.

[4] B. Gross and R. Kosfeld. Application of spin-echo method in measurement of auto-diffusion. *Messtechnik*, 77(7-8):171, 1969.

[5] M. Schachter, M. D. Does, A. W. Anderson, and J. C. Gore. Measurements of restricted diffusion using an oscillating gradient spin-echo sequence. *Journal of Magnetic Resonance*, 147(2):232–237, 2000.

[6] J. C. Gore, J. Xu, D. C. Colvin, T. E. Yankeelov, E. C. Parsons, and M. D. Does. Characterization of tissue structure at varying length scales using temporal diffusion spectroscopy. *NMR in Biomedicine*, 23(7):745–756, 2010.

[7] D. G. Norris and J. M. S. Hutchison. Concomitant magnetic field gradients and their effects on imaging at low magnetic field strengths. *Magnetic Resonance Imaging*, 8(1):33–37, 1990.

[8] D. K. Jones and M. Cercignani. Twenty-five pitfalls in the analysis of diffusion mri data. *NMR in Biomedicine*, 23(7):803–820, 2010.

[9] S. B. Vos, D. K. Jones, M. A. Viergever, and A. Leemans. Partial volume effect as a hidden covariate in dti analyses. *NeuroImage*, 55(4):1566–1576, 2011.

[10] A. L. Alexander, K. M. Hasan, M. Lazar, J. S. Tsuruda, and D. L. Parker. Analysis of partial volume effects in diffusion-tensor mri. *Magnetic Resonance in Medicine*, 45(5):770–780, 2001.

[11] A. Pfefferbaum and E. V. Sullivan. Increased brain white matter diffusivity in normal adult aging: Relationship to anisotropy and partial voluming. *Magnetic Resonance in Medicine*, 49(5):953–961, 2003.

[12] K. K. Kwong, R. C. McKinstry, D. Chien, A. P. Crawley, J. D. Pearlman, and B. R. Rosen. Csf-suppressed quantitative single-shot diffusion imaging. *Magnetic Resonance in Medicine*, 21(1):157–163, 1991.

[13] M. E. Moseley, Y. Cohen, J. Mintorovitch, L. Chileuitt, H. Shimizu, J. Kucharczyk, M. F. Wendland, and P. R. Weinstein. Early detection of regional cerebral ischemia in cats: Comparison of diffusion- and

t2-weighted mri and spectroscopy. *Magnetic Resonance in Medicine*, 14(2):330–346, 1990.

[14] K. Benameur, J. Bykowski, M. Luby, S. Warach, and L. Latour. Higher prevalence of cortical lesions observed in patients with acute stroke using high-resolution diffusion-weighted imaging. *American Journal of Neuroradiology*, 27(9):1987–1989, 2006.

[15] A. Bertrand, C. Oppenheim, C. Lamy, S. Rodrigo, O. Naggara, J. Mas, and J. Meder. Comparison of optimized and standard diffusion-weighted imaging at 1.5t for the detection of acute lesions in patients with transient ischemic attack. *American Journal of Neuroradiology*, 29(2):363–365, 2008.

[16] T. Sorimachi, Y. Ito, K. Morita, and Y. Fujii. Thin-section diffusion-weighted imaging of the infratentorium in patients with acute cerebral ischemia without apparent lesion on conventional diffusion-weighted imaging. *Neurologia medico-chirurgica*, 48(3):108–113, 2008.

[17] S. Waxman. *Clinical Neuroanatomy 27/E*. McGraw-Hill Education, 2013.

[18] E. Widmaier, H. Raff, and K. Strang. *Vander's Human Physiology: The Mechanisms of Body Function with ARIS*. McGraw-Hill Companies,Incorporated, 2007.

[19] R. W. Neumar. Molecular mechanisms of ischemic neuronal injury. *Ann Emerg Med*, 36(5):483–506, 2000.

[20] E. Haacke, R. Brown, M. Thompson, and R. Venkatesan. *Magnetic Resonance Imaging: Physical Principles and Sequence Design*. Wiley, 1999.

[21] P. Mansfield. Multi-planar image-formation using nmr spin echoes. *Journal of Physics C-Solid State Physics*, 10(3):L55–L58, 1977.

[22] W. S. Price, K. Hayamizu, H. Ide, and Y. Arata. Strategies for diagnosing and alleviating artifactual attenuation associated with large gradient pulses in pgse nmr diffusion measurements. *Journal of Magnetic Resonance*, 139(2):205–212, 1999.

[23] J. I. Jackson, C. H. Meyer, D. G. Nishimura, and A. Macovski. Selection of a convolution function for fourier inversion using gridding [computerised tomography application]. *IEEE Trans Med Imaging*, 10(3):473–8, 1991.

[24] M. D. Robson, A. W. Anderson, and J. C. Gore. Diffusion-weighted multiple shot echo planar imaging of humans without navigation. *Magnetic Resonance in Medicine*, 38(1):82–88, 1997.

[25] J. M. Gomori, G. A. Holland, R. I. Grossman, W. B. Gefter, and R. E. Lenkinski. Fat suppression by section-select gradient reversal on spin-echo mr imaging - work in progress. *Radiology*, 168(2):493–495, 1988.

[26] R. M. Lebel and A. H. Wilman. Transverse relaxometry with stimulated echo compensation. *Magnetic Resonance in Medicine*, 64(4):1005–1014, 2010.

[27] R. M. Lebel, A. Eissa, P. Seres, G. Blevins, and A. H. Wilman. Quantitative high-field imaging of sub-cortical gray matter in multiple sclerosis. *Multiple Sclerosis Journal*, 18(4):433–441, 2012.

[28] H. C. Torrey. Bloch equations with diffusion terms. *Physical Review*, 104(3):563–565, 1956.

[29] V. M. Kenkre, E. Fukushima, and D. Sheltraw. Simple solutions of the torreybloch equations in the nmr study of molecular diffusion. *Journal of Magnetic Resonance*, 128(1):62–69, 1997.

[30] P. J. Basser, J. Mattiello, and D. LeBihan. Estimation of the effective self-diffusion tensor from the nmr spin echo. *J Magn Reson B*, 103(3):247–54, 1994.

[31] D. Jones. *Diffusion MRI: Theory, Methods, and Applications*. Oxford University Press, USA, 2010.

[32] E. O. Stejskal and J. E. Tanner. Spin diffusion measurements: Spin echoes in the presence of a time-dependent field gradient. *The Journal of Chemical Physics*, 42(1):288–292, 1965.

[33] R. Turner and D. Le Bihan. Single-shot diffusion imaging at 2.0 tesla. *Journal of Magnetic Resonance*, 86(3):445–52, 1990.

[34] D. Le Bihan, E. Breton, D. Lallemand, M. L. Aubin, J. Vignaud, and M. Laval-Jeantet. Separation of diffusion and perfusion in intravoxel incoherent motion mr imaging. *Radiology*, 168(2):497–505, 1988.

[35] T. Reese, O. Heid, R. Weisskoff, and V. Wedeen. Reduction of eddy-current-induced distortion in diffusion mri using a twice-refocused spin echo. *Magnetic Resonance in Medicine*, 49(1):177–182, 2003.

[36] D. J. Jensen, W. W. Brey, J. L. Delayre, and P. A. Narayana. Reduction of pulsed gradient settling time in the superconducting magnet of a magnetic resonance instrument. *Medical Physics*, 14(5):859–862, 1987.

[37] P. Jehenson, M. Westphal, and N. Schuff. Analytical method for the compensation of eddy-current effects induced by pulsed magnetic field gradi-

ents in nmr systems. *Journal of Magnetic Resonance (1969)*, 90(2):264–278, 1990.

[38] C. Beaulieu. The basis of anisotropic water diffusion in the nervous system a technical review. *NMR in Biomedicine*, 15(7-8):435–455, 2002.

[39] C. Beaulieu and P. S. Allen. An in vitro evaluation of the effects of local magnetic-susceptibility-induced gradients on anisotropic water diffusion in nerve. *Magnetic Resonance in Medicine*, 36(1):39–44, 1996.

[40] C. A. Clark, G. J. Barker, and P. S. Tofts. An in vivo evaluation of the effects of local magnetic susceptibility-induced gradients on water diffusion measurements in human brain. *J Magn Reson*, 141(1):52–61, 1999.

[41] C. Beaulieu and P. S. Allen. Determinants of anisotropic water diffusion in nerves. *Magnetic Resonance in Medicine*, 31(4):394–400, 1994.

[42] C. Beaulieu and P. S. Allen. Water diffusion in the giant axon of the squid: Implications for diffusion-weighted mri of the nervous system. *Magnetic Resonance in Medicine*, 32(5):579–583, 1994.

[43] M. Takahashi, D. B. Hackney, G. Zhang, S. L. Wehrli, A. C. Wright, W. T. O'Brien, H. Uematsu, F. W. Wehrli, and M. E. Selzer. Magnetic resonance microimaging of intraaxonal water diffusion in live excised lamprey spinal cord. *Proceedings of the National Academy of Sciences*, 99(25):16192–16196, 2002.

[44] P. S. Huppi, S. E. Maier, S. Peled, G. P. Zientara, P. D. Barnes, F. A. Jolesz, and J. J. Volpe. Microstructural development of human newborn cerebral white matter assessed in vivo by diffusion tensor magnetic resonance imaging. *Pediatr Res*, 44(4):584–90, 1998.

[45] J. J. Neil, S. I. Shiran, R. C. McKinstry, G. L. Schefft, A. Z. Snyder, C. R. Almli, E. Akbudak, J. A. Aronovitz, J. P. Miller, B. C. Lee, and T. E. Conturo. Normal brain in human newborns: apparent diffusion coefficient and diffusion anisotropy measured by using diffusion tensor mr imaging. *Radiology*, 209(1):57–66, 1998.

[46] V. Gulani, A. G. Webb, I. D. Duncan, and P. C. Lauterbur. Apparent diffusion tensor measurements in myelin-deficient rat spinal cords. *Magn Reson Med*, 45(2):191–5, 2001.

[47] A. Einstein. On the movement of particles suspended in stationary liquids required by the molecular-kinetic theory of heat. *Annalen dir Physik*, 17:549–560, 1905.

[48] E. C. Parsons, M. D. Does, and J. C. Gore. Modified oscillating gradient pulses for direct sampling of the diffusion spectrum suitable for imaging sequences. *Magnetic Resonance Imaging*, 21(34):279–285, 2003.

[49] J. Stepinik. Analysis of nmr self-diffusion measurements by a density matrix calculation. *Physica B+C*, 104(3):350–364, 1981.

[50] U. Balucani, J. P. Brodholt, and R. Vallauri. Analysis of the velocity autocorrelation function of water. *Journal of Physics-Condensed Matter*, 8(34):6139–6144, 1996.

[51] D. S. Novikov, E. Fieremans, J. H. Jensen, and J. A. Helpern. Random walk with barriers. *Nat Phys*, 7(6):508–514, 2011.

[52] A. Macovski. Noise in mri. *Magnetic Resonance in Medicine*, 36(3):494–497, 1996.

[53] A. T. Van, S. J. Holdsworth, and R. Bammer. In vivo investigation of restricted diffusion in the human brain with optimized oscillating diffusion gradient encoding. *Magnetic Resonance in Medicine*, 71(1):83–94, 2014.

[54] M. A. Griswold, P. M. Jakob, R. M. Heidemann, M. Nittka, V. Jellus, J. Wang, B. Kiefer, and A. Haase. Generalized autocalibrating partially parallel acquisitions (grappa). *Magnetic Resonance in Medicine*, 47(6):1202–1210, 2002.

[55] P. M. Robson, A. K. Grant, A. J. Madhuranthakam, R. Lattanzi, D. K. Sodickson, and C. A. McKenzie. Comprehensive quantification of signal-to-noise ratio and g-factor for image-based and k-space-based parallel imaging reconstructions. *Magnetic Resonance in Medicine*, 60(4):895–907, 2008.

[56] C. A. Meriles, D. Sakellariou, and A. H. Trabesinger. Theory of mri in the presence of zero to low magnetic fields and tensor imaging field gradients. *Journal of Magnetic Resonance*, 182(1):106–114, 2006.

[57] N. Kelso, S.-K. Lee, L.-S. Bouchard, V. Demas, M. Mck, A. Pines, and J. Clarke. Distortion-free magnetic resonance imaging in the zero-field limit. *Journal of Magnetic Resonance*, 200(2):285–290, 2009.

[58] Y. P. Du, X. Joe Zhou, and M. A. Bernstein. Correction of concomitant magnetic field-induced image artifacts in nonaxial echo-planar imaging. *Magnetic Resonance in Medicine*, 48(3):509–515, 2002.

[59] R. M. Weisskoff, M. S. Cohen, and R. R. Rzedzian. Nonaxial whole-body instant imaging. *Magnetic Resonance in Medicine*, 29(6):796–803, 1993.

[60] X. J. Zhou, Y. P. Du, M. A. Bernstein, H. G. Reynolds, J. K. Maier, and J. A. Polzin. Concomitant magnetic-field-induced artifacts in axial echo planar imaging. *Magnetic Resonance in Medicine*, 39(4):596–605, 1998.

[61] X. J. Zhou, S. G. Tan, and M. A. Bernstein. Artifacts induced by concomitant magnetic field in fast spin-echo imaging. *Magnetic Resonance in Medicine*, 40(4):582–591, 1998.

[62] W. Chen, C. T. Sica, and C. H. Meyer. Fast conjugate phase image reconstruction based on a chebyshev approximation to correct for b0 field inhomogeneity and concomitant gradients. *Magnetic Resonance in Medicine*, 60(5):1104–1111, 2008.

[63] K. F. King, A. Ganin, X. J. Zhou, and M. A. Bernstein. Concomitant gradient field effects in spiral scans. *Magnetic Resonance in Medicine*, 41(1):103–112, 1999.

[64] M. A. Bernstein, X. J. Zhou, J. A. Polzin, K. F. King, A. Ganin, N. J. Pelc, and G. H. Glover. Concomitant gradient terms in phase contrast mr: Analysis and correction. *Magnetic Resonance in Medicine*, 39(2):300–308, 1998.

[65] C. T. Sica and C. H. Meyer. Concomitant gradient field effects in balanced steady-state free precession. *Magnetic Resonance in Medicine*, 57(4):721–730, 2007.

[66] B. A. Poser and D. G. Norris. 3d single-shot vaso using a maxwell gradient compensated grase sequence. *Magnetic Resonance in Medicine*, 62(1):255–262, 2009.

[67] B. J. Wilm, C. Barmet, M. Pavan, and K. P. Pruessmann. Higher order reconstruction for mri in the presence of spatiotemporal field perturbations. *Magnetic Resonance in Medicine*, 65(6):1690–1701, 2011.

[68] C. Meier, M. Zwanger, T. Feiweier, and D. Porter. Concomitant field terms for asymmetric gradient coils: Consequences for diffusion, flow, and echo-planar imaging. *Magnetic Resonance in Medicine*, 60(1):128–134, 2008.

[69] J. Finsterbusch. Eddy-current compensated diffusion weighting with a single refocusing rf pulse. *Magnetic Resonance in Medicine*, 61(3):748–754, 2009.

[70] J. N. Morelli, V. M. Runge, T. Feiweier, J. E. Kirsch, K. W. Williams, and U. I. Attenberger. Evaluation of a modified stejskal-tanner diffusion encoding scheme, permitting a marked reduction in te, in diffusion-weighted imaging of stroke patients at 3 t. *Invest Radiol*, 45(1):29–35, 2010.

[71] S. J. Holdsworth, S. Skare, R. D. Newbould, and R. Bammer. Robust grappa-accelerated diffusion-weighted readout-segmented (rs)-epi. *Magnetic Resonance in Medicine*, 62(6):1629–1640, 2009.

[72] J. G. Pipe. Motion correction with propeller mri: Application to head motion and free-breathing cardiac imaging. *Magnetic Resonance in Medicine*, 42(5):963–969, 1999.

[73] D. K. Jones. The effect of gradient sampling schemes on measures derived from diffusion tensor mri: A monte carlo study. *Magnetic Resonance in Medicine*, 51(4):807–815, 2004.

[74] D. C. Noll, D. G. Nishimura, and A. Macovski. Homodyne detection in magnetic resonance imaging. *IEEE Transactions on Medical Imaging*, 10(2):154–163, 1991.

[75] R. Bammer, M. Markl, A. Barnett, B. Acar, M. T. Alley, N. J. Pelc, G. H. Glover, and M. E. Moseley. Analysis and generalized correction of the effect of spatial gradient field distortions in diffusion-weighted imaging. *Magnetic Resonance in Medicine*, 50(3):560–569, 2003.

[76] A. Leemans and D. K. Jones. The b-matrix must be rotated when correcting for subject motion in dti data. *Magnetic Resonance in Medicine*, 61(6):1336–1349, 2009.

[77] C. Pierpaoli, P. Jezzard, P. J. Basser, A. Barnett, and G. Di Chiro. Diffusion tensor mr imaging of the human brain. *Radiology*, 201(3):637–648, 1996.

[78] C. Pierpaoli and P. J. Basser. Toward a quantitative assessment of diffusion anisotropy. *Magnetic Resonance in Medicine*, 36(6):893–906, 1996.

[79] R. G. Nunes, I. Drobnjak, S. Clare, P. Jezzard, and M. Jenkinson. Performance of single spin-echo and doubly refocused diffusion-weighted sequences in the presence of eddy current fields with multiple components. *Magnetic Resonance Imaging*, 29(5):659–667, 2011.

[80] J. Finsterbusch. Double-spin-echo diffusion weighting with a modified eddy current adjustment. *Magnetic Resonance Imaging*, 28(3):434–440, 2010.

[81] Q. Gao, G. Srinivasan, R. L. Magin, and X. Joe Zhou. Anomalous diffusion measured by a twice-refocused spin echo pulse sequence: Analysis

using fractional order calculus. *Journal of Magnetic Resonance Imaging*, 33(5):1177–1183, 2011.

[82] A. Pfefferbaum, E. Adalsteinsson, and E. V. Sullivan. Replicability of diffusion tensor imaging measurements of fractional anisotropy and trace in brain. *Journal of Magnetic Resonance Imaging*, 18(4):427–433, 2003.

[83] B. Taouli, M. Chouli, A. J. Martin, A. Qayyum, F. V. Coakley, and V. Vilgrain. Chronic hepatitis: Role of diffusion-weighted imaging and diffusion tensor imaging for the diagnosis of liver fibrosis and inflammation. *Journal of Magnetic Resonance Imaging*, 28(1):89–95, 2008.

[84] M. Kataoka, A. Kido, A. Yamamoto, Y. Nakamoto, T. Koyama, H. Isoda, Y. Maetani, S. Umeoka, K. Tamai, T. Saga, N. Morisawa, S. Mori, and K. Togashi. Diffusion tensor imaging of kidneys with respiratory triggering: Optimization of parameters to demonstrate anisotropic structures on fraction anisotropy maps. *Journal of Magnetic Resonance Imaging*, 29(3):736–744, 2009.

[85] V. Callot, G. Duhamel, P. J. Cozzone, and F. Kober. Short-scan-time multi-slice diffusion mri of the mouse cervical spinal cord using echo planar imaging. *NMR in Biomedicine*, 21(8):868–877, 2008.

[86] D. S. Tuch, T. G. Reese, M. R. Wiegell, N. Makris, J. W. Belliveau, and V. J. Wedeen. High angular resolution diffusion imaging reveals intravoxel white matter fiber heterogeneity. *Magnetic Resonance in Medicine*, 48(4):577–582, 2002.

[87] L. R. Frank. Anisotropy in high angular resolution diffusion-weighted mri. *Magnetic Resonance in Medicine*, 45(6):935–939, 2001.

[88] D. S. Tuch. Q-ball imaging. *Magnetic Resonance in Medicine*, 52(6):1358–1372, 2004.

[89] P. A. Bandettini, E. C. Wong, R. S. Hinks, R. S. Tikofsky, and J. S. Hyde. Time course epi of human brain function during task activation. *Magnetic Resonance in Medicine*, 25(2):390–397, 1992.

[90] R. Turner, D. Le Bihan, J. Maier, R. Vavrek, L. K. Hedges, and J. Pekar. Echo-planar imaging of intravoxel incoherent motion. *Radiology*, 177(2):407–14, 1990.

[91] Q. X. Yang, J. Wang, M. B. Smith, M. Meadowcroft, X. Sun, P. J. Eslinger, and X. Golay. Reduction of magnetic field inhomogeneity artifacts in echo planar imaging with sense and gesepi at high field. *Magnetic Resonance in Medicine*, 52(6):1418–1423, 2004.

[92] R. Bammer, M. Auer, S. L. Keeling, M. Augustin, L. A. Stables, R. W. Prokesch, R. Stollberger, M. E. Moseley, and F. Fazekas. Diffusion tensor imaging using single-shot sense-epi. *Magnetic Resonance in Medicine*, 48(1):128–136, 2002.

[93] T. Jaermann, K. P. Pruessmann, A. Valavanis, S. Kollias, and P. Boesiger. Influence of sense on image properties in high-resolution single-shot echo-planar dti. *Magnetic Resonance in Medicine*, 55(2):335–342, 2006.

[94] S. Skare, R. D. Newbould, D. B. Clayton, G. W. Albers, S. Nagle, and R. Bammer. Clinical multishot dw-epi through parallel imaging with considerations of susceptibility, motion, and noise. *Magnetic Resonance in Medicine*, 57(5):881–890, 2007.

[95] C. Preibisch, U. Pilatus, J. Bunke, F. Hoogenraad, F. Zanella, and

H. Lanfermann. Functional mri using sensitivity-encoded echo planar imaging (sense-epi). *NeuroImage*, 19(2):412–421, 2003.

[96] P. P. Klaas, W. Markus, B. S. Markus, and B. Peter. Sense: Sensitivity encoding for fast mri. *Magnetic Resonance in Medicine*, 42(5):952–962, 1999.

[97] N.-k. Chen, K. Oshio, and L. P. Panych. Improved image reconstruction for partial fourier gradient-echo echo-planar imaging (epi). *Magnetic Resonance in Medicine*, 59(4):916–924, 2008.

[98] S. Skare, D. B. Clayton, R. D. Newbould, M. E. Moseley, and R. Bammer. A fast and robust minimum entropy based ghost correction. In *Proceedings of the 14th Annual Meeting of the ISMRM*, page 2349, Seattle, USA, 2006.

[99] M. S. Atkins and B. T. Mackiewich. Fully automatic segmentation of the brain in mri. *Medical Imaging, IEEE Transactions on*, 17(1):98–107, 1998.

[100] M.-C. Chou, Y.-R. Lin, T.-Y. Huang, C.-Y. Wang, H.-W. Chung, C.-J. Juan, and C.-Y. Chen. Flair diffusion-tensor mr tractography: Comparison of fiber tracking with conventional imaging. *American Journal of Neuroradiology*, 26(3):591–597, 2005.

[101] L. Concha, D. W. Gross, and C. Beaulieu. Diffusion tensor tractography of the limbic system. *AJNR Am J Neuroradiol*, 26(9):2267–74, 2005.

[102] S. Li, B. Wang, P. Xu, Q. Lin, G. Gong, X. Peng, Y. Fan, Y. He, and R. Huang. Increased global and local efficiency of human brain anatomical networks detected with flair-dti compared to non-flair-dti. *PLoS ONE*, 8(8):e71229, 2013.

[103] C. Metzler-Baddeley, M. J. O'Sullivan, S. Bells, O. Pasternak, and D. K. Jones. How and how not to correct for csf-contamination in diffusion mri. *NeuroImage*, 59(2):1394–1403, 2012.

[104] L. Concha, C. Beaulieu, and D. W. Gross. Bilateral limbic diffusion abnormalities in unilateral temporal lobe epilepsy. *Annals of Neurology*, 57(2):188–196, 2005.

[105] M. Liu, L. Concha, C. Beaulieu, and D. W. Gross. Distinct white matter abnormalities in different idiopathic generalized epilepsy syndromes. *Epilepsia*, 52(12):2267–2275, 2011.

[106] N. L. Voets, J. E. Adcock, R. Stacey, Y. Hart, K. Carpenter, P. M. Matthews, and C. F. Beckmann. Functional and structural changes in the memory network associated with left temporal lobe epilepsy. *Human Brain Mapping*, 30(12):4070–4081, 2009.

[107] M. M. Mielke, O. C. Okonkwo, K. Oishi, S. Mori, S. Tighe, M. I. Miller, C. Ceritoglu, T. Brown, M. Albert, and C. G. Lyketsos. Fornix integrity and hippocampal volume predict memory decline and progression to alzheimers disease. *Alzheimer's and Dementia*, 8(2):105–113, 2012.

[108] M. J. Firbank, A. M. Blamire, A. Teodorczuk, E. Teper, D. Mitra, and J. T. O'Brien. Diffusion tensor imaging in alzheimer's disease and dementia with lewy bodies. *Psychiatry Research: Neuroimaging*, 194(2):176–183, 2011.

[109] N. Kunimatsu, S. Aoki, A. Kunimatsu, O. Abe, H. Yamada, Y. Masutani, K. Kasai, H. Yamasue, and K. Ohtomo. Tract-specific analysis of white matter integrity disruption in schizophrenia. *Psychiatry Research: Neuroimaging*, 201(2):136–143, 2012.

[110] A. Qiu, T. A. Tuan, P. S. Woon, M. F. Abdul-Rahman, S. Graham, and K. Sim. Hippocampal-cortical structural connectivity disruptions in schizophrenia: An integrated perspective from hippocampal shape, cortical thickness, and integrity of white matter bundles. *NeuroImage*, 52(4):1181–1189, 2010.

[111] C. Lebel, M. Gee, R. Camicioli, M. Wieler, W. Martin, and C. Beaulieu. Diffusion tensor imaging of white matter tract evolution over the lifespan. *NeuroImage*, 60(1):340–352, 2012.

[112] S. Sala, F. Agosta, E. Pagani, M. Copetti, G. Comi, and M. Filippi. Microstructural changes and atrophy in brain white matter tracts with aging. *Neurobiology of Aging*, 33(3):488–498.e2, 2012.

[113] C. Metzler-Baddeley, D. K. Jones, B. Belaroussi, J. P. Aggleton, and M. J. O'Sullivan. Frontotemporal connections in episodic memory and aging: A diffusion mri tractography study. *The Journal of Neuroscience*, 31(37):13236–13245, 2011.

[114] K. C. Kern, A. D. Ekstrom, N. A. Suthana, B. S. Giesser, M. Montag, A. Arshanapalli, S. Y. Bookheimer, and N. L. Sicotte. Fornix damage limits verbal memory functional compensation in multiple sclerosis. *NeuroImage*, 59(3):2932–2940, 2012.

[115] J. C. Falconer and P. A. Narayana. Cerebrospinal fluid-suppressed high-resolution diffusion imaging of human brain. *Magnetic Resonance in Medicine*, 37(1):119–123, 1997.

[116] N. G. Zacharopoulos and P. A. Narayana. Selective measurement of white matter and gray matter diffusion trace values in normal human brain. *Med Phys*, 25(11):2237–41, 1998.

[117] N. G. Papadakis, K. M. Martin, M. H. Mustafa, I. D. Wilkinson, P. D. Griffiths, C. L. H. Huang, and P. W. R. Woodruff. Study of the effect of csf suppression on white matter diffusion anisotropy mapping of healthy human brain. *Magnetic Resonance in Medicine*, 48(2):394–398, 2002.

[118] Y. A. Bhagat and C. Beaulieu. Diffusion anisotropy in subcortical white matter and cortical gray matter: Changes with aging and the role of csf-suppression. *Journal of Magnetic Resonance Imaging*, 20(2):216–227, 2004.

[119] O. Pasternak, N. Sochen, Y. Gur, N. Intrator, and Y. Assaf. Free water elimination and mapping from diffusion mri. *Magnetic Resonance in Medicine*, 62(3):717–730, 2009.

[120] E. S. Hui, J. A. Helpern, and E. X. Wu. Effective reduction of csf partial volume effect in dti by acquiring additional dwis with smaller b-value, 2009.

[121] P. Jezzard, S. Duewell, and R. S. Balaban. Mr relaxation times in human brain: measurement at 4 t. *Radiology*, 199(3):773–779, 1996.

[122] N. Takaya, H. Watanabe, and F. Mitsumori. Elongated t1 values in human brain and the optimization of mdeft measurements at 4.7t, 2004.

[123] D. K. Jones, M. A. Horsfield, and A. Simmons. Optimal strategies for measuring diffusion in anisotropic systems by magnetic resonance imaging. *Magnetic Resonance in Medicine*, 42(3):515–525, 1999.

[124] P. A. Taylor and B. Biswal. Geometric analysis of the b-dependent effects of rician signal noise on diffusion tensor imaging estimates and determining an optimal b value. *Magnetic Resonance Imaging*, 29(6):777–788, 2011.

[125] R. M. Henkelman, G. J. Stanisz, J. K. Kim, and M. J. Bronskill. Anisotropy of nmr properties of tissues. *Magnetic Resonance in Medicine*, 32(5):592–601, 1994.

[126] W. F. Eddyy, M. Fitzgerald, and D. C. Noll. Improved image registration by using fourier interpolation. *Magnetic Resonance in Medicine*, 36(6):923–931, 1996.

[127] D. A. Feinberg, S. Moeller, S. M. Smith, E. Auerbach, S. Ramanna, M. F. Glasser, K. L. Miller, K. Ugurbil, and E. Yacoub. Multiplexed echo planar imaging for sub-second whole brain fmri and fast diffusion imaging. *PLoS ONE*, 5(12):e15710, 2010.

[128] D. J. Larkman, J. V. Hajnal, A. H. Herlihy, G. A. Coutts, I. R. Young, and G. Ehnholm. Use of multicoil arrays for separation of signal from multiple slices simultaneously excited. *Journal of Magnetic Resonance Imaging*, 13(2):313–317, 2001.

[129] J. E. Tanner and E. O. Stejskal. Restricted self-diffusion of protons in colloidal systems by the pulsed-gradient, spin-echo method. *The Journal of Chemical Physics*, 49(4):1768–1777, 1968.

[130] Y. Seo, Y. Morita, Y. Kusaka, M. C. Steward, and M. Murakami. Diffusion of water in rat sciatic nerve measured by h-1 pulsed field gradient nmr: Compartmentation and anisotropy. *Japanese Journal of Physiology*, 46(2):163–169, 1996.

[131] G. J. Stanisz and R. M. Henkelman. Diffusional anisotropy of t2 components in bovine optic nerve. *Magnetic Resonance in Medicine*, 40(3):405–410, 1998.

[132] A. Bar-Shir and Y. Cohen. High b-value q-space diffusion mrs of nerves: structural information and comparison with histological evidence. *NMR in Biomedicine*, 21(2):165–174, 2008.

[133] T. Niendorf, D. G. Norris, and D. Leibfritz. Detection of apparent restricted diffusion in healthy rat brain at short diffusion times. *Magnetic Resonance in Medicine*, 32(5):672–677, 1994.

[134] D. Le Bihan, R. Turner, and P. Douek. Is water diffusion restricted in human brain white-matter - an echo-planar nmr imaging study. *Neuroreport*, 4(7):887–890, 1993.

[135] C. A. Clark, M. Hedehus, and M. E. Moseley. Diffusion time dependence of the apparent diffusion tensor in healthy human brain and white matter disease. *Magnetic Resonance in Medicine*, 45(6):1126–1129, 2001.

[136] M. Nilsson, J. Ltt, E. Nordh, R. Wirestam, F. Sthlberg, and S. Brockstedt. On the effects of a varied diffusion time in vivo: is the diffusion in white matter restricted? *Magnetic Resonance Imaging*, 27(2):176–187, 2009.

[137] F. Aboitiz, A. B. Scheibel, R. S. Fisher, and E. Zaidel. Fiber composition of the human corpus callosum. *Brain Research*, 598(12):143–153, 1992.

[138] D. C. Alexander, P. L. Hubbard, M. G. Hall, E. A. Moore, M. Ptito, G. J. M. Parker, and T. B. Dyrby. Orientationally invariant indices of axon diameter and density from diffusion mri. *NeuroImage*, 52(4):1374–1389, 2010.

[139] J. Xu, M. D. Does, and J. C. Gore. Dependence of temporal diffusion spectra on microstructural properties of biological tissues. *Magnetic Resonance Imaging*, 29(3):380–390, 2011.

[140] J. Xu, M. D. Does, and J. C. Gore. Quantitative characterization of tissue microstructure with temporal diffusion spectroscopy. *Journal of Magnetic Resonance*, 200(2):189–197, 2009.

[141] D. S. Novikov and V. G. Kiselev. Surface-to-volume ratio with oscillating gradients. *Journal of Magnetic Resonance*, 210(1):141–145, 2011.

[142] M. D. Does, E. C. Parsons, and J. C. Gore. Oscillating gradient measurements of water diffusion in normal and globally ischemic rat brain. *Magnetic Resonance in Medicine*, 49(2):206–215, 2003.

[143] M. Aggarwal, M. V. Jones, P. A. Calabresi, S. Mori, and J. Zhang. Probing mouse brain microstructure using oscillating gradient diffusion mri. *Magnetic Resonance in Medicine*, 67(1):98–109, 2012.

[144] J. Kershaw, C. Leuze, I. Aoki, T. Obata, I. Kanno, H. Ito, Y. Yamaguchi, and H. Handa. Systematic changes to the apparent diffusion tensor of in vivo rat brain measured with an oscillating-gradient spin-echo sequence. *NeuroImage*, 70(0):10–20, 2013.

[145] K. D. Harkins, J.-P. Galons, J. L. Divijak, and T. P. Trouard. Changes in intracellular water diffusion and energetic metabolism in response to ischemia in perfused c6 rat glioma cells. *Magnetic Resonance in Medicine*, 66(3):859–867, 2011.

[146] J. Xu, M. D. Does, and J. C. Gore. Sensitivity of mr diffusion measurements to variations in intracellular structure: Effects of nuclear size. *Magnetic Resonance in Medicine*, 61(4):828–833, 2009.

[147] J. Xu, K. Li, R. A. Smith, J. C. Waterton, P. Zhao, H. Chen, M. D. Does, H. C. Manning, and J. C. Gore. Characterizing tumor response

to chemotherapy at various length scales using temporal diffusion spectroscopy. *PLoS ONE*, 7(7):e41714, 2012.

[148] A. Ianu, B. Siow, I. Drobnjak, H. Zhang, and D. C. Alexander. Gaussian phase distribution approximations for oscillating gradient spin echo diffusion mri. *Journal of Magnetic Resonance*, 227(0):25–34, 2013.

[149] S. Portnoy, J. J. Flint, S. J. Blackband, and G. J. Stanisz. Oscillating and pulsed gradient diffusion magnetic resonance microscopy over an extended b-value range: Implications for the characterization of tissue microstructure. *Magnetic Resonance in Medicine*, 69(4):1131–1145, 2013.

[150] R. V. Mulkern, H. Gudbjartsson, C.-F. Westin, H. P. Zengingonul, W. Gartner, C. R. G. Guttmann, R. L. Robertson, W. Kyriakos, R. Schwartz, D. Holtzman, F. A. Jolesz, and S. E. Maier. Multi-component apparent diffusion coefficients in human brain. *NMR in Biomedicine*, 12(1):51–62, 1999.

[151] J. A. D. Farrell, B. A. Landman, C. K. Jones, S. A. Smith, J. L. Prince, P. C. M. van Zijl, and S. Mori. Effects of signal-to-noise ratio on the accuracy and reproducibility of diffusion tensor imagingderived fractional anisotropy, mean diffusivity, and principal eigenvector measurements at 1.5t. *Journal of Magnetic Resonance Imaging*, 26(3):756–767, 2007.

[152] A. L. Sukstanskii, J. J. H. Ackerman, and D. A. Yablonskiy. Effects of barrier-induced nuclear spin magnetization inhomogeneities on diffusion-attenuated mr signal. *Magnetic Resonance in Medicine*, 50(4):735–742, 2003.

[153] A. L. Sukstanskii. Exact analytical results for adc with oscillating diffu-

sion sensitizing gradients. *Journal of Magnetic Resonance*, 234(0):135–140, 2013.

[154] H. Zhang, T. Schneider, C. A. Wheeler-Kingshott, and D. C. Alexander. Noddi: Practical in vivo neurite orientation dispersion and density imaging of the human brain. *NeuroImage*, 61(4):1000–1016, 2012.

[155] P. P. Mitra and B. I. Halperin. Effects of finite gradient-pulse widths in pulsed-field-gradient diffusion measurements. *Journal of Magnetic Resonance, Series A*, 113(1):94–101, 1995.

[156] C.-H. Yeh, J. D. Tournier, K.-H. Cho, C.-P. Lin, F. Calamante, and A. Connelly. The effect of finite diffusion gradient pulse duration on fibre orientation estimation in diffusion mri. *NeuroImage*, 51(2):743–751, 2010.

[157] L. L. Latour, K. Svoboda, P. P. Mitra, and C. H. Sotak. Time-dependent diffusion of water in a biological model system. *Proceedings of the National Academy of Sciences*, 91(4):1229–1233, 1994.

[158] D. G. Norris. The effects of microscopic tissue parameters on the diffusion weighted magnetic resonance imaging experiment. *NMR in Biomedicine*, 14(2):77–93, 2001.

[159] C. H. Sotak. Nuclear magnetic resonance (nmr) measurement of the apparent diffusion coefficient (adc) of tissue water and its relationship to cell volume changes in pathological states. *Neurochemistry International*, 45(4):569–582, 2004.

[160] A. van der Toorn, R. M. Dijkhuizen, C. A. F. Tulleken, and K. Nicolay. Diffusion of metabolites in normal and ischemic rat brain measured by localized 1h mrs. *Magnetic Resonance in Medicine*, 36(6):914–922, 1996.

[161] R. M. Dijkhuizen, R. A. de Graaf, K. A. F. Tulleken, and K. Nicolay. Changes in the diffusion of water and intracellular metabolites after excitotoxic injury and global ischemia in neonatal rat brain. *J Cereb Blood Flow Metab*, 19(3):341–349, 1999.

[162] O. Abe, T. Okubo, N. Hayashi, N. Saito, N. Iriguchi, I. Shirouzu, Y. Kojima, T. Masumoto, K. Ohtomo, and Y. Sasaki. Temporal changes of the apparent diffusion coefficients of water and metabolites in rats with hemispheric infarction[colon] experimental study of transhemispheric diaschisis in the contralateral hemisphere at 7 tesla. *J Cereb Blood Flow Metab*, 20(4):726–735, 2000.

[163] W. Dreher, E. Busch, and D. Leibfritz. Changes in apparent diffusion coefficients of metabolites in rat brain after middle cerebral artery occlusion measured by proton magnetic resonance spectroscopy. *Magnetic Resonance in Medicine*, 45(3):383–389, 2001.

[164] J. A. Goodman, J. J. H. Ackerman, and J. J. Neil. Cs + adc in rat brain decreases markedly at death. *Magnetic Resonance in Medicine*, 59(1):65–72, 2008.

[165] M. Harada, M. Uno, F. Hong, S. Hisaoka, H. Nishitani, and T. Matsuda. Diffusion-weighted in vivo localized proton mr spectroscopy of human cerebral ischemia and tumor. *NMR in Biomedicine*, 15(1):69–74, 2002.

[166] D. Zheng, Z. Liu, J. Fang, X. Wang, and J. Zhang. The effect of age and cerebral ischemia on diffusion-weighted proton mr spectroscopy of the human brain. *American Journal of Neuroradiology*, 33(3):563–568, 2012.

[167] M. D. Budde and J. A. Frank. Neurite beading is sufficient to decrease

the apparent diffusion coefficient after ischemic stroke. *Proc Natl Acad Sci U S A*, 107(32):14472–7, 2010.

[168] S. Ochs, R. Pourmand, R. A. Jersild Jr, and R. N. Friedman. The origin and nature of beading: A reversible transformation of the shape of nerve fibers. *Progress in Neurobiology*, 52(5):391–426, 1997.

[169] T. H. Murphy, P. Li, K. Betts, and R. Liu. Two-photon imaging of stroke onset in vivo reveals that nmda-receptor independent ischemic depolarization is the major cause of rapid reversible damage to dendrites and spines. *J Neurosci*, 28(7):1756–72, 2008.

[170] D. S. Novikov, J. H. Jensen, J. A. Helpern, and E. Fieremans. Revealing mesoscopic structural universality with diffusion. *Proceedings of the National Academy of Sciences*, 111(14):5088–5093, 2014.

[171] C. A. Baron and C. Beaulieu. Oscillating gradient spin-echo (ogse) diffusion tensor imaging of the human brain. *Magnetic Resonance in Medicine*, page DOI: 10.1002/mrm.24987, 2013.

[172] M. G. Hall and D. C. Alexander. Convergence and parameter choice for monte-carlo simulations of diffusion mri. *Medical Imaging, IEEE Transactions on*, 28(9):1354–1364, 2009.

[173] E. S. Hui, E. Fieremans, J. H. Jensen, A. Tabesh, W. Feng, L. Bonilha, M. V. Spampinato, R. Adams, and J. A. Helpern. Stroke assessment with diffusional kurtosis imaging. *Stroke*, 43(11):2968–2973, 2012.

[174] A. de Crespigny, J. Rother, N. van Bruggen, C. Beaulieu, and M. E. Moseley. Magnetic resonance imaging assessment of cerebral hemodynamics during spreading depression in rats. *J Cereb Blood Flow Metab*, 18(9):1008–1017, 1998.

[175] J. D. Easton, J. L. Saver, G. W. Albers, M. J. Alberts, S. Chaturvedi, E. Feldmann, T. S. Hatsukami, R. T. Higashida, S. C. Johnston, C. S. Kidwell, H. L. Lutsep, E. Miller, and R. L. Sacco. Definition and evaluation of transient ischemic attack: A scientific statement for healthcare professionals from the american heart association/american stroke association stroke council; council on cardiovascular surgery and anesthesia; council on cardiovascular radiology and intervention; council on cardiovascular nursing; and the interdisciplinary council on peripheral vascular disease: The american academy of neurology affirms the value of this statement as an educational tool for neurologists. *Stroke*, 40(6):2276–2293, 2009.

[176] C. Beaulieu, A. De Crespigny, D. C. Tong, M. E. Moseley, G. W. Albers, and M. P. Marks. Longitudinal magnetic resonance imaging study of perfusion and diffusion in stroke: Evolution of lesion volume and correlation with clinical outcome. *Annals of Neurology*, 46(4):568–578, 1999.

[177] G. J. Thomalla, T. Kucinski, V. Schoder, J. Fiehler, R. Knab, H. Zeumer, C. Weiller, and J. Rther. Prediction of malignant middle cerebral artery infarction by early perfusion- and diffusion-weighted magnetic resonance imaging. *Stroke*, 34(8):1892–1899, 2003.

[178] S. T. Engelter, J. Provenzale, J. R. Petrella, D. M. DeLong, and M. J. Alberts. Infarct volume on apparent diffusion coefficient maps correlates with length of stay and outcome after middle cerebral artery stroke. *Cerebrovasc Dis*, 15(3):188–91, 2003.

[179] D. G. Na, V. N. Thijs, G. W. Albers, M. E. Moseley, and M. P. Marks. Diffusion-weighted mr imaging in acute ischemia: Value of apparent diffusion coefficient and signal intensity thresholds in predicting tis-

sue at risk and final infarct size. *American Journal of Neuroradiology*, 25(8):1331–1336, 2004.

[180] K. C. Johnston, K. M. Barrett, Y. H. Ding, D. P. Wagner, and f. t. A. Investigators. Clinical and imaging data at 5 days as a surrogate for 90-day outcome in ischemic stroke. *Stroke*, 40(4):1332–1333, 2009.

[181] T. D. Farr and S. Wegener. Use of magnetic resonance imaging to predict outcome after stroke: a review of experimental and clinical evidence. *J Cereb Blood Flow Metab*, 30(4):703–717, 2010.

[182] J. M. Wardlaw, S. L. Keir, M. E. Bastin, P. A. Armitage, and A. K. Rana. Is diffusion imaging appearance an independent predictor of outcome after ischemic stroke? *Neurology*, 59(9):1381–7, 2002.

[183] P. J. Hand, J. M. Wardlaw, C. S. Rivers, P. A. Armitage, M. E. Bastin, R. I. Lindley, and M. S. Dennis. Mr diffusion-weighted imaging and outcome prediction after ischemic stroke. *Neurology*, 66(8):1159–63, 2006.

[184] N. J. Beauchamp, A. M. Ulug, T. J. Passe, and P. C. van Zijl. Mr diffusion imaging in stroke: review and controversies. *RadioGraphics*, 18(5):1269–1283, 1998.

[185] N. kuei Chen, A. Guidon, H.-C. Chang, and A. W. Song. A robust multi-shot scan strategy for high-resolution diffusion weighted {MRI} enabled by multiplexed sensitivity-encoding (muse). *NeuroImage*, 72(0):41 – 47, 2013.

[186] E. M. Haacke, E. D. Lindskogj, and W. Lin. A fast, iterative, partial-fourier technique capable of local phase recovery. *Journal of Magnetic Resonance*, 92(1):126–145, 1991.